TU Delft

Delft University of Technology

MSc Thesis Report

Transfer of Polarized Light in an (Exo)planetary Atmosphere-Ocean System

Victor Trees

June 10, 2020

Transfer of Polarized Light in an (Exo)planetary Atmosphere-Ocean System

by

Victor Trees

to obtain the degree of Master of Science
at the Delft University of Technology,
to be defended publicly on Friday September 7, 2018

Student number:	4115937	
Thesis committee:	Prof. Dr. L.L.A. Vermeersen	Delft University of Technology
	Dr. D.M. Stam	Delft University of Technology, (Supervisor)
	Dr. A. Menicucci	Delft University of Technology
	Dr. J.F. de Haan	Royal Netherlands Meteorological Institute (KNMI)

Faculty of Aerospace Engineering
Delft University of Technology
The Netherlands

An electronic version of this thesis is available at http://repository.tudelft.nl/.

Cover page image: specular reflection in the ocean observed from space, retrieved from VuNature.com.

TU Delft

Abstract

Fresnel reflection of starlight in the oceans of exoplanets results in two main phenomena: (1) a glint in the exoplanetary ocean, whose size increases with wind speed, and (2) a maximum degree of polarization at the Brewster angle. The corresponding features in the planetary phase curve, i.e. the flux and degree of polarization of the reflected light by the exoplanet orbiting its parent star, have been studied before. However, these studies did not use (1) horizontally inhomogeneous models, allowing the analysis of the glint appearing and hiding behind patchy clouds and (2) a set of consecutive wavelengths together with (3) a gas layer on top of the clouds. We present the phase curves of the (polarized) flux and degree of polarization of oceanic exoplanets with patchy cloud covers and a substellar cloud for tidally-locked planets. We discuss the spectropolarimetric signatures that could potentially be observed in the near future or that may be considered in the design of future telescopes. We show that (1) a previously suggested method to detect an ocean on an exoplanet, based on the shift of the peak value of the degree of polarization towards the Brewster angle, is sensitive to atmospheric surface pressure, (2) the clouds are not necessarily a limiting factor for detecting an ocean when a gas layer on top of the cloud is considered and a set of wavelengths is used, (3) the phase curves of the different wavelengths intersect in one point whose location could help estimating the cloud fraction and that (4) such an intersection in the polarized flux could be observed in the presence of an ocean for surface pressures up to 10 bar and cloud fractions up to 95%, while it never occurs in the absence of an ocean. We conclude that this color reversal in the polarized flux could potentially be used for detecting oceans on exoplanets.

Delft, August 2018

Contents

Acknowledgements vii

Background and Motivation ix

Research Objective and Report Structure xi

I Transfer of Polarized Light in Planetary Atmospheres: Basic Principles and Definitions 1

1 Introduction to Polarized Light 3

1.1 Intensity and Flux . . . 3
1.2 Polarization Ellipse . . . 4
1.3 Stokes Polarization Parameters . . . 5
1.4 Measurement of the Stokes Polarization Parameters . . . 7

2 Scattering of Light in Planetary Atmospheres 9

2.1 Single Scattering . . . 9
2.1.1 Basic Principles of Single Scattering . . . 9
2.1.2 Special Cases of Single Scattering . . . 11
2.1.3 Single Scattering Matrix . . . 13
2.1.4 The Phase Matrix . . . 13
2.2 Multiple Scattering . . . 16
2.2.1 Orders of Scattering . . . 16
2.2.2 Multiple-Scattering Matrices . . . 17
2.3 Fourier Decomposition . . . 19

3 Adding-Doubling Method 21

3.1 Basic Principles of the Adding-Doubling Method . . . 21
3.2 Expansion in Fourier series . . . 24
3.3 Supermatrices . . . 24
3.4 Reflecting Ground Surfaces . . . 25
3.5 Stokes Vector Retrieval . . . 26

II Transfer of Polarized Light in an Atmosphere-Ocean System 29

4 Fresnel Reflection and Transmission 31

4.1 Fresnel's Reflection and Transmission Coefficients . . . 31
4.1.1 $\vec{\mathbf{E}}$ is Perpendicular to the Scattering Plane . . . 32
4.1.2 $\vec{\mathbf{E}}$ is Parallel to the Scattering Plane . . . 36
4.1.3 Brewster Angle and Grazing Angles . . . 39
4.2 Amplitude Matrices for Fresnel Reflection and Transmission . . . 40
4.3 Fresnel's Reflection and Transmission Matrices for Polarized Light . . . 42
4.4 Conservation of Energy at the Fresnel Interface . . . 43
4.4.1 Coherent Stokes Vector . . . 43
4.4.2 Diffuse Stokes Vector . . . 45
4.5 Reflection and Transmission Matrix Elements versus Incidence Angle . . . 48
4.5.1 Air-incident Radiance . . . 48
4.5.2 Water-incident Radiance . . . 48

5 Reflection and Transmission by the Wind-Ruffled Air-Water Interface 53
5.1 Reflection by a Wind Ruffled Air-Water Interface . . . 53
5.2 Slope Distribution Models of Ocean Surface Waves . . . 56
5.2.1 The Cox and Munk Model . . . 56
5.2.2 Alternative Slope Distribution Models . . . 57
5.2.3 Comparison of the Slope Distribution Models . . . 58
5.3 The Reflection Matrix for a Wind Ruffled Air-Water Interface . . . 59
5.4 Transmission by a Wind Ruffled Air-Water Interface . . . 61
5.5 The Transmission Matrix for a Wind Ruffled Air-Water Interface . . . 63
5.6 Reflection and Transmission Matrices for Illumination from Below . . . 66
5.6.1 Water-incident Reflection . . . 66
5.6.2 Water-incident Transmission . . . 67
5.7 Energy Balance and Wave Shadows . . . 68
5.8 Polar Plots of the Interface Reflection and Transmission . . . 72

6 Reflection by the Ocean System (Water + Interface) 77
6.1 Whitecaps . . . 77
6.2 Scattering of Polarized Light in the Ocean Water . . . 78
6.3 Adding the Bulk Ocean to the Interface . . . 80
6.4 Polar Plots of the Ocean Reflection . . . 81

III Flux and Degree of Polarization of Starlight Reflected by Extrasolar Planets 83

7 Phase Curves of Exoplanet Models Containing Oceans 85
7.1 Integration over the Planetary Disk . . . 85
7.2 Horizontally Homogeneous Planets . . . 88
7.2.1 Lambertian Planet vs. Ocean Planet . . . 88
7.2.2 Effect of Ocean Color . . . 92
7.2.3 Effect of Wind Speed . . . 92
7.2.4 Effect of Surface Pressure . . . 96
7.2.5 Cloudy Ocean Planet . . . 100
7.2.6 Effect of Refractive Index . . . 104
7.3 Horizontally Inhomogeneous Planets . . . 106
7.3.1 Patchy Clouds . . . 106
7.3.2 Substellar Cloud . . . 111
7.3.3 Quasi Horizontally Inhomogeneous Planets . . . 115

IV Discussion, Concluding Remarks and Recommendations 121

8 Discussion and Concluding Remarks 123

9 Recommendations 127

A Appendix 129
A.1 Relation between the Amplitude and Scattering Matrix . . . 129
A.2 Second Order of Scattering . . . 131
A.3 Derivation of the Adding Equations . . . 133
A.4 Supermatrix Multiplications . . . 139
A.4.1 Square Supermatrices . . . 139
A.4.2 Rectangular Supermatrices . . . 140

B Appendix 143
B.1 Brewster Angle . . . 143
B.2 Total Internal Reflection . . . 145
B.3 Computing the Bulk Ocean Reflection with a Bio-optical Model for Case 1 Waters . . . 149
B.4 Effect of Assumption of Geometric Water Layer Thickness . . . 153

Bibliography 155

Acknowledgements

I have had the honor of working together with and learning from several radiative transfer experts during the course of this work to whom I wish to express my sincerest gratitude. First of all, I am thankful to my supervisor, Dr. Daphne M. Stam (Delft University of Technology), who has supported me and directed me when necessary while at the same time giving me the freedom and responsibility to independently manage the project. Her exceptional expertise in both radiative transfer and planetary sciences, her critical view and her willingness to share her knowledge contributed to the development of my passion for planetary sciences. I am indebted to her for her faith in me. I gratefully acknowledge Dr. Johan F. de Haan (KNMI/Royal Netherlands Meteorological Institute), for our productive discussions and his technical questions about the early results. These questions helped me to find detailed explanations for the features in the code output. It was an honor to be able to evaluate my ideas and doubts with him, which greatly strengthened this research. Also, I want to thank him for reviewing this thesis and for his assessment during the defense. I am thankful to Dr. Piet Stammes (KNMI), for his interest in my research and suggestions he made while I was still doing my internship at KNMI. I want to thank Dr. Loïc Rossi (Delft University of Technology), for his clear explanation of the PyMieDAP code and his critical review during the Midterm Meeting. I also owe many thanks to Dr. Jacek Chowdhary (NASA/Goddard Institute of Space Studies), for our e-mail discussions, which gave me the confidence to follow a similar numerical approach to the one he applied in his PhD Thesis for extending the adding-doubling method, and to Dr. Michael Zugger (Pennsylvania State University), who provided me with an explanation of the code he used for his papers that allowed for a better comparison of our work. I want to deeply thank Prof. Dr. Bert L.A. Vermeersen and Dr. Alessandra Meniccuci, for their time and effort to review this thesis and for their assessment during the defense.

Special thanks go to my friend and fellow student Floor Melman who has a talent for being able to give critique of research that is not part of his expertise. This thesis would not have reached this quality without his constructive comments. I would like to deeply thank my friend Max Verhoeven, who helped me editing the figures in this report. This thesis has greatly benefited from his graphic design skills. During this research, I also made a new friend, Ashwyn Groot, who worked on his master thesis in the same research group. I want to thank Ashwyn for all his questions every time I showed him new results and for our endless online discussions. I truly believe that our cooperation made both our theses a bigger success.

Lastly, I would like to thank my parents and my sister, who supported me in many ways the past six months. Their patience and understanding gave me the peace to write much content of this report at my home town. Special thanks go to my mother, who carefully read this thesis. She has a talent for detecting typos, which saved me a lot of time in the last days of writing this work. I am deeply grateful for all her corrections and suggestions.

Background and Motivation

Since the first confirmed exoplanet discovery in January 1992 (Wolszczan and Frail 1992), the discovery of 3796 planets outside our solar system, often called *exoplanets*, in 2840 planetary systems is confirmed,[1] primarily using radial velocity measurements[2] and the transit method.[3] This number is expected to grow rapidly with for example the measurements of TESS (Transiting Exoplanet Survey Satellite) launched in April 2018. It is expected that TESS will discover more than a thousand planets smaller than Neptune, including dozens that are comparable in size to Earth (Ricker et al. 2014). In depth research on these exoplanets and their atmospheres will be conducted by e.g. the NIRCam (Near Infrared Camera) (Beichman et al. 2014) and MIRI (Mid-Infrared Instrument) (Boccaletti et al. 2015) which has been mounted on the James Webb Telescope, scheduled to be launched in 2021.[4]

The analysis of the properties of extrasolar planetary systems is not necessarily limited to flux measurements at various wavelengths. Light that is perceived by our eyes has hardly ever traveled directly from its source. Most of this light has been reflected somewhere by a surface or has been scattered by molecules, dust or water droplets. In the processes of reflection and scattering, light may become polarized meaning that the oscillations of the light wave are confined to certain directions. In general, light originating from a solar type star may be considered as unpolarized (Kemp et al. 1987) and usually gets polarized by scattering in a planetary atmosphere or reflection by an ocean or ground surface. This property may allow distinguishing between stellar light and light reflected by a planet through the measurement of the degree and direction of polarization, also known as *polarimetry*. Additionally, by modelling the polarimetric signal the dimensions, shape and composition of the scatterers and directionality of the surface reflection may be characterized since they may strongly influence the degree and direction of polarization of the scattered light (Hansen and Travis 1974).

Polarimetry has widely been applied in Earth-observation, for example for the retrieval of aerosol properties by satellites (Boesche et al. 2009; Levy et al. 2004; Mishchenko and Travis 1997), but also for studying the atmospheres of Venus (Hansen and Hovenier 1974*a*,*b*), Mars (Shkuratov et al. 2005) and the giant planets of our solar system (see e.g. Joos et al. 2005). Forward radiative transfer modelling of light reflected by exoplanets including polarimetry was performed by Stam (2008), who investigated the spectropolarimetric features of the exoplanets in their planetary phase curves. These sample signals are needed for the design and development of instruments for directly detecting (polarized) reflected light from Earth-like exoplanets. An example of such an instrument is EPICS (Earth-like Planets Imaging Camera Spectrograph) (Kasper et al. 2010), envisioned for the E-ELT (European Extremely Large Telescope) which is currently under construction in Chile.

Being able to realistically model the spectropolarimetric features of the presence of an ocean in the phase curves of *Earth-like* exoplanets is of particular interest because (1) more than 70 % of the Earth's surface is covered by an ocean (NOAA 2016), (2) the presence of liquid water requires an atmosphere with a significant pressure and moderate surface temperatures and (3) the presence of liquid water is often considered as the pre-requisite for a planet to be able to harbor life because of its beneficial chemical properties as a solvent. Stam (2008) computed the flux and degree of polarization as functions of wavelength and planetary phase angle for planets with a specular reflecting ocean, but did not include wind-driven oceanic surface waves which give rise to a wide mirror image of the star in the ocean surface, called the stellar glint. This glint may influence the observed brightness as functions of planetary phase angle since the Fresnel reflection by the air-water interface is stronger at larger reflection angles and, during the orbital revolution of the planet around its parent star, the fraction of disk illumination (and so the glint contribution) varies as seen from the observer for orbital inclinations larger than zero. With developing wind speeds the shadows of the waves and reflection by foam and whitecaps need to be taken into account as well. Furthermore, the absorption and

[1] `http://exoplanet.eu/catalog/`, retrieved on: 06-30-2018.
[2] Measurements of the redshift of the light of the parent star may indicate the motion of the parent star due to the gravitational attraction of an orbiting planet.
[3] Measurements of starlight which is periodically dimmed may be used to detect a transiting planet between the star and the observer.
[4] `https://jwst.nasa.gov/facts.html`, retrieved on 06-30-2018.

scattering of light at various wavelengths in the subinterface oceanic water layer depends strongly on phytoplankton chlorophyll concentration in the water. The traceability of all these ocean related parameters and how they together affect the reflected flux and degree of polarization by an exoplanet at various wavelengths are still unanswered questions.

The detectability of an ocean with a rough wind-ruffled ocean surface on extrasolar planets has been studied before. For example, Williams and Gaidos (2008) found strong signatures of the glint in the planet's crescent phase, but they neglected the atmospheric effects such as Rayleigh scattering and scattering by clouds. Zugger et al. (2010, 2011*a*) did include atmospheric Rayleigh scattering, scattering by maritime aerosols in the atmosphere and Lambertian reflecting clouds. They found a shift of the polarization peak in the planetary phase curve towards higher planetary phase angles, which is normally around 90 degrees due to Rayleigh scattering, caused by the polarization by the Fresnel reflection from the air-water interface at the Brewster angle. They concluded, however, that the retrieval of a single explanation of the polarimetric features observed in the received signal may be challenging when a scattering atmosphere with clouds, aerosols, varying wind speeds and combinations of them are introduced in the models.

It should be noted that the planet models of Zugger et al. (2010, 2011*a*,*b*) are *horizontal homogeneous*, that is, the atmosphere and surface are invariant with latitude and longitude. Therefore, they could, for example, not study the signatures of the glint appearing and hiding behind *patchy clouds*, which are clouds of varying horizontal shapes randomly located over the planet. Another example of a horizontal inhomogeneity are multiple surface types, either land or ocean, on the planet. It is expected that such horizontal inhomogeneities induce rapid oscillations in the planetary phase curve signal while the planet rotates around its axis. A recent paper of Rossi and Stam (2017) shows the features that could potentially be observed in the phase curves of such *horizontally inhomogeneous* exoplanet models using various cloud cover types. Their ocean reflection was, however, again modeled using a flat air-water interface, yielding an infinitely narrow beam of reflected light representing the stellar glint.

An interesting feature in the phase curve for polarization curve is the rainbow which is a strong indicator of the presence of spherical particles in the atmosphere, such as cloud droplets (Bailey 2007; Hansen and Travis 1974; Karalidi et al. 2012). Unfortunately, Zugger et al. (2010, 2011*a*,*b*) modeled their clouds as Lambertian (i.e. isotropically and unpolarized) reflecting surfaces, and could therefore not see the rainbow feature of the clouds around 40 degrees planetary phase angle. Also, they did not include a gaseous layer on top of the clouds causing Rayleigh scattering above the clouds. At short wavelengths (300 nm) Rossi and Stam (2017) showed that Rayleigh scattering above the clouds becomes increasingly significant with increasing cloud top pressures (corresponding to lower cloud top altitudes).

All authors mentioned above did not model the planetary phase curves of oceanic exoplanets using a large *set of wavelengths*. Modelling the planetary phase curves for a set of consecutive wavelengths allows the analysis of the gradual spectral behaviour of the reflected light along the planetary phase angles. This may give additional insight into the sources causing the observable features in the phase curves since the spectral dependency of the scattered light may strongly be determined by its main contributors. For example, Fresnel reflection from the ocean is approximately equally intensive at all wavelengths in the visible domain, while the effectiveness of Rayleigh scattering is significantly larger at shorter wavelengths. Zugger et al. (2011*b*) already concluded that at longer wavelengths (in the near infra-red) the ocean detectability increases because of less effective Rayleigh scattering from the atmosphere while the Fresnel reflection by the ocean is still present. However, they did not use multiple wavelengths in the visible domain, and, they did not study the polarized flux separately.

The aim of this study is to present the planetary phase curves of the flux and degree of polarization of light reflected by realistic oceanic exoplanets by implementing the reflection of light by an ocean in the local planetary radiative transfer algorithm. We model these phase curves at a set of consecutive wavelengths and allow the planets to be either horizontally homogeneous or inhomogeneous when analyzing the effect of the cloud cover. Also, using this set of wavelengths, we compute the 'true' RGB-color of the model planet when the planet orbits its parent star. We discuss the spectropolarimetric features in the phase curves of different types of oceanic exoplanets that could potentially be observed in the near future or that may be considered in the design of future telescopes.

Research Objective and Report Structure

From the Background and Motivation pages, we state the following research objective:

The research objective is to investigate the signatures of an ocean in the planetary phase curves of the flux, polarized flux and degree of polarization of light reflected by different types of oceanic exoplanets orbiting solar type stars, for a set of wavelengths, by implementing a realistic ocean reflection model in the local radiative transfer algorithm and by allowing the planets to have horizontally inhomogeneous cloud covers.

This report is divided into four parts.

The aim of Part I is to expound in a systematic and concise way the physical principles of the transfer of polarized light in the planetary atmosphere-ocean system and to give an overview of the numerical methods that are used. First, Chapter 1 explains the basic principles of polarized light and its mathematical representations. Chapter 2 then discusses how this light beam is affected by the molecules and particles in the atmosphere. Both Chapters 1 and 2 provide the physical background for Chapter 3 which treats the computation of the radiative transfer of polarized light in the atmosphere by the algorithm of de Haan et al. (1987) called the adding-doubling method.

In Part II the implementation of the reflection by the ocean in the adding-doubling method are discussed. First, the theory of Fresnel reflection and transmission is treated in Chapter 4, such that we can set up the reflection and transmission matrices of the air-water interface in Chapter 5. Then, in Chapter 6, it is explained how the scattering of underwater light can be added such that the reflection by the complete ocean is modeled.

A full solution of the reflection by the atmosphere-ocean system locally on an exoplanet is obtained from Part I and Part II, which we use in Part III to study the signal in the direction of the observer. Chapter 7 explains what the properties of the polarized light emerging from the top of the atmosphere of the planet may look like when captured by an instrument in our solar system. The features indicating the presence of an ocean are the guiding principle in this chapter.

Finally, in Part IV we present a discussion of our results and concluding remarks in Chapter 8 and some recommendations for future studies in Chapter 9.

I

Transfer of Polarized Light in Planetary Atmospheres: Basic Principles and Definitions

1 Introduction to Polarized Light

In this chapter, the physical principles of polarized light will be discussed that will be relevant in the remainder of this report. First the representations of radiation will be treated in Section 1.1. Then, starting from the plane-wave solution of Maxwell's equations, the nomenclature for describing polarization is discussed in Section 1.2 and in terms of the Stokes vector in Section 1.3. Finally, Section 1.4 presents the Stokes intensity formula for the measurement of the four Stokes polarization parameters.

1.1. Intensity and Flux

The classical radiative transfer theory states that the radiative energy is supposed to be transported in a medium across surface elements along so-called pencils of rays (Chandrasekhar 1950, Section 1.2). The radiative energy $\mathrm{d}E$ of the pencil (see Figure 1.1) depends on the frequency interval $(\nu, \nu + \mathrm{d}\nu)$, area of the surface element $\mathrm{d}\sigma$, solid angle $\mathrm{d}\Omega$ and time $\mathrm{d}t$. Electromagnetic radiation travelling through a medium, such as a planetary atmosphere or an ocean, is commonly quantified by its (specific) intensity I expressed in the SI-units $\mathrm{W\,Hz^{-1}m^{-2}sr^{-1}}$ (Hovenier et al. 2004).

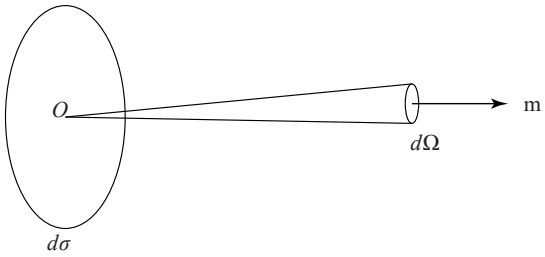

Figure 1.1: A graphical representation of a pencil of light rays. Surface element $\mathrm{d}\sigma$ and solid angle $\mathrm{d}\Omega$ are used to define the intensity at a point O in the direction m of a unit vector $\boldsymbol{m}$. (Hovenier et al. 2004, Fig. 1.1).

The *net flux* however is defined as the radiative energy per unit of frequency interval, surface area and time and can be obtained by the following integration over solid angle Ω (Hovenier et al. 2004, Eq. 1.2)

$$\pi \boldsymbol{\Phi} = \int \mathrm{d}\Omega \boldsymbol{I} \cos\theta \tag{1.1}$$

where θ is the angle between the intensity vector and the normal vector to surface element $\mathrm{d}\sigma$. A large amount of descriptions of intensity and flux exists in literature (see, e.g., Chandrasekhar 1950; van de Hulst 1957). In this report the terminology of Hovenier et al. (2004) is followed, i.e. considering (specific) intensity, radiance and brightness as something per unit solid angle contrary to (net) flux, irradiance or flux density which decrease by the inverse of the distance to the light source squared.

1.2. Polarization Ellipse

In empty space a changing electric field produces a magnetic field and a changing magnetic field will, in turn, produce an electric field. The Scottish physicist James Clerk Maxwell (1831-1879) consolidated the description of all electric and magnetic phenomena into one set of four equations, known as Maxwell's equations. Nowadays the derivation of the solution for the electric field and magnetic field as functions position and time is treated in many academic books (see e.g. Giancoli 2008, Sec. 31.5). An important result is the harmonic behavior of electromagnetic radiation described by the wave equation, e.g. for the electric field component

$$\nabla^2 \mathbf{E}(\mathbf{r},t) = \frac{1}{v^2}\frac{\partial^2 \mathbf{E}(\mathbf{r},t)}{\partial t^2} \tag{1.2}$$

where $\mathbf{E}$ is the electric field vector, $\mathbf{r} = \mathbf{r}(x,y,z)$ is the position vector and v is the propagation speed of the electromagnetic wave. In 1818 Fresnel and Arago discovered that light consisted of only transverse components, that is, assuming the direction of propagation in the positive z direction (see Goldstein 2003)

$$E_x = E_{0x} e^{i(\omega t - kz - \epsilon_x)} \tag{1.3a}$$

$$E_y = E_{0y} e^{i(\omega t - kz - \epsilon_y)} \tag{1.3b}$$

where E_{0x} and E_{0y} are the positive amplitudes, $i = \sqrt{-1}$, ω is the circular frequency, k is the wave number $2\pi/\lambda$, t is the time and ϵ_x and ϵ_y are the initial phases. Instead of the x and y axes van de Hulst (1957) and Chandrasekhar (1950) defined the r and l axes perpendicular and parallel to *the plane of reference*[1] respectively. In the field far from the radiation source, which is referred to as the *far field* in this report, a plane wave[2] can be assumed. Since the electric vector is transverse the l component may be presented by its phasor, i.e. the real part of Equation 1.3, according to (van de Hulst 1957)

$$\begin{aligned} E_l &= Re[E_{0l} e^{i(\omega t - kz - \epsilon_l)} e^{-i(\pi/2)}] \\ &= E_{0l}\cos(\omega t - kz - \epsilon_l - \pi/2) \\ &= E_{0l}\sin(\omega t - kz - \epsilon_l) \end{aligned} \tag{1.4}$$

Similarly, for the r direction

$$E_r = E_{0r}\sin(\omega t - kz - \epsilon_r) \tag{1.5}$$

where $\mathbf{r}\times\mathbf{l}$ is the direction of propagation. The phase shift of $\pi/2$ was introduced to initialize the wave at point O. Considering a monochromatic beam at point O (such that $z = 0$) the components of the electric field vector are expressed by

$$E_l = E_{0l}\sin(\omega t - \epsilon_l), \qquad E_r = E_{0r}\sin(\omega t - \epsilon_r) \tag{1.6}$$

which are the definitions stated by Hovenier et al. (2004) and Hovenier and van der Mee (1983) and will be used in the remainder of this report.

As the electric field propagates in the $\mathbf{r}\times\mathbf{l}$ direction the projection of the resultant of the vectors E_l and E_r on the xy-plane at point O describe an ellipse. The mathematical description of the ellipse (see e.g. Goldstein 2003, Sec. 3.2) is given by

$$\frac{(E_r)^2}{E_{0r}^2} + \frac{(E_l)^2}{E_{0l}^2} - 2\frac{E_r}{E_{0r}}\frac{E_l}{E_{0l}}\cos\delta = \sin^2\delta \tag{1.7}$$

where

$$\delta = \epsilon_l - \epsilon_r \tag{1.8}$$

It may be noted that characteristics of the ellipse illustrated in Figure 1.2[3] are easily derived from Equation 1.7 by for example considering $\delta = 0$ or π. Equation 1.7 reduces to

$$E_l = \pm\left(\frac{E_{0l}}{E_{0r}}\right)E_r \tag{1.9}$$

[1] The plane of reference is equivalent to the scattering plane in scattering problems, which is the plane through the direction of the incident light beam and that of the scattered beam by, for example, a particle. Scattering will be discussed in Chapter 2 in more detail.

[2] The electric and magnetic fields are perpendicular to each other and to the direction of propagation at any point in the far field (Giancoli 2008).

[3] Care should be taken with definition of the positive direction of propagation $\mathbf{r}\times\mathbf{l}$. For example, Mishchenko et al. (2002) presents the polarization ellipse with the direction of propagation towards the reader and Hovenier et al. (2004) and van de Hulst (1957) presented the polarization ellipse with the direction of propagation into the page.

which may be recognized as the equation of a straight line with slope $\pm(E_{0l}/E_{0r})$. In this case the wave is *linearly polarized* with slope $\pm(E_{0l}/E_{0r})$. If $E_{0l} = \pm E_{0r}$ the wave is called *linear* $+45^o$ *polarized* $(L+45)$ or *linear* -45^o *polarized* $(L-45)$. Other polarization states are *linear horizontally polarized* light (LHP), *linear vertically polarized* light (LVP), *right circularly polarized* light (RCP) and *left circularly polarized* light (LCP) (see Goldstein 2003, Sec. 4.2 and 4.3).

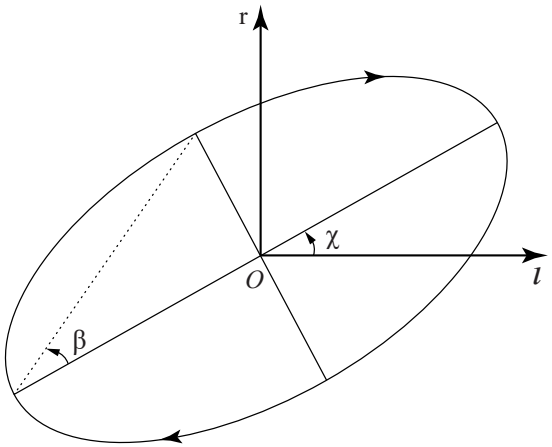

Figure 1.2: Polarization ellipse. The direction of propagation is into the paper perpendicular to **r** and **l** for this right-handed polarized wave (Hovenier et al. 2004, Sect. 1.2).

The ellipse sketched in Figure 1.2 is also known as the *polarization ellipse*. The angle β and χ are defined such that $-\pi/4 \leq \beta \leq \pi/4$ and $0 \leq \chi < \pi$, the latter one being the angle between the major axis and the positive l-axis. The ellipticity of the ellipse is given by $|\tan\beta|$.

1.3. Stokes Polarization Parameters

The states of polarization as mentioned in Section 1.2 may be expressed in the Stokes parameters introduced by Sir George Gabriel Stokes in 1852. These parameters are usually represented in the Stokes vector (see e.g. Hovenier et al. 2004; Mishchenko et al. 2002) which is not a geometrical vector but a representation of the state of polarization of the wave. The Stokes parameters can be derived from the polarization ellipse (see e.g. Goldstein 2003, Sec. 4.2) resulting in

$$I = E_{0l}^2 + E_{0r}^2 \tag{1.10a}$$
$$Q = E_{0l}^2 - E_{0r}^2 \tag{1.10b}$$
$$U = 2E_{0l}E_{0r}\cos\delta \tag{1.10c}$$
$$V = 2E_{0l}E_{0r}\sin\delta \tag{1.10d}$$

The amplitude of the major and the minor axis of the polarization ellipse may be expressed by

$$E_{major} = E_0\cos\beta\sin\omega t, \qquad E_{minor} = E_0\sin\beta\cos\omega t \tag{1.11}$$

From this result, the Stokes parameters may be derived again, now as functions of E_0, β and χ (see e.g. Hovenier et al. 2004, Sec. 1.2).

$$I = (E_0)^2 \tag{1.12a}$$
$$Q = (E_0)^2\cos 2\beta\cos 2\chi \tag{1.12b}$$
$$U = (E_0)^2\cos 2\beta\sin 2\chi \tag{1.12c}$$
$$V = (E_0)^2\sin 2\beta \tag{1.12d}$$

Vice versa, once the Stokes parameters have been measured, the angle β and χ may be obtained by $\tan 2\beta = V/\sqrt{Q^2+U^2}$ and $\tan 2\chi = U/Q$. The expressions of Equations 1.12a to 1.12d are very useful for the rotation of the polarization ellipse. Considering a rotation of the l and r axis through an angle α which is assumed to be positive in the counterclockwise direction when looking in the direction of propagation, the transformation $\chi \rightarrow \chi - \alpha$ needs to be performed. By substituting $\chi - \alpha$ for χ into Equations 1.12a to 1.12d the following rotation matrix for the Stokes vector may be derived (Hovenier and van der Mee 1983, Eq. 18)

$$\boldsymbol{L}(\alpha) = \begin{pmatrix} 1 & 0 & 0 & 0 \\ 0 & \cos 2\alpha & \sin 2\alpha & 0 \\ 0 & -\sin 2\alpha & \cos 2\alpha & 0 \\ 0 & 0 & 0 & 1 \end{pmatrix} \tag{1.13}$$

In nature light is usually quasi-monochromatic, that is, the amplitudes of the electric field are harmonic functions of time as well with an oscillating frequency range $\Delta\omega$ small compared to the circular frequency of the actual sinusoid. The observables are obtained by taking the average over the time of observation (assume infinite) of the Stokes parameters (Goldstein 2003), i.e.

$$I = \langle E_l E_l^* + E_r E_r^* \rangle = \langle E_{0l}^2 + E_{0r}^2 \rangle = \langle (E_0)^2 \rangle \tag{1.14a}$$
$$Q = \langle E_l E_l^* - E_r E_r^* \rangle = \langle E_{0l}^2 - E_{0r}^2 \rangle = \langle (E_0)^2 \rangle \cos 2\beta\cos 2\chi \tag{1.14b}$$
$$U = \langle E_l E_r^* + E_r E_l^* \rangle = \langle 2E_{0l}E_{0r}\cos\delta \rangle = \langle (E_0)^2 \rangle \cos 2\beta\sin 2\chi \tag{1.14c}$$
$$V = i\langle E_l E_r^* - E_r E_l^* \rangle = \langle 2E_{0l}E_{0r}\sin\delta \rangle = \langle (E_0)^2 \rangle \sin 2\beta \tag{1.14d}$$

where the asterisk denotes the complex conjugate and by Schwarz inequality

$$I^2 \leq Q^2 + U^2 + V^2 \tag{1.15}$$

is always satisfied for any state of polarized light. Fully polarized light is computed in case of an equality sign, whereas an inequality sign indicates partly or unpolarized (i.e. elliptically polarized) light. The degree of polarization is defined by (Hansen and Travis 1974)

$$P = \frac{I_{pol}}{I_{tot}} = \frac{\sqrt{Q^2+U^2+V^2}}{I} \qquad 0 \leq P \leq 1 \tag{1.16}$$

and the degrees of circular and linear polarization are respectively

$$P_c = \frac{V}{I} \qquad P_l = \frac{\sqrt{Q^2+U^2}}{I} \tag{1.17}$$

In the consideration of a disk-integrated signal of a planet which is symmetric with respect to the planetary scattering plane, the disk integrated Stokes parameter U will be zero and the degree of linear polarization is defined as (Rossi and Stam 2017):

$$P_s = \frac{-Q}{F} \tag{1.18}$$

where the direction of polarization is included in the definition. That is, P_s is positive for perpendicular polarization with respect to the planetary scattering plane and negative if it is parallel to the planetary scattering plane. In the remainder of this report, we will, however, consider the total degree of polarization P ranging from 0 to 1 (Equation 1.16).

It is important to realize that variations on the representation of the Stokes parameters as given by Equation 1.14 occur in literature (see, e.g. Goldstein 2003, Section 4.6 and 4.7). The circular polarization (CP) representation may be used for the sake of simpler transformations[4](see Hovenier and van der Mee 1983, Eq. 22). For some applications it may be convenient to express the polarized light in the time averaged products themselves stored in a coherency matrix (see e.g. Mishchenko et al. 2002, Sec. 2.6). Mishchenko et al. (2002) introduced a minus sign in the Stokes parameter U.

1.4. Measurement of the Stokes Polarization Parameters

The Stokes polarization parameters described in Section 1.3 are quantities that can be measured because they are formulated as intensity parameters, i.e. the intensity is defined by (Goldstein 2003, Eq. 4.54)

$$I = E \cdot E^* \tag{1.19}$$

An incident monochromatic light beam may be considered to be phase shifted by a retarder in a polarization filter as illustrated in Figure 1.3 such that (see Goldstein 2003, Sec. 4.4)

$$E_l' = E_l e^{i\varphi/2} \qquad E_r' = E_r e^{-i\varphi/2} \tag{1.20}$$

Subsequently the light beam may be rotated over an angle θ in the polarization filter by a so-called polarizer. Goldstein (2003) showed that the intensity measured after passing the retarder and polarizer equals

$$I(\theta,\varphi) = \frac{1}{2}\left[\left(E_l E_l^* + E_r E_r^*\right) + \left(E_l E_l^* - E_r E_r^*\right)\cos 2\theta + \left(E_l E_r^* + E_r E_l^*\right)\cos\varphi \sin 2\theta + i\left(E_l E_r^* - E_r E_l^*\right)\sin\varphi \sin 2\theta\right] \tag{1.21}$$

The Stokes polarization parameters between the round brackets may be recognized in Equation 1.21. The Stokes polarization parameters can therefore be obtained by simply varying the phase shift φ in the retarder and the rotation angle θ by the polarizer which may be expressed as (see Hansen and Travis 1974, Sec. 1.2)

$$I = I(0°,0°) + I(90°,0°) \tag{1.22a}$$
$$Q = I(0°,0°) - I(90°,0°) \tag{1.22b}$$
$$U = I(45°,0°) - I(135°,0°) \tag{1.22c}$$
$$V = I(45°,90°) - I(135°,90°) \tag{1.22d}$$

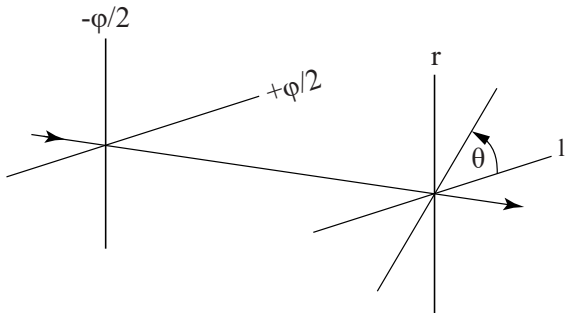

Figure 1.3: Measurement of the Stokes polarization parameters (Goldstein 2003, Section 4.4), φ indicates the phase shift and θ is the rotation angle.

[4]The entries $Q + iU$ and $Q - iU$ are used which have simpler rotation properties than Q and U.

It may be concluded that at least at four angles the intensity of the light beam needs to be measured in order to obtain the Stokes parameters. In modern polarimetry, however, various types of modulators are used rather than polarization filters (see Keller 2006; Schmid et al. 2006).

2

Scattering of Light in Planetary Atmospheres

In Chapter 1 the definitions to describe polarized light were introduced. The aim of this chapter is to present a brief summary of the principles of scattering of (polarized) light in planetary atmospheres that will be relevant for the subsequent chapters of this report.

The restrictions laid by van de Hulst (1957) in the discussion of the basic scattering theory (see van de Hulst 1957, Sec. 1.2) were that of *coherent*[1] and *independent scattering*. Independent scatterers are for example cloud droplets and dust grains in the atmosphere, separated sufficiently far from each other, such that no systematic phase relations exist between the electromagnetic waves scattered by neighbouring particles. Once these assumptions are made, the theoretical modeling of light scattering in planetary atmospheres may be divided into two categories: scattering for which a direct proportionality exists of the extinction to the number of particles, so-called *single scattering* (discussed in Section 2.1), and scattering without such a direct proportionality, so-called *multiple scattering* (discussed in Section 2.2).

2.1. Single Scattering

This section treats the basic principles of single scattering, some special cases of single scattering and the phase matrix for the description of the single scattering event with respect to the scattering plane.

2.1.1. Basic Principles of Single Scattering

Let us consider a plane-parallel monochromatic light beam as described by Equations 1.6 incident on a single particle of arbitrary size and shape as illustrated in Figure 2.1. The light beam scattered by the particle at a distance R from the particle may be written in the combined form as (see van de Hulst 1957, Sec. 4.4)

$$\begin{pmatrix} E_l \\ E_r \end{pmatrix} = \begin{pmatrix} S_2(\Theta,\varphi) & S_3(\Theta,\varphi) \\ S_4(\Theta,\varphi) & S_1(\Theta,\varphi) \end{pmatrix} \frac{e^{-ikR+ikz}}{ikR} \begin{pmatrix} E_l^0 \\ E_r^0 \end{pmatrix} \tag{2.1}$$

where the 2 x 2 matrix **S** is defined as the *amplitude matrix* as functions of scattering angle Θ and azimuth φ (see Figure 2.1), the incident electric field components are denoted by the subscript '0' and $k = 2\pi/\lambda$ is the wave number. After the scattering event by the particle by the angle Θ the electric field components in the l and r directions are transformed (for $\Theta \neq 0$). Van de Hulst (1957) derived the amplitude matrices for a rotation of 180 degrees about the bisectrix (analogous to *reciprocity*[2]), mirroring with respect to the scattering plane and mirroring with respect to the bisectrix plane which are respectively

$$\begin{pmatrix} S_2(\Theta,\varphi) & -S_4(\Theta,\varphi) \\ -S_3(\Theta,\varphi) & S_1(\Theta,\varphi) \end{pmatrix} \tag{2.2a}$$

$$\begin{pmatrix} S_2(\Theta,\varphi) & -S_3(\Theta,\varphi) \\ -S_4(\Theta,\varphi) & S_1(\Theta,\varphi) \end{pmatrix} \tag{2.2b}$$

$$\begin{pmatrix} S_2(\Theta,\varphi) & S_4(\Theta,\varphi) \\ S_3(\Theta,\varphi) & S_1(\Theta,\varphi) \end{pmatrix} \tag{2.2c}$$

[1] This is the assumption of equal wavelength of the scattered and incident light.

[2] An action of the r component affecting the l component can be equally traversed for the light beam in the opposite direction in any linear physical system (see Hovenier et al. 2004, Sec. 3.1).

The derivation of the symmetry relation represented by the amplitude matrix of Equation 2.2a for reciprocity was discussed by Hovenier et al. (2004). However, the other two mirror symmetry cases (Equations 2.2b and 2.2c) were only briefly discussed. The qualitative derivation of the matrices of Equation 2.2a to 2.2c may be found in Sec. 5.2 of van de Hulst (1957).

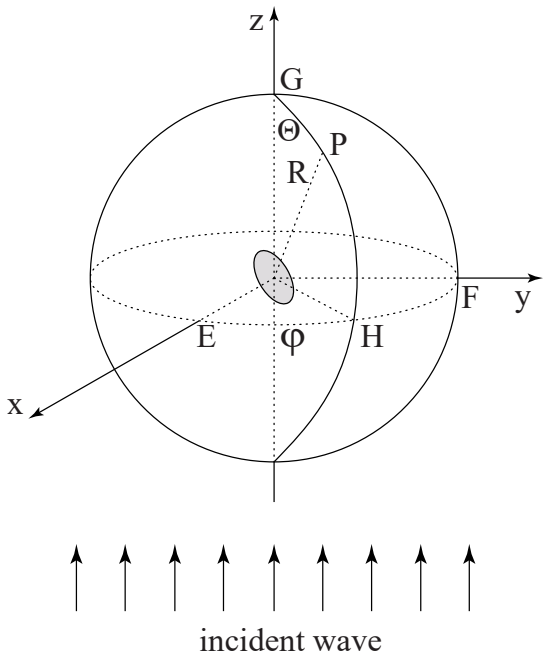

Figure 2.1: Coordinates definition for the scattering by a single particle illuminated by a parallel incident light beam travelling in the z-direction. G, F and E are the intersection points of the x-, y- and z-axes with the sphere respectively. The scattering angle Θ and azimuth ϕ (denoted as φ in the text below) correspond to Arc(G,P) and Arc(E,H) respectively (Hovenier et al. 2004, Figure 2.1).

The same scattering event as described above can be expressed by the Stokes parameters in the form (Hovenier et al. 2004, Eq. 2.24)

$$\boldsymbol{\Phi}(\Theta,\varphi) = \frac{1}{k^2R^2}\boldsymbol{F}(\Theta,\varphi)\boldsymbol{L}(-\varphi)\boldsymbol{\Phi}^{\times}(\Theta,\varphi) \tag{2.3}$$

where the net flux is defined as $\pi\boldsymbol{\Phi} = \pi[I,\ Q,\ U,\ V]$ (cf. Equation 1.1) in units W m^{-2} (or W m^{-3} if taken as functions of wavelength λ), $\boldsymbol{F} = \boldsymbol{F}^p$ is the 4 x 4 scattering matrix of the particle and $\boldsymbol{\Phi}^0 = \boldsymbol{L}(-\varphi)\boldsymbol{\Phi}^{\times}$ is the incident light beam with respect to the scattering plane.[3] The substitution of the electric field components of the scattered beam (see Equation 2.1) into the description of the Stokes parameters (Equations 1.12a to 1.12d) gives the relation between the amplitude matrix $\boldsymbol{S}$ and the scattering matrix $\boldsymbol{F}^p$ (see van de Hulst 1957, Sec. 5.14). Because we will use this relation in Chapter 4 it is attached in Appendix A.1.

Since the assumptions of independent and coherent scattering were made[4] the Stokes parameters may also describe the situation of light scattered by *a collection of particles* at point O (in Figure 2.1). Hansen and Travis (1974) and Hovenier et al. (2004) defined the scattering event by particles in a volume-element dV, using the scattering coefficient k_{sca}[5], which may readily be derived from Equation 2.3 and may be written as

$$\boldsymbol{\Phi}(\Theta,\varphi) = \frac{k_{sca}dV}{4\pi R^2}\boldsymbol{F}(\Theta,\varphi)\boldsymbol{\Phi}_0(\Theta,\varphi) \tag{2.4}$$

[3] Hovenier et al. (2004) assumed the incident light beam $\boldsymbol{\Phi}^{\times}$ to be defined with respect to the xz-plane where a rotation over φ is needed to transform the Stokes parameters such that they are defined with respect to the scattering plane (using Equation 1.13).

[4] Due to the absence of observed interference effects under these assumptions the Stokes parameters will suffice as well when a collection of particles is considered (van de Hulst 1957).

[5] $k_{sca} = \sigma_{sca}/dV$, where σ_{sca} is the sum of the scattering cross sections of the particles in the volume element, in unit length (see e.g. Hansen and Travis 1974, Chap. 2).

The corresponding scattering matrix $\boldsymbol{F} = \boldsymbol{F}^c$ is the sum of the scattering matrices $\boldsymbol{F}_i^p$ for all individual particles in the cloud and is therefore a sum of pure Mueller (SPM) matrices. Extensive surveys on Mueller calculus were carried out by Goldstein (2003) (Chap. 5, 8, 9 and 10) and by Hovenier et al. (2004) (their App. A).

Van de Hulst (1957) showed 13 examples of scattering matrices each one resulting from different assumptions about the distribution of particles among their symmetry positions in the cloud. From the amplitude matrix for a particle mirrored in the scattering plane (Equation 2.2b) the scattering matrix $\boldsymbol{F}_m^p$ for this mirrored particle may be derived from the equations in Appendix A.1 resulting in $\boldsymbol{F}_m^p = \Delta_{3,4}\boldsymbol{F}_p^p\Delta_{3,4}$ where $\Delta_{3,4}$ is a 4 x 4 identity matrix with negative signs for the third and fourth entry on the diagonal (Hovenier et al. 2004, Sec. 2.4). As discussed above, under the assumption of independent scattering the matrices may be summed up in order to obtain the scattering matrix for the cloud ($\boldsymbol{F}_m^c = \Delta_{3,4}\boldsymbol{F}_p^c\Delta_{3,4}$)[6]. Considering a cloud containing an equal number of asymmetric particles and their mirrored particles with respect to the scattering plane (i.e. $\boldsymbol{F}_m^c = \boldsymbol{F}_p^c = \boldsymbol{F}^c$) 8 entries of the $\boldsymbol{F}^c$ matrix vanish. Taking into account reciprocity[7] the scattering matrix of the cloud may be written as (see van de Hulst 1957, no. 4, p. 50)

$$\boldsymbol{F}(\Theta) = \begin{pmatrix} F_{11} & F_{12} & 0 & 0 \\ F_{12} & F_{22} & 0 & 0 \\ 0 & 0 & F_{33} & F_{34} \\ 0 & 0 & -F_{34} & F_{44} \end{pmatrix} \tag{2.5}$$

where the superscript c indicating the cloud is omitted. This scattering matrix contains 6 independent parameters and may also be used for a collection of randomly oriented particles with planes of symmetry.[8] The matrix $\boldsymbol{F}$ is often normalized such that the element F_{11}, usually referred to as the *phase function*, averaged over all scattering directions (Θ, φ) equals 1 (Hansen and Travis 1974). The phase function depends on size distribution (effective radiance and effective variance), wavelength, scattering angle, complex refractive index[9] and shape distribution. In the methods of Rayleigh and Mie scattering (see next section) this matrix will be used.

2.1.2. Special Cases of Single Scattering

In this subsection geometrical, Rayleigh and Mie scattering will be discussed. The aim of this section is not to provide a comprehensive review on these single scattering cases, rather, it points out the most relevant aspects of geometrical, Rayleigh and Mie scattering for the remainder of this report. For a more detailed description of these types of scattering the reader is referred to Hansen and Travis (1974).

Geometrical Scattering

The scattering of light by large particles (size ≥ wavelength) may be explained by geometrical optics, i.e. based on the ray-tracing technique. The contributions to the scattered light by a large particle are diffraction, external reflection, twice refracted rays, one internal reflection and two internal reflections which were indicated by Hansen and Travis (1974) as $l = 0$, 1, 2, 3 and 4 respectively. These contributions may be summed up in order to obtain the phase function (see Section 2.1.1) $F(\Theta) = \sum_{l=0}^{\infty} F_l(\Theta)$ where $F \equiv F_{11}$.

The phase function may be considered as the probability of scattering of unpolarized light in any given direction. The reflection coefficients[10] in r and l directions follow from the Fresnel formulae (see Born and Wolf 1959, Sec. 13.4) which may be used to compute the intensity and polarization of the reflected and refracted light by the particle surface. The direction of the light rays may be obtained by Snell's law (see e.g. Kamp 2007, Sec. 2.1.3) yielding the contributions ($l = 0, 1, 2$ etc.) to the scattered light.

Rayleigh Scattering

The scattering behavior by spherical or randomly oriented particles[11] much smaller than the wavelength of the incident and outgoing radiation from the particle may be described by *Rayleigh scattering*. The oscillation

[6] It may be noted that this relation also holds for quasi-monochromatic light (Hovenier et al. 2004).

[7] This results in 10 independent elements of the scattering matrix instead of 16, with $F_{21} = F_{12}$, $F_{31} = -F_{13}$, $F_{32} = -F_{23}$, $F_{41} = F_{14}$, $F_{42} = F_{24}$ and $F_{43} = -F_{34}$ (see van de Hulst 1957, no. 1, p. 49).

[8] It may be noted that Hansen and Travis (1974) wrote the entries F_{43} instead of F_{34} where $F_{43} = -F_{34}$ by reciprocity.

[9] The real part refers to scattering, the imaginary part refers to absorption.

[10] Born and Wolf (1959) defined the reflection coefficients as the ratio of the amplitudes of the electric vectors of the reflected light and the incident light (see Born and Wolf 1959, Sec. 1.6.3).

[11] See Section 2.1.1 for the necessary conditions to obtain the scattering matrix of Equation 2.5.

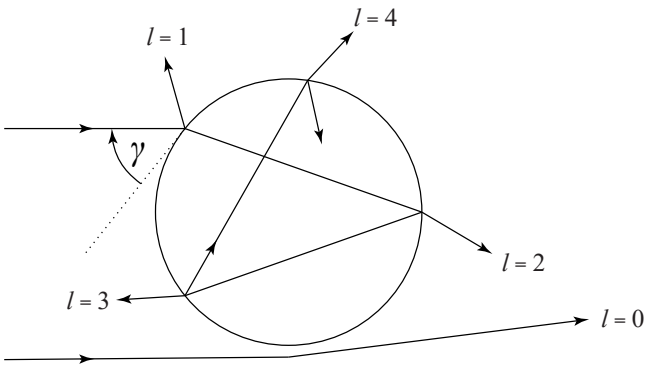

Figure 2.2: Geometrical scattering by a non-absorbing particle where γ is the incident angle on the particle. The fraction of the total scattered light for each l value is given in a table in (Hansen and Travis 1974, Fig. 4).

of the electrons in the small particles in response to the incident wave causes a dipole moment in the particles confining the direction of radiation from the particles to directions different than the directions of vibration (Hansen and Travis 1974). Rayleigh scattering may be applied to gaseous molecular scattering, however the molecules are generally not isotropic. Young (1982) warns in his review on Rayleigh scattering that more definitions exist of *depolarization* that occurs at right angles due to the anisotropy of the molecules, depending on how the incident beam is defined if the depolarization would be measured. We use the depolarization factor for unpolarized incident light of Hansen and Travis (1974), which allows us to compute the scattering optical thickness b^m_{sca} of the gas according to

$$b^m_{sca}(\lambda) = N_{gas}\sigma_{sca} \tag{2.6}$$

where N_{gas} is the column density of the gas molecules for a layer bounded by the pressures p_{top} and p_{bottom} (with Avogadro's constant N_A, m the mass per mole in atomic mass units and g the acceleration of gravity) in the column:

$$N_{gas} = N_A \frac{p_{bottom} - p_{top}}{mg} \tag{2.7}$$

and σ_{sca} is the scattering cross section of the gas molecules:

$$\sigma_{sca}(\lambda) = \frac{24\pi^3}{N_L^2} \frac{(n^2-1)^2}{(n^2+2)^2} \frac{6+3\delta}{6-7\delta} \frac{1}{\lambda^4} \tag{2.8}$$

where, N_L is Loschmidt's number, n is the real refractive index of air dependent on wavelength according to the dispersion formula of Peck and Reeder (1972), λ is the wavelength and $\frac{6+3\delta}{6-7\delta}$ is the King correction factor using the depolarization factor δ for unpolarized incident light.

The nonzero elements of the scattering matrix $\boldsymbol{F}^m(\Theta)$ for anisotropic Rayleigh scattering are (Hansen and Travis 1974):

$$F_{11} = 1 - \frac{1}{4}\Delta(1 - 3\cos^2\Theta) \tag{2.9}$$

$$F_{12} = F_{21} = -\frac{3}{4}\Delta\sin^2\Theta \tag{2.10}$$

$$F_{22} = \frac{3}{4}\Delta(1 + \cos^2\Theta) \tag{2.11}$$

$$F_{33} = \frac{3}{2}\Delta\cos\Theta \tag{2.12}$$

$$F_{44} = \frac{3}{2}\Delta\Delta'\cos\Theta \tag{2.13}$$

with

$$\Delta = \frac{1-\delta}{1+\delta/2} \qquad \text{and} \qquad \Delta' = \frac{1-2\delta}{1-\delta} \tag{2.14}$$

The depolarization factor does depend on wavelength, however, typical wavelength-independent values for δ are: ≈0.02 for H_2, ≈0.03 for N_2, ≈0.03 for air, ≈0.06 for O_2 and ≈0.09 for CO_2. The degree of linear polarization for Rayleigh scattering is given by Eq. 2.17 in Hansen and Travis (1974) showing that the degree of linear polarization decreases with anisotropy of the molecule. In our computations, however, we use the elements of the scattering matrix expressed by their expansions in generalized spherical functions (de Rooij and van der Stap 1984; Stam et al. 2002).

Mie Scattering

Scattering of light by spherical particles having a diameter similar to or larger than the wavelength of the incident light is called Mie scattering. Mie (1908) derived the scattering matrix in the form of infinite series for scattering by single spheres. Hansen and Travis (1974) carried out an extensive review on the resulting phase functions and degrees of polarization as functions of particle size distributions and refractive indices. These particles in the atmospheres are often referred to as *aerosols*. The Mie-algorithm may be used to calculate the expansion coefficients in the scattering matrix $\boldsymbol{F}^a$ for spherical, homogeneous aerosols (Stam et al. 2014). In this research, spherical cloud droplets are used, which are aerosols with a relatively big diameter. The computations of the Mie coefficients a_n and b_n, which are the main parameters of the series, will not be treated in this report and can be found in de Rooij and van der Stap (1984).

2.1.3. Single Scattering Matrix

The flux that is reflected by an atmospheric layer depends on the optical thickness b of the layer, the single scattering albedo a of the particles in the layer and the single scattering matrix of the layer's particles. The optical thickness is defined as the sum of the scattering optical thickness and absorption optical thickness. However, for this research, we choose our wavelengths outside the absorption bands in the visible spectrum and therefore we do not include gaseous absorption in our computations, i.e. $b = b^m_{sca} + b^a_{sca} + b^a_{abs}$ where b^m_{sca} is the scattering optical thickness of the gas, b^a_{sca} is the scattering optical thickness of the aerosols (i.e. spherical cloud droplets) and b^a_{abs} is the absorption optical thickness of these aerosols.

The aerosol optical thickness b^a_{sca} and aerosol scattering albedo are, if included in the computations, provided by the Mie-program. Note that the single scattering albedo of a homogeneous layer is

$$a = \frac{b^m_{sca} + b^a_{sca}}{b^m_{sca} + b^a_{sca} + b^m_{abs} + b^a_{abs}} \tag{2.15}$$

The single scattering matrix for the mixture of the gas and the aerosols in the layer is computed according to

$$\boldsymbol{F}(\Theta) = \frac{b^m_{sca}\mathbf{F}^m(\Theta) + b^a_{sca}\boldsymbol{F}^a(\Theta)}{b^m_{sca} + b^a_{sca}} \tag{2.16}$$

For a similar explanation of the computation of **F** to the one presented in this section and the former two sections, but somewhat more detailed, we refer to Stam et al. (2014), and the more recent paper Rossi et al. (2018). The input parameters used in our model atmospheres for the exoplanets will be presented in Chapter 7.

2.1.4. The Phase Matrix

In Section 2.1.1 the transfer of polarized light scattered by a particle was described in an arbitrary coordinate system defined with respect to the incident beam. Hovenier and van der Mee (1983) described the transfer of polarized light scattered by a small volume-element containing randomly oriented particles each with a plane of symmetry in a local right-handed Cartesian coordinate system fixed in space with the volume-element in its origin O (see Figure 2.3b). Assuming the azimuth angle φ measured positive in the clockwise direction when looking in the positive z-direction, the azimuth difference between the incident beam and the scattered beam may be denoted by $\varphi' - \varphi$. Hovenier and van der Mee (1983) distinguished two cases: $0 < \varphi' - \varphi < \pi$ (Figure 2.3a) and $\pi < \varphi' - \varphi < 2\pi$ or equivalently $0 < \varphi - \varphi' < \pi$ (Figure 2.3b).[12]

[12] $\pi < \varphi' - \varphi < 2\pi$ is equivalent to $0 < \varphi - \varphi' < \pi$ because the phase matrix is periodic with period π due to the double angles involved.

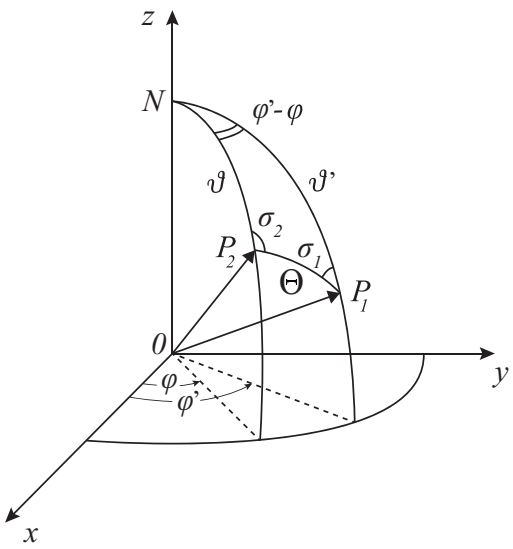

(a) In this case the azimuth difference is $0 < \varphi' - \varphi < \pi$ (Hovenier and van der Mee 1983, Fig. 2).

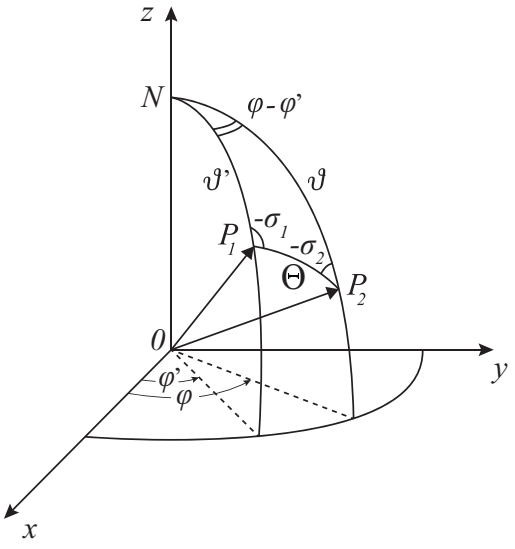

(b) The same as Figure 2.3a, but now for $0 < \varphi - \varphi' < \pi$ (Hovenier and van der Mee 1983, Fig. 3).

Figure 2.3: Scattering by particles in a volume element in a local right handed Cartesian coordinate system. The direction of the incident beam is OP_1 and the direction of the scattered beam is OP_2.

In a *plane-parallel medium*[13] the z-axis in this coordinate system is the local vertical such that the incident beam in the OP_1 direction and the z-axis define a local meridian plane which is the reference plane of the incident beam.[14] Similarly the reference plane for the scattered beam is the local meridian plane defined by the z-axis and the scattered beam in the OP_2 direction (specified by local zenith angle ϑ). However, the scattering matrix $\boldsymbol{F} = \boldsymbol{F}^c$ for the randomly oriented particles each one with a plane of symmetry in the volume element was defined with respect to the scattering plane OP_1P_2 (see Section 2.1.1). For that reason Hovenier and van der Mee (1983) defined the *phase matrix* $\boldsymbol{Z}$ as the scattering matrix $\boldsymbol{F}$ multiplied by the rotation matrices (see Equation 1.13) needed to transform the planes of reference for the incident and scattered light from the local meridians to the scattering plane.[15] For example, for $0 < \varphi' - \varphi < \pi$, we have (Hovenier and van der Mee 1983, Eq. 87, 88 and 89)

$$\boldsymbol{Z}(\vartheta,\varphi;\vartheta',\varphi') = \boldsymbol{L}(\pi-\sigma_2)\boldsymbol{F}(\Theta)(-\sigma_1) \tag{2.17}$$

Performing this multiplication gives the following matrix elements of the phase matrix:

[13] A medium, such as an atmosphere or an ocean, stratified in parallel planes of infinite horizontal extend. The assumption of a plane-parallel medium implies rotational symmetry of the medium about the vertical due to the absence of horizontal inhomogeneities. Consequently, only the differences in azimuth need to be considered (see e.g. Hovenier et al. 2004, Chap. 3).

[14] The polarization axes l and r are directed parallel and perpendicular respectively with respect to the reference plane (see Section 1.2).

[15] It should be noted that the rotation is considered to be positive in the counterclockwise direction when looking into the direction of propagation (see Section 1.2).

$$Z_{11} = F_{11}(\Theta) \tag{2.18}$$
$$Z_{12} = F_{12}(\Theta)\cos 2\sigma_1 \tag{2.19}$$
$$Z_{13} = -F_{12}(\Theta)\sin 2\sigma_1 \tag{2.20}$$
$$Z_{14} = 0 \tag{2.21}$$
$$Z_{21} = F_{12}(\Theta)\cos 2\sigma_2 \tag{2.22}$$
$$Z_{22} = \cos 2\sigma_2 F_{22}(\Theta)\cos 2\sigma_1 - \sin 2\sigma_2 F_{33}(\Theta)\sin 2\sigma_1 \tag{2.23}$$
$$Z_{23} = -\cos 2\sigma_2 F_{22}(\Theta)\sin 2\sigma_1 - \sin 2\sigma_2 F_{33}(\Theta)\cos 2\sigma_1 \tag{2.24}$$
$$Z_{24} = -F_{34}(\Theta)\sin 2\sigma_2 \tag{2.25}$$
$$Z_{31} = F_{12}(\Theta)\sin 2\sigma_2 \tag{2.26}$$
$$Z_{32} = \sin 2\sigma_2 F_{22}(\Theta)\cos 2\sigma_1 + \cos 2\sigma_2 F_{33}(\Theta)\sin 2\sigma_1 \tag{2.27}$$
$$Z_{33} = -\sin 2\sigma_2 F_{22}(\Theta)\sin 2\sigma_1 + \cos 2\sigma_2 F_{33}(\Theta)\cos 2\sigma_1 \tag{2.28}$$
$$Z_{34} = F_{34}(\Theta)\cos 2\sigma_2 \tag{2.29}$$
$$Z_{41} = 0 \tag{2.30}$$
$$Z_{42} = -F_{34}(\Theta)\sin 2\sigma_1 \tag{2.31}$$
$$Z_{43} = -F_{34}(\Theta)\cos 2\sigma_1 \tag{2.32}$$
$$Z_{44} = F_{44}(\Theta) \tag{2.33}$$
$$\tag{2.34}$$

where for i=1,2

$$\cos 2\sigma_i = 2\cos^2\sigma_i - 1 \tag{2.35}$$
$$\sin 2\sigma_i = 2\sqrt{1-\cos^2\sigma_i}\cos\sigma_i \tag{2.36}$$

In the second case ($0 < \varphi - \varphi' < \pi$) the similar phase matrix of Equation 2.17 may be used introducing a minus sign in the expression for $\sin 2\sigma_i$. Defining the parameters $u = -\cos\vartheta$ and $u' = -\cos\vartheta'$ and applying spherical trigonometric relations to the spherical triangle NP_1P_2 Hovenier and van der Mee (1983) derived

$$\cos\Theta = uu' + \sqrt{1-u^2}\sqrt{1-u'^2}\cos(\varphi-\varphi') \tag{2.37}$$
$$\cos\sigma_1 = \frac{-u + u'\cos\Theta}{\sqrt{1-u'^2}\sqrt{1-\cos^2\Theta}} \tag{2.38}$$
$$\cos\sigma_2 = \frac{-u' + u\cos\Theta}{\sqrt{1-u^2}\sqrt{1-\cos^2\Theta}} \tag{2.39}$$

By the substitution of Equations 2.37 to 2.38 into Equations 2.35, 2.36 and 2.17 the phase matrix may be written as[16] (Hovenier et al. 2004, Eq. 3.22)

$$\boldsymbol{Z}(u,u',\varphi-\varphi') = \boldsymbol{L}(-\sigma_2)\boldsymbol{F}(\Theta)\boldsymbol{L}(-\sigma_1) \tag{2.40}$$

The derivation of the phase matrix as functions of u, u' and $\varphi-\varphi'$ from the phase matrix as functions of ϑ, φ, ϑ' and φ' as presented above provides insight which is crucial for the understanding of the derivation of the symmetry relations for the phase matrix. By interchanging φ and φ', interchanging u and u' and changing the signs of u and u' simultaneously Hovenier (1969) derived seven symmetry relations for the phase matrix. In particular, the symmetry about the azimuth difference will be very useful later in this report which reads:

$$\boldsymbol{Z}(u,u',\varphi'-\varphi) = \Delta_{3,4}\boldsymbol{Z}(u,u',\varphi-\varphi')\Delta_{3,4} \tag{2.41}$$

Finally, by combining Equations 2.4 and 2.40 and dividing by the scattering coefficient k_{sca} the so-called *source vector* $\boldsymbol{J}$ may be defined for the scattering event, having the same physical dimensions as the intensity of the incident beam I_{inc} (Hovenier et al. 2004, Eq. 4.4)

$$\boldsymbol{J}(u,\varphi) = \frac{a}{4\pi}\int_{-1}^{1} du' \int_0^{2\pi} d\varphi' \boldsymbol{Z}(u,u',\varphi-\varphi')\boldsymbol{I}_{inc}(u',\varphi') \tag{2.42}$$

[16] It may be noted that $\boldsymbol{L}(\pi-\sigma_2)$ is equivalent to $\boldsymbol{L}(-\sigma_2)$ since the rotation matrix is periodic with period π due to the double angles involved.

The source vector may be considered as the intensity of the beam scattered by the volume element for which the *single scattering albedo* is defined as $a = k_{sca}/k_{ext}$.

2.2. Multiple Scattering

This section treats the mathematical description of consecutive orders of scattering events and their representations in so-called multiple-scattering matrices.

2.2.1. Orders of Scattering

In atmospheric radiative transfer studies the vertical dimension z of the plane-parallel medium is often replaced by the dimensionless *optical depth* defined as (Hovenier et al. 2004, Eq. 3.3)

$$\tau(z) = \int_z^\infty dz' k_{ext}(z') \tag{2.43}$$

for which τ varies from 0 at the top to the *optical thickness* b at the bottom of the layer (see Figure 2.4). Also, the absolute value of the direction cosine is defined as $\mu = |u|$ where $0 \le \mu \le 1$ (see e.g. Hovenier et al. 2004). Where positive values of u correspond to downward directions, the directions indicated by μ may be ambiguous. If the scattered intensity vector is presented by (μ, φ) rather than (u, φ) the direction of the vector should explicitly be specified (Hovenier et al. 2004).

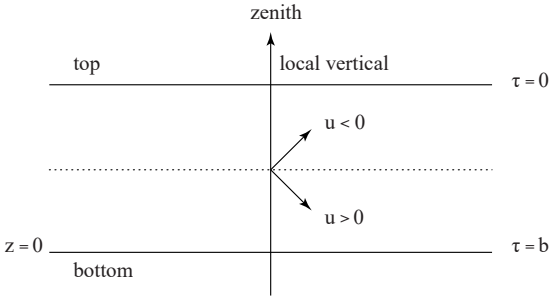

Figure 2.4: Definitions of optical depth τ, optical thickness b and direction cosine u in a plane-parallel medium (Hovenier et al. 2004, Fig. 3.1)

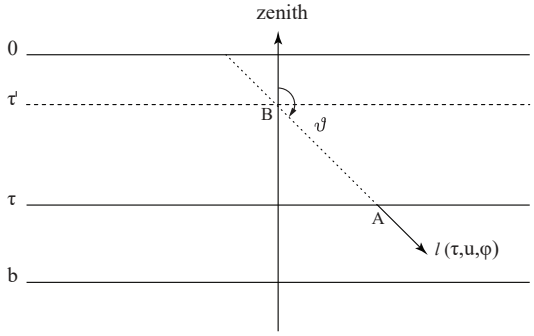

Figure 2.5: The intensity vector in the u-direction which has been scattered at least once (Hovenier et al. 2004, Fig. 4.1).

Beer's law[17] of extinction states that the transmittance of the radiant intensity in a medium decays exponentially with its optical thickness (see e.g. Wallace and Hobbs 2006, Sec. 4.5.1). Using this fact in conjunction with the derived source vector for single scattering given by Equation 2.42 the intensity of beam scattered at least once in the downward, upward and horizontal direction may respectively be represented by (see e.g. Hovenier et al. 2004, Eq. 4.10, 4.11 and 4.13)

$$\boldsymbol{I}(\tau, u, \varphi) = \int_0^\tau \frac{d\tau'}{u} \boldsymbol{J}(\tau', u, \varphi) e^{-(\tau-\tau')/u} \qquad u > 0 \tag{2.44}$$

$$\boldsymbol{I}(\tau, u, \varphi) = \int_0^\tau \frac{d\tau'}{(-u)} \boldsymbol{J}(\tau', u, \varphi) e^{-(\tau'-\tau)/(-u)} \qquad u < 0 \tag{2.45}$$

$$\boldsymbol{I}(\tau, 0, \varphi) = \boldsymbol{J}(\tau, 0, \varphi) \qquad u = 0 \tag{2.46}$$

It may be noted that the source vector $\boldsymbol{J}$ is a function of τ since a, $\boldsymbol{Z}$ and I_{inc} may depend on τ as well. Let us consider a parallel beam of light in a direction (μ_0, φ_0) incident at the top of the medium. The light of *zero order of scattering* is the light in downward direction (u, φ) that is not scattered at all may be represented by (Hovenier et al. 2004, Eq. 4.15 and 4.16)

$$\boldsymbol{I}_0(\tau, u, \mu_0, \varphi - \varphi_0) = \begin{cases} e^{-\tau/u} \boldsymbol{I}_0(0, u, \mu_0, \varphi - \varphi_0) & 0 < u < 1 \\ \boldsymbol{0} & -1 \le u < 0 \end{cases} \tag{2.47}$$

[17] Also known as *Bouguer's law* or *Lambert's law* (Wallace and Hobbs 2006).

with

$$\boldsymbol{I}_0(0,u,\mu_0,\varphi-\varphi_0)=\delta(u-\mu_0)\delta(\varphi-\varphi_0)\pi\boldsymbol{F}_0 \tag{2.48}$$

where δ is the Dirac delta function. This light beam may be scattered by a volume element (first order of scattering) after which the scattered beam may be scattered again by another volume element (second order of scattering) in the medium. From Equations 2.42 and 2.44 to 2.46 the iterative scheme to calculate the n^{th} order of scattering is summarized Display 3.1 below (see also Appendix of Hovenier 1971).[18].

Hovenier (1971) presented the resulting intensities of the scattered beam for the first two orders of scattering, although not all intermediate derivation steps were stated. Since this derivation may be very useful for the insight needed to derive symmetry relations and to define the *reflection matrix* as a function of the phase matrix below, the derivation up to $n=2$ is provided in this report in Appendix A.2.

Iterative scheme for n^{th} order of scattering

1. Compute intensity of the downward beam not scattered at all; $n=0$

$$\boldsymbol{I}_0(\tau,u,\mu_0,\varphi-\varphi_0)=\begin{cases} e^{-\tau/u}\delta(u-\mu_0)\delta(\varphi-\varphi_0)\pi\boldsymbol{F}_0 & 0<u<1 \\ \boldsymbol{0} & -1\le u<0 \end{cases} \tag{2.49}$$

2. Compute source vector of the beam scattered n times in the medium; $n\in\mathbb{N}\setminus\{0\}$

$$\boldsymbol{J_n}(\tau,u,\mu_0,\varphi-\varphi_0)=\frac{a}{4\pi}\int_{-1}^{1}du'\int_0^{2\pi}d\varphi'\boldsymbol{Z}(u,u',\varphi-\varphi')\boldsymbol{I}_{n-1}(\tau,u',\mu_0,\varphi'-\varphi_0) \tag{2.50}$$

3. Compute intensity of the beam scattered n times in the medium

$$\boldsymbol{I}_n(\tau,u,\mu_0,\varphi-\varphi_0)=\int_0^{\tau}\frac{d\tau'}{u}\boldsymbol{J}_n(\tau',u,\mu_0,\varphi-\varphi_0)e^{-(\tau-\tau')/u}; \qquad u>0 \tag{2.51}$$

$$\boldsymbol{I}_n(\tau,u,\mu_0,\varphi-\varphi_0)=\int_{\tau}^{b}\frac{d\tau'}{(-u)}\boldsymbol{J}_n(\tau',u,\mu_0,\varphi-\varphi_0)e^{-(\tau'-\tau)/(-u)}; \qquad u<0 \tag{2.52}$$

$$\boldsymbol{I}_n(\tau,0,\mu_0,\varphi-\varphi_0)=\boldsymbol{J}_n(\tau,0,\mu_0,\varphi-\varphi_0) \qquad u=0 \tag{2.53}$$

4. Set $n=n+1$ and go back to step 2

Display 3.1. References: Hovenier (1971); Hovenier et al. (2004)

2.2.2. Multiple-Scattering Matrices

Let us assume a plane-parallel planetary atmosphere (homogeneous or inhomogeneous) with a perfectly absorbing lower boundary in the absence of reflecting surface layers or internal light sources. Let us define the intensity vector $\boldsymbol{I}(0,\mu,\varphi)$ as light incident at the top of the atmosphere and let $\boldsymbol{I}(\tau,\mu,\varphi)$ and $\boldsymbol{I}(\tau,-\mu,\varphi)$ be the intensity vectors of the light emerging at the bottom and top respectively. The latter vectors are given by (see e.g. de Haan et al. 1987)

$$I(\tau,\mu,\varphi)=\frac{1}{\pi}\int_0^1\mu'd\mu'\int_0^{2\pi}d\varphi'\boldsymbol{D}(\tau,\mu,\mu',\varphi-\varphi')\boldsymbol{I}(0,\mu',\varphi')+e^{-\tau/\mu}\boldsymbol{I}(0,\mu,\varphi) \tag{2.54}$$

$$I(\tau,-\mu,\varphi)=\frac{1}{\pi}\int_0^1\mu'd\mu'\int_0^{2\pi}d\varphi'\boldsymbol{U}(\tau,\mu,\mu',\varphi-\varphi')\boldsymbol{I}(0,\mu',\varphi') \tag{2.55}$$

where $\boldsymbol{D}$ and $\boldsymbol{U}$ are so-called *multiple-scattering matrices* corresponding to light scattered downward and upward respectively defined at the optical depth τ. If the total radiation is to be considered emerging at the

[18]For the iterative scheme Hovenier (1971) assumed the medium to be homogeneous such that $a(\tau)=a$ and $\boldsymbol{Z}(\tau,u,u',\varphi-\varphi')=\boldsymbol{Z}(u,u',\varphi-\varphi')$.

top ($\tau = 0$) or bottom ($\tau = b$) of the atmosphere, $\boldsymbol{U}$ and $\boldsymbol{D}$ are replaced by a special type of multiple-scattering matrices: the reflection matrix $\boldsymbol{R}$ and transmission matrix $\boldsymbol{T}$ given by (see e.g. Hovenier et al. 2004)

$$\boldsymbol{R}(\mu,\mu',\varphi-\varphi') = \boldsymbol{U}(0,\mu,\mu',\varphi-\varphi') \tag{2.56}$$

$$\boldsymbol{T}(\mu,\mu',\varphi-\varphi') = \boldsymbol{D}(b,\mu,\mu',\varphi-\varphi') \tag{2.57}$$

Considering a monodirectional polarized light beam as given by Equation 2.48 for $\boldsymbol{I}(0,\mu,\varphi)$ incident on the top of the atmosphere, the reflected and transmitted Stokes vectors by the atmosphere may be calculated by (see Hansen and Travis 1974)

$$\boldsymbol{I}_r(\mu,\mu_0,\varphi-\varphi_0) = \mu_0\boldsymbol{R}(\mu,\mu_0,\varphi-\varphi_0)\boldsymbol{F}_0 \tag{2.58}$$

$$\boldsymbol{I}_t(\mu,\mu_0,\varphi-\varphi_0) = \mu_0\boldsymbol{T}(\mu,\mu_0,\varphi-\varphi_0)\boldsymbol{F}_0 \tag{2.59}$$

Comparing this result with the solutions for first order of scattering (Equation A.14 for $u < 0$ and A.13 for $u > 0$), and setting $\tau = 0$ and $\tau = b$ respectively, the reflection matrix $\boldsymbol{R}$ and transmission matrix $\boldsymbol{T}$ for first order of scattering in a homogeneous atmosphere may be expressed in terms of the phase matrix $\boldsymbol{Z}$ according to (Hovenier et al. 2004, Eq. 4.55 and 4.56)[19]

$$\boldsymbol{R}_1(\mu,\mu_0,\varphi-\varphi_0) = \frac{a}{4\mu_0}d(0,-\mu,\mu_0)\boldsymbol{Z}(-\mu,\mu_0,\varphi-\varphi_0) \tag{2.60}$$

$$\boldsymbol{T}_1(\mu,\mu_0,\varphi-\varphi_0) = \frac{a}{4\mu_0}c(0,\mu,\mu_0)\boldsymbol{Z}(\mu,\mu_0,\varphi-\varphi_0) \tag{2.61}$$

where the functions c and d are given by Equations A.11 and A.12. Similar expressions are found for $\boldsymbol{U}_1$ and $\boldsymbol{D}_1$ (see Hovenier et al. 2004, Eq. 4.91 to 4.93). The second order of scattering solutions $\boldsymbol{R}_2$ and $\boldsymbol{T}_2$ may be obtained by using Equation A.22 in conjunction with Equations 2.58 and 2.59. The full second order solution was provided in the appendix of Hovenier (1971), and its derivation steps are stated in Appendix A.2 of this report.

Theoretically the multiple-scattering matrices as presented in Equations 2.58 and 2.59 may be written as infinite sums of orders of scattering for n = 1 to infinity (Hovenier et al. 2004), e.g. for $\boldsymbol{R}$ we have [20]

$$\boldsymbol{R}(\mu,\mu_0,\varphi-\varphi_0) = \sum_{n=1}^{\infty}\boldsymbol{R}_n(\mu,\mu_0,\varphi-\varphi_0) \tag{2.62}$$

The reflection and transmission matrices presented above correspond to illumination of the atmosphere from above, however in case of for example a reflecting ground surface the matrices $\boldsymbol{R}^*$ and $\boldsymbol{T}^*$ may be defined where the asterisk denotes the illumination from below (Hovenier 1971). Also, for internal radiation in the atmosphere the multiple scattering matrices $\boldsymbol{U}^*$ and $\boldsymbol{D}^*$ may be defined such that (see e.g. de Haan et al. 1987)

$$\boldsymbol{I}(\tau,-\mu,\varphi) = \frac{1}{\pi}\int_0^1\mu'd\mu'\int_0^{2\pi}d\varphi'\boldsymbol{D}^*(\tau,\mu,\mu',\varphi-\varphi')\boldsymbol{I}(b,-\mu',\varphi') + e^{-(b-\tau)/\mu}\boldsymbol{I}(b,-\mu,\varphi) \tag{2.63}$$

$$\boldsymbol{I}(\tau,\mu,\varphi) = \frac{1}{\pi}\int_0^1\mu'd\mu'\int_0^{2\pi}d\varphi'\boldsymbol{U}^*(\tau,\mu,\mu',\varphi-\varphi')\boldsymbol{I}(b,-\mu',\varphi') \tag{2.64}$$

For reflecting surfaces at the bottom of the atmosphere (see Section 3.4) it is important to realize that light incident at the top of a homogeneous atmosphere is equivalent to light incident at the bottom but with a reversed sign for the azimuth difference (Hovenier et al. 2004), that is

$$\boldsymbol{R}^*(\mu,\mu_0,\varphi_0-\varphi) = \boldsymbol{R}(\mu,\mu_0,\varphi-\varphi_0) \tag{2.65}$$

$$\boldsymbol{T}^*(\mu,\mu_0,\varphi_0-\varphi) = \boldsymbol{T}(\mu,\mu_0,\varphi-\varphi_0) \tag{2.66}$$

$$\boldsymbol{U}^*(b-\tau,\mu,\mu_0,\varphi_0-\varphi) = \boldsymbol{U}(\tau,\mu,\mu_0,\varphi-\varphi_0) \tag{2.67}$$

$$\boldsymbol{D}^*(b-\tau,\mu,\mu_0,\varphi_0-\varphi) = \boldsymbol{D}(\tau,\mu,\mu_0,\varphi-\varphi_0) \tag{2.68}$$

A full list of symmetry relations for the multiple scattering matrices as can be found in Hovenier et al. (2004).

[19] In case of a inhomogeneous atmosphere a and $\boldsymbol{Z}$ both depend on τ which should be taken into account when integrating over τ to obtain the source vector (see the iterative scheme of Display 3.1 in Section 2.2.1).

[20] It should be noted that the multiple scattering matrices refer to light scattered at least once in the medium. For an atmosphere illuminated from above, the light emerging at the bottom also contains the light beam of zero order of scattering attenuated in the atmosphere according to Beer's law.

2.3. Fourier Decomposition

In Subsection 2.1.4 it was mentioned that the phase matrix of Equation 2.17 satisfies the symmetry relations that were provided by Hovenier (1969). Employing the mirror symmetry relation (cf. Equation 2.41) it becomes clear that the phase matrix consists of four 2x2 matrices that are either odd functions of $\varphi - \varphi'$ (indicated by the entries with minus sign) or even functions of $\varphi - \varphi'$ (entries without additional minus sign).

$$\boldsymbol{Z}(u,u',\varphi'-\varphi) = \Delta_{3,4}\boldsymbol{Z}(u,u',\varphi-\varphi')\Delta_{3,4} = \begin{pmatrix} Z_{11} & Z_{12} & -Z_{13} & -Z_{14} \\ Z_{21} & Z_{22} & -Z_{23} & -Z_{24} \\ -Z_{31} & -Z_{32} & Z_{33} & Z_{34} \\ -Z_{41} & -Z_{42} & Z_{43} & Z_{44} \end{pmatrix} \tag{2.69}$$

In order to reduce computing time and computer storage for numerical computations of multiple scattering algorithms it may be advantageous to make Fourier series expansions in the azimuth dependence. For the odd functions in Equation 2.69 only the odd components of the Fourier series (sine terms) may be used and for the even functions only the even components of the Fourier series (cosine terms) may be used in a Fourier series represented as (see e.g. Ziemer et al. 1993)

$$\boldsymbol{Z}(u,u',\varphi-\varphi) = \sum_{j=0}^{\infty}(2-\delta_{j0})[\boldsymbol{Z}^{cj}(u,u')\cos j(\varphi-\varphi') + \boldsymbol{Z}^{sj}(u,u')\sin j(\varphi-\varphi')] \tag{2.70}$$

where δ_{j0} is the Kronecker delta, $j = 0,1,2,3...$ and $\boldsymbol{Z}^{cj}$ and $\boldsymbol{Z}^{sj}$ are the even and odd 4x4 Fourier coefficients matrices consisting of cosine and sine terms respectively[21] given by

$$\boldsymbol{Z}^{s0}(u,u') = \boldsymbol{0} \tag{2.71}$$

$$\boldsymbol{Z}^{cj}(u,u') = \frac{1}{2\pi}\int_0^{2\pi}\boldsymbol{Z}(u,u',\varphi-\varphi')\cos j(\varphi-\varphi')d(\varphi-\varphi') \tag{2.72}$$

$$\boldsymbol{Z}^{sj}(u,u') = \frac{1}{2\pi}\int_0^{2\pi}\boldsymbol{Z}(u,u',\varphi-\varphi')\sin j(\varphi-\varphi')d(\varphi-\varphi') \tag{2.73}$$

Let us now define a 4x4 matrix $\boldsymbol{L}$ indicating any multiple scattering matrix or phase matrix satisfying this mirror symmetry relation. It follows directly from applying the mirror symmetry relation of Equation 2.69 to Equation 2.70 ($\boldsymbol{Z} = \boldsymbol{L}$) that (see Hovenier 1969)

$$\boldsymbol{L}^{cj}(\mu,\mu') = \Delta_{3,4}\boldsymbol{L}^{cj}(\mu,\mu')\Delta_{3,4} \tag{2.74}$$

$$\boldsymbol{L}^{sj}(\mu,\mu') = -\Delta_{3,4}\boldsymbol{L}^{sj}(\mu,\mu')\Delta_{3,4} \tag{2.75}$$

The matrices $\boldsymbol{L}^{cj}$ and $\boldsymbol{L}^{sj}$ may be combined in one matrix as presented by (de Haan et al. 1987)

$$\boldsymbol{L}^{j}(\mu,\mu_0) = \boldsymbol{L}^{cj}(\mu,\mu_0) - \Delta_{3,4}\boldsymbol{L}^{sj}(\mu,\mu_0) = \begin{pmatrix} \boldsymbol{L}^{cj}_{ul}(\mu,\mu_0) & -\boldsymbol{L}^{sj}_{ur}(\mu,\mu_0) \\ \boldsymbol{L}^{sj}_{ll}(\mu,\mu_0) & \boldsymbol{L}^{cj}_{lr}(\mu,\mu_0) \end{pmatrix} \tag{2.76}$$

where ul, ur, ll and lr refer to the 2x2 submatrices in the upper left, upper right, lower left and lower right corners respectively. According to de Haan et al. (1987) the Fourier series may now be written as

$$\boldsymbol{L}(\mu,\mu_0,\varphi-\varphi_0) = \frac{1}{2}\sum_{j=0}^{\infty}(2-\delta_{j0})\left[\boldsymbol{B}^{+j}(\varphi-\varphi_0)\boldsymbol{L}^{j}(\mu,\mu_0)(\boldsymbol{1}+\Delta_{3,4}) + \boldsymbol{B}^{-j}(\varphi-\varphi_0)\boldsymbol{L}^{j}(\mu,\mu_0)(\boldsymbol{1}-\Delta_{3,4})\right] \tag{2.77}$$

where $\boldsymbol{1}$ is the 4x4 unit matrix, $\boldsymbol{B}^{+j}(\alpha)$=diag(cos $j\alpha$,cos $j\alpha$,sin $j\alpha$,sin $j\alpha$) and $\boldsymbol{B}^{-j}(\alpha)$=diag(−sin $j\alpha$,−sin $j\alpha$, cos $j\alpha$,cos $j\alpha$). Furthermore, it may be noted that many formulae in this report are of the form

$$\boldsymbol{K}(\mu,\mu_0,\varphi-\varphi_0) = \frac{1}{\pi}\int_0^1\mu' d\mu'\int_0^{2\pi}d\varphi'\boldsymbol{L}(\mu,\mu',\varphi-\varphi')\boldsymbol{M}(\mu',\mu_0,\varphi'-\varphi_0) \tag{2.78}$$

where $\boldsymbol{K}$ and $\boldsymbol{M}$ are either 4x4 matrices or column vectors with 4 components such as the incident and emerging Stokes vectors[22]. Using the Fourier series Hovenier (1971) showed that each Fourier component of $\boldsymbol{K}$ may

[21] It follows directly from Equation 2.69 that $\boldsymbol{Z}^{cj}$ has two vanishing 2x2 submatrices in its lower left en upper right corners and that $\boldsymbol{Z}^{sj}$ has two vanishing 2x2 submatrices in its upper left and lower right corners.

[22] For unpolarized incident light, it follows from e.g. Equation 2.58 that the Fourier expansion of the first and second Stokes parameters contain only cosine terms and the Fourier expansion of the third and fourth parameters contain only sine terms (de Haan et al. 1987).

be computed separately according to

$$\boldsymbol{K}^{cj}(\mu,\mu_0) = 2\int_0^1 \mu' d\mu' \left[\boldsymbol{L}^{cj}(\mu,\mu')\boldsymbol{M}^{cj}(\mu',\mu_0) - \boldsymbol{L}^{sj}(\mu,\mu')\boldsymbol{M}^{sj}(\mu',\mu_0)\right] \tag{2.79}$$

$$\boldsymbol{K}^{sj}(\mu,\mu_0) = 2\int_0^1 \mu' d\mu' \left[\boldsymbol{L}^{sj}(\mu,\mu')\boldsymbol{M}^{cj}(\mu',\mu_0) + \boldsymbol{L}^{cj}(\mu,\mu')\boldsymbol{M}^{sj}(\mu',\mu_0)\right] \tag{2.80}$$

Using Equation 2.76 to combine the even and odd the Fourier coefficient matrices Equation 2.78 may be written in the azimuth independent form (see de Haan et al. 1987)

$$\boldsymbol{K}^{j}(\mu,\mu_0) = 2\int_0^1 \mu' d\mu' \boldsymbol{L}^{j}(\mu,\mu')\boldsymbol{M}^{j}(\mu',\mu_0) \tag{2.81}$$

In summary, the phase matrix $\boldsymbol{Z}(\mu,\mu',\varphi-\varphi_0)$ may be written in terms of its Fourier components combined in a matrix $\boldsymbol{Z}^j(\mu,\mu')$ (where $\boldsymbol{L}=\boldsymbol{Z}$). However, in order to obtain the Fourier coefficients $\boldsymbol{Z}^j(\mu,\mu')$, still a numerical integration has to be performed over the azimuth difference, that is, combining Equations 2.72, 2.73 and 2.76 (de Haan et al. 1987, Eq. 65)

$$\boldsymbol{Z}^j(\pm\mu,\mu') = \frac{1}{2\pi}\int_0^{2\pi} d(\varphi-\varphi')\{\boldsymbol{B}^{+j}(\varphi-\varphi') + \boldsymbol{B}^{-j}(\varphi-\varphi')\}\boldsymbol{Z}(\pm\mu,\mu'\varphi-\varphi') \tag{2.82}$$

which may be time consuming (de Haan et al. 1987). In order to avoid this Hovenier and van der Mee (1983) expressed the Fourier coefficients directly in the expansion coefficients of the scattering matrix and generalized spherical functions. De Haan et al. (1987) considered a water haze at a wavelength of 0.70 μm as a test case for the adding-doubling method (see next chapter). Using their expansion method resulted in a factor 5 to 50 less computation time compared to the integration method with approximately the same accuracy. The expansion of the phase matrix in generalized spherical functions will not be treated in depth in this report, details can be found in de Haan et al. (1987).

3

Adding-Doubling Method

In Chapter 2 the multiple-scattering problem was approached by considering orders of scattering. As an example the integration over the optical depth τ was done analytically for the first two orders of scattering. However, it should be noted that in the sum of all orders of scattering for every successive order a multiplication is involved with the single scattering albedo a (see Equation 2.50). Hence, for very thick layers ($b \gtrsim 1$) and little absorption ($a \approx 1$) a large number of scatterings are possible resulting in a slow convergence of the series in Equation 2.62 (Hansen and Travis 1974). This chapter contains the discussion of a more efficient method, the *adding-doubling method*, based on the paper of de Haan et al. (1987) and references therein. For an overview of successful applications of the adding-doubling method the reader is referred to Section 5.1 of Hovenier et al. (2004).

3.1. Basic Principles of the Adding-Doubling Method

Let us consider again light scattered by a macroscopically isotropic plane-parallel atmosphere with mirror symmetry illuminated from above as was discussed in Subsection 2.2.2. In the adding-doubling method the atmosphere is subdivided into layers placed on top of each other. Assume two homogeneous layers of optical thicknesses b' and b'' as is illustrated in Figure 3.1 where the prime and double prime indicate the top and bottom layer respectively.[1] The incident light may cross an interface indicated by the dotted line multiple times due to scattering from one layer into another. It may be assumed that the reflection and transmission matrices of the individual layers are known (see Hovenier 1971).

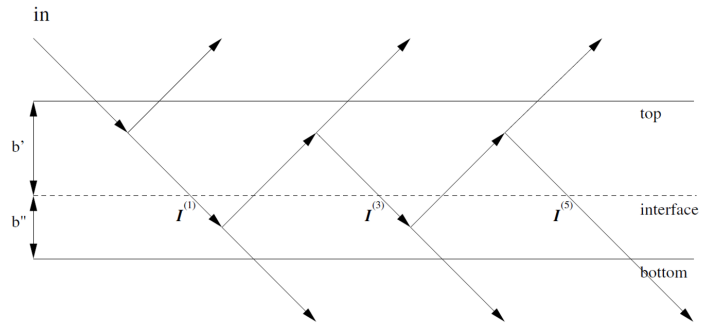

Figure 3.1: The multilayered approach of the adding-doubling method for light incident at the top of the combined layer. The arrows indicate light traveling in all directions of the solid angle 2π directed either upward or downward (Hovenier et al. 2004, Figure 5.1).

The aim of the adding-doubling method is to find the multiple-scattering matrices for the combined layer which will give the Stokes vectors of the reflected, transmitted and internal radiation according to Equations 2.54 to 2.59. Applying the same approach to the atmosphere illuminated from below and adding the Stokes

[1] The optical thickness of the combined layer equals $b = b' + b''$ (Hovenier et al. 2004).

vectors for radiation traveling downward and upward respectively may give a description of the complete radiation field in the atmosphere (de Haan et al. 1987).

Let us have a closer look at the intensity vectors crossing the interface illustrated in Figure 3.1. The Stokes vector emerging at the bottom of the top layer crossing the interface for the first time follows from Equation 2.54 (Hovenier et al. 2004, Eq. 5.1)

$$\boldsymbol{I}^{(1)}(b',\mu,\varphi) = e^{-b'/\mu}\boldsymbol{I}_0(0,\mu,\varphi) + \frac{1}{\pi}\int_0^{+1}\mu' d\mu' \int_0^{2\pi} d\varphi' \boldsymbol{T}'(\mu,\mu',\varphi-\varphi')\boldsymbol{I}_0(0,\mu',\varphi') \tag{3.1}$$

It should be noted that the transmission matrix is marked with a prime since it signifies the transmission of the top layer only. This light beam may be scattered in the bottom layer described by the reflection matrix $\boldsymbol{R}''(\mu,\mu',\varphi-\varphi')$, marked by two primes, resulting in a scattered beam traveling in the upward direction given by (Hovenier et al. 2004, Eq. 5.2)

$$\boldsymbol{I}^{(2)}(b',-\mu,\varphi) = \frac{1}{\pi}\int_0^{+1}\mu' d\mu' \int_0^{2\pi} d\varphi' \boldsymbol{R}''(\mu,\mu',\varphi-\varphi')\boldsymbol{I}^{(1)}(b',\mu',\varphi') \tag{3.2}$$

Subsequently this beam may be considered as an incident beam for another reflection in the top layer, resulting in a reflected beam traveling in the downward direction again, according to (Hovenier et al. 2004, Eq. 5.3)

$$\boldsymbol{I}^{(3)}(b',\mu,\varphi) = \frac{1}{\pi}\int_0^{+1}\mu' d\mu' \int_0^{2\pi} d\varphi' \boldsymbol{R}'^{*}(\mu,\mu',\varphi-\varphi')\boldsymbol{I}^{(2)}(b',-\mu',\varphi') \tag{3.3}$$

The latter expression contains the reflection matrix $\boldsymbol{R}'^{*}(\mu,\mu',\varphi-\varphi')$ for illumination from below because this reflection takes place in the upper layer and the incident light beam $\boldsymbol{I}^{(2)}(b',\mu',\varphi')$ crossing the interface originates from the bottom layer. Since $\boldsymbol{I}^{(3)}(b',\mu,\varphi)$ is again a light beam crossing the interface from the top layer, similar to $\boldsymbol{I}^{(1)}(b',\mu,\varphi)$, Equations 3.1 and 3.3 may be recognized as the start of an infinite series $\boldsymbol{I}^{2p+1}$ with $p = 1,2,3,\ldots$ (see Hovenier et al. 2004, Sec. 5.2). Computing the sum of this infinite series and equating it to the intensity vector of the total radiation traveling in the downward direction at the interface (cf. Equation 2.54) Hovenier (1971) derived the *adding equations* which are presented in Display 4.1 (Equations 3.4 to 3.10). The adding equations provide the computational scheme for the multiple scattering matrices of the combined layer. As an example the derivation for $\boldsymbol{D}(b',\mu,\mu_0,\varphi-\varphi)$ was partly stated by Hovenier et al. (2004); the full derivation of the adding equations is provided in Appendix A.3 of this report. It may be noted that de Haan et al. (1987) used a different notation for the superscript of the absolute directional cosines.[2]

After the sublayer is added, the combined layer with optical thickness b may be *doubled* assuming the new homogeneous sublayer to be identical such that $b' = b'' = b$ as mentioned in step 3 in Display 4.1. The reflection and transmission matrices for light incident from below $\boldsymbol{R}'^{*}$ and $\boldsymbol{T}'^{*}$ can readily be calculated from the symmetry relations of Hovenier (1969) (his relations q and r). In the absence of vertical inhomogeneity of the layers such as reflection ground surfaces; there is no need to repeat the computational scheme again for $\boldsymbol{R}'^{*}$ and $\boldsymbol{T}'^{*}$ (Takashima 1975). Nevertheless, the ground surface may be included in the system with its own particular multiple scattering matrices which are obviously not identical to the matrices obtained from the doubling method. In Section 3.4 the implementation of the reflecting ground surfaces in the adding-doubling method will be discussed.

The steps to be taken in the adding-doubling method are summarized in Display 4.1 on the next page. The integration steps however may be written in a more convenient form for the numerical implementation of the method which will be done in the following sections.

[2] For example de Haan et al. (1987) used μ' instead of μ_0 as the angle of the incident light beam at the top of the combined layer. In this report the notation of Hovenier (1971) is adopted who used μ' for the light incident at the particular layer and μ_0 for the light incident at the top of the combined layer.

Adding-doubling method

1. Compute $\boldsymbol{R}$, $\boldsymbol{T}$, $\boldsymbol{R}^*$ and $\boldsymbol{T}^*$ for two homogeneous sublayers of optical thicknesses b' and b'' sufficiently small and based on one or two orders of scattering for known a and $\boldsymbol{Z}$ (see Subsection 2.2.2).

2. Compute the multiple scattering matrices $\boldsymbol{D}, \boldsymbol{U}, \boldsymbol{R}$ and $\boldsymbol{T}$ of the combined layer with optical thickness $b = b' + b''$ using the adding equations for sufficiently large p:

$$\boldsymbol{Q}_1(\mu,\mu_0,\varphi-\varphi_0) = \frac{1}{\pi}\int_0^1 \mu' d\mu' \int_0^{2\pi} d\varphi' \boldsymbol{R}'^*(\mu,\mu',\varphi-\varphi')\boldsymbol{R}''(\mu',\mu_0,\varphi'-\varphi_0) \tag{3.4}$$

$$\boldsymbol{Q}_{p+1}(\mu,\mu_0,\varphi-\varphi_0) = \frac{1}{\pi}\int_0^1 \mu' d\mu' \int_0^{2\pi} d\varphi' \boldsymbol{Q}_1(\mu,\mu',\varphi-\varphi')\boldsymbol{Q}_p(\mu',\mu_0,\varphi'-\varphi_0) \tag{3.5}$$

$$\boldsymbol{Q}(\mu,\mu_0,\varphi-\varphi_0) = \sum_{p=1}^{\infty} \boldsymbol{Q}_p(\mu,\mu_0,\varphi-\varphi_0) \tag{3.6}$$

$$\begin{aligned}\boldsymbol{D}(b',\mu,\mu_0,\varphi-\varphi_0) &= \boldsymbol{T}'(\mu,\mu_0,\varphi-\varphi_0) + e^{-b'/\mu_0}\boldsymbol{Q}(\mu,\mu_0,\varphi-\varphi_0) \\ &\quad + \frac{1}{\pi}\int_0^1 \mu' d\mu' \int_0^{2\pi} d\varphi' \boldsymbol{Q}(\mu,\mu',\varphi-\varphi')\boldsymbol{T}'(\mu',\mu_0,\varphi'-\varphi_0)\end{aligned} \tag{3.7}$$

$$\begin{aligned}\boldsymbol{U}(b',\mu,\mu_0,\varphi-\varphi_0) &= e^{-b'/\mu_0}\boldsymbol{R}''(\mu,\mu_0,\varphi-\varphi_0) \\ &\quad + \frac{1}{\pi}\mu' d\mu' \int_0^{2\pi} d\varphi' \boldsymbol{R}''(\mu,\mu',\varphi-\varphi')\boldsymbol{D}(b',\mu',\mu_0,\varphi'-\varphi_0)\end{aligned} \tag{3.8}$$

$$\begin{aligned}\boldsymbol{R}(\mu,\mu_0,\varphi-\varphi_0) &= \boldsymbol{R}'(\mu,\mu_0,\varphi-\varphi_0) + e^{-b'/\mu}\boldsymbol{U}(b',\mu,\mu_0,\varphi-\varphi_0) \\ &\quad + \frac{1}{\pi}\int_0^1 \mu' d\mu' \int_0^{2\pi} d\varphi' \boldsymbol{T}'^*(\mu,\mu',\varphi-\varphi')\boldsymbol{U}(b',\mu',\mu_0,\varphi'-\varphi_0)\end{aligned} \tag{3.9}$$

$$\begin{aligned}\boldsymbol{T}(\mu,\mu_0,\varphi-\varphi_0) &= e^{-b''/\mu}\boldsymbol{D}(b',\mu,\mu_0,\varphi-\varphi_0) + e^{-b'/\mu_0}\boldsymbol{T}''(\mu,\mu_0,\varphi-\varphi_0) \\ &\quad + \frac{1}{\pi}\int_0^1 \mu' d\mu' \int_0^{2\pi} d\varphi' \boldsymbol{T}''(\mu,\mu',\varphi-\varphi')\boldsymbol{D}(b',\mu',\mu_0,\varphi'-\varphi_0)\end{aligned} \tag{3.10}$$

3. If the desired b is not reached yet, define $\boldsymbol{R}'$, $\boldsymbol{T}'$, $\boldsymbol{R}'^*$, $\boldsymbol{T}'^*$, $\boldsymbol{R}''$ and $\boldsymbol{T}''$ for next iteration step $(i+1)$:

   (a) If the local partial model atmosphere is homogeneous:

   - Double the combined layer by assuming the new sublayers to be identical such that $b'_{i+1} = b''_{i+1} = b_i$, $\boldsymbol{R}'_{i+1} = \boldsymbol{R}''_{i+1} = \boldsymbol{R}_i$ and $\boldsymbol{T}'_{i+1} = \boldsymbol{T}''_{i+1} = \boldsymbol{T}_i$.

   If the local partial model atmosphere is inhomogeneous:

   - Add a homogeneous layer[3] on top of the partial atmosphere by computing $\boldsymbol{R}'_{i+1}$ and $\boldsymbol{T}'_{i+1}$ (see Subsection 2.2.2) and define $b''_{i+1} = b_i$, $\boldsymbol{R}''_{i+1} = \boldsymbol{R}_i$, $\boldsymbol{T}''_{i+1} = \boldsymbol{T}_i$

   (b) If allowed:[4] compute $\boldsymbol{R}'^*_{i+1}$ and $\boldsymbol{T}'^*_{i+1}$ by symmetry relations given by Hovenier (1969):

$$\boldsymbol{R}'^*_{i+1}(\mu,\mu',\varphi-\varphi') = \Delta_{3,4}\boldsymbol{R}'_{i+1}(\mu,\mu',\varphi-\varphi')\Delta_{3,4} \tag{3.11}$$

$$\boldsymbol{T}'^*_{i+1}(\mu,\mu',\varphi-\varphi') = \Delta_{3,4}\boldsymbol{T}'_{i+1}(\mu,\mu',\varphi-\varphi')\Delta_{3,4} \tag{3.12}$$

   (c) Go back to step 2

4. Compute the Stokes vector of the reflected and transmitted radiation by substituting $\boldsymbol{R}$ and $\boldsymbol{T}$ for the multilayered atmosphere into the relevant formulae of Subsection 2.2.2

Display 4.1. References: de Haan et al. (1987); Hovenier (1969, 1971); Hovenier et al. (2004); Lacis and Hansen (1974); Takashima (1975)

[3] This homogeneous layer may itself be constructed by doubling a very thin homogeneous layer for which single scattering is dominant from known a and $\boldsymbol{Z}$ for this layer.

[4] If the model atmosphere contains different lower layers than top layers, or when reflecting ground surfaces are present, $\boldsymbol{R}^*$ and $\boldsymbol{T}^*$ may be calculated using the adding equations for illumination from below from Lacis and Hansen (1974) (see Section 3.4).

3.2. Expansion in Fourier series

The multiple scattering matrices in the adding equations as well as the $\boldsymbol{Q}$ matrix as presented in Display 4.1 satisfy the mirror symmetry relation of Equation 2.41 (Hovenier et al. 2004). Hence, the matrices in Equations 3.4 to 3.10 may be written in the combined Fourier decomposition matrix of Equation 2.69 resulting in a separate computational scheme for each Fourier component ($j = 0, 1, 2, ...$). As discussed in Section 2.3 the equations of the form of Equation 2.78 appearing in the adding-equations may be written in the azimuth independent form of Equation 2.81. Hovenier et al. (2004) showed the resulting azimuth independent adding equations:

$$\boldsymbol{Q}_1(\mu,\mu_0) = 2\int_0^1 \mu' d\mu' \boldsymbol{R}'^*(\mu,\mu')\boldsymbol{R}''(\mu',\mu_0) \tag{3.13}$$

$$\boldsymbol{Q}_{p+1}(\mu,\mu_0) = 2\int_0^1 \mu' d\mu' \boldsymbol{Q}_1(\mu,\mu')\boldsymbol{Q}_p(\mu',\mu_0) \tag{3.14}$$

$$\boldsymbol{Q}(\mu,\mu_0) = \sum_{p=1}^{\infty}(\mu,\mu_0) \tag{3.15}$$

$$\boldsymbol{D}(b',\mu,\mu_0) = \boldsymbol{T}'(\mu,\mu_0) + e^{-b'/\mu_0}\boldsymbol{Q}(\mu,\mu_0) + 2\int_0^1 \mu' d\mu' \boldsymbol{Q}(\mu,\mu')\boldsymbol{T}'(\mu',\mu_0) \tag{3.16}$$

$$\boldsymbol{U}(b',\mu,\mu_0) = e^{-b'/\mu_0}\boldsymbol{R}''(\mu,\mu_0) + 2\int_0^1 \mu' d\mu' \boldsymbol{R}''(\mu,\mu')\boldsymbol{D}(b',\mu',\mu_0) \tag{3.17}$$

$$\boldsymbol{R}(\mu,\mu_0) = \boldsymbol{R}'(\mu,\mu_0) + e^{-b'/\mu}\boldsymbol{U}(b',\mu,\mu_0) + 2\int_0^1 \mu' d\mu' \boldsymbol{T}'^*(\mu,\mu')\boldsymbol{U}(b',\mu',\mu_0) \tag{3.18}$$

$$\boldsymbol{T}(\mu,\mu_0) = e^{-b''/\mu}\boldsymbol{U}(b',\mu,\mu_0) + e^{-b'/\mu_0}\boldsymbol{T}''(\mu,\mu_0) + 2\int_0^1 \mu' d\mu' \boldsymbol{T}''(\mu,\mu')\boldsymbol{D}(b',\mu',\mu_0) \tag{3.19}$$

where the superscript j indicating the Fourier index is omitted. Substituting the results for all Fourier components indexed by j in the full expression for the Fourier decomposition given by Equation 2.77 may provide the final multiple scattering matrices.

3.3. Supermatrices

The integration over μ' in the adding equations presented in Sections 3.1 and 3.2 may be performed numerically using a quadrature formula (see Hovenier et al. 2004, Sec. 5.4) given by

$$\int_0^1 d\mu f(\mu) = \sum_{i=1}^{n}\omega_i f(\mu_i) \tag{3.20}$$

where $f(\mu)$ is the function to be integrated, $\{\omega_i\}_{i=1}^n$ are the positive weights and $\{\mu_i\}_{i=1}^n$ are the division points such that $0 \le \mu_1 < \mu_2 < ... < \mu_n \le 1$. The division points may be defined by the zeros of the Legendre polynomial $P_n(2\mu-1)$; the numerical integration is then a *Gaussian quadrature* and the division points are called the *Gaussian division points* which are used in the paper of de Haan et al. (1987). The accuracy of the quadrature increases with increasing n and if $f(\mu)$ is a polynomial of degree $2n-1$ the equality of Equation 3.20 provides the exact solution.

For example, the adding equations after Fourier decomposition given by Equations 3.13 to 3.19 are again of the form of Equation 2.81:

$$\boldsymbol{K}^j(\mu,\mu_0) = 2\int_0^1 \mu' d\mu' \boldsymbol{L}^j(\mu,\mu')\boldsymbol{M}^j(\mu',\mu_0) \tag{3.21}$$

De Haan et al. (1987) introduced the so-called *supermatrices*, that is, for the 4x4 matrix $\boldsymbol{L}(\mu,\mu_0)$ (with l rows and k columns) a $4n$ x $4n$ supermatrix $\boldsymbol{L}$ may be defined by (de Haan et al. 1987)

$$L_{4(i-1)+l,4(j-1)+k} = \sqrt{2\omega_i\mu_i}L_{l,k}(\mu_i,\mu_j)\sqrt{2\omega_j\mu_j} \tag{3.22}$$

where $l,k = 1,2,3,4$ and $i,j = 1,2,3,...,n$ and $\sqrt{2\omega\mu}$ for i and j are the corresponding so-called *supermatrix factors*. The matrix multiplication of Equation 3.21 may now be written as $\boldsymbol{K}^j = \boldsymbol{L}^j\boldsymbol{M}^j$ for $\boldsymbol{K}$, $\boldsymbol{L}$ and $\boldsymbol{M}$ in supermatrix form and j being the Fourier index.[5] If one wants to numerically interpret this multiplication in

[5] It should be noted that this j only refers to the Fourier index and is different than the j appearing in the subscripts of Equation 3.22.

an algorithm, the description above may be somewhat abstract. Since we will modify this supermatrix multiplication method later on for this study in Chapter 6, the fundamentals of this supermatrix multiplication should clearly be understood. Appendix A.4.1 therefore provides an elaborated example for the multiplication of two supermatrices $\boldsymbol{L}$ and $\boldsymbol{M}$ using a hypothetically small set of 2 Gaussian division points.

The adding equations after Fourier decomposition may now be written as a scheme of supermatrix operations which is (de Haan et al. 1987) (cf. Equations 3.13 to 3.19)

$$\boldsymbol{Q}_1 = \boldsymbol{R}'^* \boldsymbol{R}'' \tag{3.23}$$

$$\boldsymbol{Q}_{p+1} = \boldsymbol{Q}_1 \boldsymbol{Q}_p \tag{3.24}$$

$$\boldsymbol{Q} = \sum_{p=1}^{\infty} \boldsymbol{Q}_p \tag{3.25}$$

$$\boldsymbol{D} = \boldsymbol{T}' + \boldsymbol{Q}\boldsymbol{E}(b')\boldsymbol{Q}\boldsymbol{T}' \tag{3.26}$$

$$\boldsymbol{U} = \boldsymbol{R}''\boldsymbol{E}(b') + \boldsymbol{R}''\boldsymbol{D} \tag{3.27}$$

$$\boldsymbol{R} = \boldsymbol{R}' + \boldsymbol{E}(b')\boldsymbol{U} + \boldsymbol{T}'^*\boldsymbol{U} \tag{3.28}$$

$$\boldsymbol{T} = \boldsymbol{E}(b'')\boldsymbol{D} + \boldsymbol{T}''\boldsymbol{E}(b') + \boldsymbol{T}''\boldsymbol{D} \tag{3.29}$$

where the Fourier index j is omitted and the supermatrix $\boldsymbol{E}(b)$ for the attenuation may be defined by

$$E_{4(i-1)+k,4(i-1)+k}(b) = e^{-b/\mu_i} \tag{3.30}$$

De Haan et al. (1987) stated the symmetry relations for homogeneous atmospheres of Hovenier (1969) in a form that may be applied to the supermatrices (see de Haan et al. 1987, Eq. 96 to 100). It may be advantageous to perform the integration at some extra division points other then the Gaussian division points, which are kept constant while increasing the number of Gaussian division points. This is for example the case if one wants to determine the accuracy of the integration or wants to apply the adding-doubling method for specified directional cosines μ (de Haan et al. 1987). Hence, by considering additional μ-values de Haan et al. (1987) also defined the so-called *extended supermatrices* for which the adding-equations of Equations 3.23 to 3.29 are still valid (see de Haan et al. 1987, Eq. 93 and 94).

3.4. Reflecting Ground Surfaces

The ground surface may be modeled as a flat homogeneous surface of horizontal extent with reflection $\boldsymbol{R}_g$ and may be considered as a bottom layer with reflection $\boldsymbol{R}''$ in the adding-doubling method. In the preceding sections a completely absorbing ground surface, or equivalently, a perfectly black surface at the bottom of the atmosphere was assumed which implies the condition $\boldsymbol{R}'' = \boldsymbol{R}_g = 0$. Obviously, the reflection and transmission of the ground layer may be represented by $\boldsymbol{R}'' = \boldsymbol{R}_g \neq 0$ and $\boldsymbol{T}'' = 0$ respectively when a reflecting ground surface is considered.

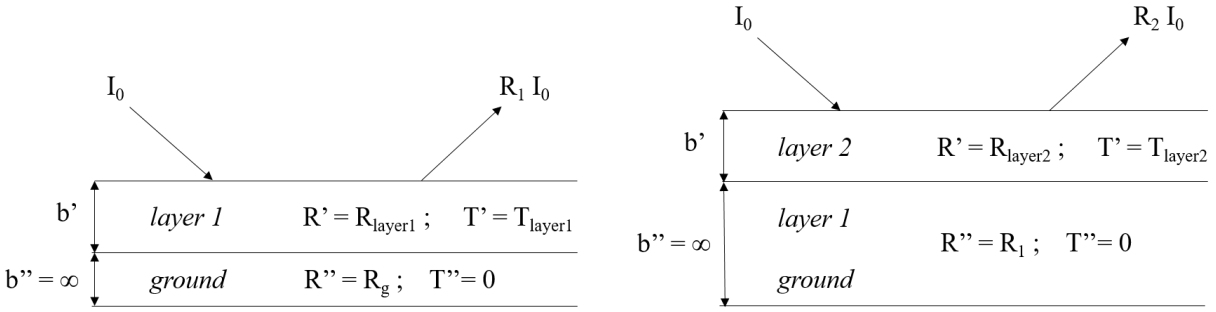

(a) The addition of the first homogeneous atmospheric layer to the ground layer.

(b) The addition of the second homogeneous atmospheric layer to the first combined layer.

Figure 3.2: Modeling the atmosphere-ground system as a ground layer with a pile of successively added homogeneous atmospheric layers on top using the adding equations. The first two iterations steps are presented in this figure.

Hovenier et al. (2004) discussed the analytical implementation of a reflecting ground surface in an atmosphere-ground system illuminated from above using the adding method (see Section 3.1). They suggested to place

a homogeneous atmosphere layer on top of the ground layer and to successively place homogeneous layers on top of the combined layers as illustrated in Figure 3.2 (cf. Display 4.1, 3(a) for an inhomogeneous model atmosphere). Since the atmospheric layers are homogeneous, the reflection and transmission matrices for these layers may be computed by applying the doubling method to a sufficiently thin initial layer with known first or second order reflection and transmission matrices, originating from its known single scattering albedo and phase matrix (see Section 2.2.2). Also, the symmetry relations of Hovenier (1969) may be used to compute $\boldsymbol{R}'^*$ and $\boldsymbol{T}'^*$ (cf. Equations 2.65 and 2.66) for the homogeneous layers. If the adding equations are considered after Fourier decomposition, similar relations may be used (see Hovenier 1969).

It should be noted that in the method described above the ground layer is fully integrated into the system; i.e. the computational scheme needs to be repeated when the ground surface changes. Lacis and Hansen (1974) discussed an alternative method in which the atmosphere, illuminated from above and below, is calculated first. They presented a computational scheme analogous to Equations 3.13 to 3.19 in order to determine $\boldsymbol{R}^*$ and $\boldsymbol{T}^*$ for the inhomogeneous atmosphere illuminated from below (see Lacis and Hansen 1974, Eq. 3). In the end the ground surface (or lower partial atmosphere-ground system) was added.

Whether the atmosphere-ground system is built up from above or below, in either case an addition of a layer to the ground surface has to be performed as illustrated in Figure 3.2a at some point. A very well-elaborated analytical example of adding a homogeneous Rayleigh scattering atmospheric layer to a Lambert surface was provided by Hovenier et al. (2004). The reflection matrix of the Lambertian surface was given by

$$\boldsymbol{R}_L = A_g \begin{pmatrix} 1 & 0 & 0 & 0 \\ 0 & 0 & 0 & 0 \\ 0 & 0 & 0 & 0 \\ 0 & 0 & 0 & 0 \end{pmatrix} \tag{3.31}$$

where A_g is the ground or surface albedo which is 1 for a perfectly reflecting Lambertian surface and $\boldsymbol{R}'' = \boldsymbol{R}_g = \boldsymbol{R}_L$. From the inspection of this matrix it is obvious that $\boldsymbol{R}_L$ is independent of direction such that all azimuth dependent terms in the Fourier decomposition vanish (Hovenier et al. 2004).

3.5. Stokes Vector Retrieval

De Haan et al. (1987) tested the adding-doubling method for a planetary atmosphere illuminated by the Sun or another solar type star assuming this is equivalent to an unpolarized monodirectional light beam incident at the top of the atmosphere (cf. Equation 2.48 for $\boldsymbol{F}_0 = [F_0, 0, 0, 0]$).[6] Stam et al. (2014), who applied the adding-doubling method to exoplanets illuminated by solar type stars, mentioned that in this case only the first column vector of the reflection matrix $\boldsymbol{R}$ is needed, that is (cf. Eq. 2.58)

$$\boldsymbol{I}_r(\mu, \mu_0, \varphi - \varphi_0) = \mu_0 \boldsymbol{R}_1(\mu, \mu_0, \varphi - \varphi_0) F_0 \tag{3.32}$$

where $\boldsymbol{R}_1 = [R_{11}, R_{21}, R_{31}, R_{41}]^T$. By expanding this four-vector in Fourier series (cf. Equation 2.77) and substituting the result in Equation 3.32 Stam et al. (2014) derived the expressions for the locally reflected light by the planet as

$$I(\mu, \mu_0, \varphi - \varphi_0)/\mu_0 F_0 = R^0_{11}(\mu, \mu_0) + 2 \sum_{j-1}^{M} \cos j(\varphi - \varphi_0) R^j_{11}(\mu, \mu_0) \tag{3.33}$$

$$Q(\mu, \mu_0, \varphi - \varphi_0)/\mu_0 F_0 = R^0_{21}(\mu, \mu_0) + 2 \sum_{j-1}^{M} \cos j(\varphi - \varphi_0) R^j_{21}(\mu, \mu_0) \tag{3.34}$$

$$U(\mu, \mu_0, \varphi - \varphi_0)/\mu_0 F_0 = 2 \sum_{j-1}^{M} \sin j(\varphi - \varphi_0) R^j_{31}(\mu, \mu_0) \tag{3.35}$$

$$V(\mu, \mu_0, \varphi - \varphi_0)/\mu_0 F_0 = 2 \sum_{j-1}^{M} \sin j(\varphi - \varphi_0) R^j_{41}(\mu, \mu_0) \tag{3.36}$$

[6] They set the flux equal to π such that $F_0 = 1$ (see de Haan et al. 1987, Chap. 8).

where the Fourier index j runs from 0 to the finite number M.[7] Test results of the Stokes parameters for the adding-doubling method considering the water-haze of Deirmendjian (1969), for various combinations of absolute directional cosines for incident and reflected light, were presented in Table 5 in de Haan et al. (1987).

[7] de Haan et al. (1987) discussed how to determine the number of Fourier terms that are needed based on the accuracy of the adding-doubling calculations.

II

Transfer of Polarized Light in an Atmosphere-Ocean System

4

Fresnel Reflection and Transmission

In the previous chapters the fundamentals of radiative transfer theory for polarized light in a planetary atmosphere-ground system were discussed. It was mentioned that the assumption of a Lambertian reflecting ground surface is reasonable for a planetary surface covered with Earth-like vegetation. However, since more than 70% of the Earth's surface is covered by an ocean a proper implementation of a reflection matrix for an oceanic surface into the adding-doubling method is needed in order to do reliable computations of the total or/and polarized fluxes received from these planets. Therefore, we need to take a step back to the physics of reflection and transmission by an *air-water interface*, or more general, a dielectric interface separating two media with distinct refractive indices, which can be modelled with Fresnel's equations.

In this chapter, Fresnel's equations for reflection and transmission and their representation in a reflection matrix for Stokes vector multiplication are derived. Parts of this derivation could be found in academic books (e.g. Giancoli 2008; Goldstein 2003). However, it is useful to present the full derivation starting from Maxwell's equations using the sinusoidal wave and Stokes vector representations of Hovenier et al. (2004) in order to preserve consistency in notation. Also, the air refractive index, which may not be necessarily equal to 1 in our (exo)planetary application, is kept as a free parameter in what follows.

4.1. Fresnel's Reflection and Transmission Coefficients

This section shows the derivation of Fresnel's equations for the electric field wave amplitude change due to reflection and transmission (refraction) by an interface dividing two media with different refractive indices. Before deriving the Fresnel's equations, Maxwell's equations describing the physics of electromagnetic waves need to be stated. In the absence magnetic materials, a flowing current and a nonzero net charge enclosed within a closed surface, the simplified Maxwell's equations in integral form and differential form are (Giancoli 2008, Eq. 31.6; Table E-1):

$$\oiint \vec{\mathbf{E}} \cdot d\vec{\mathbf{A}} = 0 \qquad \nabla \cdot \vec{\mathbf{E}} = 0 \tag{4.1a}$$

$$\oiint \vec{\mathbf{B}} \cdot d\vec{\mathbf{A}} = 0 \qquad \nabla \cdot \vec{\mathbf{B}} = 0 \tag{4.1b}$$

$$\oint \vec{\mathbf{E}} \cdot d\vec{l} = -\frac{d}{dt} \iint \vec{\mathbf{B}} \cdot d\vec{\mathbf{A}} \qquad \nabla \times \vec{\mathbf{E}} = -\frac{d\vec{\mathbf{B}}}{dt} \tag{4.1c}$$

$$\oint \vec{\mathbf{B}} \cdot d\vec{l} = \mu\epsilon \frac{d}{dt} \iint \vec{\mathbf{E}} \cdot d\vec{\mathbf{A}} \qquad \nabla \times \vec{\mathbf{B}} = \mu\epsilon \frac{d\vec{\mathbf{E}}}{dt} \tag{4.1d}$$

where $\vec{\mathbf{E}}$ and $\vec{\mathbf{B}}$ are the electric and magnetic field vectors respectively and μ and ϵ are the permeability and permittivity of the medium respectively. The four equations on the right are Maxwell's equations in differential form. Using Stokes' theorem and Gauss' theorem the corresponding integral form of the equations, presented on the left, may be derived (see Giancoli 2008, App. E). Equations 4.1a and 4.1b represent Gauss' law for electricity and Gauss' law for magnetism respectively. Equations 4.1c and 4.1d represent Faradays law and Ampère's law respectively explaining the production of an electric field by a changing magnetic field and

the production of a magnetic field by a changing electric field.

4.1.1. $\vec{\mathbf{E}}$ is Perpendicular to the Scattering Plane

Let us consider an electromagnetic wave incident on an interface dividing two media with permittivities ϵ_1 and ϵ_2 respectively, as illustrated in Figure 4.1. A positive right handed reference system is assumed such that the x-axis points out of the plane of the paper. The incident wave is reflected by an angle similar to the incident angle θ_i, while the transmitted beam is refracted according to Snell's law: $\sin\theta_t / \sin\theta_i = n_1/n_2$ where n_1 and n_2 are the refractive indices of medium 1 and 2 respectively. The refractive index is defined by $n = c/v = 1/\sqrt{\mu_0\epsilon_0}/(1/\sqrt{\mu\epsilon}) = \sqrt{\mu\epsilon/\mu_0\epsilon_0}$ where the 0's indicate free space (Giancoli 2008).

In the derivation of this chapter it is assumed that media 1 is air and media 2 is water. Since the permeabilities of air, μ_1, and water, μ_2, are approximately equal to the permeability of free space ($\mu_0 = 4\pi \cdot 10^{-7}\, T \cdot m/A$)[1], it is assumed constant in this derivation ($\mu_1 = \mu_2 = \mu_0$) following Goldstein (2003).

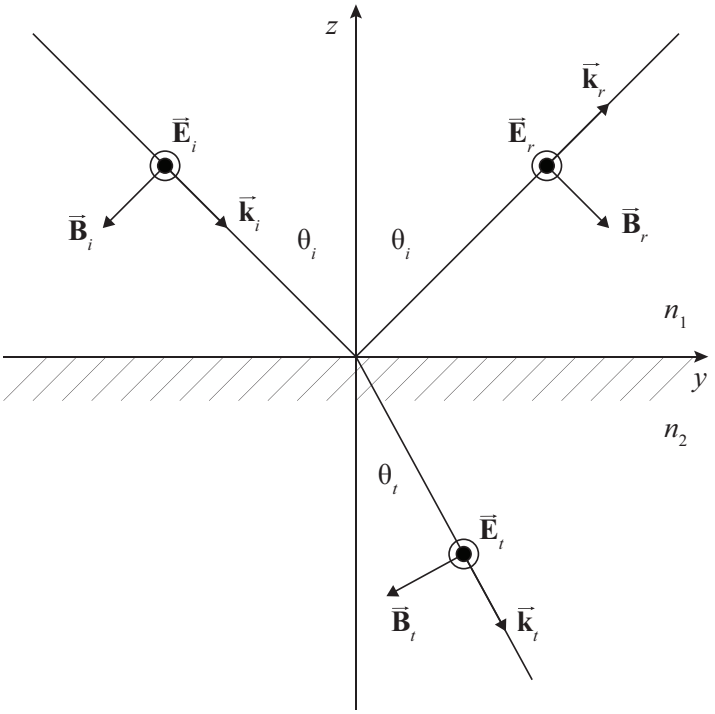

Figure 4.1: Reflection and refraction of an electromagnetic wave incident on an interface dividing two media with distinct refractive indices. $\vec{\mathbf{E}}$ is perpendicular to the scattering plane pointing in the positive x-direction out of the plane of the paper.

Figure 4.1 also illustrates the orientation of the local electric and magnetic field vectors, together with the direction of wave propagation, for the incident, reflected and transmitted wave. It may be noted that $\vec{\mathbf{E}}$ and $\vec{\mathbf{B}}$ only have a component in the positive x direction and the remaining perpendicular direction respectively. The third Maxwell equation (Equation 4.1c) in differential form may then be written as

$$\begin{pmatrix} \frac{\partial}{\partial x} \\ \frac{\partial}{\partial y'} \\ \frac{\partial}{\partial z'} \end{pmatrix} \times \begin{pmatrix} E_x \\ 0 \\ 0 \end{pmatrix} = - \begin{pmatrix} 0 \\ \frac{\partial B_{y'}}{\partial t} \\ 0 \end{pmatrix} \tag{4.2}$$

where the quotation marks indicate the *local* reference system with z' pointing in the direction of propagation, $x' = x$ and y' follows from the right hand rule for a right handed reference system. Note that in Equation

[1] Engineering ToolBox, (2016): Permeability. See https://www.engineeringtoolbox.com/permeability-d_1923.html, retrieved on 02-26-2018.

4.2, for example, $B_{y'}$ represents the y' component of either $\vec{\mathbf{B}}_i$, $\vec{\mathbf{B}}_r$ or $\vec{\mathbf{B}}_t$ in Figure 4.1. Evaluating the outer product gives

$$\frac{\partial E_x}{\partial z'} - \frac{\partial E_x}{\partial y'} = -\frac{\partial B_{y'}}{\partial t} \tag{4.3}$$

The sine representation of the electromagnetic wave is used as in Hovenier et al. (2004). Recall from Section 1.2 that we can write for the electric field component $E_x = E_{0_x} \sin(\omega t - kz')$, similarly, for the magnetic field component we write $B_{y'} = B_{0_{y'}} \sin(\omega t - kz')$, where $k = \lambda/2\pi$ is the wave number, t is time and ω is the circular frequency. Expression 4.3 may then be written as

$$-kE_{0_x} \cos(\omega t - kz') = -\omega B_{0_{y'}} \cos(\omega t - kz') \tag{4.4}$$

or

$$kE_{0_x} \sin(\omega t - kz') = \omega B_{0_{y'}} \sin(\omega t - kz') \tag{4.5}$$

This may be written again as an outer product of vectors in the local reference plane as

$$\begin{pmatrix} 0 \\ 0 \\ k \end{pmatrix} \times \begin{pmatrix} E_x \\ 0 \\ 0 \end{pmatrix} = \omega \begin{pmatrix} 0 \\ B_{y'} \\ 0 \end{pmatrix} \tag{4.6}$$

In vector notation this gives

$$\boxed{\vec{\mathbf{k}} \times \vec{\mathbf{E}} = \omega \vec{\mathbf{B}}} \quad \checkmark \text{Goldstein (2003)} \tag{4.7}$$

The green check mark, ✓, right from the Equation 4.7 indicates that this equation can be found in the mentioned paper.

Equation 4.7 can be rewritten as

$$\vec{\mathbf{B}} = \sqrt{\mu_0 \epsilon}\, \hat{\mathbf{a}} \times \vec{\mathbf{E}} \tag{4.8}$$

by formulating $\vec{\mathbf{k}} = k\hat{\mathbf{a}} = 2\pi/\lambda \hat{\mathbf{a}} = 2\pi f/(\lambda f)\hat{\mathbf{a}} = \omega/v\hat{\mathbf{a}} = \omega\sqrt{\mu_0\epsilon}\,\hat{\mathbf{a}}$ where $\hat{\mathbf{a}}$ is the unit vector in the direction of propagation and $v = 1/\sqrt{\mu_0\epsilon}$. The unit vectors of the incident, reflected and transmitted waves presented in Figure 4.1 may be expressed as functions of their components in the xyz-coordinate system by

$$\hat{\mathbf{a}}_i = \sin\theta_i \hat{\mathbf{a}}_y - \cos\theta_i \hat{\mathbf{a}}_z \tag{4.9a}$$

$$\hat{\mathbf{a}}_r = \sin\theta_i \hat{\mathbf{a}}_y + \cos\theta_i \hat{\mathbf{a}}_z \tag{4.9b}$$

$$\hat{\mathbf{a}}_t = \sin\theta_t \hat{\mathbf{a}}_y - \cos\theta_t \hat{\mathbf{a}}_z \tag{4.9c}$$

Recall from Figure 4.1 that the electric field vector points in the positive x-direction (i.e. $\vec{\mathbf{E}}_i = E_i\hat{\mathbf{a}}_x$, $\vec{\mathbf{E}}_r = E_r\hat{\mathbf{a}}_x$ and $\vec{\mathbf{E}}_t = E_t\hat{\mathbf{a}}_x$). Substituting Equations 4.9a to 4.9c into Equation 4.8 then gives

$$\vec{\mathbf{B}}_i = \sqrt{\mu_0\epsilon_1} \begin{pmatrix} 0 \\ \sin\theta_i \\ -\cos\theta_i \end{pmatrix} \times \begin{pmatrix} E_i \\ 0 \\ 0 \end{pmatrix} = \sqrt{\mu_0\epsilon_1}(-E_i\cos\theta_i\hat{\mathbf{a}}_y - E_i\sin\theta_i\hat{\mathbf{a}}_z) \tag{4.10a}$$

$$\vec{\mathbf{B}}_r = \sqrt{\mu_0\epsilon_1} \begin{pmatrix} 0 \\ \sin\theta_i \\ \cos\theta_i \end{pmatrix} \times \begin{pmatrix} E_r \\ 0 \\ 0 \end{pmatrix} = \sqrt{\mu_0\epsilon_1}(E_r\cos\theta_i\hat{\mathbf{a}}_y - E_r\sin\theta_i\hat{\mathbf{a}}_z) \tag{4.10b}$$

$$\vec{\mathbf{B}}_t = \sqrt{\mu_0\epsilon_2} \begin{pmatrix} 0 \\ \sin\theta_t \\ -\cos\theta_t \end{pmatrix} \times \begin{pmatrix} E_t \\ 0 \\ 0 \end{pmatrix} = \sqrt{\mu_0\epsilon_2}(-E_t\cos\theta_t\hat{\mathbf{a}}_y - E_t\sin\theta_t\hat{\mathbf{a}}_z) \tag{4.10c}$$

Applying Ampère's law to the interface, it can be shown that the tangential component of the magnetic field vector to the interface is continuous (see Display A.1). Substituting Equations 4.10a to 4.10c into Equation 4.19 gives

$$\sqrt{\mu_0\epsilon_1}\,(E_i\cos\theta_i - E_r\cos\theta_i) = \sqrt{\mu_0\epsilon_2}\,(E_t\cos\theta_t) \tag{4.11}$$

or

$$\sqrt{\mu_0\epsilon_1}\left(E_{0_i}\sin(\omega_i t-\vec{\mathbf{k}}_i\cdot\vec{\mathbf{r}})\cos\theta_i - E_{0_r}\sin(\omega_r t-\vec{\mathbf{k}}_r\cdot\vec{\mathbf{r}})\cos\theta_i\right)=\sqrt{\mu_0\epsilon_2}\left(E_{0_t}\sin(\omega_t t-\vec{\mathbf{k}}_t\cdot\vec{\mathbf{r}})\cos\theta_t\right) \tag{4.12}$$

where $\vec{\mathbf{r}}=(x,y,z)$ and $\vec{\mathbf{k}}$ points in the direction of wave propagation defined in x,y,z-coordinates. The boundary condition of Display A.1 must be valid at all times, that is, all waves must have the same time dependence and $\omega_i=\omega_r=\omega_t$. In other words, although some interfaces may reflect some frequencies better than others, the reflection by an interface cannot *change the frequency* of the wave.[2] At the origin location at the interface ($\vec{\mathbf{r}}$=0), we can write Equation 4.12 as functions of wave amplitudes only as

$$\sqrt{\mu_0\epsilon_1}\left(E_{0_i}\cos\theta_i - E_{0_r}\cos\theta_i\right)=\sqrt{\mu_0\epsilon_2}\left(E_{0_t}\cos\theta_t\right) \tag{4.13}$$

Since, according to Faraday's law, also the tangential component of the magnetic field vector to the interface is continuous (see Display A.1), we can write

$$\sqrt{\mu_0\epsilon_1}\left(E_{0_i}\cos\theta_i - E_{0_r}\cos\theta_i\right)=\sqrt{\mu_0\epsilon_2}\left((E_{0_i}+E_{0_r})\cos\theta_t\right) \tag{4.14}$$

Dividing by $\sqrt{\mu_0}$ and rearranging gives

$$E_{0_i}(\sqrt{\epsilon_1}\cos\theta_i-\sqrt{\epsilon_2}\cos\theta_t)=E_{0_r}(\sqrt{\epsilon_2}\cos\theta_t+\sqrt{\epsilon_1}\cos\theta_i) \tag{4.15}$$

Since we assumed that μ is constant the refractive indices equal to $n_1=\sqrt{\epsilon_1/\epsilon_0}$ and $n_2=\sqrt{\epsilon_2/\epsilon_0}$. Hence, Equation 4.15 yields

$$\boxed{R_\perp=\frac{E_{0_r}}{E_{0_i}}=\frac{n_1\cos\theta_i-n_2\cos\theta_t}{n_1\cos\theta_i+n_2\cos\theta_t}} \quad \checkmark\text{Goldstein (2003)} \tag{4.21}$$

Using $\sin\alpha^2+\cos\alpha^2=1$ gives

$$R_\perp=\frac{n_1\cos\theta_i-n_2\sqrt{1-\sin^2\theta_t}}{n_1\cos\theta_i+n_2\sqrt{1-\sin^2\theta_t}} \tag{4.22}$$

Snell's law can be applied to write Equation 4.22 as a function of n_1, n_2 and θ_i only. That is, substituting $\sin^2\theta_t=n_1^2\sin^2\theta_i/n_2^2$ gives

$$\boxed{R_\perp=\frac{n_1\cos\theta_i-\sqrt{n_2^2-n_1^2\sin^2\theta_i}}{n_1\cos\theta_i+\sqrt{n_2^2-n_1^2\sin^2\theta_i}}} \quad \begin{array}{l}\checkmark\text{Deuzé et al. (1989)}\\ \checkmark\text{Tsang et al. (1985)}\\ \checkmark\text{Zhai et al. (2010)}\end{array} \tag{4.23}$$

Mishchenko and Travis (1997) then applied the $\sin\alpha^2+\cos\alpha^2=1$ rule again to write

$$\boxed{R_\perp=\frac{\cos\theta_i-\sqrt{n_2^2-1+\cos^2\theta_i}}{\cos\theta_i+\sqrt{n_2^2-1+\cos^2\theta_i}}} \quad \checkmark\text{Mishchenko and Travis (1997)} \tag{4.24}$$

where they assumed $n_1=1$ for the refractive index of air.

The next step is to derive Fresnel's expression for the transmission amplitude, i.e. $T_\perp=E_{0_t}/E_{0_i}$. Using again $E_i+E_r=E_t$ from Display A.1 and substituting in Equation 4.11 gives

$$\sqrt{\mu_0\epsilon_1}\left(E_{0_i}\cos\theta_{0_i}-(E_{0_t}-E_{0_i})\cos\theta_i\right)=\sqrt{\mu_0\epsilon_2}\left(E_{0_t}\cos\theta_t\right) \tag{4.25}$$

Dividing by $\sqrt{\mu_0}$ and rearranging gives

$$E_{0_i}(2\sqrt{\epsilon_1}\cos\theta_i)=E_{0_t}(\sqrt{\epsilon_2}\cos\theta_t+\sqrt{\epsilon_1}\cos\theta_i) \tag{4.26}$$

Again, we use $n_1=\sqrt{\epsilon_1/\epsilon_0}$ and $n_2=\sqrt{\epsilon_2/\epsilon_0}$ such that

[2] See lecture: http://pcwww.liv.ac.uk/~awolski/Teaching/Liverpool/PHYS370/AdvancedElectromagnetism-Part4.pdf, retrieved on 03-04-2018.

Application of Ampère's law and Faraday's law to a Fresnel interface

According to the integral form of Ampère's law in the absence of a flowing current (Equation 4.1d), the magnetic field of a closed loop may be produced by a changing electric field of the corresponding enclosed surface $\boldsymbol{A}$. In Figure 4.2 a sketch of the loop is shown. The shaded area is the enclosed surface. The magnetic field vector components in the loop tangential and normal to the interface are presented as B^{tan} and B^{norm} respectively. Equation 4.1d may then be written as

$$B_1^{norm}h + B_1^{tan}w + B_2^{norm}h + B_2^{tan}w = \mu_0\epsilon\frac{d}{dt}\oiint \vec{\mathbf{E}}\cdot d\vec{\mathbf{A}} \tag{4.16}$$

where h and w are the vertical and horizontal dimensions of the rectangle loop respectively. Let us now take the limit where the vertical dimensions of the loop approach zero. Consequently, the surface area $\boldsymbol{A}$ approaches zero and Equation 4.16 becomes

$$B_1^{tan}w + B_2^{tan}w = 0 \tag{4.17}$$

Since the clockwise direction is the positive direction of the loop and the magnetic field vector components of the incident, reflected and transmitted waves were defined positive in the positive y-direction, the tangential components are

$$B_1^{tan} = -B_{i_y} - B_{r_y} \tag{4.18a}$$

$$B_2^{tan} = B_{t_y} \tag{4.18b}$$

Substituting these components into Equation 4.17 gives

$$B_{i_y} + B_{r_y} = B_{t_y} \tag{4.19}$$

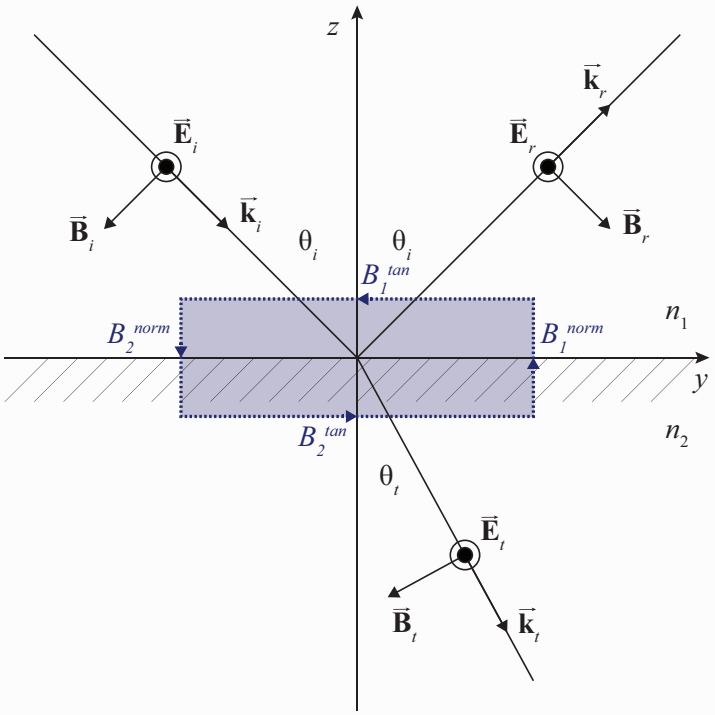

Figure 4.2: Sketch of the closed loop of the fourth Maxwell equation applied to a Fresnel reflecting and transmitting interface. The shaded area is the enclosed area $\boldsymbol{A}$ of the loop.

A similar analysis can be performed for the electric field component using Faraday's law (Equations 4.1c). It may be noted that this derivation is even shorter since the electric field vectors only have components in the x-direction. The result is analogous to Equation 4.19:

$$E_{i_x} + E_{r_x} = E_{t_x} \tag{4.20}$$

$$\boxed{T_\perp = \frac{E_{0_t}}{E_{0_i}} = \frac{2n_1\cos\theta_i}{n_1\cos\theta_i + n_2\cos\theta_t}} \quad \checkmark\text{Goldstein (2003)} \tag{4.27}$$

Using $\sin\alpha^2 + \cos\alpha^2 = 1$ and Snell's law Equation 4.27 becomes

$$\boxed{T_\perp = \frac{2n_1\cos\theta_i}{n_1\cos\theta_i + \sqrt{n_2^2 - n_1^2\sin^2\theta_i}}} \quad \checkmark\text{Zhai et al. (2010)} \tag{4.28}$$

or

$$T_\perp = \frac{2\cos\theta_i}{\cos\theta_i + \sqrt{n_2^2 - 1 + \cos^2\theta_i}} \tag{4.29}$$

assuming $n_1 = 1$.

4.1.2. $\vec{\mathbf{E}}$ is Parallel to the Scattering Plane

An analogous but more concise version of the derivation of Fresnel's equations where the electric field vector is parallel to the scattering plane is presented in this section. Figure 4.3 illustrates the reflection and transmission of an electromagnetic wave where $\vec{\mathbf{E}}$ is parallel to the scattering plane. $\vec{\mathbf{B}}$ points in the positive x-direction out of the plane of the paper.

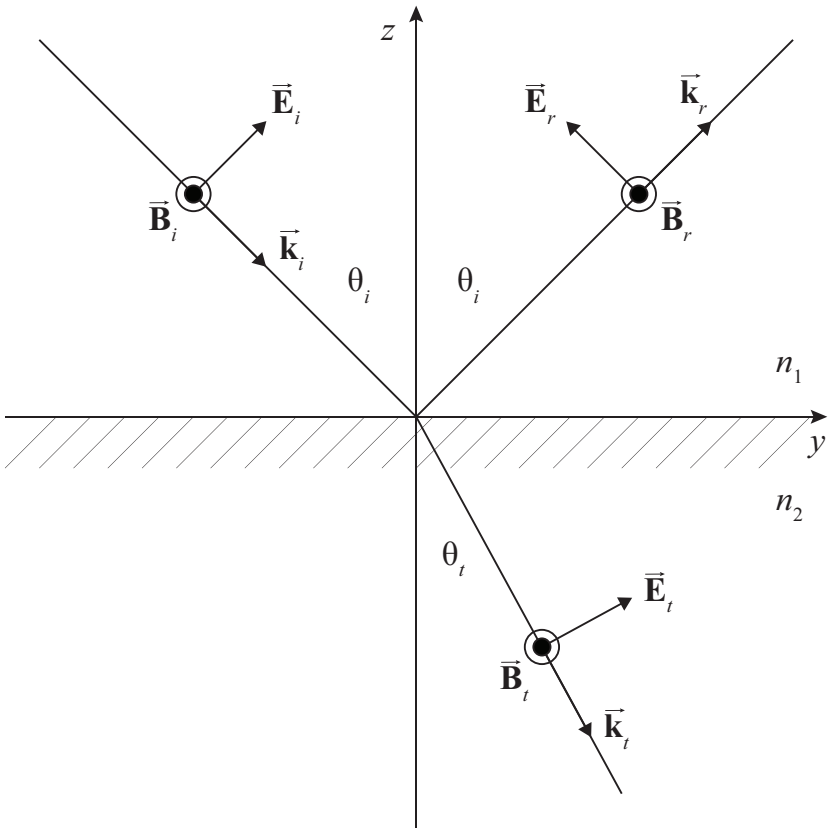

Figure 4.3: Reflection and refraction of an electromagnetic wave incident on an interface dividing two media with distinct refractive indices. $\vec{\mathbf{E}}$ is parallel to the scattering plane and $\vec{\mathbf{B}}$ points in the positive x-direction out of the plane of the paper.

The fourth Maxwell equation (Equation 4.1d) in differential form may be written as

$$\begin{pmatrix} \frac{\partial}{\partial x} \\ \frac{\partial}{\partial y'} \\ \frac{\partial}{\partial z'} \end{pmatrix} \times \begin{pmatrix} B_x \\ 0 \\ 0 \end{pmatrix} = \mu_0\epsilon \begin{pmatrix} 0 \\ \frac{-\partial E_{y'}}{\partial t} \\ 0 \end{pmatrix} \tag{4.30}$$

where the quotation marks indicate the *local* reference system with z' pointing in the direction of propagation, $x' = x$ and y' follows from the right hand rule for a right handed reference system. Note that E_y has a negative sign to be consistent with the local coordinate systems orientation of Section 4.1.1. Evaluating the outer product gives

$$\frac{\partial B_x}{\partial z'} - \frac{\partial B_x}{\partial y'} = -\mu_0 \epsilon \frac{\partial E_{y'}}{\partial t} \tag{4.31}$$

Using again the sine representation of the electromagnetic wave from Hovenier et al. (2004), expression 4.31 may then be written as

$$-kB_{0_x} \cos(\omega t - kz') = -\omega \mu_0 \epsilon E_{0_{y'}} \cos(\omega t - kz') \tag{4.32}$$

or

$$kB_{0_x} \sin(\omega t - kz') = \omega \mu_0 \epsilon E_{0_{y'}} \sin(\omega t - kz') \tag{4.33}$$

This may be written again as an outer product of vectors in the local reference plane as

$$\begin{pmatrix} 0 \\ 0 \\ k \end{pmatrix} \times \begin{pmatrix} B_x \\ 0 \\ 0 \end{pmatrix} = \omega \mu_0 \epsilon \begin{pmatrix} 0 \\ E_{y'} \\ 0 \end{pmatrix} \tag{4.34}$$

In vector notation this gives

$$\vec{\mathbf{k}} \times \vec{\mathbf{B}} = \omega \mu_0 \epsilon \vec{\mathbf{E}} \tag{4.35}$$

Using again $\vec{\mathbf{k}} = \omega \sqrt{\mu_0 \epsilon} \hat{\mathbf{a}}$ Equation 4.35 becomes

$$\vec{\mathbf{E}} = \frac{1}{\sqrt{\mu_0 \epsilon}} \hat{\mathbf{a}} \times \vec{\mathbf{B}} \tag{4.36}$$

Since the orientation of $\vec{\mathbf{k}}$ did not change compared to the derivation of Section 4.1.1, the unit vectors $\hat{\mathbf{a}}_i$, $\hat{\mathbf{a}}_r$ and $\hat{\mathbf{a}}_t$ equal Equations 4.9a to 4.9c. Also, $\vec{\mathbf{B}}_i = B_i \hat{\mathbf{a}}_x$, $\vec{\mathbf{B}}_r = B_r \hat{\mathbf{a}}_x$ and $\vec{\mathbf{B}}_t = B_t \hat{\mathbf{a}}_x$ and Equation 4.36 can be evaluated for the incident, reflected and transmitted waves as

$$\vec{\mathbf{E}}_i = \frac{1}{\sqrt{\mu_0 \epsilon_1}} \begin{pmatrix} 0 \\ \sin\theta_i \\ -\cos\theta_i \end{pmatrix} \times \begin{pmatrix} B_i \\ 0 \\ 0 \end{pmatrix} = \frac{1}{\sqrt{\mu_0 \epsilon_1}} (-B_i \cos\theta_i \hat{\mathbf{a}}_y - B_i \sin\theta_i \hat{\mathbf{a}}_z) \tag{4.37a}$$

$$\vec{\mathbf{E}}_r = \frac{1}{\sqrt{\mu_0 \epsilon_1}} \begin{pmatrix} 0 \\ \sin\theta_i \\ \cos\theta_i \end{pmatrix} \times \begin{pmatrix} B_r \\ 0 \\ 0 \end{pmatrix} = \frac{1}{\sqrt{\mu_0 \epsilon_1}} (B_r \cos\theta_i \hat{\mathbf{a}}_y - B_r \sin\theta_i \hat{\mathbf{a}}_z) \tag{4.37b}$$

$$\vec{\mathbf{E}}_t = \frac{1}{\sqrt{\mu_0 \epsilon_2}} \begin{pmatrix} 0 \\ \sin\theta_t \\ -\cos\theta_t \end{pmatrix} \times \begin{pmatrix} B_t \\ 0 \\ 0 \end{pmatrix} = \frac{1}{\sqrt{\mu_0 \epsilon_2}} (-B_t \cos\theta_t \hat{\mathbf{a}}_y - B_t \sin\theta_t \hat{\mathbf{a}}_z) \tag{4.37c}$$

Applying Faraday's law to the interface, it can be shown that the tangential component of the electric field vector to the interface is continuous (not shown, but analogous to Display A.1), therefore

$$\frac{1}{\sqrt{\mu_0 \epsilon_1}} (B_i \cos\theta_i - B_r \cos\theta_i) = \frac{1}{\sqrt{\mu_0 \epsilon_2}} (B_t \cos\theta_t) \tag{4.38}$$

Again, we are allowed to continue the derivation for the wave amplitudes only if we consider the origin location at the interface (see Section 4.1.1). Since, according to Ampère's law, also the tangential component of the magnetic field vector to the interface is continuous, we can write

$$\frac{1}{\sqrt{\mu_0 \epsilon_1}} \left(B_{0_i} \cos\theta_i - B_{0_r} \cos\theta_i\right) = \frac{1}{\sqrt{\mu_0 \epsilon_2}} \left((B_{0_i} + B_{0_r}) \cos\theta_t\right) \tag{4.39}$$

Multiplying by $\sqrt{\mu_0}$ and rearranging gives

$$B_{0_i} \left(\frac{1}{\sqrt{\epsilon_1}} \cos\theta_i - \frac{1}{\sqrt{\epsilon_2}} \cos\theta_t\right) = B_{0_r} \left(\frac{1}{\sqrt{\epsilon_2}} \cos\theta_t + \frac{1}{\sqrt{\epsilon_1}} \cos\theta_i\right) \tag{4.40}$$

From Equation 4.33 $kB_{0_x} = \omega\mu_0\epsilon E_{0_{y'}}$, or $E_{0_{y'}}/B_{0_x} = k/(\omega\mu_0\epsilon) = 1/(v\mu_0\epsilon)$. Since $E_{0_{y'}}$ and B_{0_x} are the amplitudes of the electric and magnitude field vectors and the propagation speed $v = 1/\sqrt{\mu_0\epsilon}$ (see Giancoli 2008, p. 821), we can write $E_0/B_0 = 1/\sqrt{\mu_0\epsilon}$ such that

$$R_\parallel = \frac{E_{0_r}}{E_{0_i}} = \frac{B_{0_r}}{\mu_0\epsilon_1} \Big/ \frac{B_{0_i}}{\mu_0\epsilon_1} = \frac{B_{0_r}}{B_{0_i}} \tag{4.41a}$$

$$T_\parallel = \frac{E_{0_t}}{E_{0_i}} = \frac{B_{0_t}}{\mu_0\epsilon_2} \Big/ \frac{B_{0_i}}{\mu_0\epsilon_1} = \frac{\sqrt{\epsilon_1}}{\sqrt{\epsilon_2}} \frac{B_{0_t}}{B_{0_i}} \tag{4.41b}$$

Noting that $n_1 = \sqrt{\epsilon_1/\epsilon_0}$ and $n_2 = \sqrt{\epsilon_2/\epsilon_0}$ and substituting B_{0_r}/B_{0_i} from Equation 4.40 into Equation 4.41a yields

$$R_\parallel = \frac{\frac{1}{n_1}\cos\theta_i - \frac{1}{n_2}\cos\theta_t}{\frac{1}{n_1}\cos\theta_i + \frac{1}{n_2}\cos\theta_t} \tag{4.42}$$

or

$$\boxed{R_\parallel = \frac{n_2\cos\theta_i - n_1\cos\theta_t}{n_2\cos\theta_i + n_1\cos\theta_t}} \quad \checkmark \text{Goldstein (2003)} \tag{4.43}$$

Applying Snell's law and $\cos^2\alpha + \sin^2\alpha = 1$ again gives

$$\boxed{R_\parallel = \frac{n_2^2\cos\theta_i - n_1\sqrt{n_2^2 - n_1^2\sin^2\theta_i}}{n_2^2\cos\theta_i + n_1\sqrt{n_2^2 - n_1^2\sin^2\theta_i}}} \quad \begin{array}{l}\checkmark \text{Zhai et al. (2010)} \\ \times \text{Deuzé et al. (1989)}\end{array} \tag{4.44}$$

Extra care should be taken when using the paper of Deuzé et al. (1989) because they introduced a minus sign for $R_\parallel$ and their $R_\parallel$ does therefore not match Equation 4.44. Because this equation does not completely match the equation of the paper of Deuzé et al. (1989), we have put a crossmark, ✗, next to the box. Mishchenko and Travis (1997) then applied the $\sin\alpha^2 + \cos\alpha^2 = 1$ rule again to write

$$\boxed{R_\parallel = \frac{n_2^2\cos\theta_i - \sqrt{n_2^2 - 1 + \cos^2\theta_i}}{n_2^2\cos\theta_i + \sqrt{n_2^2 - 1 + \cos^2\theta_i}}} \quad \checkmark \text{Mishchenko and Travis (1997)} \tag{4.45}$$

where they assumed $n_1 = 1$ for the refractive index of air.

Using again the continuous identity of the magnetic field vector across the interface from Ampère's law, Equation 4.38 may be written as

$$\frac{1}{\sqrt{\mu_0\epsilon_1}}\left(B_{0_i}\cos\theta_i - (B_{0_t} - B_{0_i})\cos\theta_i\right) = \frac{1}{\sqrt{\mu_0\epsilon_2}}\left(B_{0_t}\cos\theta_t\right) \tag{4.46}$$

Multiplying by $\sqrt{\mu_0}$ and rearranging gives

$$B_{0_i}\left(\frac{2}{\sqrt{\epsilon_1}}\cos\theta_i\right) = B_{0_t}\left(\frac{1}{\sqrt{\epsilon_2}}\cos\theta_t + \frac{1}{\sqrt{\epsilon_1}}\cos\theta_i\right) \tag{4.47}$$

Again, we use $n_1 = \sqrt{\epsilon_1/\epsilon_0}$ and $n_2 = \sqrt{\epsilon_2/\epsilon_0}$ and Equation 4.41b to write

$$T_\parallel = \frac{E_{0_t}}{E_{0_i}} = \frac{n_1}{n_2}\frac{B_{0_t}}{B_{0_i}} = \frac{n_1}{n_2}\left(\frac{\frac{2}{n_1}\cos\theta_i}{\frac{1}{n_1}\cos\theta_i + \frac{1}{n_2}\cos\theta_t}\right) = \frac{n_1}{n_2}\left(\frac{2n_2\cos\theta_i}{n_2\cos\theta_i + n_1\cos\theta_t}\right) \tag{4.48}$$

or

$$\boxed{T_\parallel = \frac{2n_1\cos\theta_i}{n_2\cos\theta_i + n_1\cos\theta_t}} \quad \checkmark \text{Goldstein (2003)} \tag{4.49}$$

Using $\sin\alpha^2 + \cos\alpha^2 = 1$ and Snell's law Equation 4.49 becomes

$$\boxed{T_\parallel = \frac{2n_1n_2\cos\theta_i}{n_2^2\cos\theta_i + n_1\sqrt{n_2^2 - n_1^2\sin^2\theta_i}}} \quad \checkmark \text{Zhai et al. (2010)} \tag{4.50}$$

or

$$T_{\parallel} = \frac{2n_2 \cos\theta_i}{n_2^2 \cos\theta_i + \sqrt{n_2^2 - 1 + \cos^2\theta_i}} \tag{4.51}$$

assuming $n_1 = 1$.

4.1.3. Brewster Angle and Grazing Angles

The Fresnel reflection coefficients of Equations 4.23 and 4.44 and transmission coefficients of Equations 4.28 and 4.50 are plotted against incidence angle in Figures 4.4 and 4.5 respectively.[3] Note that $R_{\parallel}$ has a negative sign for all incidence angles and $R_{\perp}$ is negative for $\theta_i > 53^o$ corresponding to a 180^o phase shift as will be explained in Section 4.2. The incidence angle of 53^o at which $R_{\parallel} = 0$ is called the *Brewster angle*. The origin of the Brewster angle is straightforward by expressing $R_{\parallel}$ as

$$R_{\parallel} = \frac{\tan(\theta_i - \theta_t)}{\tan(\theta_i - \theta_t)} \tag{4.52}$$

derived from the substitution of Snell's law in Equation 4.23 (see Appendix B.1). Consequently, $R_{\perp} = 0$ for $\theta_i + \theta_t = 90^o$ and the Brewster angle can be computed according to (Equation B.7)

$$\theta_{i,B} = \tan^{-1}\left(\frac{n_2}{n_1}\right) \tag{4.53}$$

Figures 4.6 and 4.7 show the associated Fresnel reflection coefficients squared which are important to relate the incidence and reflected intensities (Section 4.3). Also, we saw that at the Brewster angle the reflection intensity of the perpendicular component becomes zero. In other words, at the Brewster angle unpolarized incident radiance converts into totally horizontally polarized radiance upon reflection by the Fresnel interface.

Note that, at grazing incidence angles ($\theta_i > 80^o$), the reflection intensity rapidly increases towards 1.0 with increasing θ_i while the transmission intensity approaches zero.

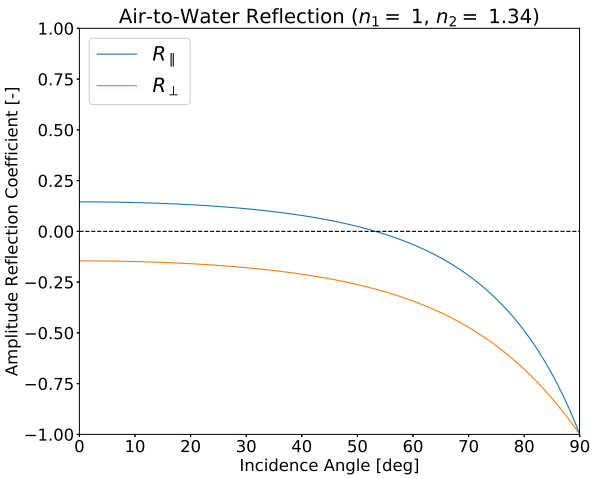

Figure 4.4: Air-to-water Fresnel reflection coefficients for the parallel and perpendicular electric field vector components against incidence angle. Orange line: $R_{\perp}$, blue line: $R_{\parallel}$

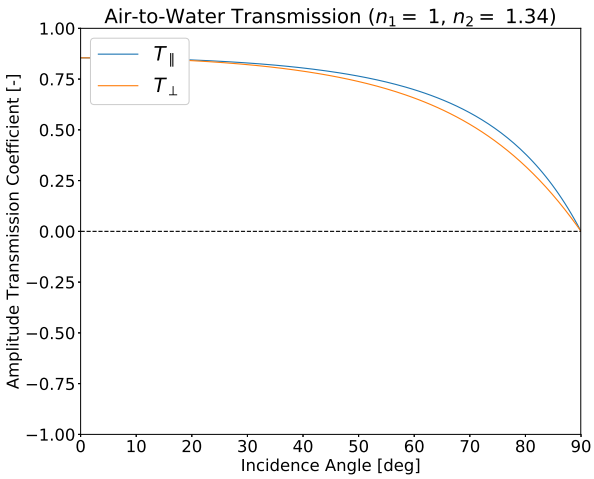

Figure 4.5: Air-to-water Fresnel transmission coefficients for the parallel and perpendicular electric field vector components against incidence angle. Orange line: $T_{\perp}$, blue line: $T_{\parallel}$

[3] The graphs of $R_{\parallel}$, $R_{\perp}$, $|R_{\parallel}|^2$ and $|R_{\perp}|^2$ were also presented in figures 8.4 and 8.8 of Goldstein (2003) and are consistent with the graphs presented in this section.

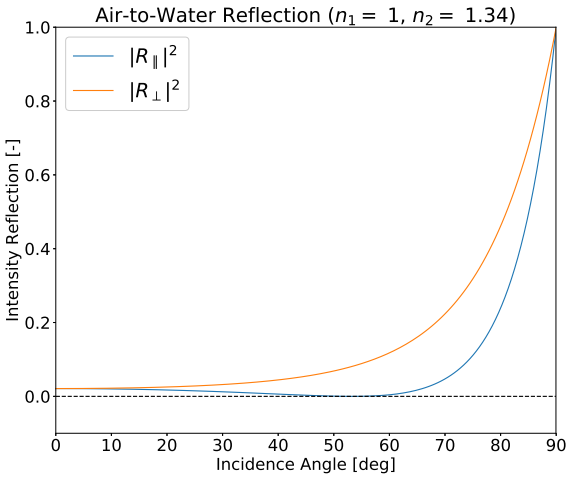

Figure 4.6: Air-to-water Fresnel reflection coefficients squared of the parallel and perpendicular electric field vector components against incidence angle. Orange line: $|R_\perp|^2$, blue line: $|R_\parallel|^2$

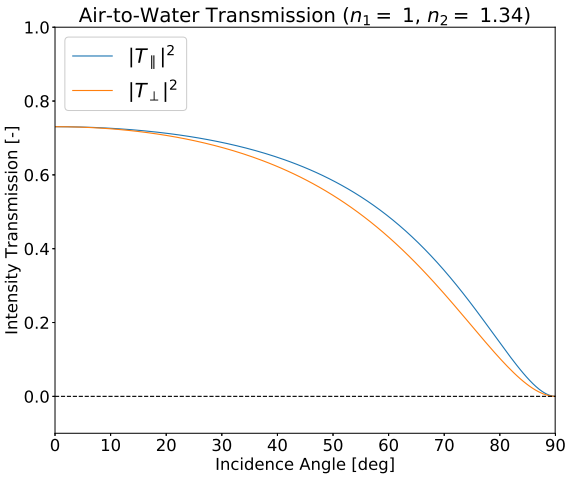

Figure 4.7: Air-to-water Fresnel transmission coefficients squared of the parallel and perpendicular electric field vector components against incidence angle. Orange line: $|T_\perp|^2$, blue line: $|T_\parallel|^2$

4.2. Amplitude Matrices for Fresnel Reflection and Transmission

In Section 4.1 Fresnel's equations for the electric field wave amplitude change due to reflection and transmission (refraction) by an interface dividing two media with different refractive indices were derived. The resulting reflection and transmission coefficients for the electric field component perpendicular ($R_\perp$ and $T_\perp$) and parallel ($R_\parallel$ and $T_\parallel$) to the scattering plane may be considered equivalent to the amplitude changes of the perpendicular (**r**) and parallel (**l**) electric wave components respectively of the polarization ellipse (Hovenier et al. 2004, Sec. 1.2). Van de Hulst (1957) then defined the conversion from the amplitude matrix to the phase matrix for the complete Stokes vector. However, care should be taken in defining the proper amplitude matrix before applying this conversion. This section shows this derivation of the Fresnel phase (reflection) matrix.

Let us consider a plane-parallel monochromatic incident light beam. The complete notation of the wave may be given by (cf. Hovenier et al. 2004, Eq. 2.1)

$$\begin{pmatrix} E_\parallel \\ E_\perp \end{pmatrix}_i = e^{i\omega t - ikz} \begin{pmatrix} E_{0_\parallel} e^{-i\alpha_1} \\ E_{0_\perp} e^{-i\alpha_2} \end{pmatrix}_i \tag{4.54}$$

where α_1 and α_2 are initial phase shifts and $E_{0_\parallel}$ and $E_{0_\perp}$ are initial amplitudes for the parallel and perpendicular components respectively. The subscript i refers to the 'incident' wave, while the parameter i is $\sqrt{-1}$. Recall from Section 2.1 that the light beam scattered at a distance R from the scattering location may be written in the combined form as (cf. Equation 2.1)

$$\begin{pmatrix} E_\parallel \\ E_\perp \end{pmatrix}_r = \begin{pmatrix} S_2(\Theta,\varphi) & S_3(\Theta,\varphi) \\ S_4(\Theta,\varphi) & S_1(\Theta,\varphi) \end{pmatrix} \frac{e^{-ikR+ikz}}{ikR} \begin{pmatrix} E_\parallel \\ E_\perp \end{pmatrix}_i \tag{4.55}$$

where the 2 x 2 matrix **S** is defined as the *amplitude matrix* as functions of scattering angle Θ and azimuth φ and $k = 2\pi/\lambda$. The subscript r denotes the 'reflected' wave. Substituting Equation 4.54 into Equation 4.55 gives

$$\begin{aligned} \begin{pmatrix} E_\parallel \\ E_\perp \end{pmatrix}_r &= \begin{pmatrix} S_2(\Theta,\varphi) & S_3(\Theta,\varphi) \\ S_4(\Theta,\varphi) & S_1(\Theta,\varphi) \end{pmatrix} \frac{e^{-ikR+ikz}}{ikR} e^{i\omega t - ikz} \begin{pmatrix} E_{0_\parallel} e^{-i\alpha_1} \\ E_{0_\perp} e^{-i\alpha_2} \end{pmatrix}_i \\ &= \begin{pmatrix} S_2(\Theta,\varphi) & S_3(\Theta,\varphi) \\ S_4(\Theta,\varphi) & S_1(\Theta,\varphi) \end{pmatrix} \frac{e^{-ikR+i\omega t}}{ikR} \begin{pmatrix} E_{0_\parallel} e^{-i\alpha_1} \\ E_{0_\perp} e^{-i\alpha_2} \end{pmatrix}_i \end{aligned} \tag{4.56}$$

The reflected beam, however, may also be expressed in terms of its own amplitude as (Hovenier et al. 2004, Eq.2.35)

$$\begin{pmatrix} E_{\parallel} \\ E_{\perp} \end{pmatrix}_r = \frac{e^{i\omega t - ikR}}{ikR} \begin{pmatrix} E_{0_{\parallel}} e^{-i\beta_1} \\ E_{0_{\perp}} e^{-i\beta_2} \end{pmatrix}_r \tag{4.57}$$

where β_1 and β_2 are the phase shifts of the reflected wave for the parallel and perpendicular component respectively. Equating Equations 4.56 and 4.57 gives

$$\begin{pmatrix} E_{0_{\parallel}} e^{-i\beta_1} \\ E_{0_{\perp}} e^{-i\beta_2} \end{pmatrix}_r = \begin{pmatrix} S_2(\Theta,\varphi) & S_3(\Theta,\varphi) \\ S_4(\Theta,\varphi) & S_1(\Theta,\varphi) \end{pmatrix} \begin{pmatrix} E_{0_{\parallel}} e^{-i\alpha_1} \\ E_{0_{\perp}} e^{-i\alpha_2} \end{pmatrix}_i \tag{4.58}$$

Evaluate the multiplication of Equation 4.58:

$$E_{0_{\parallel_r}} e^{-i\beta_1} = S_2 E_{0_{\parallel_i}} e^{-i\alpha_1} + S_3 E_{0_{\perp_i}} e^{-i\alpha_1} \tag{4.59a}$$

$$E_{0_{\perp_r}} e^{-i\beta_2} = S_4 E_{0_{\parallel_i}} e^{-i\alpha_2} + S_1 E_{0_{\perp_i}} e^{-i\alpha_2} \tag{4.59b}$$

In Section 4.1 the amplitude reflection coefficients were derived for both the perpendicular and parallel components. Thus, introducing the subscripts $\parallel$ and $\perp$ to distinct the two cases, we derived the Fresnel expressions for $E_{\parallel 0_r} = R_{\parallel} E_{\parallel 0_i}$ and $E_{\perp 0_r} = R_{\perp} E_{\perp 0_i}$. This means that $S_3 = 0$ and $S_4 = 0$. Also, from Equation 4.58

$$R_{\parallel} = \frac{E_{0_{\parallel_r}}}{E_{0_{\parallel_i}}} = S_2 \frac{e^{-i\beta_1}}{e^{-i\alpha_1}} = S_2 e^{-i(\beta_1 - \alpha_1)} = \pm S_2 \tag{4.60a}$$

$$R_{\perp} = \frac{E_{0_{\perp_r}}}{E_{0_{\perp_i}}} = S_2 \frac{e^{-i\beta_2}}{e^{-i\alpha_2}} = S_1 e^{-i(\beta_2 - \alpha_2)} = \pm S_1 \tag{4.60b}$$

Since we know that $R_{\parallel}$ and $R_{\perp}$ do not have an imaginary part (see Equations 4.23 and 4.44), the exponential terms are equal to ± 1. Note that the minus sign needs to be considered as well because potential negative $R_{\parallel}$ and $R_{\perp}$ values are not physically possible. However, it can be shown that the negative Fresnel coefficients presented in Figure 4.4 indicate a phase shift between the incident and reflected wave

$$-i(\beta_1 - \alpha_1) = \begin{cases} \ln(+1) = 0 & \text{if } R_{\parallel} > 0 \\ \ln(-1) = i\pi & \text{if } R_{\parallel} < 0 \end{cases} \tag{4.61a}$$

$$-i(\beta_2 - \alpha_2) = \begin{cases} \ln(+1) = 0 & \text{if } R_{\perp} > 0 \\ \ln(-1) = i\pi & \text{if } R_{\perp} < 0 \end{cases} \tag{4.61b}$$

or by defining the phase shifts $\delta_1 = \beta_1 - \alpha_1$ and $\delta_2 = \beta_2 - \alpha_2$ this yields

$$\begin{cases} \delta_1 = 0 & \text{if } R_{\parallel} > 0 \\ \delta_1 = -\pi & \text{if } R_{\parallel} < 0 \end{cases} \tag{4.62a}$$

$$\begin{cases} \delta_2 = 0 & \text{if } R_{\perp} > 0 \\ \delta_2 = -\pi & \text{if } R_{\perp} < 0 \end{cases} \tag{4.62b}$$

Finally, the amplitude matrix for Fresnel reflection of Equation 4.55 may be defined as

$$\begin{pmatrix} S_2(\Theta,\varphi) & S_3(\Theta,\varphi) \\ S_4(\Theta,\varphi) & S_1(\Theta,\varphi) \end{pmatrix} = \begin{pmatrix} R_{\parallel} & 0 \\ 0 & R_{\perp} \end{pmatrix} \tag{4.63}$$

where negative entries indicate a phase shift of π between the reflected and incident wave.

Similarly, for the transmission the amplitude matrix is

$$\begin{pmatrix} S_2(\Theta,\varphi) & S_3(\Theta,\varphi) \\ S_4(\Theta,\varphi) & S_1(\Theta,\varphi) \end{pmatrix} = \begin{pmatrix} T_{\parallel} & 0 \\ 0 & T_{\perp} \end{pmatrix} \tag{4.64}$$

4.3. Fresnel's Reflection and Transmission Matrices for Polarized Light

The results of the conversion from the 2x2 amplitude matrix to the 4x4 phase (reflection) matrix of van de Hulst (1957) are given by (Hovenier et al. 2004, Eq. 2.7 to 2.22)

$$F_{11} = \frac{1}{2}(|S_2|^2 + |S_3|^2 + |S_4|^2 + |S_1|^2) \tag{4.65a}$$
$$F_{12} = \frac{1}{2}(|S_2|^2 - |S_3|^2 + |S_4|^2 - |S_1|^2) \tag{4.65b}$$
$$F_{13} = \mathrm{Re}(S_2 S_3^* + S_1 S_4^*) \tag{4.65c}$$
$$F_{14} = \mathrm{Im}(S_2 S_3^* - S_1 S_4^*) \tag{4.65d}$$
$$F_{21} = \frac{1}{2}(|S_2|^2 + |S_3|^2 - |S_4|^2 - |S_1|^2) \tag{4.65e}$$
$$F_{22} = \frac{1}{2}(|S_2|^2 - |S_3|^2 - |S_4|^2 + |S_1|^2) \tag{4.65f}$$
$$F_{23} = \mathrm{Re}(S_2 S_3^* - S_1 S_4^*) \tag{4.65g}$$
$$F_{24} = \mathrm{Im}(S_2 S_3^* + S_1 S_4^*) \tag{4.65h}$$
$$F_{31} = \mathrm{Re}(S_2 S_4^* + S_1 S_3^*) \tag{4.65i}$$
$$F_{32} = \mathrm{Re}(S_2 S_4^* - S_1 S_3^*) \tag{4.65j}$$
$$F_{33} = \mathrm{Re}(S_2 S_1^* + S_3 S_4^*) \tag{4.65k}$$
$$F_{34} = \mathrm{Re}(S_2 S_1^* + S_4 S_3^*) \tag{4.65l}$$
$$F_{41} = \mathrm{Im}(S_4 S_2^* + S_1 S_3^*) \tag{4.65m}$$
$$F_{42} = \mathrm{Im}(S_4 S_2^* - S_1 S_3^*) \tag{4.65n}$$
$$F_{43} = \mathrm{Im}(S_1 S_2^* - S_3 S_4^*) \tag{4.65o}$$
$$F_{44} = \mathrm{Re}(S_1 S_2^* - S_3 S_4^*) \tag{4.65p}$$

where the asterisk denotes the complex conjugate and $|S_k|^2 = S_k S_k^*$. Substituting $S_3 = S_4 = 0$, $S_2 = R_\parallel$ and $S_1 = R_\perp$ yields the Fresnel reflection matrix (Zhai et al. 2010, Eq. 47)

$$\boldsymbol{R}_f = \begin{pmatrix} \frac{1}{2}(|R_\parallel|^2 + |R_\perp|^2) & \frac{1}{2}(|R_\parallel|^2 - |R_\perp|^2) & 0 & 0 \\ \frac{1}{2}(|R_\parallel|^2 - |R_\perp|^2) & \frac{1}{2}(|R_\parallel|^2 + |R_\perp|^2) & 0 & 0 \\ 0 & 0 & \mathrm{Re}(R_\parallel R_\perp^*) & \mathrm{Im}(R_\parallel R_\perp^*) \\ 0 & 0 & \mathrm{Im}(R_\perp R_\parallel^*) & \mathrm{Re}(R_\perp R_\parallel^*) \end{pmatrix} \quad \checkmark \text{Zhai et al. (2010)} \tag{4.66}$$

The Fresnel reflection matrix can straightforwardly be used to compute the conversion of the diffuse Stokes vector: $\mathbf{I}_r = \boldsymbol{R}_f \mathbf{I}_i$ where $\mathbf{I}_i$ and $\mathbf{I}_r$ are the incident and reflected Stokes vectors respectively in W m $^{-2}$ sr^{-1}.[4] (Zhai et al. 2012).

A similar matrix can be derived for the transmission (Zhai et al. 2010, Eq. 48):

$$\boldsymbol{T}_f = f_T \begin{pmatrix} \frac{1}{2}(|T_\parallel|^2 + |T_\perp|^2) & \frac{1}{2}(|T_\parallel|^2 - |T_\perp|^2) & 0 & 0 \\ \frac{1}{2}(|T_\parallel|^2 - |T_\perp|^2) & \frac{1}{2}(|T_\parallel|^2 + |T_\perp|^2) & 0 & 0 \\ 0 & 0 & \mathrm{Re}(T_\parallel T_\perp^*) & \mathrm{Im}(T_\parallel T_\perp^*) \\ 0 & 0 & \mathrm{Im}(T_\perp T_\parallel^*) & \mathrm{Re}(T_\perp T_\parallel^*) \end{pmatrix} \tag{4.67}$$

It should be noted, however, that an extra factor f_T is introduced accounting for the change of the angle of the direction of wave propagation with the local vertical and the change of the solid angle of the diffuse Stokes vector across the Fresnel interface when travelling from medium 1 to medium 2. This factor f_T will be defined in the following section.

[4] Note that $\boldsymbol{R}_f$ is *not* yet a reflection matrix of the form that can be used in an adding equation of the adding-doubling method, see next section.

4.4. Conservation of Energy at the Fresnel Interface

In Section 4.3 the reflection and transmission matrices for polarized light were derived. For the transmission matrix an extra factor f_T was introduced. This section aims to derive this factor f_T such that energy is conserved (assuming the absence of absorption). It is important to note that, in order to define the proper reflection and transmission matrices for the Stokes vector, an unambiguous definition of the Stokes vector is needed. This chapter explains the difference in resulting transmission matrices obtained by assuming a coherent Stokes vector (i.e. flux or irradiance in W m^{-2}) employed by Mishchenko et al. (2002) and a diffuse Stokes vector (i.e. radiance in W m^{-2} sr^{-1}) which appears in the radiative transfer equation and was employed by Hovenier et al. (2004).[5]

4.4.1. Coherent Stokes Vector

In Section 4.1 the electromagnetic wave was expressed in its electric and magnetic field vector components. The radiative power per unit area of a light wave may be described by its *Poynting vector*. The Poynting vector is the cross product of the electric and magnetic fields and consequently points in the direction of wave propagation as illustrated in Figure 4.8. Its mathematical representation is (Goldstein 2003, Eq. 16.32):

$$\vec{\mathbf{S}} = \vec{\mathbf{E}} \times \vec{\mathbf{H}} \tag{4.68}$$

where $\vec{\mathbf{H}} = \vec{\mathbf{B}}/\mu_0$. The units of $\vec{\mathbf{E}}$ are V m^{-1} or kg m s^{-3} A^{-1}, the units of $\vec{\mathbf{B}}$ are T or kg A^{-1} s^{-2} and the units of μ are Wb A^{-1} m^{-1}. Using Wb = V s and W = V A = kg m^2 s^3 it can be shown that the units of $\vec{\mathbf{S}}$ are W m^{-2}.

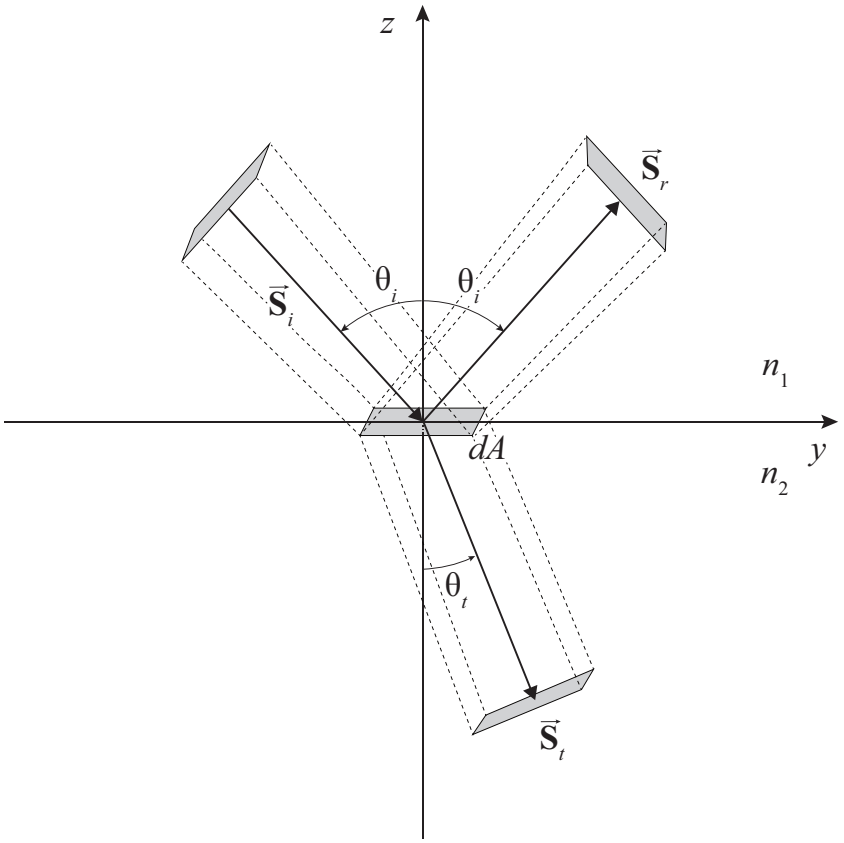

Figure 4.8: A sketch of the Poynting vector of the incident, reflected and transmitted beams. The projected areas of dA perpendicular to the incident and reflected directions at a similar distance from the origin are both equal to $\cos\theta_i\, dA$. The projected area of dA perpendicular to the transmitted direction equals $\cos\theta_t\, dA$.

Let us now define again the unit vector $\hat{\mathbf{a}} = \hat{\mathbf{a}}_{z'}$ in the local direction of propagation as in Equation 4.8 and the

[5] An extensive discussion of this issue may be found in the paper of Garcia (2012*a*), the comment on this paper of Zhai et al. (2012) and the response to this comment of Garcia (2012*b*).

unit vectors in the positive parallel and positive perpendicular directions respectively: $\hat{\mathbf{a}}_\parallel$ and $\hat{\mathbf{a}}_\perp$. Then, by substituting Equation 4.36 we can write (Thomas and Stamnes 2002, Eq. H.6,H.7)

$$\vec{\mathbf{E}} = \vec{\mathbf{E}}_\parallel + \vec{\mathbf{E}}_\perp = E_\parallel \hat{\mathbf{a}}_\parallel + E_\perp \hat{\mathbf{a}}_\perp \tag{4.69a}$$

$$\vec{\mathbf{H}} = \vec{\mathbf{H}}_\parallel + \vec{\mathbf{H}}_\perp = \frac{1}{\mu_0}\vec{\mathbf{B}}_\parallel + \frac{1}{\mu_0}\vec{\mathbf{B}}_\perp = \sqrt{\frac{\epsilon}{\mu_0}}\vec{\mathbf{a}}_{z'} \times \vec{\mathbf{E}}_\parallel + \sqrt{\frac{\epsilon}{\mu_0}}\vec{\mathbf{a}}_{z'} \times \vec{\mathbf{E}}_\perp \tag{4.69b}$$

Substituting Equations 4.69a and 4.69b into the cross product of the Poynting vector in Equation 4.68 gives

$$\begin{aligned}
\vec{\mathbf{S}} &= \begin{pmatrix} E_\parallel \\ E_\perp \\ 0 \end{pmatrix} \times \sqrt{\frac{\epsilon}{\mu_0}} \left[\begin{pmatrix} 0 \\ 0 \\ 1 \end{pmatrix} \times \begin{pmatrix} E_\parallel \\ 0 \\ 0 \end{pmatrix} + \begin{pmatrix} 0 \\ 0 \\ 1 \end{pmatrix} \times \begin{pmatrix} 0 \\ E_\perp \\ 0 \end{pmatrix} \right] \\
&= \sqrt{\frac{\epsilon}{\mu_0}} \begin{pmatrix} E_\parallel \\ E_\perp \\ 0 \end{pmatrix} \times \begin{pmatrix} -E_\perp \\ E_\parallel \\ 0 \end{pmatrix} \\
&= \sqrt{\frac{\epsilon}{\mu_0}} \left[E_\parallel E_\parallel + E_\perp E_\perp \right] \vec{\mathbf{a}}_{z'}
\end{aligned} \tag{4.70}$$

By considering a complex version of the Poynting vector, the magnitude of the time-averaged Poynting vector for the plane wave results in (as explained in Section 2.4 and 2.6 of Mishchenko et al. (2002) and Section 16.3 of Goldstein (2003)):

$$\langle S \rangle = \frac{1}{2}\sqrt{\frac{\epsilon}{\mu_0}} \left(E_\parallel E_\parallel^* + E_\perp E_\perp^* \right) \tag{4.71}$$

where the factor $\frac{1}{2}$ originates from $\left(\frac{1}{\sqrt{2}}\right)^2$, i.e. the root mean square of the wave amplitude. Note that Equation 4.71 is equivalent to the magnitude of the first element of the *coherent* Stokes vector (Zhai et al. 2010, Eq. 6)[6]

$$\pi \boldsymbol{I} = \frac{1}{2}\sqrt{\frac{\epsilon}{\mu_0}} \begin{pmatrix} E_\parallel E_\parallel^* + E_\perp E_\perp^* \\ E_\parallel E_\parallel^* - E_\perp E_\perp^* \\ E_\parallel E_\perp^* + E_\perp E_\parallel^* \\ i(E_\parallel E_\perp^* - E_\perp E_\parallel^*) \end{pmatrix} \tag{4.72}$$

Expression 4.72 is called the coherent Stokes vector because no division by the solid angle has been done yet. In other words, this element of coherent Stokes vector equals the flux in W m $^{-2}$, which may be verified by the units check:

$$[\pi \boldsymbol{I}] = \sqrt{\frac{[\epsilon]}{[\mu_0]}}[E]^2 = \sqrt{\frac{\mathrm{F\,m^{-1}}}{\mathrm{Wb\,A^{-1}m^{-1}}}}(\mathrm{V\,m^{-1}})^2 = \sqrt{\frac{\mathrm{A^2\,s^4\,kg^{-1}\,m^{-3}}}{\mathrm{kg\,m\,s^{-2}\,A^{-2}}}}\mathrm{kg^2\,m^2\,s^{-6}\,A^{-2}} = \mathrm{kg\,s^{-3}} = \mathrm{W\,m^{-2}} \tag{4.73}$$

At the Fresnel interface the conservation of energy must be satisfied. That is, the power of the incident wave (in Watt) equals the sum of the power of the reflected and transmitted waves. Since the radiative power per unit area of a light wave could be described by its Poynting vector, at the Fresnel boundary we have

$$\langle S_i \rangle \cos(\theta_i) dA = \langle S_r \rangle \cos(\theta_i) dA + \langle S_t \rangle \cos(\theta_t) dA \tag{4.74}$$

or (Zhai et al. 2012, Eq. 7)

$$\frac{1}{2}\sqrt{\frac{\epsilon_1}{\mu_0}} \left(E_x E_x^* \right)_i \cos(\theta_i) dA = \frac{1}{2}\sqrt{\frac{\epsilon_1}{\mu_0}} \left(E_x E_x^* \right)_r \cos(\theta_i) dA + \frac{1}{2}\sqrt{\frac{\epsilon_2}{\mu_0}} \left(E_x E_x^* \right)_t \cos(\theta_t) dA \tag{4.75}$$

[6] Because ϵ is often assumed constant, the factor $\sqrt{\frac{1}{2}\frac{\epsilon}{\mu_0}}$ is omitted in some literature (e.g. Hovenier et al. 2004; van de Hulst 1957), but this is physically incorrect.

where the subscript x denotes the parallel or perpendicular component and i, r and t indicate the incident, reflected and transmitted coherent Stokes vector respectively and dA is the unit area at the reflection/transmission location as illustrated in Figure 4.8. Note that the projection of dA in the transmission direction is different than in the incident and reflected directions for $\theta_t \neq \theta_i$.

Dividing both sides of Equation 4.75 by its left hand side and using $n_1 = \sqrt{\epsilon_1/\epsilon_0}$ and $n_2 = \sqrt{\epsilon_2/\epsilon_0}$ the energy balance becomes (Zhai et al. 2010, Eq. 8)

$$1 = \frac{(E_x E_x^*)_r}{(E_x E_x^*)_i} + \frac{n_2}{n_1}\frac{\cos\theta_t}{\cos\theta_i}\frac{(E_x E_x^*)_t}{(E_x E_x^*)_i} \tag{4.76}$$

or

$$1 = R_x R_x^* + \frac{n_2}{n_1}\frac{\cos\theta_t}{\cos\theta_i} T_x T_x^* \tag{4.77}$$

where R_x and T_x are the Fresnel reflection coefficients of either the perpendicular or parallel component as derived in Section 4.1 and the asterisk denotes the complex conjugate. Since these components are orthogonal by definition, any combination of $\parallel$ and $\perp$ can be substituted for the two subsequent x subscripts such that $\boldsymbol{R}_f$ of Equation 4.66 still holds and $\boldsymbol{T}_f$ becomes (Zhai et al. 2010, Eq. 9)

$$\boldsymbol{T}_f^c = \frac{n_2}{n_1}\frac{\cos\theta_t}{\cos\theta_i}\begin{pmatrix} \frac{1}{2}(|T_\parallel|^2+|T_\perp|^2) & \frac{1}{2}(|T_\parallel|^2-|T_\perp|^2) & 0 & 0 \\ \frac{1}{2}(|T_\parallel|^2-|T_\perp|^2) & \frac{1}{2}(|T_\parallel|^2+|T_\perp|^2) & 0 & 0 \\ 0 & 0 & \mathrm{Re}(T_\parallel T_\perp^*) & \mathrm{Im}(T_\parallel T_\perp^*) \\ 0 & 0 & \mathrm{Im}(T_\perp T_\parallel^*) & \mathrm{Re}(T_\perp T_\parallel^*) \end{pmatrix} \quad \checkmark \text{Zhai et al. (2010)} \tag{4.78}$$

and

$$1 = \boldsymbol{R}_f + \boldsymbol{T}_f^c \tag{4.79}$$

The superscript 'c' emphasizes the fact that Equation 4.78 is only valid for transforming coherent Stokes vectors: $\pi \boldsymbol{I}_t = \boldsymbol{T}_f^c \pi \boldsymbol{I}_i$. Consequently, the multiplication factor f_T in Equation 4.67 equals $(n_2/n_1)(\cos\theta_t/\cos\theta_i)$ in case of a coherent Stokes vector. In summary, the factor f_T is needed because of a changing permittivity across the Fresnel interface and a changing projection of area dA due to the changing angle between the Poynting vector and the local vertical.

4.4.2. Diffuse Stokes Vector

The objective of this section is to derive the matrices $\boldsymbol{F}_t$ and $\boldsymbol{T}_t$ that may be utilized in the adding-doubling method of de Haan et al. (1987). For example, they must be able to replace the matrices $\boldsymbol{R}$ and $\boldsymbol{T}$ in the following simplified equations for the reflection and transmission of an incident beam from the direction (μ_0, φ_0) (cf. Eq. 3.8 of Hansen and Travis 1974)

$$\boldsymbol{I}_r(\mu,\varphi) = \mu_0 \boldsymbol{R}(\mu,\mu_0,\varphi-\varphi_0)\boldsymbol{I}_0 \tag{4.80a}$$

$$\boldsymbol{I}_t(\mu,\varphi) = \mu_0 \boldsymbol{T}(\mu,\mu_0,\varphi-\varphi_0)\boldsymbol{I}_0 \tag{4.80b}$$

where $\boldsymbol{I}_r$, $\boldsymbol{I}_t$ and $\boldsymbol{I}_0$ are the diffuse reflected, transmitted and incident Stokes vectors respectively in W m^{-2} sr^{-1}. Furthermore, $\mu = |\cos\theta|$, θ is the zenith angle of the reflected beam, $\mu_0 = |\cos\theta_0|$, θ_0 is the solar (incidence) zenith angle, φ is the azimuth angle of the reflected beam and φ_0 is the azimuth angle of the incident beam. Figure 4.9 illustrates the diffuse Stokes vectors of the incident, reflected and transmitted beams. Note that $\theta = \theta_0 = \theta_i$ according to the law of reflection.

Because the diffuse Stokes vectors in Equations 4.80a and 4.80b are in units W m^{-2} sr^{-1}, their radiative powers may be obtained through the multiplication by their solid angle $d\Omega$ and the projection of area dA perpendicular to their direction of propagation. Note that, from Equation 4.77, we know that the incident, reflected

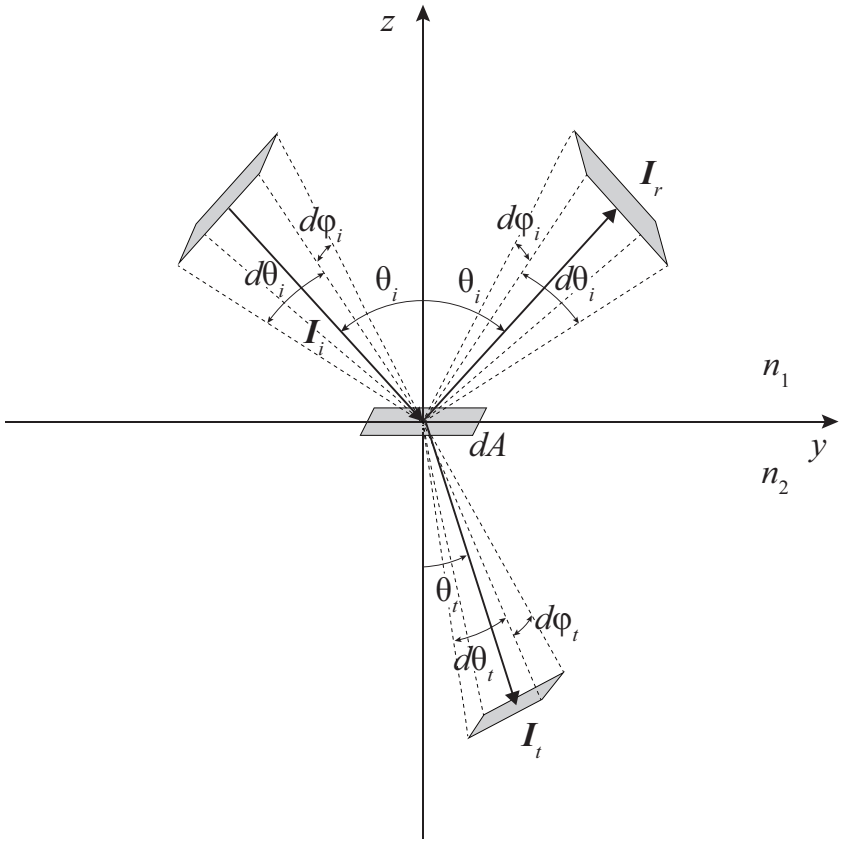

Figure 4.9: A sketch of the diffuse Stokes vector of the incident, reflected and transmitted beams. The projected areas of dA perpendicular to the incident and reflected directions at a similar distance from the origin are both equal to $\cos\theta_i dA$. The solid angle of the transmitted beam changes across the Fresnel interface as a result of a different refractive index of medium 2 compared to medium 1.

and transmitted radiative powers (P_i, P_r and P_t) are related through

$$P_r = R_x R_x^* P_i \tag{4.81a}$$

$$P_t = \frac{n_2}{n_1}\frac{\cos\theta_t}{\cos\theta_i} T_x T_x^* P_i \tag{4.81b}$$

Substituting the expressions for the radiative powers gives (cf. Eq. 10 of Zhai et al. 2012)

$$I_r d\Omega_i dA\cos\theta_i = R_x R_x^* (I_i d\Omega_i dA\cos\theta_i) \tag{4.82a}$$

$$I_t d\Omega_t dA\cos\theta_t = \frac{n_2}{n_1}\frac{\cos\theta_t}{\cos\theta_i} T_x T_x^* (I_i d\Omega_i dA\cos\theta_i) \tag{4.82b}$$

where $d\Omega_i = \sin\theta_i d\theta_i d\varphi$ and $d\Omega_t = \sin\theta_t d\theta_t d\varphi$ are the solid angles and I is the first element of the Stokes vector $\boldsymbol{I}$. Note that $d\varphi_i = d\varphi_t = d\varphi$.

From Equation 4.82a it immediately becomes clear that

$$I_r = R_x R_x^* I_i \tag{4.83}$$

Following the argumentation of Section 4.4.1, it can be proven that the Fresnel reflection matrix $\boldsymbol{R}_f$ is applicable to a diffuse Stokes vector without further modifications:

$$\boldsymbol{I}_r = \boldsymbol{R}_f \boldsymbol{I}_i \tag{4.84}$$

The final goal of this section is to find a reflection matrix that may be implemented in a radiative transfer algorithm such as the adding-doubling method (de Haan et al. 1987) based on the reflection by an atmospheric layer mathematically decribed by (Hovenier et al. 2004, Eq. 5.2):

$$\boldsymbol{I}_r(\mu,\varphi) = \frac{1}{\pi}\int_0^{+1} \mu_0 d\mu_0 \int_0^{2\pi} d\varphi_0 \boldsymbol{R}(\mu,\mu_0,\varphi-\varphi_0)\boldsymbol{I}_0(\mu_0,\varphi_0) \tag{4.85}$$

If we assume, for simplicity, that the incident beam on the air-water interface is monodirectional and unpolarized, we could write for the incident *radiance* vector (see Hansen and Travis 1974):

$$\boldsymbol{I}_0 = \delta(\mu-\mu_0)\delta(\varphi-\varphi_0)\pi\boldsymbol{F}_0 \tag{4.86}$$

where $\boldsymbol{E}_0 = \pi\boldsymbol{F}_0$ is again the incident irradiance and δ is the Dirac delta function such that expression 4.85 gives (Hansen and Travis 1974, Eq. 3.8)

$$\boldsymbol{R}(\mu,\mu_0,\varphi-\varphi_0) = \frac{\pi\boldsymbol{I}_r}{\mu_0\boldsymbol{E}_0} = \frac{\pi\boldsymbol{I}_r}{\mu_0\pi\boldsymbol{F}_0} \tag{4.87}$$

Finally, substituting the expression for $\boldsymbol{I}_r$ of Equation 4.84 into Equation 4.87 leads to the desired reflection matrix (Rozanov et al. 2014):

$$\boxed{\boldsymbol{R}(\mu,\mu_0,\varphi-\varphi_0) = \frac{\pi}{\mu_0}\boldsymbol{R}_f(\theta_i,n_1,n_2)\delta(\mu-\mu_0)\delta(\mu-\varphi_0)} \quad \checkmark\text{Rozanov et al. (2014)} \tag{4.88}$$

The transmitted and incident first diffuse Stokes vector elements in Equation 4.82b are related according to

$$I_t = \frac{n_2}{n_1}\frac{\cos\theta_t}{\cos\theta_i}T_x T_x^* \frac{d\Omega_i\cos\theta_i}{d\Omega_t\cos\theta_t} I_i \tag{4.89}$$

Substituting the solid angles $d\Omega_i = \sin\theta_i d\theta_i d\varphi$ and $d\Omega_t = \sin\theta_t d\theta_t d\varphi$ gives

$$I_t = \frac{n_2}{n_1}\frac{\cos\theta_t}{\cos\theta_i}T_x T_x^* \frac{\sin\theta_i d\theta_i d\varphi\cos\theta_i}{\sin\theta_t d\theta_t d\varphi\cos\theta_t} I_i \tag{4.90}$$

Substituting $\sin\theta_i = n_2\sin\theta_t/n_1$ from Snell's law and noting that $d\varphi$ is constant along the Fresnel interface yields

$$I_t = \frac{n_2}{n_1}\frac{\cos\theta_t}{\cos\theta_i}T_x T_x^* \frac{n_2}{n_1}\frac{\cos\theta_i d\theta_i}{\cos\theta_t d\theta_t} I_i \tag{4.91}$$

Squaring Snell's law and differentiation both sides yields the relation $n_1\cos\theta_i d\theta_i = n_2\cos\theta_t d\theta_t$. Therefore Equation 4.91 can be written as

$$I_t = \frac{n_2^3}{n_1^3}\frac{\cos\theta_t}{\cos\theta_i}T_x T_x^* I_i \tag{4.92}$$

Consequently, the Fresnel transmission matrix $\boldsymbol{T}_f$ for a flat Fresnel interface may be multiplied by a diffuse Stokes vector according to

$$\boldsymbol{I}_t = \boldsymbol{T}_f\boldsymbol{I}_i \tag{4.93}$$

where the transmission matrix equals (Zhai et al. 2012)

$$\boldsymbol{T}_f = \frac{n_2^3}{n_1^3}\frac{\cos\theta_t}{\cos\theta_i}\begin{pmatrix} \frac{1}{2}(|T_\parallel|^2+|T_\perp|^2) & \frac{1}{2}(|T_\parallel|^2-|T_\perp|^2) & 0 & 0 \\ \frac{1}{2}(|T_\parallel|^2-|T_\perp|^2) & \frac{1}{2}(|T_\parallel|^2+|T_\perp|^2) & 0 & 0 \\ 0 & 0 & \mathrm{Re}(T_\parallel T_\perp^*) & \mathrm{Im}(T_\parallel T_\perp^*) \\ 0 & 0 & \mathrm{Im}(T_\perp T_\parallel^*) & \mathrm{Re}(T_\perp T_\parallel^*) \end{pmatrix} \quad \checkmark\text{Zhai et al. (2012)} \tag{4.94}$$

In summary, the multiplication factor $f_T = (n_2^3\cos\theta_t)/(n_1^3\cos\theta_i)$ is needed because of a changing permittivity across the Fresnel interface and a changing projection of area dA due to the changing angle between the Poynting vector and the local vertical. The extra factor n_2^2/n_1^2, compared to the coherent Stokes vector case, accounts for the solid angle change of the diffuse Stokes vector travelling from medium 1 to medium 2.

Finally, comparing Equations 4.80b and 4.94 the Fresnel transmission matrix for a flat Fresnel interface may be implemented in a radiative transfer code as

$$\boxed{\boldsymbol{T}(\mu,\mu_0,\varphi-\varphi_0)=\frac{\pi}{\mu_0}\boldsymbol{T}_f(\theta_i,n_1,n_2)\delta(\mu-\mu_0)\delta(\varphi-\varphi_0)} \tag{4.95}$$

4.5. Reflection and Transmission Matrix Elements versus Incidence Angle

In this section, the elements of the reflection matrix of Equation 4.66 and transmission matrix of Equation 4.94 are evaluated for $0^o < \theta_i < 90^o$. First, the air-to-water case is discussed where medium 1 is air medium 2 is water, as before. Subsequently the case is discussed where the properties of medium 1 and 2 are reversed. All elements of the reflection and transmission matrices presented in this section, for the air-incident and water incident case, are verified with the results of Garcia (2012*a*), Garcia (2012*b*) and Zhai et al. (2012) that were summarized on the web page `http://www.oceanopticsbook.info/view/surfaces/level_2/fresnel_equations_for_polarization`.

4.5.1. Air-incident Radiance

Let us consider again a radiance vector in W m^{-2} sr^{-1} incident on a Fresnel interface as in Figure 4.9 where $n_1 = 1$ is again the refractive index of air and $n_2 = 1.34$ is the refractive index of water. The elements of the reflection matrix $\boldsymbol{R}_f$ and transmission matrix $\boldsymbol{T}_f$ for the transformation of this incidence radiance vector are plotted against incidence angle in Figure 4.10. For example, upper left subplot shows the 1,1 element of $\boldsymbol{R}_f$ (red line) and $\boldsymbol{T}_f$ (blue line).

Note that the transmission values may exceed 1 due to the extra factor n_2^2/n_1^2 that accounts for the change in solid angle of the diffuse Stokes vector across the Fresnel interface. In the end, the law of conservation of energy applies, and not the law of conservation of radiance. Therefore, it should also be mentioned that the transmitted directions are limited to a so-called Fresnel cone (i.e. θ_t does not span the full range $[0,\pi/2]$). Hence, by computing the integral of the transmitted radiance over all transmitted directions it may be shown that conservation of energy is not violated (see Sec. 4.2 of Mobley 1994). In Section 5.7 this energy balance will be further analyzed when we include the ocean waves.

Figure 4.11 shows the elements of the normalized matrices $\boldsymbol{R}_f/R_{f1,1}$ and $\boldsymbol{T}_f/T_{f1,1}$. An important result is the significant linear polarization of the reflected wave at the Brewster angle, which occurs indeed at approximately 53°(cf. Equation 4.53). That is, elements $R_{f1,2}/R_{f1,1}$ and $R_{f2,1}/R_{f1,1}$ decrease to a negative peak value at -1.0. Note that this is a direct consequence of the disappearance of the perpendicular component $R_\perp$ in Figure 4.6 such that $R_{f1,2}/R_{f1,1} = R_{f2,1}/R_{f1,1} = -1$ (cf. Equation 4.66).

4.5.2. Water-incident Radiance

Let us now consider a radiance vector in W m^{-2} sr^{-1} incident on a Fresnel interface as in Figure 4.9 where $n_1 = 1.34$ is again the refractive index of water and $n_2 = 1$ is the refractive index of air. That is, the refractive indices are interchanged compared to the air-incident case. The elements of the reflection matrix $\boldsymbol{R}_f$ and transmission matrix $\boldsymbol{T}_f$ for the transformation of the incidence radiance vector are plotted against incidence angle in Figure 4.12.

Note that the transmitted values for small θ_i do not approach 1.0. This is again the result of the n_2^2/n_1^2 factor that takes into account the change of solid angle of the diffuse Stokes vector across the Fresnel interface. Because for the water-incident case we have $n_2 < n_1$, the transmission is smaller than 1.
It may be noted that the upper left element of the reflection matrix is rapidly increased towards the limit value of 1.0 at the *critical angle* $\theta_{i,c}$. For incidence angles $\geq \theta_{i,c}$ total internal reflection occurs, that is, all the light travels in the grazing direction at an angle $\theta_t = 90^o$. Substituting $\theta_t = 90^o$ into Snell's law gives

$$\theta_{i,c} = \sin^{-1}\left(\frac{n_2}{n_1}\right) \tag{4.96}$$

which is around 48° for $n_2 = 1$ and $n_1 = 1.34$. The question to be answered is: how can total internal reflection mathematically be expressed? The answer lies in the complex part of the Fresnel reflection and transmission

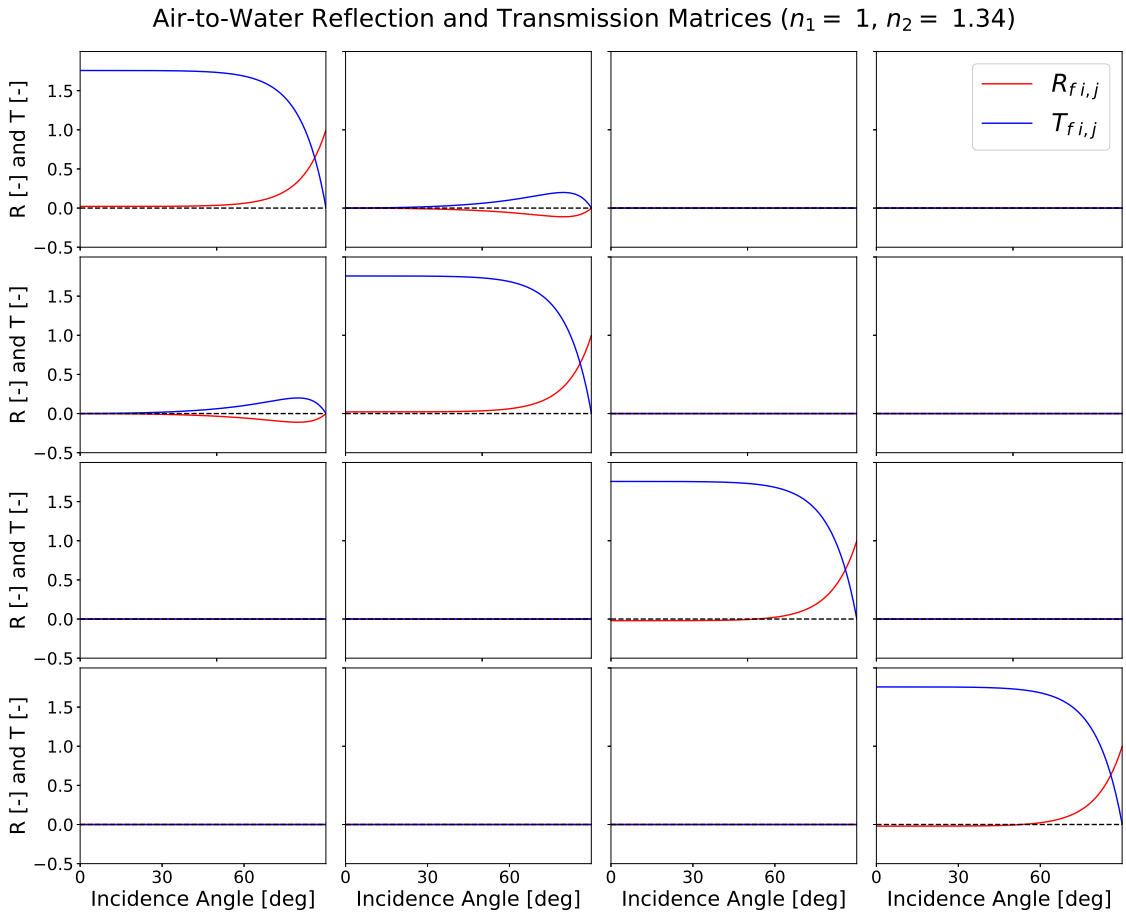

Figure 4.10: Air-to-water reflection and transmission matrix elements. Upper left is entry (1,1) and lower right is entry (4,4). The red line illustrates the reflection, the blue line illustrates the transmission.

coefficients. In Appendix B.2 we derive these coefficients. Thus, for incidence angles bigger than the critical angle we find

$$R_{f1,1} = \frac{1}{2}(|R_\parallel|^2 + |R_\perp|)^2 = 1 \tag{4.97}$$

$$R_{f1,2} = \frac{1}{2}(|R_\parallel|^2 + |R_\perp|)^2 = 0 \tag{4.98}$$

$$R_{f2,1} = \frac{1}{2}(|R_\parallel|^2 + |R_\perp|)^2 = 0 \tag{4.99}$$

$$R_{f2,2} = \frac{1}{2}(|R_\parallel|^2 + |R_\perp|)^2 = 1 \tag{4.100}$$

and

$$R_{f3,3} = \mathrm{Re}(R_\parallel R_\perp^*) \tag{4.101}$$

$$R_{f3,4} = \mathrm{Im}(R_\parallel R_\perp^*) \tag{4.102}$$

$$R_{f4,3} = \mathrm{Im}(R_\perp R_\parallel^*) \tag{4.103}$$

$$R_{f4,4} = \mathrm{Re}(R_\parallel R_\perp^*) \tag{4.104}$$

It should be noted that at incidence angles > $\theta_{i,c}$ the polarization upon reflection and transmission versus incidence angle is not constant, as illustrated by the elements (3,3), (3,4), (4,3) and (4,4) in Figures 4.12 and 4.13, even though all light is internally reflected.

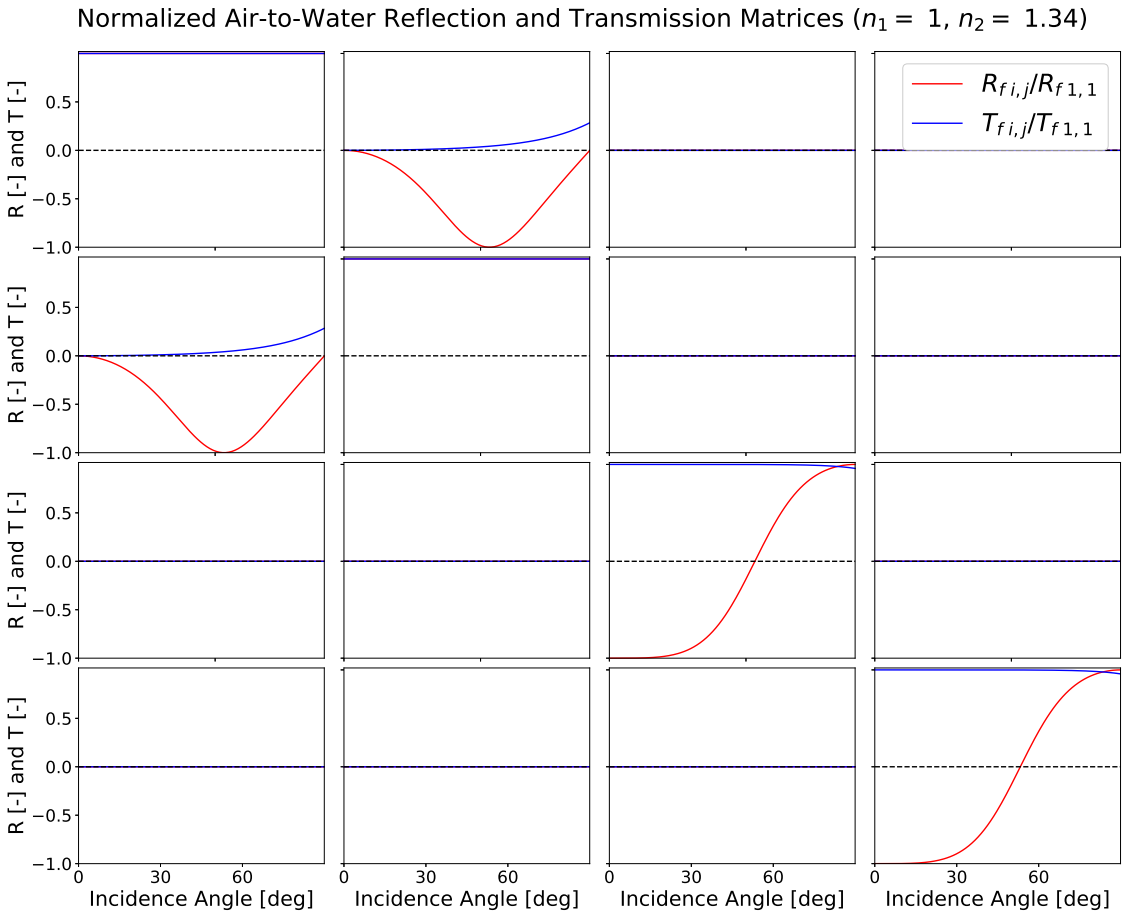

Figure 4.11: Normalized air-to-water reflection and transmission matrix elements. Upper left is entry (1,1) and lower right is entry (4,4). The red line illustrates the reflection, the blue line illustrates the transmission.

Figure 4.13 shows the normalized water-to-air reflection and transmission matrix elements as a function of incidence angle (illuminated from below). Note that, also for water incident reflected, a Brewster angle occurs at approximately 37°, which follows directly from Equation 4.53.

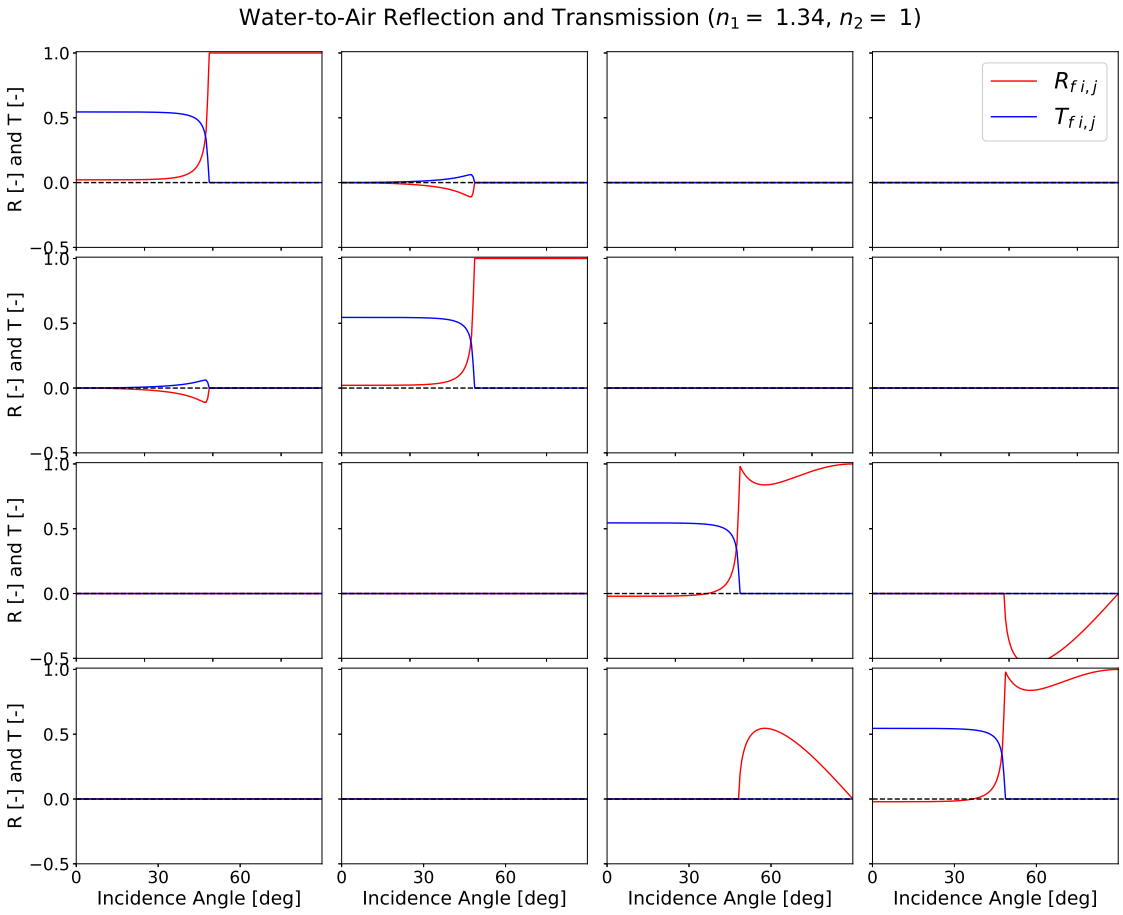

Figure 4.12: Water-to-air reflection and transmission matrix elements. Upper left is entry (1,1) and lower right is entry (4,4). The red line illustrates the reflection, the blue line illustrates the transmission.

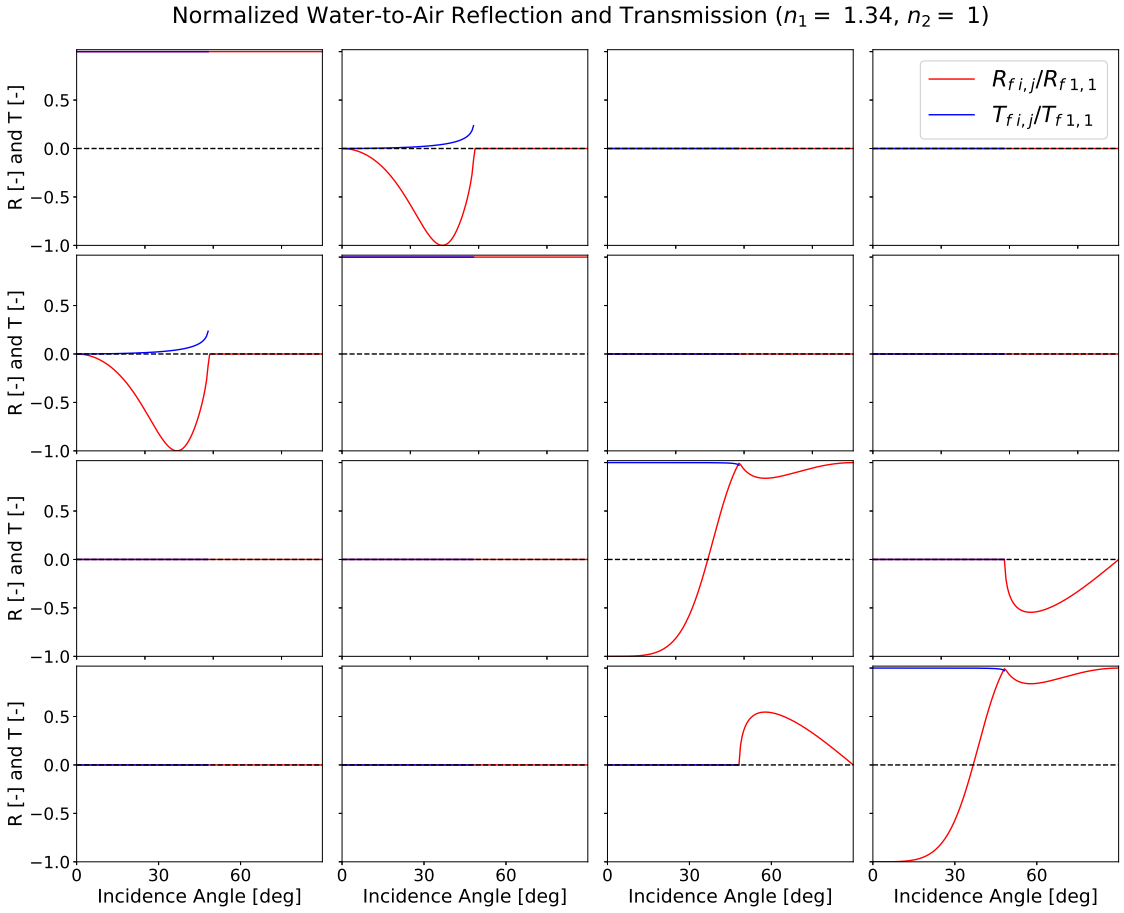

Figure 4.13: Normalized water-to-air reflection and transmission matrix elements. Upper left is entry (1,1) and lower right is entry (4,4). The red line illustrates the reflection, the blue line illustrates the transmission.

5

Reflection and Transmission by the Wind-Ruffled Air-Water Interface

In the previous chapter the reflection and transmission matrices for a flat interface separating two media with distinct refracting indices were derived. A realistic oceanic surface is, however, likely to be ruffled by the wind resulting in a rough air-ocean interface, thus an ocean surface with waves. This roughness causes the incident light to be diffusely reflected, having a peak value in one certain direction depending on the orientation of waves. In this chapter, the reflection and transmission matrices for a wind ruffled air-water interface are derived.

5.1. Reflection by a Wind Ruffled Air-Water Interface

In this section, the reflection of incident light on a wind ruffled air-water interface will be discussed. The air-water interface will be modeled as a collection of randomly oriented wave facets (small surface areas) with their normals pointing in the direction (μ_n, ϑ_n), where φ_n is the azimuth angle of the wave facet normal vectors as illustrated in Figure 5.1, ϑ_n is the zenith angle of these normal vector and ϑ' and ϑ are the solar zenith angle and viewing zenith angles respectively. Furthermore, we define $u = -\cos\vartheta$ and $\mu = |u|$ where $u > 0$ for downward vectors and $u < 0$ for upward vectors. Also we define $u' = -\cos\vartheta'$, $\mu' = |u'|$, $u_n = -\cos\vartheta_n$, and $\mu_n = |u_n|$. It should be noted that often the angles $\theta' = \pi - \vartheta'$ and $\theta_n = \vartheta_n$ are used. Generally, θ is defined as viewing angle with respect to the outward normal ($\theta = \vartheta$ for reflection and $\theta = \pi - \vartheta$ for transmission) (see e.g. Hansen and Travis 1974). If we now only employ θ', θ and θ_n on the interval $[0, \pi/2]$, we can define $\mu' = \cos\theta'$, $\mu_n = \cos\theta_n$ and $\mu = \cos\theta$.

The area of the collection of all wave facets in Figure 5.1 pointing in one particular direction (μ_n, φ_n) within the solid angle $d\Omega_n$ may mathematically be expressed as

$$dA_1^* = dA_{1,1}^* + dA_{1,2}^* + \ldots = \sum_{i=1}^{\infty} dA_{1,i}^* \tag{5.1}$$

The projection of $dA_{1,1}^*$ on the local horizontal is

$$dA_{1,1} = \cos\vartheta_n dA_{1,1}^* \tag{5.2}$$

Combining Equations 5.1 and 5.2 for each facet i having this orientation yields

$$dA_1 = \sum_{i=1}^{\infty} dA_{1,i} = \cos\vartheta_n dA_1^* \tag{5.3}$$

Note that dA_1 represents all the horizontal projections of the inclined wave facets pointing in the direction (μ_n, φ_n) within the solid angle Ω_n. Following Lenoble et al. (2007), the probability P that an incident beam is reflected by a wave facet pointing in the direction (μ_n, φ_n) within the solid angle Ω_n equals

$$\frac{dA_1}{A} = P(\mu_n, \varphi_n) d\Omega_n \tag{5.4}$$

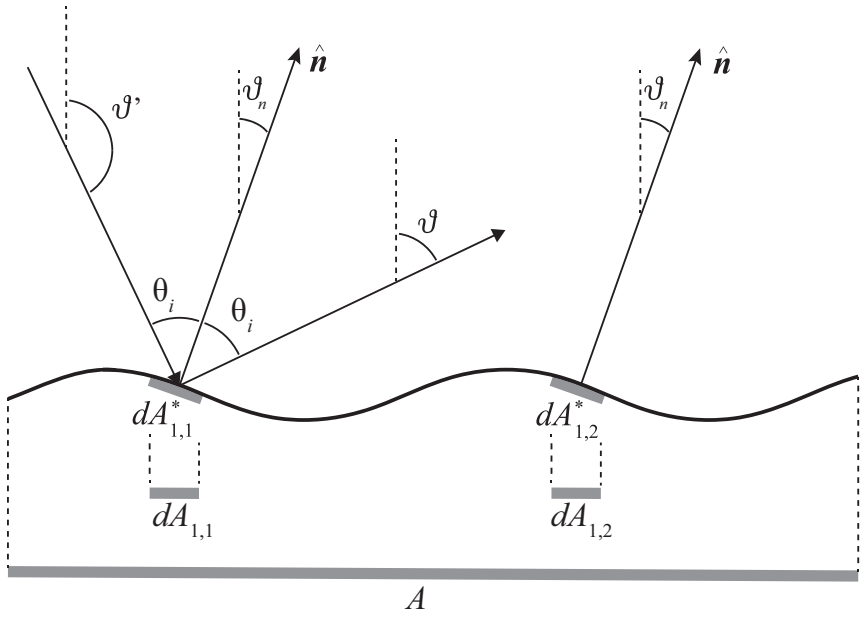

Figure 5.1: A 2D-sketch of piece of a wind ruffled water interface within the horizontal area A. The incident and reflected beams point in the directions (μ_0,φ') and (μ,φ) respectively, however, their zenith angles ϑ' and ϑ are drawn. The normals to the wave facets $dA^*_{1,1}$ and $dA^*_{1,2}$ point in the direction (μ_n,φ_n). $dA_{1,1}$ and $dA_{1,2}$ are their horizontal projections respectively. The sum of $dA_{1,i}$ for $i = 1,2,...,\infty$ is the fraction of A that has normals in the particular direction (μ_n,φ_n).

where P is the wind-isotropic Cox and Munk (1954, 1956) wave facet slope probability distribution which will be discussed in Section 5.2.

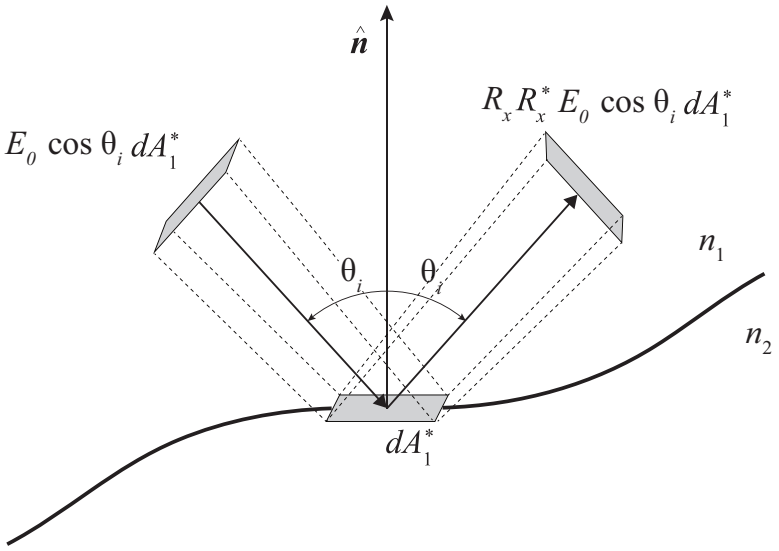

Figure 5.2: Illustration of the reflected power per unit area, where dA^*_1 represents the collection of wave facets whose normals point in a similar direction.

Let us assume that the incident beam is unpolarized light with irradiance E_0 in W m^{-2} monodirectional in the direction μ_0. The objective of this section is to derive an expression for the air-water interface reflection in Figure 5.1 in the viewing direction within the solid angle $d\Omega_r$ taking into account the randomly oriented wave facets. That is, we need to find a relation between E_0 and the corresponding reflected radiance I_r in W m^{-2} sr^{-1}. Therefore, we need to analyze the power balance at the collection of specular reflecting wave facets dA^*_1 whose normals point in the direction (μ_n,φ_n) within $d\Omega_n$ (see Section 4.4). Recall that the reflected power

by this collection of wave facets could be expressed in two ways. First, as the reflected part of the incident irradiance on this collection of wave facets dA_1^*, which is illustrated in Figure 5.2, and reads (cf. Equations 4.75 and 4.81a):

$$P_r = R_x R_x^* E_0 \cos(\theta_i) dA_1^* \tag{5.5}$$

where R_x and R_x^* are either the parallel or perpendicular Fresnel coefficients and their complex conjugate respectively.

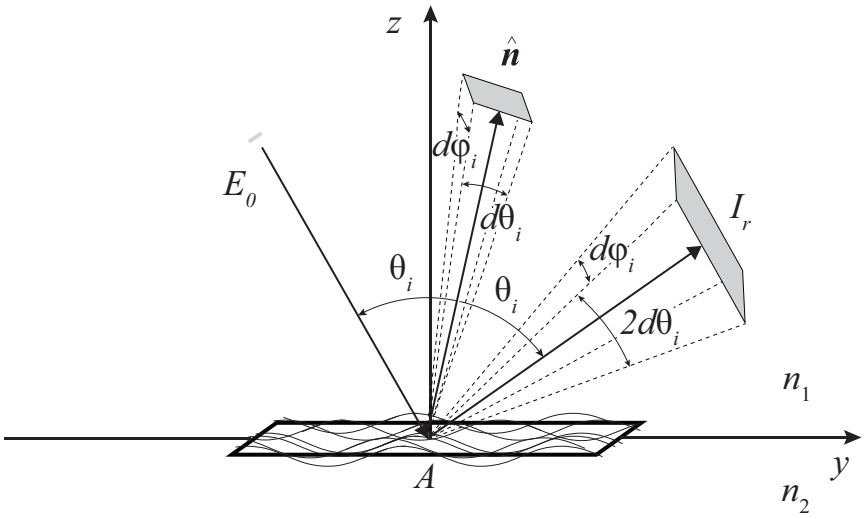

Figure 5.3: Reflected radiance by the area A containing all different kind of wave facets whose normals point in random directions.

Second, assuming that the solid angle of the reflected radiance I_r by this collection of wave facets is $d\Omega_r$, the reflected power from the horizontal surface area A as illustrated in Figure 5.3 in the direction μ within $d\Omega_r$ may be expressed by

$$P_r = I_r \cos\theta A d\Omega_r \tag{5.6}$$

Equating expressions 5.5 and 5.6 gives (Zhai et al. 2010, Eq. 19)

$$I_r \cos\theta A d\Omega_r = R_x R_x^* E_0 \cos\theta_i dA_1^* \tag{5.7}$$

Isolating I_r yields

$$I_r = \frac{R_x R_x^* E_0 \cos\theta_i dA_1^*}{d\Omega_r A \cos\theta} \tag{5.8}$$

The expression for I_r may be written as functions of solely its involved angles by eliminating the areas as follows (cf. Equation 5.4):

$$\frac{dA_1^*}{A} = \frac{dA_1^*}{dA_1}\frac{dA_1}{A} = \frac{1}{\mu_n} P(\mu_n, \varphi_n) d\Omega_n \tag{5.9}$$

where $\mu = \cos\theta$ and

$$I_r = \frac{R_x R_x^* E_0}{\mu_n \mu}\frac{\cos\theta_i d\Omega_n}{d\Omega_r} P(\mu_n, \varphi_n) \tag{5.10}$$

The solid angle of the wave facet normal is $\sin\theta_i d\theta_i \varphi$. Since, from the law of reflection, we know that the angle between the reflected beam and the incident beam equals $2\theta_i$ and that the specular reflection does not change the azimuthal direction of the beam (see Figure 5.3), the solid angle of the reflected beam is $\sin(2\theta_i) 2 d\theta_i d\varphi$ and the following holds (see Lenoble et al. 2007):

$$\frac{\cos\theta_i d\Omega_n}{d\Omega_r} = \frac{\sin\theta_i \cos\theta_i d\theta_i d\varphi}{\sin 2\theta_i 2 d\theta_i d\varphi} = \frac{\frac{1}{2}\sin 2\theta_i d\theta_i d\varphi}{2\sin 2\theta_i d\theta_i d\varphi} = \frac{1}{4} \tag{5.11}$$

Substituting the expression for $\cos\theta_i d\Omega_n / d\Omega_r$ of Equation 5.11 into Equation 5.10 gives (Zhai et al. 2010, Eq. 20)

$$I_r = \frac{R_x R_x^* E_0}{4\mu_n \mu} P(\mu_n, \varphi_n) \tag{5.12}$$

Because $R_x R_x^*$ represent every possible combination of the perpendicular and parallel Fresnel reflection coefficients (Zhai et al. 2012), it can readily be verified that Equation 5.12 also applies when replacing $R_x R_x^*$ by the 4x4 Fresnel reflection matrix $\boldsymbol{R}_f$ (Equation 4.66) such that the reflected diffuse Stokes vector in the scattering plane ($\varphi - \varphi' = 0$) may be computed according to

$$\boldsymbol{I}_r = \frac{\boldsymbol{R}_f \boldsymbol{E}_0}{4\mu_n \mu} P(\mu_n, \varphi_n) \tag{5.13}$$

5.2. Slope Distribution Models of Ocean Surface Waves

The distribution of the slopes of the wave facets $P(\mu_n, \varphi_n)$ was investigated by Cox and Munk (1954, 1956) who made photographs from a plane of the pattern of the specular reflection of the sunlight by the ocean wave facets, better known as the *Sun's glitter* or *sunglint*. If no waves are present the glitter would reduce to the *horizontal specular point* which is the location of the mirror-image of the Sun in the water as seen from the observer. In case of a wind-driven rough ocean surface the presence of the slopes of the wave facets allow the glitter pattern to be wider than the horizontal specular point. Cox and Munk (1954, 1956) found indeed that the width of the glitter pattern increases linearly with wind speed and were able to translate the statistics of the glitter into statistics of the slope distribution.

5.2.1. The Cox and Munk Model

Cox and Munk (1954, 1956) considered a wave facet to be tilted by an angle β such that the slopes in the x and y direction are respectively denoted by Z_x and Z_y. Let the x-axis point in the horizontal direction from the facet to the Sun[1]; the slopes Z_x and Z_y may then be given by (see e.g. Sun and Lukashin 2013)

$$Z_x = \frac{\partial Z}{\partial x} = \frac{\sin\vartheta \cos(\varphi - \varphi') - \sin\vartheta'}{\cos\vartheta + \cos\vartheta'} \tag{5.14}$$

$$Z_y = \frac{\partial Z}{\partial y} = \frac{\sin\vartheta \sin(\varphi - \varphi_0)}{\cos\vartheta + \cos\vartheta'} \tag{5.15}$$

where ϑ, ϑ' and $\varphi - \varphi_0$ are the zenith angle of the reflected beam, the solar zenith angle and the azimuth difference between the reflected and incident beam as in Section 2.1.4. It may be noted that Cox and Munk (1954, 1956) defined the slope components as $Z_x = \sin\alpha \tan\beta$ and $Z_y = \cos\alpha \tan\beta$ where α is the azimuth of the diagonal of the wave facet.

Cox and Munk (1954, 1956) assumed the probability distribution of the water facet normals to be Gaussian. They expressed the probability distributions of the slopes in three forms: wind-isotropic, wind-anisotropic and wind-anisotropic with an additional Gram-Charlier series correction term. The wind-isotropic form was used by Mishchenko and Travis (1997) who applied the probability density function (pdf) of Cox and Munk (1954, 1956) in the form (see Breon 1993; Zhai et al. 2010) [2]

$$P(Z_x, Z_y, \sigma) \approx \frac{1}{\pi\sigma^2} \exp\left(-\frac{Z_x^2 + Z_y^2}{\sigma^2}\right) \quad \text{or} \quad P(\mu_n, \sigma) = \frac{1}{\mu_n^3} \frac{1}{\pi\sigma^2} \exp\left(-\frac{1-\mu_n^2}{\sigma^2 \mu_n^2}\right) \tag{5.16}$$

[1] Contrary to Cox and Munk (1954, 1956) in this report the x-axis points in the horizontal direction towards the Sun rather than the y-axis following the convention of Breon (1993); Sun and Lukashin (2013).

[2] Care should be taken when comparing this relation with the one used by Mishchenko and Travis (1997); they defined the variance of the pdf as $2\sigma^2$ and applied this in the formula for P yielding the same result as obtained by Equation 5.16.

which may easily be verified by noting that $\tan\beta = \sqrt{Z_x^2 + Z_y^2}$, $\tan\beta = \sin\beta/\cos\beta = \sqrt{1-\cos^2\beta}/\cos\beta$ and $\mu_n = |\cos\beta|$. The factor $1/\mu_n^3$ is caused by the change of differential $dZ_x dZ_y$ to $d\Omega_n$ (see appendix of Breon 1993). Cox and Munk (1954, 1956) showed that the variance σ^2 is related to the wind speed v by (cf. Cox and Munk 1954, Section 6.3)[3]

$$\sigma^2 = 0.003 + 0.00512\,v \tag{5.17}$$

In the wind-*anisotropic* form of this pdf the upwind and crosswind components are separated. The upwind and crosswind components of the sea surface slope, Z_{up} and Z_{cr}, may readily be derived from Z_x and Z_y according to (see e.g. Bréon and Henriot 2006)

$$Z_{up} = Z_x \cos\phi_{wind} + Z_y \sin\phi_{wind} \tag{5.18}$$

$$Z_{cr} = -Z_x \sin\phi_{wind} + Z_y \cos\phi_{wind} \tag{5.19}$$

where ϕ_{wind} is the upwind direction with respect to the x-axis. By defining the parameters $\xi = Z_{cr}/\sigma_{cr}$ and $\eta = Z_{up}/\sigma_{up}$ Cox and Munk (1954, 1956) suggested to write the pdf as a Gram Charlier series as follows (Cox and Munk 1954, Eq. 18)

$$\begin{aligned} P(Z_{up}, Z_{cr}) = \frac{1}{2\pi\sigma_{up}\sigma_{cr}} \exp\left(-\frac{\xi^2+\eta^2}{2}\right) \cdot \Bigg[1 - \frac{1}{2}c_{21}(\xi^2-1)\eta - \frac{1}{6}c_{03}(\eta^3 - 3\eta) \\ + \frac{1}{24}c_{40}(\xi^4 - 6\xi^2 + 3) + \frac{1}{24}c_{04}(\eta^4 - 6\eta^2 + 3) \\ + \frac{1}{4}c_{22}(\xi^2-1)(\eta^2-1) \Bigg] \end{aligned} \tag{5.20}$$

The Gram Charlier term in Equation 5.20 accounts for the deviation from the Gaussian nature of the distribution (see Cox and Munk 1956). The coefficients c_{21} and c_{03} describe the skewness of the upwind slope component and the c_{40}, c_{04} and c_{22} express the peakedness of the pdf. Cox and Munk (1954, 1956) estimated σ_{up}, σ_{cr}, c_{21} and c_{03} to vary linearly with wind speed while the peakedness coefficients were set constant. Recently Bréon and Henriot (2006) used wind vector data from the NASA Scatterometer (NSCAT) (Naderi et al. 1991) and reflected radiance data from the POLDER radiometer (Deschamps et al. 1994) to estimate the Gram-Charlier coefficients again. They found, however, that the modeled mean squared surface slope of Cox and Munk (1954, 1956) was in perfect agreement with the results obtained from the satellite data (see Bréon and Henriot 2006, Fig. 3 and 4). Because of the large satellite data set they were able to increase the order of the c_{21}-v and c_{03}-v relations and to slightly correct the peakedness coefficients c_{40}, c_{04} and c_{22}. These refinements only had a small impact on the resulting pdf (see Bréon and Henriot 2006).

5.2.2. Alternative Slope Distribution Models

Besides the work of Bréon and Henriot (2006) other estimations of the Gram Charlier coefficients and slope variances related to wind speed have been done. Wu (1972) used the data set of Cox and Munk (1954) to divide the slope variance dependency in two ranges ($v \le 7$ m/s and $v > 7$ m/s) and proposed two logarithmic functions. Mermelstein et al. (1994) obtained the wind-anisotropic slope standard deviations by integrating the sea-wave height power spectral density provided by Donelan and Pierson (1987) resulting in a flatter glitter peak (i.e. higher σ_{up} and σ_{cr} values) for wind speeds lower than 20 m/s compared to the results of Cox and Munk (1954). Shaw and Churnside (1997) did wind speed measurements with a sonic anemometer and measured the glitter reflectance with their so-called reflective scanning-laser glint sensor. They divided the slope variance dependency in two ranges defined by the stability of the atmosphere and sea using the reduced Richardson number ($-0.23 < Ri < 0.27$ and $Ri \ge 0.27$), which depends on the wind speed at a certain height and average air and water temperatures. Ebuchi and Kizu (2001) analyzed glitter images taken by a radiometer on the Geostationary Meteorological Satellite (GMS) in combination with sea surface wind data from spaceborn scatterometers, such as the the NSCAT, the European Remote sensing Satellite (ERS)-1 and -2, the Active Microwave Instrument (AMI) and the ADvanced Earth Observation Satellite (ADEOS). They obtained a narrower slope distribution (smaller σ_{up},σ_{cr} and σ values) compared to the pdf of Cox and Munk (1954).

[3] Similar relations for the upwind and crosswind components ($\sigma_{up} - v$ and $\sigma_{cr} - v$) may be found in Cox and Munk (1954, 1956).

5.2.3. Comparison of the Slope Distribution Models

Zhang and Wang (2010) compared the results of the various models mentioned in the latter section with measurements from the Moderate Resolution Imaging Spectroradiometer (MODIS) at wavelengths of 859 nm, 1240 nm and 2130 nm with an image resolution of 1 km. They applied atmospheric corrections for the atmospheric absorption, Rayleigh scattering and scattering by aerosols. It was pointed out that the model of Shaw and Churnside (1997) could not accurately be compared since no reduced Richardson number data was available for the data sets from which the other models were generated and was therefore omitted. Figure 5.4 shows the normalized sunglint radiance comparison of the wind-isotropic (left) and the wind-anisotropic glitter models (right) to the MODIS measurements. An accurate fit of the Cox and Munk (1954, 1956) and Bréon and Henriot (2006) anisotropic models may be observed.

Zhang and Wang (2010) also computed the correlation coefficients of the modeled and measured radiance emerging at the top of the atmosphere for 12 different scenarios[4] (see Zhang and Wang 2010, Table 2 and 3). The highest correlation coefficients (between 0.951 and 0.985) were achieved by the wind-anisotropic Cox and Munk (1954, 1956) and wind-anisotropic Bréon and Henriot (2006) models for 9 out of 12 scenarios. The second best models in terms of correlation coefficients were the wind-isotropic and wind-anisoptropic Gram Charlies Cox and Munk (1954, 1956) models. The good performance of the wind-isotropic Cox and Munk (1954, 1956) model could, according to Zhang and Wang (2010), be explained by the large variability of wind directions above open oceans. The final conclusion of Zhang and Wang (2010) was:

"Overall, the wind-direction-dependent Cox-Munk models have the highest correlations with MODIS measurements. The Cox-Munk wind-direction-independent model, however, is very close to the wind-direction-dependent ones, and for some cases it is even better. The Breon-Henriot models have about the same performance results as from the Cox-Munk models because the Breon-Henriot and Cox-Munk models are in fact very similar. [...] It is amazing that the Cox-Munk glint models that were developed 50 years ago are still among the best," (Zhang and Wang 2010, p. 505).

Nowadays the wind-isotropic Cox and Munk model is still the standard model used by NASA for sunglint corrections in ocean color satellite data processing (see Mobley et al. 2016).

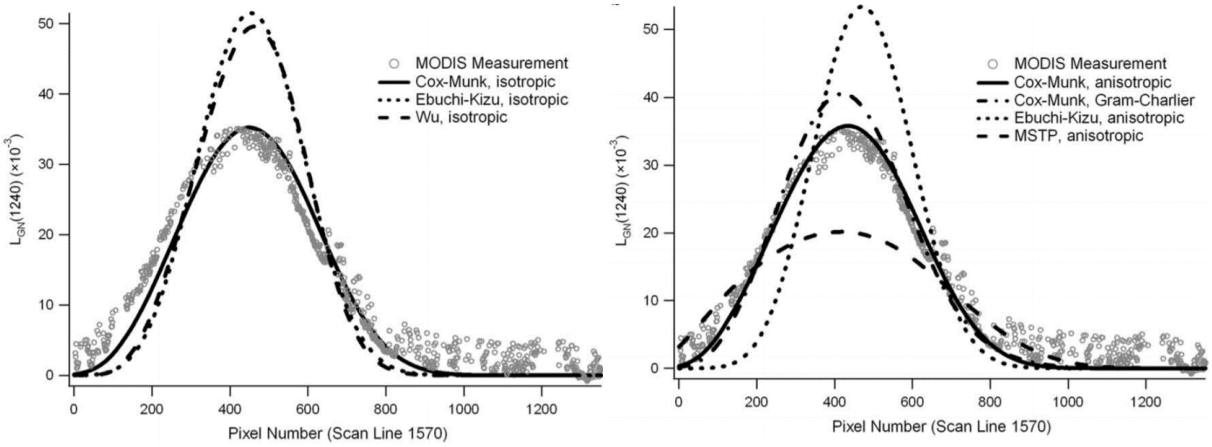

Figure 5.4: Comparison of the wind-isotropic glitter models of Cox and Munk (1954, 1956); Ebuchi and Kizu (2001); Wu (1972) (left) and the wind-anisotropic glitter models of Bréon and Henriot (2006); Cox and Munk (1954, 1956); Ebuchi and Kizu (2001); Mermelstein et al. (1994) (right). The Gram-Charlies expanded wind-anisotropic Cox and Munk (1954, 1956) is also included in the right figure. The Bréon and Henriot (2006) anisotropic and Gram-Charlies models almost coincide with their Cox-Munk counterparts and are therefore not shown. Scenario: January 26, 2004, Pacific Ocean (1.8°S, 104.4°W), $\bar{v}$ = 6.4 m/s and ϑ' = 12-39° (Zhang and Wang 2010, Fig. 6).

In what follows, we will consider the wind-isotropic Cox and Munk (1954, 1956) slope distribution model. Except for its convincing performance at moderate wind speeds and simplicity (only the wind speed is needed), symmetry in the azimuth direction is preserved which allows us to do a Fourier decomposition of the reflection and transmission matrices of the interface matrices by computing the integral over the azimuth difference (Equation 2.82). Using this wind-isotropic model, it should be remembered that (1) the analysis of Zhang

[4] The MODIS scenarios varied in date, location (Indian Ocean / Pacific Ocean / Atlantic Ocean), aerosol model, aerosol optical thickness, wind speed and solar zenith (see Zhang and Wang 2010, Table 2).

and Wang (2010) was done only for moderate wind speeds and (2) the Cox and Munk (1954, 1956) model did not measure wind speeds higher than 14 m/s. The wind speed in the model planets of this research do therefore not exceed 14 m/s.

5.3. The Reflection Matrix for a Wind Ruffled Air-Water Interface

It should be noted that up till now the reference plane of the Fresnel reflection is also the scattering plane. That is, we assumed that the perpendicular component of the electric field vector is perpendicular to the plane of Fresnel reflection. However, since the wave facets normals may point in directions where $\varphi_n - \varphi_0 \neq 0$, the reference plane may transform from the meridian plane of the incident beam into the Fresnel reflection plane through the rotation $-\sigma_1$, and subsequently may transform again in the meridian plane of the reflected beam through the rotation $-\sigma_2$ (see also Section 2.1.4). In this section, the mathematical expressions for these rotations and the azimuth dependent rough air-water interface reflection matrix are derived.

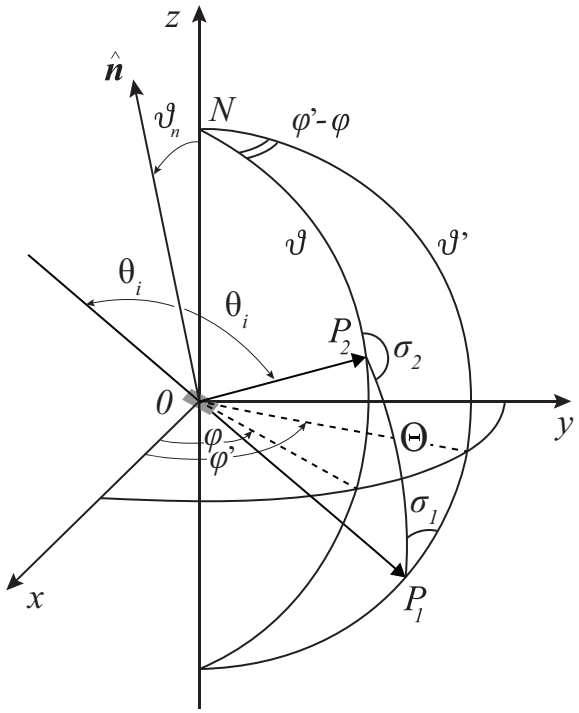

Figure 5.5: Sketch of an incident beam OP_1 reflected at the wave facet at O in the direction OP_2. The wave facet is tilted by the angle ϑ_n with respect to the z-axis and points in the azimuth angle φ_n (not indicated). The scattering angle Θ equals $\pi - 2\theta_i$.

Let us define the coordinate system of the reflection event as a right handed Cartesian coordinate system fixed in space with the wave facet located at its origin O (see Figure 5.5), analogous to the approach of Hovenier and van der Mee (1983). We assume the azimuth angle φ measured positive in the clockwise direction when looking in the positive z-direction. The incidence beam points in the (OP_1) direction and the reflected beam points in the (OP_2) direction. The normal vector to the wave facet is indicated by $\hat{\boldsymbol{n}}$ and θ_i indicates the Fresnel reflection angle of the wave facet with respect to $\hat{\boldsymbol{n}}$ as in Section 4.4. The scattering angle is indicated by Θ. Hence, by defining $\theta' = \pi - \vartheta'$, $\theta_n = \vartheta_n$ and $\theta = \vartheta$ we can write the unit vectors of the incident, normal and reflected beams as

$$\hat{\boldsymbol{i}} = \begin{pmatrix} \sin\theta'\cos\varphi' \\ \sin\theta'\sin\varphi' \\ -\cos\theta' \end{pmatrix}, \quad \hat{\boldsymbol{n}} = \begin{pmatrix} \sin\theta_n\cos\varphi_n \\ -\sin\theta_n\sin\varphi_n \\ \cos\theta_n \end{pmatrix}, \quad \hat{\boldsymbol{r}} = \begin{pmatrix} \sin\theta\cos\varphi \\ \sin\theta\sin\varphi \\ \cos\theta \end{pmatrix} \tag{5.21}$$

respectively. Note the minus sign of the z-component of $\hat{\boldsymbol{i}}$ due to the downward incidence direction. The angle between $\hat{\boldsymbol{i}}$ and $\hat{\boldsymbol{r}}$ equals $\cos\Theta$. Computing the dot product of $\hat{\boldsymbol{i}}$ and $\hat{\boldsymbol{r}}$ yields

$$\cos\Theta = -\cos\theta'\cos\theta + \sin\theta'\sin\theta(\cos\varphi'\cos\varphi + \sin\varphi'\sin\varphi) \tag{5.22}$$
$$= -\cos\theta'\cos\theta + \sin\theta'\sin\theta\cos(\varphi' - \varphi) \tag{5.23}$$

If we only use θ' and θ between 0 and $\pi/2$, we can write $\cos\theta' = |\cos\theta'| = \mu'$ and $\cos\theta = |\cos\theta| = \mu$ and

$$\cos\Theta = -\mu'\mu + \sqrt{1-\mu'^2}\sqrt{1-\mu^2}\cos(\varphi' - \varphi) \tag{5.24}$$

The rotation angles σ_2 and σ_1 in Figure 5.5 are equivalent to σ_2 and σ_1 in Figure 2.3a of Display 2.1. Applying the cosine rules to the spherical triangle ONP_1P_2 gives

$$\cos\sigma_1 = \frac{\cos\vartheta - \cos\Theta\cos\vartheta'}{\sin\Theta\sin\vartheta'} = \frac{\cos\theta + \cos\Theta\cos\theta'}{\sin\Theta\sin\theta'} \tag{5.25}$$

$$\cos\sigma_2 = \frac{\cos\vartheta' - \cos\Theta\cos\vartheta}{\sin\Theta\sin\vartheta} = \frac{-\cos\theta' - \cos\Theta\cos\theta}{\sin\Theta\sin\theta} \tag{5.26}$$

Substituting again for $\cos\theta' = |\cos\theta'| = \mu'$ and $\cos\theta = |\cos\theta| = \mu$ yields

$$\cos\sigma_1 = \frac{\mu + \mu'\cos\Theta}{\sqrt{1-\mu'^2}\sqrt{1-\cos^2\Theta}} \tag{5.27}$$

$$\cos\sigma_2 = \frac{-\mu' - \mu\cos\Theta}{\sqrt{1-\mu^2}\sqrt{1-\cos^2\Theta}} \tag{5.28}$$

Note that the expressions in Equations 5.27 and 5.28 are consistent with Equations 100 and 101 of Hovenier and van der Mee (1983) if we realize that for the reflection case: $\mu = \cos\theta = \cos\vartheta = -u$ and $\mu' = \cos\theta' = \cos(\pi - \vartheta') = -\cos\vartheta' = u'$.

It may be recalled from Chapter 1 that the rotation matrices $\boldsymbol{L}(-\sigma_1)$ and $\boldsymbol{L}(-\sigma_2)$ that are needed for the reference plane transformations are given by Equation 1.13 where the rotation angle is positive in the anticlockwise direction when looking in the direction of wave propagation. Hence, the expression of the reflected radiance vector $\boldsymbol{I}_r$ of Equation 5.13 in the coordinate system of Figure 5.5 is

$$\boldsymbol{I}_r = \frac{\boldsymbol{L}(-\sigma_2)\boldsymbol{R}_f(\theta_i, n_1, n_2)\boldsymbol{L}(-\sigma_1)\boldsymbol{E}_0}{4\mu_n\mu} P(\mu_n, \varphi_n) \tag{5.29}$$

The final goal of this section is to find a reflection matrix for the interface, $\boldsymbol{R}_i$, that may be implemented in a radiative transfer algorithm such as the adding-doubling method (de Haan et al. 1987) based on the reflection mathematically described by (Hovenier et al. 2004, Eq. 5.2):

$$\boldsymbol{I}_r(\mu,\varphi) = \frac{1}{\pi}\int_0^{+1}\mu' d\mu' \int_0^{2\pi} d\varphi' \boldsymbol{R}_i(\mu,\mu',\varphi-\varphi')\boldsymbol{I}_{inc}(\mu',\varphi') \tag{5.30}$$

Since we assumed, for simplicity, that the incident beam on the air-water interface is monodirectional and unpolarized, we could write for the incident *radiance* vector (see Hansen and Travis 1974):

$$\boldsymbol{I}_{inc} = \delta(\mu - \mu_0)\delta(\varphi - \varphi_0)\pi\boldsymbol{F}_0 \tag{5.31}$$

where $\boldsymbol{E}_0 = \pi\boldsymbol{F}_0$ is again the incident irradiance such that expression 5.30 gives (Hansen and Travis 1974, Eq. 3.8)

$$\boldsymbol{R}_i(\mu,\mu',\varphi-\varphi') = \frac{\pi\boldsymbol{I}_r}{\mu'\pi\boldsymbol{F}_0} = \frac{\pi\boldsymbol{I}_r}{\mu'\boldsymbol{E}_0} \tag{5.32}$$

Substituting the expression for $\boldsymbol{I}_r$ of Equation 5.29 into Equation 5.32 leads to the desired reflection matrix (Zhai et al. 2010, Eq. 25):

$$\boxed{\boldsymbol{R}_i(\mu,\mu',\varphi-\varphi') = S(\mu,\mu',\sigma)\frac{\pi}{\mu'}\frac{P(\mu_n,\varphi_n)}{4\mu\mu_n}\boldsymbol{L}(-\sigma_2)\boldsymbol{R}_f(\theta_i,n_1,n_2)\boldsymbol{L}(-\sigma_1)} \quad \checkmark\text{Zhai et al. (2010)} \tag{5.33}$$

Note that we already introduced the multiplication by the shadowing function $S(\mu,\mu',\sigma)$ correcting for the shadows of the waves which will be further explained in Section 5.7. The reflection matrix for a wind ruffled ocean as presented by Equation 5.33 is only a function of $n_1, n_2, \sigma, \mu, \mu'$ and $\varphi-\varphi'$ if μ_n, θ_i, σ_2 and σ_1 can be written as functions of μ, μ' and $\varphi-\varphi'$. They are discussed case-by-case below:

- The incidence Fresnel angle θ_i and the scattering angle Θ are related by $2\theta_i = \pi - \Theta$ (see Figure 5.5). Substituting for $\theta_i = (\pi-\Theta)/2$ in the Fresnel matrix $\boldsymbol{R}_f(\theta_i, n_1, n_2)$ yields $\boldsymbol{R}_f(\Theta, n_1, n_2)$. Equation 5.23 shows that Θ can be expressed as functions of μ, μ' and $\varphi'-\varphi$. Therefore the Fresnel matrix $\boldsymbol{R}_f(\mu,\mu',\varphi-\varphi', n_1, n_2)$ may be obtained.
- According to the law of reflection the angle between the incident and reflected wave equals $2\theta_i$ and the projections of the unit normal vector of the wave facet on the incident and reflected unit vectors are -$\hat{\boldsymbol{i}} = \cos\theta_i \hat{\boldsymbol{n}}$ and $\hat{\boldsymbol{r}} = \cos\theta_i \hat{\boldsymbol{n}}$ respectively. Note again the minus sign is needed here to reverse the direction of $\hat{\boldsymbol{i}}$. Consequently we can write (Cox and Munk 1956, Eq. 3-3):

$$\hat{\boldsymbol{r}} - \hat{\boldsymbol{i}} = 2\cos\theta_i \hat{\boldsymbol{n}} \tag{5.34}$$

  Now, if we only consider the z-components of $\hat{\boldsymbol{r}}$, $\hat{\boldsymbol{i}}$ and $\hat{\boldsymbol{n}}$, combining Equations 5.21 and 5.34 gives

$$\cos\theta + \cos\theta' = 2\cos\theta_i \cos\theta_n \tag{5.35}$$

  or

$$\mu_n = \frac{\mu+\mu'}{2\cos\theta_i} \tag{5.36}$$

  In the former bullet point we stated $2\theta_i = \pi - \Theta$. Hence, $2\cos\theta_i = 2\cos((\pi-\Theta)/2) = \sqrt{2\cos(\pi-\Theta)+2} = \sqrt{2-2\cos\Theta}$ and Equation 5.36 becomes

$$\mu_n = \frac{\mu+\mu'}{\sqrt{2-2\cos\Theta}} \tag{5.37}$$

  Since $\cos\Theta$ was expressed in terms of μ, μ' and $\varphi-\varphi'$ in the former bullet point, μ_n can be expressed in terms of μ, μ' and $\varphi-\varphi'$ and consequently we can compute $P(\mu,\mu',\varphi-\varphi')$.

Note that the approach presented in this section is equivalent to the approach of Zhai et al. (2010), but we keep μ, μ' and μ_n in the range [0,1] and therefore the z-component of our incident unit vector $\hat{\boldsymbol{i}}$ is negative. Zhai et al. (2010) chose to employ $\mu' = \cos\theta' < 0$ such that no minus sign appears in their incident unit vector (since their μ' is already negative). Hence, Equation 5.37 is equivalent to Equation 28 of Zhai et al. (2010) and our expression for $\cos\Theta$ (Equation 5.24) is equivalent to the one of Zhai et al. (2010).

Figure 5.6 shows the result of the interface reflection matrix $\boldsymbol{R}$ (Equation 5.33) for an incidence angle of 33.3° and an azimuth difference of 0°.

We tested the matrix elements of **R** as shown Figure 5.6 with the output of the code of Dr. Mishchenko available on the web page `https://www.giss.nasa.gov/staff/mmishchenko/brf/` and we find an identical result.[5] The tests were performed with and without a correction for the wave shadows (the shadowing function will be treated Section 5.7).

5.4. Transmission by a Wind Ruffled Air-Water Interface

Analogous to the discussion of the reflection by a wind ruffled air-water interface of Section 4.5, the *transmission* by a wind ruffled air-water interface will be discussed in this section. The transmitted power of a light beam incident on the rough air-water interface as in Figure 5.2 is described by (cf. Equations 4.75 and 4.81b)

$$P_t = \frac{n_2}{n_1}\frac{\cos\theta_t}{\cos\theta_i} T_x T_x^* P_i = \frac{n_2}{n_1}\frac{\cos\theta_t}{\cos\theta_i} T_x T_x^* E_0 \cos(\theta_i) dA_1^* \tag{5.38}$$

[5] We tested our results also for the cases $\varphi-\varphi_0 < 0$ and $\varphi-\varphi_0 > 0$.

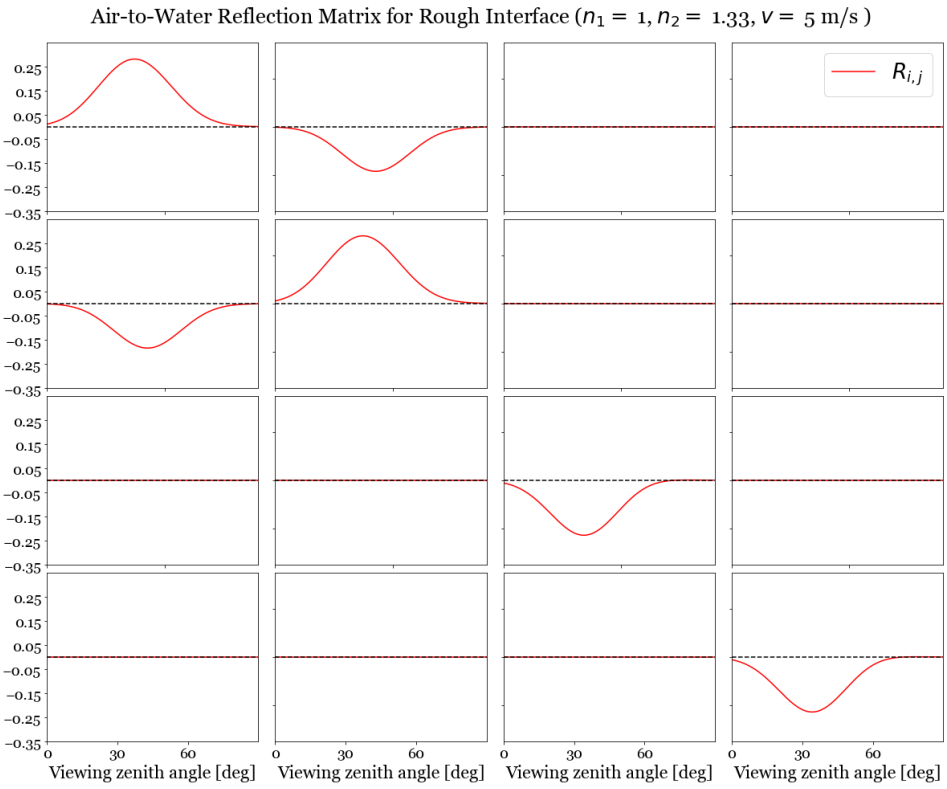

Figure 5.6: Reflection matrix elements for the rough air-water interface. $\theta_0 = 33.3°$, $\varphi - \varphi_0 = 0°$. The correction for the wave shadows was already applied in this figure to suppress the infinite reflection at $\theta = 90$ degrees (see Section 5.7).

where again E_0 is the incident irradiance in W m^{-2}, T_x and T_x^* are either the parallel or perpendicular Fresnel transmission coefficients and their complex conjugates respectively, θ_i is the reflection angle and dA_1^* is the area of the collection of all wave facets in Figure 5.1 pointing in direction (μ_n, φ_n) within the solid angle $d\Omega_n$.

Second, assuming that the solid angle of the reflected radiance I_t by this collection of wave facets is $d\Omega_t$, the reflected power from the horizontal surface area A as illustrated in Figure 5.3 in the direction μ within $d\Omega_t$ may be expressed by

$$P_t = I_t \cos\theta A d\Omega_t \tag{5.39}$$

Note that μ is the directional cosine with respect to the outward normal, hence $\mu = \cos\theta$ where θ is the angle between the transmitted beam and the negative z-axis in Figure 5.3. Equating Equations 5.38 and 5.39 and substituting dA_1^*/A of Equation 5.9 yields

$$I_t = \frac{n_2}{n_1}\frac{\cos\theta_t}{\cos\theta_i} T_x T_x^* \frac{\cos\theta_i E_0}{\mu_n \mu} \frac{d\Omega_n}{d\Omega_t} P(\mu_n, \varphi_n) \tag{5.40}$$

where $P(\mu_n, \varphi_n)$ is again the wave slope distribution model of Cox and Munk (1954).

Recall that for the reflected beam we could write the solid angle as functions of θ_i (Lenoble et al. 2007). Similarly, we can write the solid angle of the transmitted beam as $\sin(\pi - (\theta_i - \theta_t)) = \sin(\theta_i - \theta_t)$ and evaluate the solid angle fraction $d\Omega_n/d\Omega_t$ as follows:

$$\frac{d\Omega_n}{d\Omega_t} = \frac{\sin\theta_i d\theta_i d\varphi}{\sin(\theta_i - \theta_t)(d\theta_i - d\theta_t) d\theta_i d\varphi} \tag{5.41}$$

or by applying Snell's law (Zhai et al. 2010, Eq.31)

$$\frac{d\Omega_n}{d\Omega_t} = \frac{\sin\theta_i}{(\sin\theta_i\cos\theta_t - \cos\theta_i\sin\theta_t)(1 - n_1\cos\theta_i/(n_2\cos\theta_t))} \tag{5.42}$$

$$= \frac{n_2^2\cos\theta_t}{(n_2\cos\theta_t - n_1\cos\theta_i)^2} \tag{5.43}$$

Substituting Equation 5.43 into Equation 5.40 yields

$$I_t = \frac{n_2}{n_1}\frac{\cos\theta_t}{\cos\theta_i}T_x T_x^* \frac{\cos\theta_i E_0}{\mu_n\mu}\frac{n_2^2\cos\theta_t}{(n_2\cos\theta_t - n_1\cos\theta_i)^2}P(\mu_n,\varphi_n) \tag{5.44}$$

The term $\frac{n_2}{n_1}\frac{\cos\theta_t}{\cos\theta_i}T_x T_x^*$ may be recognized as the transmission of the irradiance (see Equation 4.77) and may accordingly be written in its matrix form including polarization given by Equation 4.78. Hence, the expression for the transmitted diffuse Stokes vector $\boldsymbol{I}_t$ in the scattering plane (i.e. $\varphi - \varphi' = 0$) in W m^{-2} sr^{-1} is (Zhai et al. 2010, Eq. 32)

$$\boldsymbol{I}_t = \boldsymbol{T}_f^c\frac{\cos\theta_i\boldsymbol{E}_0}{\mu_n\mu}\frac{n_2^2\cos\theta_t}{(n_2\cos\theta_t - n_1\cos\theta_i)^2}P(\mu_n,\varphi_n) \tag{5.45}$$

where $\boldsymbol{T}_f^c$ is the Fresnel matrix for the coherent Stokes vector given by Equation 4.78.

5.5. The Transmission Matrix for a Wind Ruffled Air-Water Interface

This section is analogous to Section 5.3 where we derived the reflection matrix for a wind ruffled air-water interface. Here the derivation of the transmission matrix for a wind ruffled air-water interface as functions of μ, μ' and $\varphi - \varphi'$ will be presented.

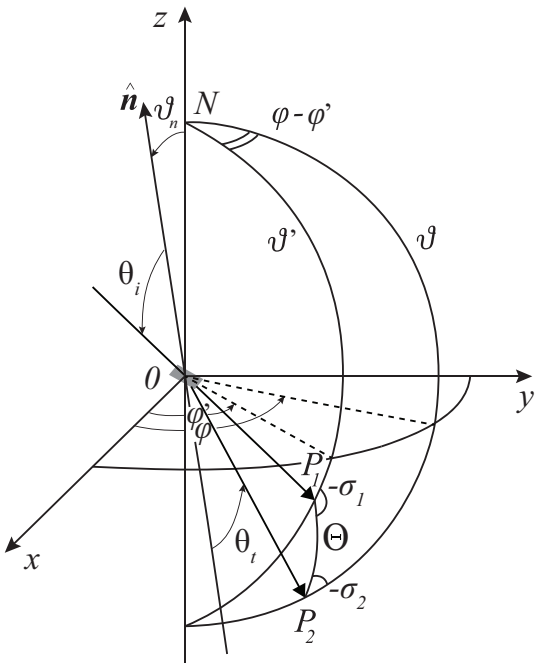

Figure 5.7: Sketch of an incident beam OP_1 transmitted at the wave facet at O in the direction OP_2. The wave facet is tilted by the angle ϑ_n with respect to the z-axis and points in the azimuth angle φ_n (not indicated). The scattering angle Θ equals $\theta_i - \theta_t$.

The same right handed Cartesian coordinate system that was used to describe the reflection event in Section 5.3 may be used to describe the transmission, as illustrated in Figure 5.7. The incidence beam points in the (OP_1) direction and the transmitted beam points in the (OP_2) direction. The normal vector to the wave facet is indicated by $\hat{\boldsymbol{n}}$ and θ_i indicates the Fresnel reflection angle of the wave facet with respect to $\hat{\boldsymbol{n}}$ as in Section

4.4. The transmission angle with respect to $\hat{\boldsymbol{n}}$ is indicated by θ_t and the scattering angle is indicated by Θ. Note that the transmitted beam points in the negative z-directions and therefore we will use $\theta = \pi - \vartheta$ here. Hence, by defining $\theta' = \pi - \vartheta'$ and $\theta_n = \vartheta_n$ we can write the unit vectors of the incident, normal and transmitted beams as

$$\hat{\boldsymbol{i}} = \begin{pmatrix} \sin\theta'\cos\varphi' \\ \sin\theta'\sin\varphi' \\ -\cos\theta' \end{pmatrix}, \quad \hat{\boldsymbol{n}} = \begin{pmatrix} \sin\theta_n\cos\varphi_n \\ -\sin\theta_n\sin\varphi_n \\ \cos\theta_n \end{pmatrix}, \quad \hat{\boldsymbol{t}} = \begin{pmatrix} \sin\theta\cos\varphi \\ \sin\theta\sin\varphi \\ -\cos\theta \end{pmatrix} \tag{5.46}$$

respectively. Note the minus sign of the z-component of $\hat{\boldsymbol{i}}$ and $\hat{\boldsymbol{t}}$ due to their downward directions. The angle between $\hat{\boldsymbol{i}}$ and $\hat{\boldsymbol{t}}$ equals $\cos\Theta$. Computing the dot product of $\hat{\boldsymbol{i}}$ and $\hat{\boldsymbol{t}}$ yields

$$\cos\Theta = \cos\theta'\cos\theta + \sin\theta'\sin\theta(\cos\varphi'\cos\varphi + \sin\varphi'\sin\varphi) \tag{5.47}$$

$$= \cos\theta'\cos\theta + \sin\theta'\sin\theta\cos(\varphi' - \varphi) \tag{5.48}$$

If we only use θ' and θ between 0 and $\pi/2$, we can write $\cos\theta' = |\cos\theta'| = \mu'$ and $\cos\theta = |\cos\theta| = \mu$ and

$$\cos\Theta = \mu'\mu + \sqrt{1-\mu'^2}\sqrt{1-\mu^2}\cos(\varphi' - \varphi) \tag{5.49}$$

It should be noted that the scattering angle is also defined by $\Theta = \theta_i - \theta_t$ (Figure 5.7). Hence, the minimum value of Θ satisfies $\theta_i = \theta_t$ and its maximum value is found when $\theta_i = \pi/2$. Therefore, Θ only has a physical meaning on the interval $0 < \Theta < \pi/2 - \sin^{-1}(n_1/n_2)$ or equivalently $n_1/n_2 < \cos\Theta < 1$.

The rotation angles -σ_2 and -σ_1 in Figure 5.7 are equivalent to -σ_2 and -σ_1 in Figure 2.3b. Applying the cosine rules to the spherical triangle ONP_1P_2 gives

$$\cos\sigma_1 = \cos(-\sigma_1) = \frac{\cos\vartheta - \cos\Theta\cos\vartheta'}{\sin\Theta\sin\vartheta'} = \frac{-\cos\theta + \cos\Theta\cos\theta'}{\sin\Theta\sin\theta'} \tag{5.50}$$

$$\cos\sigma_2 = \cos(-\sigma_2) = \frac{\cos\vartheta' - \cos\Theta\cos\vartheta}{\sin\Theta\sin\vartheta} = \frac{-\cos\theta' + \cos\Theta\cos\theta}{\sin\Theta\sin\theta} \tag{5.51}$$

Substituting again for $\cos\theta' = |\cos\theta'| = \mu'$ and $\cos\theta = |\cos\theta| = \mu$ yields

$$\cos\sigma_1 = \frac{-\mu + \mu'\cos\Theta}{\sqrt{1-\mu'^2}\sqrt{1-\cos^2\Theta}} \tag{5.52}$$

$$\cos\sigma_2 = \frac{-\mu' + \mu\cos\Theta}{\sqrt{1-\mu^2}\sqrt{1-\cos^2\Theta}} \tag{5.53}$$

Note that the expressions in Equations 5.52 and 5.53 are consistent with Equations 100 and 101 of Hovenier and van der Mee (1983) if we realize that for the transmission case: $\mu = \cos\theta = \cos(\pi - \vartheta) = -\cos\vartheta = u$ and $\mu' = \cos\theta' = \cos(\pi - \vartheta') = -\cos\vartheta' = u'$. Because we now have expressions for $\cos\sigma_1$ and $\cos\sigma_2$ as functions of Θ and consequently of μ, μ', $\varphi' - \varphi$, we may express $\cos 2\sigma_1$ and $\cos 2\sigma_2$ and the rotation matrices $\boldsymbol{L}(-\sigma_1)$ and $\boldsymbol{L}(-\sigma_2)$ as functions of μ, μ', $\varphi' - \varphi$. The conversion of $\cos\sigma_1$ and $\cos\sigma_2$ into $\cos 2\sigma_1$ and $\cos 2\sigma_2$ is similar to this conversion in the reflection case (see Display 2.1).

Analogous to the reflection case, assuming a monodirectional and unpolarized incident beam, the transmission matrix that may be employed in a radiative transfer algorithm is (Hansen and Travis 1974, Eq. 3.8)

$$\boldsymbol{T}_i(\mu, \mu', \varphi - \varphi') = \frac{\pi \boldsymbol{I}_t}{\mu'\pi\boldsymbol{F}_0} = \frac{\pi \boldsymbol{I}_t}{\mu'\boldsymbol{E}_0} \tag{5.54}$$

Substituting the expression for $\boldsymbol{I}_t$ of Equation 5.45 into Equation 5.54 leads to the desired transmission matrix for the interface (Zhai et al. 2010, Eq. 34):

$$\boxed{\boldsymbol{T}_i(\mu,\mu',\varphi-\varphi') = S(\mu,\mu',\sigma)\frac{\pi}{\mu'}\frac{P(\mu_n,\varphi_n)}{\mu\mu_n}\boldsymbol{L}(-\sigma_2)\boldsymbol{T}_f^c(\theta_i,n_1,n_2)\boldsymbol{L}(-\sigma_1)\frac{n_2^2\cos\theta_t\cos\theta_i}{(n_2\cos\theta_t-n_1\cos\theta_i)^2}}$$ ✓Zhai et al. (2010)

(5.55)

where we again already introduced that shadowing function $S(\mu,\mu',\sigma)$ which will be further explained in Section 5.7. The transmission matrix for a wind ruffled ocean as presented by Equation 5.55 is only a function of μ,μ' and $\varphi-\varphi'$ if also μ_n, θ_i and θ_t can be written as functions of μ,μ' and $\varphi-\varphi'$. This may be achieved by the following steps.

- Contrary to the reflection case, the scattering angle Θ is not only a function of θ_i but also of θ_t through $\Theta=\theta_i-\theta_t$. Hence, in order to express $\boldsymbol{T}_f^c(\theta_i,n_1,n_2)$ as functions of μ, μ' and $\varphi-\varphi'$ we seek expressions for θ_i and θ_t as functions of μ, μ' and $\varphi-\varphi'$ in the next bullet points.

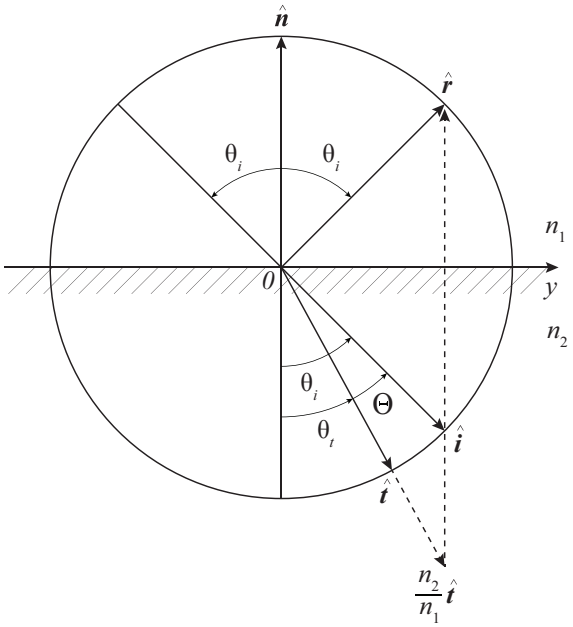

Figure 5.8: Unit circle at the wave facet of the air-water interface for air-incident reflection and transmission.

- Figure 5.8 represents the unit circle in the scattering plane of the wave facet located at point O. The incident unit vector $\hat{\boldsymbol{i}}$, reflected unit vector $\hat{\boldsymbol{r}}$ and transmitted unit vector $\hat{\boldsymbol{t}}$ are shown together with the unit vector $\hat{\boldsymbol{n}}$ normal to the wave facet. According to Snell's law, the magnitude of the y-component of $\hat{\boldsymbol{r}}$ (i.e. $\sin\theta_i$) equals n_2/n_1 times the magnitude of the y-component of $\hat{\boldsymbol{t}}$ (i.e. $n_2/n_1\sin\theta_t$). The vector $n_2/n_1\,\hat{\boldsymbol{t}}$ is also shown in Figure 5.8 satisfying (Mobley 1994, Eq. 4.9)

$$\frac{n_2}{n_1}\hat{\boldsymbol{t}} = \hat{\boldsymbol{i}} + \cos\theta_i\hat{\boldsymbol{n}} - \frac{n_2}{n_1}\cos\theta_t\hat{\boldsymbol{n}} \tag{5.56}$$

$$= \hat{\boldsymbol{i}} - C\hat{\boldsymbol{n}} \tag{5.57}$$

where

$$C = -\cos\theta_i + \frac{n_2}{n_1}\cos\theta_t \tag{5.58}$$

Consequently, the expression for $\hat{\boldsymbol{n}}$ becomes (Zhai et al. 2010, Eq. 35)

$$\hat{\boldsymbol{n}} = \frac{\hat{\boldsymbol{i}} - \frac{n_2}{n_1}\hat{\boldsymbol{t}}}{C} \tag{5.59}$$

Let us consider only the z-components of Equation 5.59

$$\cos\theta_n = \frac{-\cos\theta' - \frac{n_2}{n_1}(-\cos\theta)}{C} \tag{5.60}$$

or

$$\mu_n = \frac{\frac{n_2}{n_1}\mu - \mu'}{C} \tag{5.61}$$

Note that Equation 5.61 is equivalent to Equation 39 of Zhai et al. (2010) if we realize that our μ and μ' are positive while Zhai et al. (2010) used $\mu < 0$ and $\mu' < 0$ for downward directions.

- Following Chowdhary (1999), we set the transmission matrix elements equal to zero when the normal vector of the wave facet disappears below the air-water interface ($\mu_n < 0$). This only may occur for certain awkward combinations of μ and μ' in the transmission case and not when considering reflection (see Equations 5.36 and 5.61).

- Note that $\hat{\boldsymbol{i}} \cdot \hat{\boldsymbol{t}} = \cos\Theta$ (see again Figure 5.8). Then the expressions for $\cos\theta_i$ and $\cos\theta_t$ are (Zhai et al. 2010, Eq. 37)

$$\cos\theta_i = -\hat{\boldsymbol{n}} \cdot \hat{\boldsymbol{i}} = -\left(\frac{\hat{\boldsymbol{i}} - \frac{n_2}{n_1}\hat{\boldsymbol{t}}}{C}\right) \cdot \hat{\boldsymbol{i}} = -\left(\frac{1 - \frac{n_2}{n_1}\cos\Theta}{C}\right) = \frac{\frac{n_2}{n_1}\cos\Theta - 1}{C} \tag{5.62}$$

$$\cos\theta_t = -\hat{\boldsymbol{n}} \cdot \hat{\boldsymbol{t}} = -\left(\frac{\hat{\boldsymbol{i}} - \frac{n_2}{n_1}\hat{\boldsymbol{t}}}{C}\right) \cdot \hat{\boldsymbol{t}} = -\left(\frac{\cos\Theta - \frac{n_2}{n_1}}{C}\right) = \frac{\frac{n_2}{n_1} - \cos\Theta}{C} \tag{5.63}$$

- The last step is to find an expression for the parameter C as functions of μ, μ' and or $\varphi - \varphi'$. Substituting the expressions for $\cos\theta_i$ (Equation 5.62) and $\cos\theta_t$ (Equation 5.63) into the definition of C (Equation 5.58) yields (cf. Zhai et al. 2010, Eq. 38)

$$C = \sqrt{\frac{n_2^2}{n_1^2} + 1 - 2\frac{n_2}{n_1}\cos\Theta} \tag{5.64}$$

Since the expression for $\cos\Theta$ as functions of μ, μ' and $\varphi - \varphi'$ was already found (Equation 5.49), we have expressions for μ_n, $\cos\theta_i$ and $\cos\theta_t$ as functions of μ, μ' and $\varphi - \varphi'$. Therefore, the transmission matrix for a wind ruffled Fresnel interface of Equation 5.55 is only a function of μ, μ' and $\varphi - \varphi'$ and the refractive indices.

5.6. Reflection and Transmission Matrices for Illumination from Below

In the preceding sections the reflection and transmission matrices, $\boldsymbol{R}_i$ and $\boldsymbol{T}_i$, were derived for light incident on the top of a wind-ruffled rough air-water interface. However, for a complete description of the radiative transfer of light travelling through the interface, the reflection and transmission matrices $\boldsymbol{R}_i^*$ and $\boldsymbol{T}_i^*$ for light incident at the bottom of the interface are required as well.

5.6.1. Water-incident Reflection

The derivation for the reflection matrix for illumination of a rough water-interface from below is analogous to the derivation of the reflection matrix for illumination from above. That is, the sketch of the reflection case of Figure 5.5 still applies, but the refractive index of the medium of the incident beam (n_1) is bigger than the refractive index of the medium of the transmitted beam (n_2). Therefore, we have to take into account total internal reflection when computing the flat Fresnel reflection matrix $\boldsymbol{R}_f$ (see Section 4.5.2). That is, at incidence angles bigger than the critical angle, all light is internally reflected at an angle of 90 degrees which can be mathematically described by the imaginary part of the Fresnel reflection coefficients (Appendix B.2).

5.6.2. Water-incident Transmission

The derivation for the transmission matrix for illumination of a rough water-interface from below is analogous to the derivation of the transmission matrix for illumination from above. That is, the sketch of the transmission case of Figure 5.7 still applies, but the refractive index of the medium of the incident beam (n_1) is bigger than the refractive index of the medium of the transmitted beam (n_2). Hence, the following differences need to be mentioned:

- Because $n_1 > n_2$, we have to take into account total internal reflection when computing the flat Fresnel transmission matrix $\boldsymbol{T}_f$ (see Section 4.5.2). That is, at incidence angles bigger than the critical angle, no light is transmitted.
- The scattering angle for transmission through an interface illuminated from below is different than for illumination from above, because we assume that $n_1 > n_2$ and therefore $\theta_t > \theta_i$. Hence, $\Theta = \theta_t - \theta_i$. Consequently, the expressions for θ_i and θ_t as functions of μ, μ' and $\varphi - \varphi'$ are slightly different and will be discussed below.

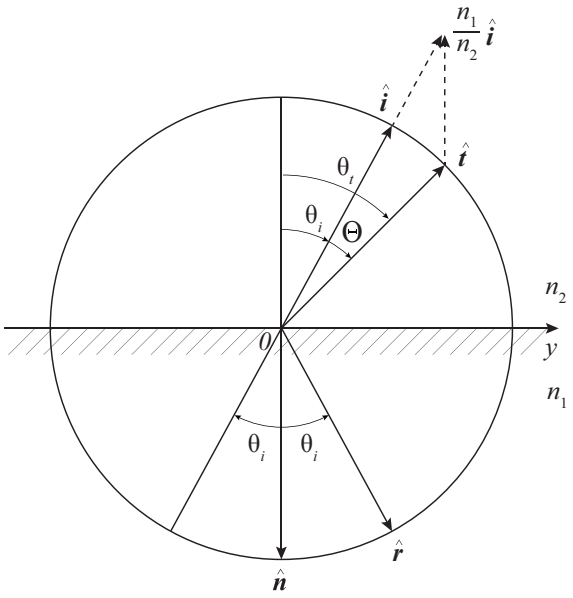

Figure 5.9: Unit circle at the wave facet of the air-water interface for water-incident reflection and transmission.

Figure 5.9 represents the unit circle in the scattering plane of the wave facet located at point O. The incident unit vector $\hat{\boldsymbol{i}}$, reflected unit vector $\hat{\boldsymbol{r}}$ and transmitted unit vector $\hat{\boldsymbol{t}}$ are shown together with the unit vector $\hat{\boldsymbol{n}}$ normal to the wave facet. Note that $\hat{\boldsymbol{n}}$ points in the (positive) downward direction such that it points in the direction of medium 1 (containing the incident and reflected beams). According to Snell's law, the magnitude of the y-component of $\hat{\boldsymbol{t}}$ (i.e. $\sin\theta_t$) equals n_1/n_2 times the magnitude of the y-component of $\hat{\boldsymbol{i}}$ (i.e. $n_1/n_2 \sin\theta_i$). Hence, we can write

$$\hat{\boldsymbol{t}} = \frac{n_1}{n_2}\hat{\boldsymbol{i}} + \frac{n_1}{n_2}\cos\theta_i\hat{\boldsymbol{n}} - \cos\theta_t\hat{\boldsymbol{n}} \tag{5.65}$$

$$= \frac{n_1}{n_2}\hat{\boldsymbol{i}} + C\hat{\boldsymbol{n}} \tag{5.66}$$

where

$$C = \frac{n_1}{n_2}\cos\theta_i - -\cos\theta_t \tag{5.67}$$

Consequently, the expression for $\hat{\boldsymbol{n}}$ becomes

$$\hat{\boldsymbol{n}} = \frac{\hat{\boldsymbol{t}} - \frac{n_1}{n_2}\hat{\boldsymbol{i}}}{C} \tag{5.68}$$

Let us consider only the z-components of Equation 5.68

$$\cos\theta_n = \frac{-\cos\theta - \frac{n_1}{n_2}(-\cos\theta')}{C} \tag{5.69}$$

or

$$\mu_n = \frac{\frac{n_1}{n_2}\mu' - \mu}{C} \tag{5.70}$$

Note that $\hat{\boldsymbol{i}} \cdot \hat{\boldsymbol{t}} = \cos\Theta$ (see again Figure 5.9). Then the expressions for $\cos\theta_i$ and $\cos\theta_t$ are

$$\cos\theta_i = -\hat{\boldsymbol{n}} \cdot \hat{\boldsymbol{i}} = -\left(\frac{\hat{\boldsymbol{t}} - \frac{n_1}{n_2}\hat{\boldsymbol{i}}}{C}\right) \cdot \hat{\boldsymbol{i}} = -\left(\frac{\cos\Theta - \frac{n_1}{n_2}}{C}\right) = \frac{\frac{n_1}{n_2} - \cos\Theta}{C} \tag{5.71}$$

$$\cos\theta_t = -\hat{\boldsymbol{n}} \cdot \hat{\boldsymbol{t}} = -\left(\frac{\hat{\boldsymbol{t}} - \frac{n_1}{n_2}\hat{\boldsymbol{i}}}{C}\right) \cdot \hat{\boldsymbol{t}} = -\left(\frac{1 - \frac{n_1}{n_2}\cos\Theta}{C}\right) = \frac{\frac{n_1}{n_2}\cos\Theta - 1}{C} \tag{5.72}$$

The last step is to find an expression for C as functions of μ, μ' and or $\varphi - \varphi'$. Substituting the expressions for $\cos\theta_i$ (Equation 5.71) and $\cos\theta_t$ (Equation 5.72) into the definition of C (Equation 5.67) yields again

$$C = \sqrt{\frac{n_1^2}{n_2^2} + 1 - 2\frac{n_1}{n_2}\cos\Theta} \tag{5.73}$$

Since the expression for $\cos\Theta$ as functions of μ, μ' and $\varphi - \varphi'$ is similar to Equation 5.49 for the air-incidence case, we have expressions for μ_n, $\cos\theta_i$ and $\cos\theta_t$ as functions of μ, μ' and $\varphi - \varphi'$. Therefore, the transmission matrix for a wind ruffled Fresnel interface for illumination from below is again only a function of μ, μ' and $\varphi - \varphi'$ and the refractive indices.

- Lastly, because the definition of the scattering angle changed with respect to the air-incidence case, also the restriction on the interval of the scattering angle needs to be adjusted. Recall that the scattering angle in this section is defined by $\Theta = \theta_t - \theta_i$. Hence, the minimum value of Θ satisfies $\theta_i = \theta_t$ and its maximum value is found when $\theta_t = \pi/2$. Therefore, Θ only has a physical meaning on the interval $0 < \Theta < \pi/2 - \sin^{-1}(n_2/n_1)$ or equivalently $n_2/n_1 < \cos\Theta < 1$.

5.7. Energy Balance and Wave Shadows

Conservation of energy should be satisfied at the rough air-water interface. That is, the sum of the fractions of the incident flux reflected and transmitted through the interface should add up to 1. These fractions are equivalent to the albedo A_r and the 'transmitted albedo' A_t respectively:

$$A_r(\mu') = \frac{1}{\pi}\int_0^1 \mu d\mu \int_0^{2\pi} R_{1,1}(\mu, \mu', \varphi - \varphi')\, d(\varphi - \varphi') \tag{5.74a}$$

$$A_t(\mu') = \frac{1}{\pi}\int_0^1 \mu d\mu \int_0^{2\pi} T_{1,1}(\mu, \mu', \varphi - \varphi')\, d(\varphi - \varphi') \tag{5.74b}$$

where $R_{1,1}$ and $T_{1,1}$ are the upper left elements of Equations 5.33 and 5.55. Thus, the energy deficiency across the rough interface may be computed according to

$$\epsilon(\mu') = 1 - A_r(\mu') - A_t(\mu') \tag{5.75}$$

Note that A_r, A_t and ϵ are functions of the cosine of the zenith angle θ' of a hypothetical monodirectional incident beam. Similar equations for illumination of the interface *from below* can be set up: we define ϵ^* as the energy deficiency across the interface for a hypothetical monodirectional beam incident at an angle θ' with the negative zenith direction.

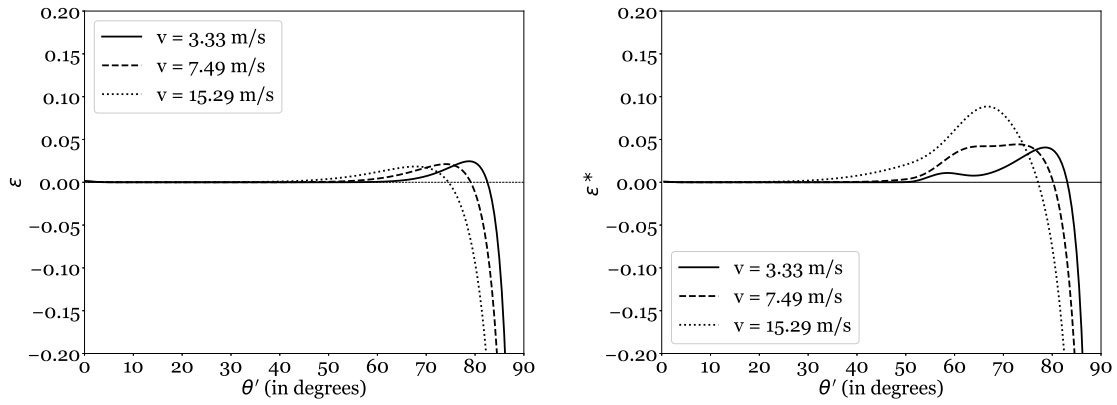

(a) (b)

Figure 5.10: Energy deficiency across the rough interface for illumination from above (a) and illumination from below (b). No shadow correction is included.

In Figures 5.10a and 5.10b, ϵ and ϵ^* are plotted respectively for our computations. There are two phenomena that play a role here:

1. The energy deficiency increases with increasing incidence angle. Tsang et al. (1985) explained this energy loss by the fact that multiple scattering, i.e. scattering between the wave facets, is ignored. In other words, our Fresnel solution combined with the wave slope distribution model of Cox and Munk (1954) is a 'geometrical optics' approach describing the single scattering by the rough interface only, and we miss the part of the reflected incident light that is multiply scattered between the waves.

2. At even higher incidence angles, the trend reverses towards an infinite 'energy abundance' at $\theta' = 90°$. This is because the Fresnel reflection is strongest at grazing angles (Section 4.5) and dominates deficiency from the multiple scattering ignorance. In reality, the adjacent waves would block the light path of the incident beam on the wave facet at this high incident angle. These *wave shadows* would increase with increasing incidence angle and ultimately cause full obscuration at $\theta' = 90°$.

The infinite energy abundance at grazing angles due to the ignorance of the wave shadows (point 2 above) may be accounted for. We use the shadowing function derived by Smith (1967) and Sancer (1969) to modify the reflection and transmission matrices, which was employed by many authors (Chowdhary 1999; Mishchenko and Travis 1997; Sun and Lukashin 2013; Tsang et al. 1985; Zhai et al. 2010).

Suppose we have a random wave facet located at point F in Figure 5.11, at a vertical distance ξ_0 separated from the mean horizontal plane. Let us assume that the orientation of all surrounded wave facets are described by the same wave slope probability distribution, and, that the incident beam GF lies in the $yz-$plane of this 2D sketch. The probability that the wave facet at F is *not* shadowed by a facet of a surrounded wave, is equivalent to the probability S' that no wave facet to the right of F intersects GF, or

$$S'(F,\theta') = \lim_{\epsilon\to\infty} S'(F,\theta',\epsilon) \tag{5.76}$$

where $S'(F,\theta',\epsilon)$ is the probability that no wave facet between $y = 0$ and $y = \epsilon$ intersects the incident beam GF. Using the well-known relation between joint probability and conditional probability from probability theory, Smith (1967) wrote the problem as:

$$S'(F,\theta',\epsilon+\Delta\epsilon) = S'(F,\theta',\epsilon)\cdot Q(\Delta\epsilon|F,\theta',\epsilon) \tag{5.77}$$

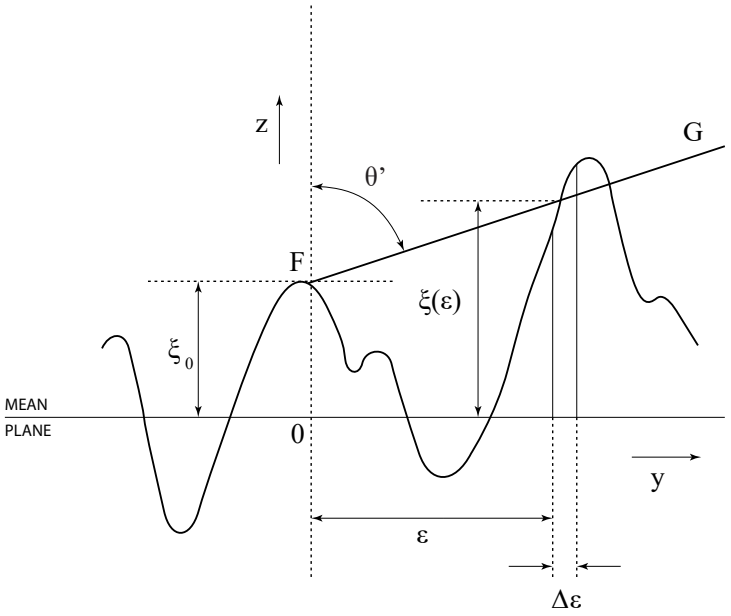

Figure 5.11: 2D sketch of the geometry of wave shadowing. The light beam GF in the yz-plane incident on wave facet F, which is located at a vertical distance ξ_0, may be blocked by a wave facet located somewhere in the vertical interval $\xi(\Delta\epsilon)$ and a horizontal interval $\Delta\epsilon$ from the origin at the mean plane. It is assumed that inclinations of the wave facets at F and in $y = \Delta\epsilon$ are both drawn from the wave slope probability distribution of Cox and Munk (1954, 1956). The shadowing function S' is the probability that the incident beam on F is not blocked by a surrounding wave facet. The shadowing function S is the probability that both the incident beam on F and the scattered beam towards the observer are not blocked by a surrounding wave facet. A similar figure, using a somewhat different notation, may be found in the paper of Smith (1967).

where $Q(\Delta\epsilon|F,\theta',\epsilon)$ is the conditional probability that GF will not be intersected in the interval $\Delta\epsilon$, given it does not in the interval ϵ. The conditional probability Q is in turn mutually exclusive with the conditional probability $g(\epsilon)\Delta\epsilon$ that the incident beam GF will be intersected by a wave facet in the interval $\Delta\epsilon$ given that it is not intersected in the interval ϵ, and we can write

$$S'(F,\theta',\epsilon+\Delta\epsilon) = S'(F,\theta',\epsilon)\cdot(1-g(\epsilon)\Delta\epsilon) \tag{5.78}$$

The problem can be solved by finding the expression for $g(\epsilon)$ and the integration over the entire range of ϵ, which was done by Smith (1967).[6]

The reflected ray may, of course, also be blocked by a surrounded wave facet. A complete description was found by Sancer (1969). Note that, following this approach, the probability S that an incident or scattered beam on a wave facet is not blocked by a surrounded wave facet depends only on the lightning geometry (θ,θ') and the standard deviation of the wave slope inclinations σ (Section 5.2). The commonly used form of the shadowing function employed by the authors mentioned above is the one of Tsang et al. (1985), who wrote:

$$S(\theta,\theta',\sigma) = \frac{1}{1+\Lambda(\theta,\sigma)+\Lambda(\theta',\sigma)} \tag{5.79}$$

where

$$\Lambda(\gamma,\sigma) = \frac{1}{2}\left\{\frac{\sigma}{\cos\gamma}\left[\frac{1-\cos^2\gamma}{\pi}\right]^{1/2}\exp\left[-\frac{\cos^2\gamma}{\sigma^2(1-\cos^2\gamma)}\right]-\operatorname{erfc}\left[\frac{\cos\gamma}{\sigma\sqrt{1-\cos^2\gamma}}\right]\right\} \tag{5.80}$$

and $\operatorname{erfc}(x)$ is the complementary error function.

[6] In order to avoid the difficulty of autocorrelation between points in $\Delta\epsilon$ and ϵ Smith (1967) approximated the problem by replacing $g(\epsilon)\Delta\epsilon$ as the conditional probability that the wave facet at F will be shadowed by a wave facet in $\Delta\epsilon$ given that it was not shadowed at $y = \epsilon$ (instead of the interval ϵ.)

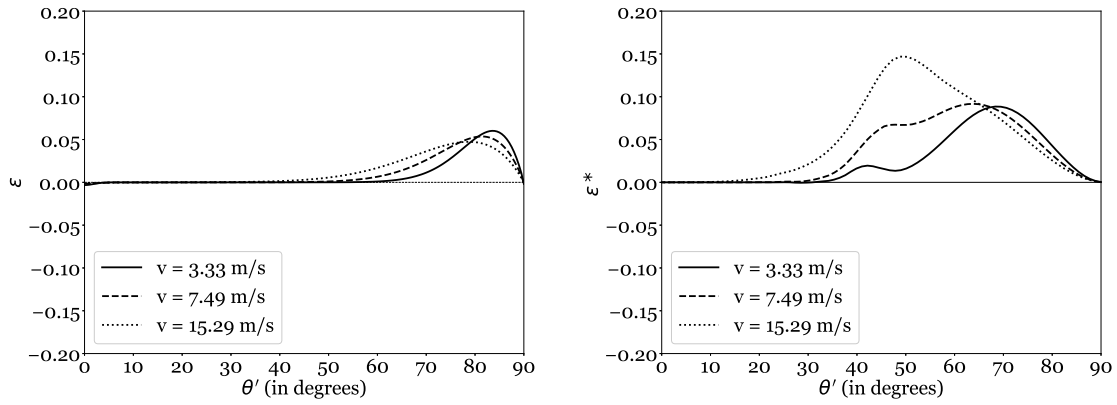

(a) (b)

Figure 5.12: Energy deficiency across the rough interface for illumination from above (a) and illumination from below (b). The reflection and transmission matrices are multiplied with the shadowing function (Equation 5.79).

The energy deficiencies ϵ and ϵ^* across the interface, after multiplying $\boldsymbol{R}_i$, $\boldsymbol{T}_i$, $\boldsymbol{R}_i^*$ and $\boldsymbol{T}_i^*$ by the shadowing function (Equation 5.79), are plotted in Figures 5.12a and 5.12b. We compare these with Figure 4 of Nakajima (1983) and find an almost identical result. The energy deficiency for illumination from below is more severe than the energy deficiency for illumination from above. According to Nakajima (1983), this may be explained by the angular size difference of the transmitted cone of light. That is, light travelling from water to air is refracted into a wider cone compared to the narrow cone of light transmitted from the air into the water (see Figure 5.15). Therefore, the number of grazing angle geometries of the rays refracted from the ocean into the atmosphere is larger, which means that the ignorance of the multiple scattered light by the wave facets causes a larger error. This explains also the bimodal behaviour of ϵ^*: the energy deficiency for illumination from below is a superposition of the ignorance of two modes of multiple scattering, which are the reflected and refracted beams that encounter surrounded wave facets along their path at grazing angles. For ϵ, the transmitted beam into the water is too narrow to encounter surrounded wave facets, even after multiplying by the wave slope probability distribution function.

Although the energy deficiencies are less than unity, the problem remains to completely satisfy conservation of energy at the interface in order to avoid nonphysical absorbing behaviour. Unfortunately, to the best of our knowledge, no reliable radiative transfer solution is available for the rough interface including multiple scattering among wave facets. As long as no such complete model is available, a normalization is needed at the interface to account for the energy deficiency. Zhai et al. (2010) mentioned that radiative transfer codes for atmospheres bounded by a rough ocean surface that ignore the sub-interface water layer generally do not account for this problem at all (see e.g. Mishchenko and Travis 1997). We choose to follow the approach of Nakajima (1983), who renormalized their reflection and transmission matrices of the interface through the division by the scattered fraction of the incident flux:

$$\overline{R}_i(\mu,\mu',\varphi-\varphi') = \frac{1}{1-\epsilon(\mu')} R_i(\mu,\mu',\varphi-\varphi') \tag{5.81a}$$

$$\overline{T}_i(\mu,\mu',\varphi-\varphi') = \frac{1}{1-\epsilon(\mu')} T_i(\mu,\mu',\varphi-\varphi') \tag{5.81b}$$

$$\overline{R}_i^*(\mu,\mu',\varphi-\varphi') = \frac{1}{1-\epsilon^*(\mu')} R_i^*(\mu,\mu',\varphi-\varphi') \tag{5.81c}$$

$$\overline{T}_i^*(\mu,\mu',\varphi-\varphi') = \frac{1}{1-\epsilon^*(\mu')} T_i^*(\mu,\mu',\varphi-\varphi') \tag{5.81d}$$

5.8. Polar Plots of the Interface Reflection and Transmission

In this section, we show the polar plots of the upper left element of the reflection and transmission matrices (Equations 5.33 and 5.55) and the corresponding degree of polarization. The light source is located at $\varphi - \varphi_0 = 180°$.

Figure 5.13 shows the polar plots of the upper left element (left column) and degree of polarization (right column) of the interface reflection matrix for an incidence angle of 40° and wind speeds of 7.5 m/s (top row), 3 m/s (middle row) and 1 m/s (bottom row). With increasing wind speed, the reflected intensity is more concentrated at the specular point. Outside the glint region, the reflectance decreases rapidly but never reaches 0 which is caused by the long tails of the Gaussian probability distribution of the wave facet inclinations. The degree of polarization is unaffected by the varying wind speed, however, at 1 m/s the degree of polarization becomes 0 at the edge in the backscattering direction, because of the low values of Q and I. We encounter values for both around 10^{-205}, but squaring Q in the computation of the degree of polarization results in a zero, which is due to computational limitations.

In Figure 5.14 the polar plots of the upper left element (left column) and degree of polarization (right column) of the interface reflection matrix for a wind speed of 7.5 m/s and incidence angles of 40° (top row), 50 ° (middle row) and 60 ° (bottom row). With increasing incidence angle, the reflection angles at the wave facets increase which results in stronger Fresnel reflection (Chapter 4). The band of maximum polarization shifts slightly towards the backscattering direction.

Figure 5.15 shows the upper left elements of $\boldsymbol{R}_i$ and $\boldsymbol{R}_i^*$ (top row) and $\boldsymbol{T}_i^*$ and $\boldsymbol{T}_i^*$ (bottom row) for an incidence angle of 40 degrees and a wind speed of 7.5 m/s. The concentrated transmittance around a certain transmission angle. For the air-to-water transmission the transmission cone is sharper than the cone for water-to-air transmission, as expected. Due to the tails of the Gaussian distribution of the wave facet inclinations, very small but nonzero reflectance values are found outside the transmission cone. Physically, these long Gaussian tails represent the few wave facets in these geometries that allow for the transmittance of light into the water. This may appear somewhat counter-intuitive, but it should be remembered that our solution describes the reflection and transmission by the air-water *interface*, while statistically correcting for the orientations of its wave facets, rather than the reflection by a single wave facet. It should be noted that, strictly speaking, the polar plot of $\boldsymbol{R}_i$ and $\boldsymbol{R}_i^*$ cannot accurately be compared using *the same incidence angle* of 40 degrees (for illumination from above and below respectively), since the directional cosines of the geometries in the atmosphere should be refracted when translating it to geometries in the water according to Snell's law.

The reflection from illumination from below is heavily affected by the total internal reflection of the wave facets (upper right plot of Figure 5.15). As explained in Section 4.5.2, for reflection angles *on the wave facet* bigger than the critical angle, all light is reflected parallel to the interface. Since we multiply with the probability distribution for the wave facet inclinations, the point where the critical angle is reached depends on wave facet inclination and therefore varies for each wave facet (of distinct orientation).

Figure 5.16 shows the degree of polarization of the matrices in Figure 5.15. The band of maximum degree of polarization for $\boldsymbol{R}_i^*$ is shifted to the backward scattering direction. However, as explained above, we should take care in this comparison when using the same incidence angle for illumination from above and below. The polarization of light transmitted, for either the air-incident and water-incident cases, is relatively low as expected from 4.5, where we saw that the Fresnel transmission coefficients $T_\parallel$ and $T_\perp$ do not vary much with incidence angle (i.e. reflection angle at the wave facet). The transmitted light is not significantly polarized, compared to the reflected light, where $R_\parallel$ reaches zero at the Brewster angle. Furthermore, we encounter again zero degree of polarization values due to computational limitations (as explained above). Additionally, $\boldsymbol{T}_i^*$ becomes zero in the nadir viewing zenith angle direction which explains the NaN values inside in these geometries.

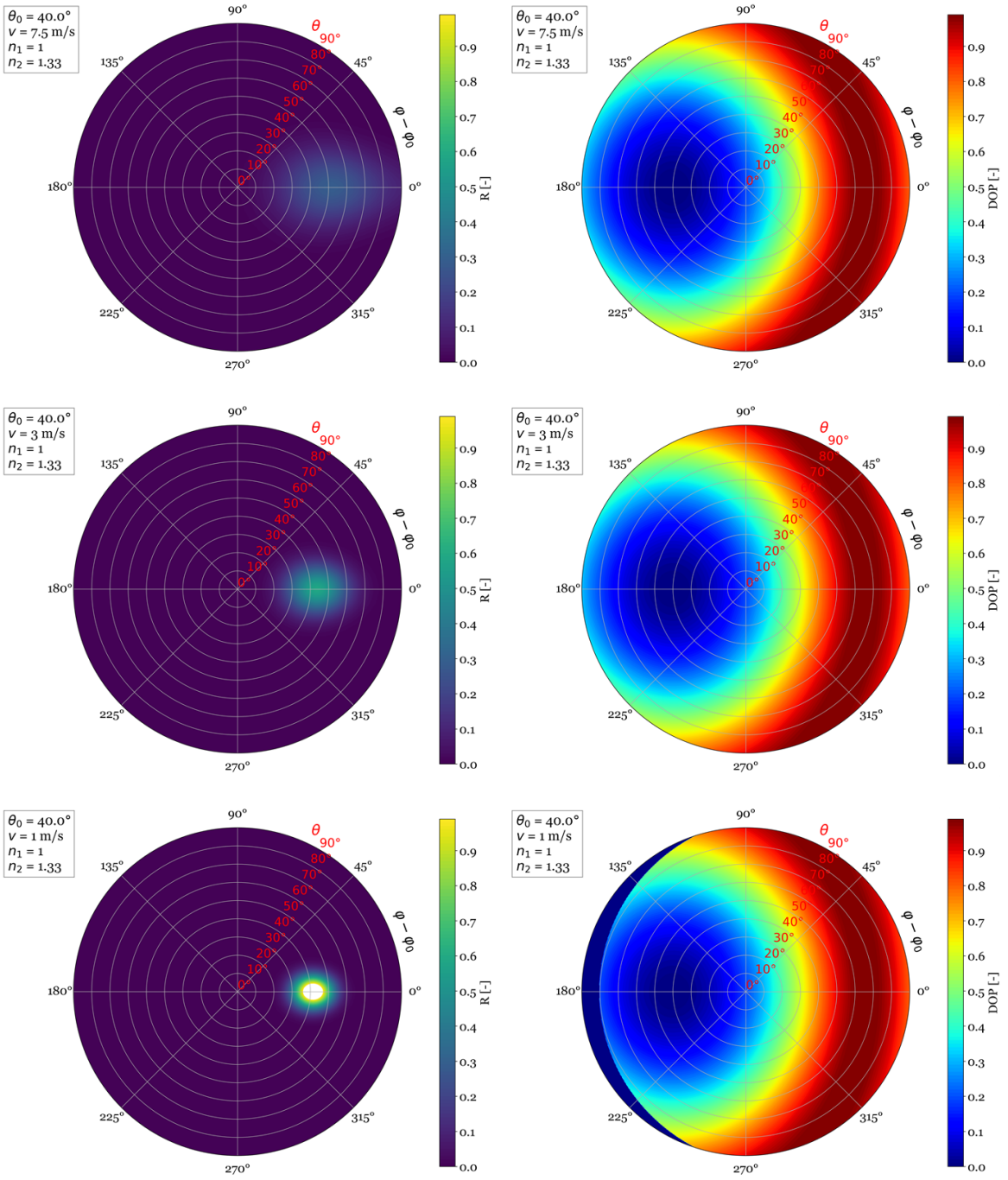

Figure 5.13: Polar plots of the upper left element (left column) and degree of polarization (right column) of the interface reflection matrix for an incidence angle of 40° and wind speeds of 7.5 m/s (top row), 3 m/s (middle row) and 1 m/s (bottom row). The light source is located at $\varphi - \varphi_0 = 180°$. The viewing zenith angle is indicated in red. As explained in the text, the degree of polarization becomes zero at the edge in the backscattering direction because of computational limitations.

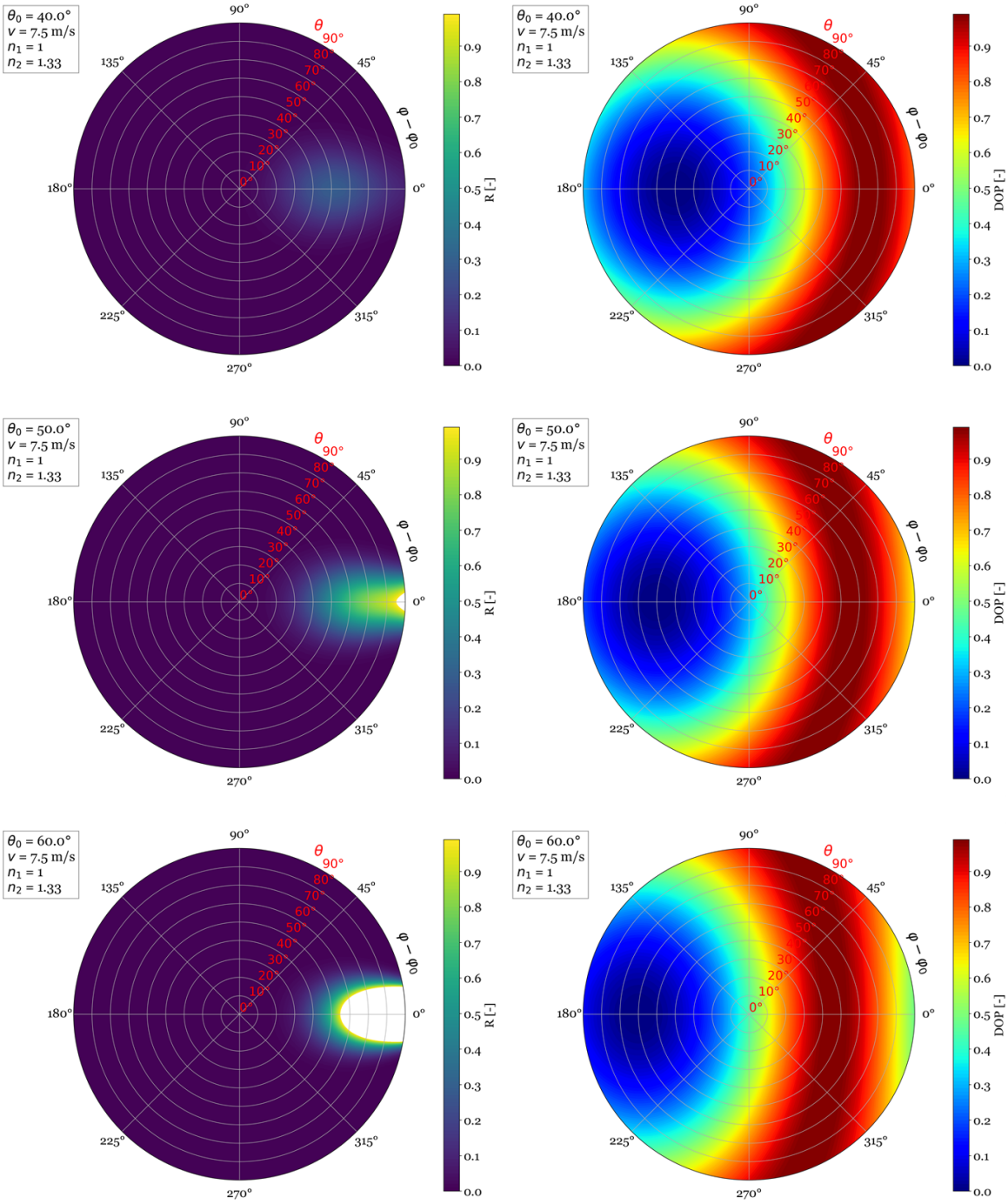

Figure 5.14: Polar plots of the upper left element (left column) and degree of polarization (right column) of the interface reflection matrix for a wind speed of 7.5 m/s and incidence angles of 40° (top row), 50° (middle row) and 60° (bottom row). The light source is located at $\varphi - \varphi_0 = 180°$. The viewing zenith angle is indicated in red.

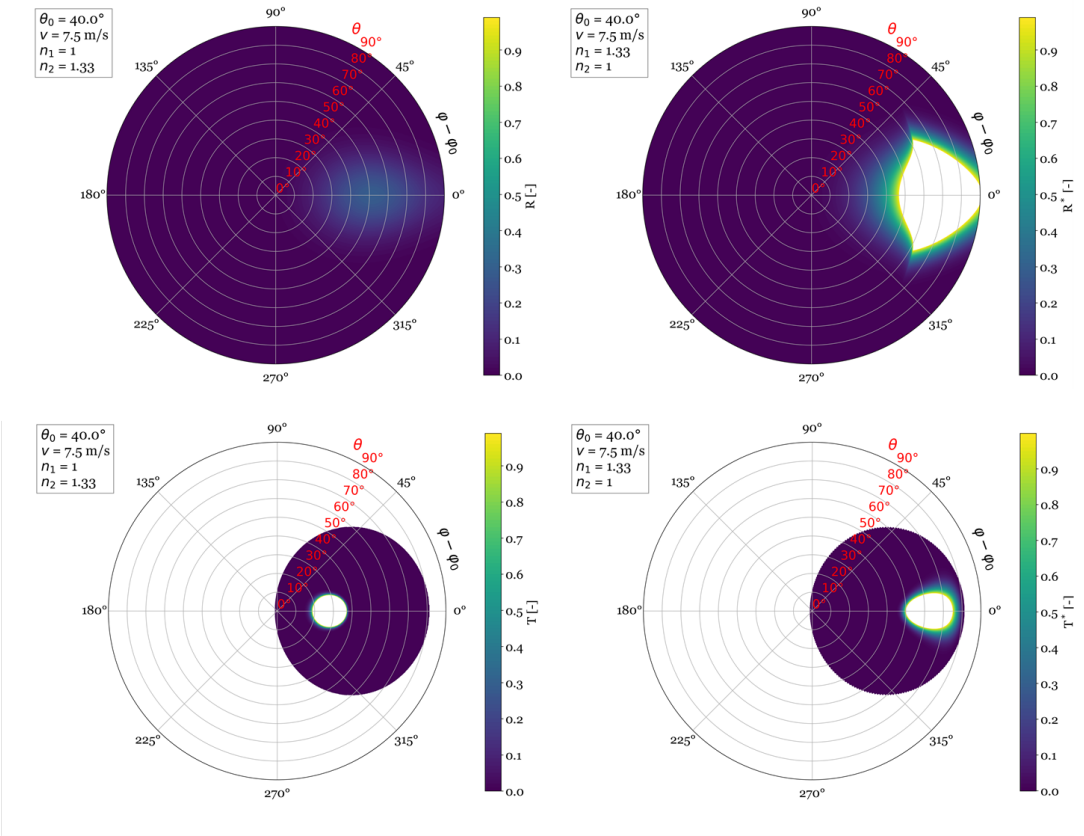

Figure 5.15: The upper left element of $\boldsymbol{R}_i$, $\boldsymbol{T}_i$, $\boldsymbol{R}_i^*$ and $\boldsymbol{T}_i^*$ for an incidence angle of 40° and a wind speed of 7.5 m/s. The scattering angle is not defined in the white area of the transmission plots (bottom row).

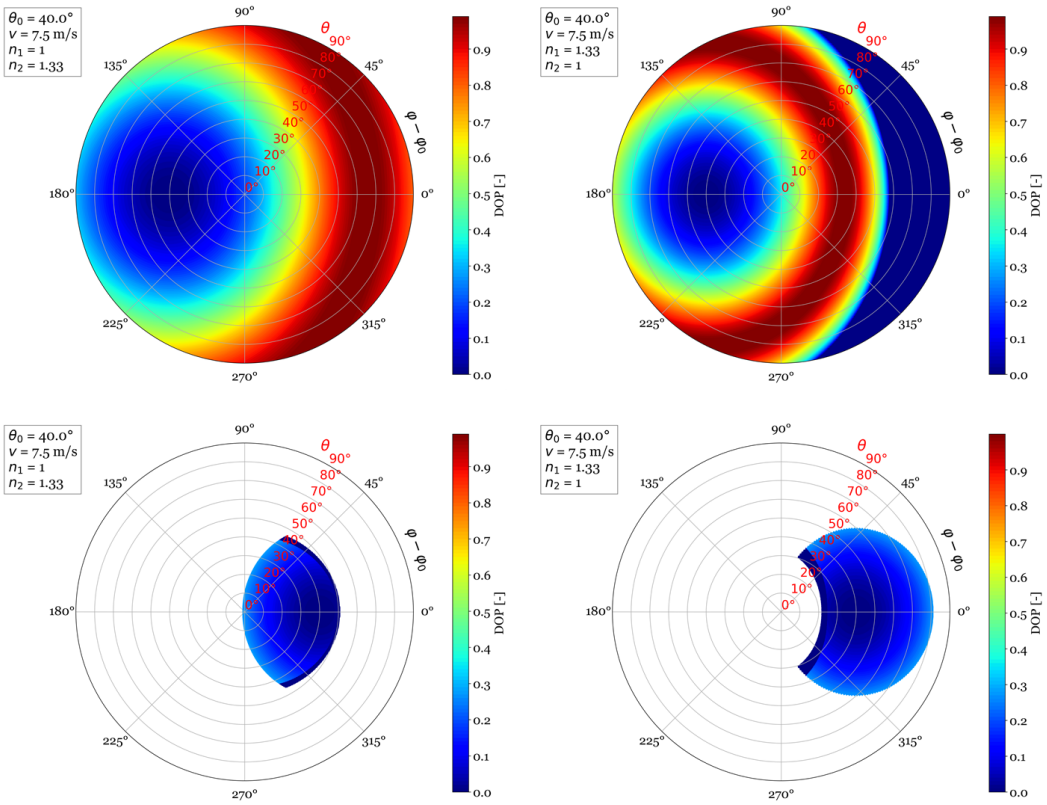

Figure 5.16: Similar as Figure 5.15, but its corresponding degree of polarization. Where the intensity becomes too small, the degree of polarization is undefined, as explained in the text.

6

Reflection by the Ocean System (Water + Interface)

In the former chapter, the reflection matrix for polarized light of the rough air-water interface, $\mathbf{R}_i$, was derived. The reflection of light by the ocean, however, cannot be described by the interface alone, if the aim is to construct a realistic reflection model. The color of the subinterface ocean, mainly caused by wavelength dependent absorption of underwater scattered light, needs to be modeled because the higher water-leaving flux at blue wavelengths may be visible at the top of the atmosphere of our exoplanet models. In this chapter we will find an expression for the reflection of light by the bulk ocean in its reflection matrix, $\boldsymbol{R}_W$, whose integral of its (1,1) element over the scattered angles will be referred to as the *ocean albedo*. However, we will fully include scattering of polarized light in the water by applying the adding-doubling method to a stack of homogeneous plane-parallel water layers to compute $\mathbf{R}_W$. This reflection of light by the bulk ocean will encounter repeated reflections with the air-water interface, and we may define the total *water-leaving reflected* (polarized) light that originates from the subinterface ocean which will be stored in the reflection matrix $\mathbf{R}_{WL}$. The reflection by the clean ocean can then by described by the sum of $\mathbf{R}_{WL}$ and $\mathbf{R}_i$. We will show that this sum is analogous to the adding equation for a reflection matrix when we write it in the form of supermatrices (recall Equation 3.28). Finally, we will account for the foam of the waves, assuming it to be a Lambertian reflector with an appropriate foam albedo, and we take the weighted sum of the foam reflectance $\boldsymbol{R}_{WC}$ (where only the (1,1) element is nonzero) and the clean ocean reflection. The complete ocean reflection may then be expressed by

$$\boldsymbol{R}_{OCEAN} = q\boldsymbol{R}_{WC} + (1-q)\boldsymbol{R}_{WL} + (1-q)\boldsymbol{R}_i \tag{6.1}$$

where q is the fraction of the ocean covered by foam. In the following subsections the individual terms of Equation 6.1 will be explained in more detail.

The approach as explained in the former paragraph has been applied already in Earth observation retrieval studies, when modeling the flux only (Sayer et al. 2010) but also when including polarization (see Sun and Lukashin 2013). The latter paper used Equation 6.1 to implement their ocean reflection of polarized light in the adding-doubling method, but assumed the water leaving reflected light to be Lambertian. Xu et al. (2016) also followed a similar approach for their aerosols and water-leaving radiance retrieval, and used the adding-doubling method to compute $\boldsymbol{R}_W$, and subsequently to compute $\boldsymbol{R}_{WL}$, which we will call in this report the *extended adding-doubling method*.

6.1. Whitecaps

A wind-ruffled ocean may develop broken waves with a foaming white crest, also known as *whitecaps* (referring to patches) and foam streaks. Koepke (1984) investigated the effective reflectance of the oceanic whitecaps and foam streaks, resulting from wind speeds of 8 m/s and ≈15 m/s respectively, by analyzing their lifetime and reflection through photographs. For convenience in this report both phenomena are referred to as 'whitecaps' in what follows, similar to the formulation of the final effective reflectance by Koepke (1984). The adjective 'effective' refers to the lower albedo of the whitecaps than concluded by Whitlock et al. (1982)

in laboratory conditions, caused by the aging of the whitecaps.[1] Koepke (1984) estimated the effective reflectance to be (22±11)% and independent of wavelength in the visible range (cf. Fig. 8 of Koepke (1984)). We would like to emphasize the error of 11 %, which should be treated with care when interpreting results when whitecaps are included.

The study of Koepke (1984), however, did not include polarization effects. Sun and Lukashin (2013) assumed the foam to be a Lambertian reflector such that only the upper left element of the 4x4 matrix $\boldsymbol{R}_{WC}$ is nonzero and represents the whitecap albedo or effective reflectance. The total reflectance due to foam may then be computed by the product of the fraction of the ocean surface covered with foam, q, and the effective reflectance by the whitecaps (cf. Equation 6.1 and Koepke (1984) Eq. 16).

Both Koepke (1984) and Sun and Lukashin (2013) used the expression for the fraction of the whitecaps q as a function of wind speed v in m/s from Monahan and Ó Muircheartaigh (1980), given by

$$q = 2.95 \cdot 10^{-6} v^{3.52} \tag{6.2}$$

which is valid for a water temperature above $14^{o}C$. It should be noted that the expression for q above is a rough approximation. The 'real' fraction depends, besides wind speed, on the wave travel distance, the water temperature and thermal stability of the lower atmosphere influencing the lifetime of the whitecaps (Koepke 1984). Nevertheless the model of Monahan and Ó Muircheartaigh (1980) has been adopted by many authors since only wind speed input data is needed (Chowdhary 1999; Sayer et al. 2010; Sun and Lukashin 2013; Xu et al. 2016).

6.2. Scattering of Polarized Light in the Ocean Water

Light that originates from the subinterface ocean water is strongly wavelength dependent since the light at long wavelengths in the visible domain is strongly absorbed by the water, while light at short wavelengths is not and is scattered in the water. The absorbing and scattering properties of seawater are determined by its constituents, ranging from water molecules (size ≈ 0.1 nm), to large organic molecules (size ≈ 10 nm), viruses, bacteria (size ≈ 0.2-1.0 μm), phytoplankton (size ≈ 1- 200μm), organic detritus to living animals (Mobley 1994). Chowdhary et al. (2006) modeled their (inorganic and organic) particles, or hydrosols, as spherical particles allowing them to use Mie theory, analogous to scattering by spherical aerosols in the atmosphere (cf. Section 2.1.2). They remarked that the hydrosols are generally not spherical, but that precise information about the representative hydrosol structures is simply not available yet. In our exoplanet models, we only consider pure seawater, and leave the implementation of hydrosols in the water of the exoplanet oceans for future studies. We do, however, model the albedo of the subinterface ocean in two ways. First, by using the bio-optical model for Case 1 Waters of Morel and Maritorena (2001), which depends on chlorophyll concentration (see Appendix B.3). The albedo computed from this bio-optical model, or its former widely employed version of Morel (1988), is often assigned to a Lambertian surface underneath the air-water interface representing the ocean color (see e.g. Sun and Lukashin 2013; Zugger et al. 2010). Since we aim to infer information from the degree of polarization at the top of the atmosphere, we decided *not* to use a Lambertian surface underneath the air-water interface, because it will depolarize the light by definition. Instead, we model the bulk ocean as a stack of homogeneous water layers using the adding-doubling method, analogous to the approach in Section 3, which was also done by Chowdhary et al. (2006, 2012); Xu et al. (2016). We do *not* include hydrosols, which would require a proper determination of the hydrosol scattering matrix elements (see e.g. Chowdhary et al. 2006). The oceans of our exoplanet models thus consist of pure seawater and belong to the clearest natural waters. Then, we recompute the albedo from the computed reflection matrix of the combined water later, $\boldsymbol{R}_{W}$, which is our second way to compute the ocean albedo, albeit without chlorophyll concentration, and we continue with this approach only. However, we use the bio-optical model for comparison in order to avoid unrealistic ocean albedos when using pure seawater, which may be caused by the various data sets available for the spectral absorption coefficients of pure seawater yielding different results due to the high measurement uncertainties at short wavelengths in the visible domain and different measurement techniques (Mason et al. 2016; Pope and Fry 1997; Smith and Baker 1981; Sogandares and Fry 1997).

[1] After a few seconds the whitecap does not reflect as effective anymore as in the moment of maximum reflection. The maximum reflection of a fresh dense foam patch is ≈ 55% found at ≈1.5 seconds after wave breaking (see Whitlock et al. (1982) and Koepke (1984) Fig. 5.

Scattering in pure water is often called Rayleigh scattering, and measurements by Voss and Fry (1984) in a variety of ocean waters indeed showed that the normalized scattering matrix elements have a comparable angular dependence. However, physically, scattering of light in water can certainly not be explained by Rayleigh theory. The proper explanation is provided by Einstein-Smoluchowski theory, which says that scattering in a liquid is caused by the random molecular motions in the liquid which give rise to density fluctuations, where the volume is small compared to the wavelength of light, resulting in fluctuations in the refractive index. An extensive review is provided by Morel (1974), who also explained that, although Rayleigh's molecular scattering theory does not physically apply to a liquid because of the strong molecular interactions, '*for the wavelength dependence, the symmetry of the scattering diagram, and the polarization the results obtained continue to exist in the theory of fluctuations*'. That is, the Einstein-Smoluchowski theory provides a new way to compute the so-called Rayleigh ratio (or the volume scattering function at an angle of 90°). However, the imperfect scattering at 90°, that was attributed to the anisotropy of the molecules in Rayleigh theory (recall Section 2.1.2), may still be computed with the Cabannes factor (Eqs. 17 and 18 of Morel (1974)), using the depolarization factor for unpolarized incident light (Young 1982). For this reason, Chowdhary et al. (2006) could model the scattering in pure seawater with the scattering matrix for anisotropic Rayleigh scattering of Hansen and Travis (1974), which will also be employed in this research. Following Chowdhary et al. (2006), we use a depolarization factor of 0.09, which was measured by Morel (1974).[2] Note that, for the determination of the scattering coefficient, b_w, we do not have to use Einstein-Smoluchowski theory since we use the tabulated values as a function of wavelength by Smith and Baker (1981).

The scattering matrix for single scattering including polarization effects in the ocean, $\boldsymbol{F}_W(\Theta,\lambda)$, may be computed by (Chowdhary et al. 2006)

$$\boldsymbol{F}_W(\Theta,\lambda) = \frac{b_w(\lambda)\boldsymbol{F}_w(\Theta,\lambda) + b_p(\lambda)\boldsymbol{F}_p(\Theta,\lambda)}{b_w(\lambda) + b_p(\lambda)} \tag{6.3}$$

where the corresponding single scattering albedo reads

$$\omega_W(\lambda) = \frac{b_w(\lambda) + b_p(\lambda)}{b_w(\lambda) + b_p(\lambda) + a(\lambda)} \tag{6.4}$$

In these equations, $b_w(\lambda)$ is the wavelength dependent scattering coefficient of pure seawater which was tabulated by Smith and Baker (1981), $b_p(\lambda)$ is the hydrosol scattering coefficient, $\boldsymbol{F}_p(\Theta,\lambda)$ is the hydrosol scattering matrix and $a(\lambda)$ is the absorption coefficient. $b_p(\lambda)$ and $a(\lambda)$ may be computed from the bio-optical model of Morel and Maritorena (2001). However, since we do not include hydrosols, the absorption coefficient equals the absorption coefficient of pure seawater, a_w, and we use the tabulated values of Pope and Fry (1997)[3]. Since we do not include hydrosols, we have:

$$\boldsymbol{F}_W(\Theta,\lambda) = \boldsymbol{F}_w(\Theta,\lambda); \qquad \omega_W(\lambda) = \frac{b_w(\lambda)}{b_w(\lambda) + a_w(\lambda)} \tag{6.5}$$

Converting the scattering matrix $\boldsymbol{F}_W$ to a phase matrix $\boldsymbol{Z}_W$ with Equation 2.40 and subsequently to reflection and transmission matrices for single scattering (Equations 2.60 and 2.61), the adding-doubling method may be applied. Vertically dividing the ocean in plane parallel layers, similar as for the atmosphere in Chapter 3, and starting from sufficiently thin layers, the reflection matrix for the oceanic water volume $\boldsymbol{R}_W$ may be computed. The ocean optical thickness τ_{ocean} is computed from the geometric ocean depth z, measured in meters positive downward from the mean sea surface, and the beam attenuation coefficient $c(\lambda) = b(\lambda) + a(\lambda)$ (see Mobley (1994) Chapter 4, 5 and 6). Note that b, a and c have units of m^{-1} while τ_{ocean} is nondimensional, and $\tau_{ocean} = c \cdot z$ (Xu et al. (2016) Eq. D23), where we assume for simplicity that c is invariant with depth.

[2] Other values of the depolarization factor have been measured, which may be attributed to the different ways that stray light is accounted for during the measurements, according to Jonasz and Fournier (2011).

[3] The lower limit of the range from 380 nm to 350 nm is extended by using the additional data of Sogandares and Fry (1997). Between 727.5 nm and 800 nm we use the values of Smith and Baker (1981).

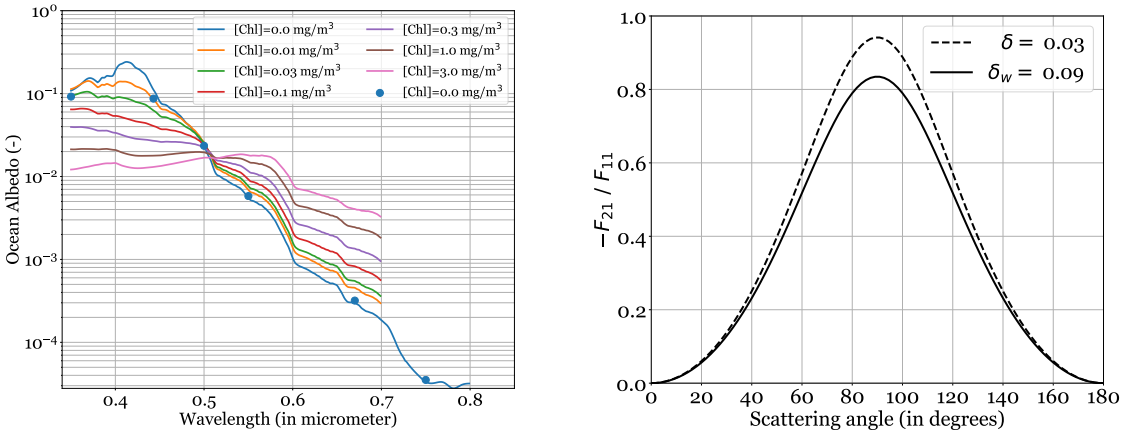

(a) (b)

Figure 6.1: (a) Albedo of the ocean just below the air-water interface for an incidence zenith angle of 30 degrees. The solid lines are the theoretical values computed with the bio-optical model of Morel and Maritorena (2001) for Case 1 Waters at various chlorophyll concentrations. The blue dots are the recomputed albedos from the doubling-adding result including polarization, where we assume [Chl] = 0 mg/m^3 and an ocean depth of 100 m. (b) Element F_{21} of the phase matrix for anisotropic Rayleigh scattering of Hansen and Travis (1974) using a depolarization factor of 0.09 (solid line), and compared to the single scattering matrix for the atmosphere where we use a value of 0.03 (dashed line).

Figure 6.1a shows ocean albedo computed with the bio-optical model of Morel and Maritorena (2001) chlorophyll concentrations ranging from 0 mg/m^3 to 3 mg/m^3 (solid line), and the ocean albedo at [Chl] = 0 mg/m^3 recomputed from the adding-doubling result of R_W at the wavelengths that will be employed in the exoplanet models in Chapter 7 (blue dots) according to

$$A_{ocean}(\mu') = \frac{1}{\pi}\int_0^1 \mu d\mu \int_0^{2\pi} R_W(\mu,\mu',\varphi-\varphi')d(\varphi-\varphi') \tag{6.6a}$$

where R_W is the (1,1) element of $\boldsymbol{R}_W$. The recomputed result is in good agreement with the bio-optical model, except for the slight deviations at the two shortest wavelengths (350 nm and 443 nm). However, it should be mentioned that (1) there are several assumptions involved in the bio-optical model[4], (2) the bio-optical model was designed for waters that contain at least some chlorophyll, (3) the uncertainty of the absorption coefficient at 443 nm and 350 nm is 9% and 13% respectively (Pope and Fry 1997; Sogandares and Fry 1997) and (4) different ocean albedos could be found at short wavelengths if other data sets would be used for $a_w(\lambda)$. Although most data sets are in agreement at $\lambda > 440$ nm (Mason et al. 2016; Pope and Fry 1997), using the data set of Mason et al. (2016) for example at $\lambda < 440$ nm, who found relatively low absorption coefficients, would result in uncomfortably high ocean albedos.

Figure 6.1b shows the scattering element F_{21} of the phase matrix of Hansen and Travis (1974) for anisotropic Rayleigh scattering, normalized by element F_{11} (recall the matrix elements stated in Section 2.1.2). As mentioned above, this matrix will be used for the single scattering matrix for water, $\boldsymbol{F}_W$. The line for $\delta_w = 0.09$ cannot be distinguished from the line for pure seawater in Fig. 3 of Chowdhary et al. (2006).

6.3. Adding the Bulk Ocean to the Interface

This section explains the coupling of the oceanic water volume to the ocean surface for the transfer of polarized light with the so-called *extended adding-doubling method*, which was explained by Xu et al. (2016), but

[4] We assumed that the ocean color is independent of viewing geometry. That is, we set α of Eq. 8 of Chowdhary et al. (2006) equal to the often used value 0.33. The shape of the spectral reflectance curve does not change with α, but a slight upward shift is expected for larger solar zenith angles, as described at the end of Sec. 3.4 of Morel and Maritorena (2001), and could be modeled with the parameterization of Morel and Gentili (1991). The parameters μ_d and μ_u in Eq. 8 of Morel and Maritorena (2001) are set at 0.9 and 0.4 respectively, as proposed by Morel (1988), which actually depend on chlorophyll concentration and wavelength.

was also already treated in the PhD Thesis of Chowdhary (1999).

The extended adding-doubling method accounts for the conversion from the underwater reflection matrix for the bulk ocean, $\boldsymbol{R}_W$, to the contribution of the underwater leaving reflected light to the total reflection by the ocean, given by $\boldsymbol{R}_{WL}$ (recall Equation 6.1). Thus, $\boldsymbol{R}_{WL}$ describes the light originating from the subinterface ocean that possibly encountered repeated reflections with the air-water interface inside the water before leaving the ocean.

First, we use Equation 2.82 to compute the Fourier coefficients of the interface matrices $\boldsymbol{R}_i$, $\boldsymbol{R}_i^*$, $\boldsymbol{T}_i$ and $\boldsymbol{T}_i^*$. The integration over the azimuth difference is done with a Runge-Kutta-Fehlberg method using adaptive stepsize control. Once also the Fourier coefficients of $\boldsymbol{R}_W$ have been computed (see Section 6.2), the matrix $\boldsymbol{R}_{WL}$ may be computed according to the scheme (see Xu et al. 2016, App. C1):

$$\boldsymbol{Q}_1 = \boldsymbol{R}_i^* \boldsymbol{R}_W \qquad (4N_w \cdot 4N_w) \cdot (4N_w \cdot 4N_w) \tag{6.7}$$

$$\boldsymbol{Q}_{p+1} = \boldsymbol{Q}_1 \boldsymbol{Q}_p \qquad (4N_w \cdot 4N_w) \cdot (4N_w \cdot 4N_w) \tag{6.8}$$

$$\boldsymbol{Q} = \sum_{p=1}^{\infty} \boldsymbol{Q}_p \qquad (4N_w \cdot 4N_w) \cdot (4N_w \cdot 4N_w) \tag{6.9}$$

$$\boldsymbol{D} = \boldsymbol{T}_i + \boldsymbol{Q}\boldsymbol{T}_i \qquad (4N_w \cdot 4N_a) + (4N_w \cdot 4N_w) \cdot (4N_w \cdot 4N_a) \tag{6.10}$$

$$\boldsymbol{U} = \boldsymbol{R}_W \boldsymbol{D} \qquad (4N_w \cdot 4N_w) \cdot (4N_w \cdot 4N_a) \tag{6.11}$$

$$\boldsymbol{R}_{WL} = \boldsymbol{T}_i^* \boldsymbol{U} \qquad (4N_a \cdot 4N_w) \cdot (4N_w \cdot 4N_a) \tag{6.12}$$

where all matrices in this scheme are supermatrices. Note that this adding scheme is analogous to the adding scheme for the atmosphere (Equations 3.13 to 3.19), where the air-water interface is assumed to be a pseudolayer without any thickness such that all attenuation related terms may be removed.

The alert reader may have noticed that a problem may arise when using a similar set of Gaussian quadrature points for the atmosphere (N_a) and ocean (N_w), since the light transmitted from air to water is refracted into a sharp cone (see Figure 5.15). That is, we would have a lower angular resolution in the cone compared to the resolution in the atmosphere and, if not enough Gauss points would be used, the sharp cone could not accurately be covered. In Sec. 3.2.4 of the PhD thesis of Chowdhary (1999), it is mentioned that the supermatrix formalism of de Haan et al. (1987) can be used in the case of two different Gauss sets N_a and N_w. We show in Appendix A.4 that this is indeed possible with an elaborated example for two different hypothetical small Gauss sets. The dimensions of the supermatrices are shown next to Equations 6.7 to 6.12. The transmission matrices of the interface, $\boldsymbol{T}_i$ and $\boldsymbol{T}_i^*$, where the transition between the two Gauss sets occurs, are thus *rectangular* supermatrices. Note that the result, $\boldsymbol{R}_{WL}$, has dimensions $(4N_a \cdot 4N_a)$ and can simply be added to $\boldsymbol{R}_i$ in Equation 6.1. Consequently, the final reflection matrix for the complete ocean system, $\boldsymbol{R}_{OCEAN}$, is *only* defined in terms of the Gauss set for the atmosphere, such that it can straightforwardly be implemented as the reflection matrix of the bottom layer in the adding scheme of the atmosphere.

6.4. Polar Plots of the Ocean Reflection

In Figure 6.2 polar plots are shown for the (1,1) element of the reflection matrix of the ocean, $\boldsymbol{R}_{OCEAN}$, (left plot) and the degree of polarization for an unpolarized incident beam (right plot). The wind speed is 7.4 m/s, the incidence zenith angle is 38.9°, the water depth is 100 m and the wavelength is 350 nm. Underneath the water layer, we place a black Lambertian surface representing the ocean bottom.[5] Compared to the degree of polarization by the reflection from the interface (recall Figure 5.16), the degree of polarization has changed significantly. This is due to the nonzero and increased reflection outside the glint because of the additional water leaving light in the blue part of the visible spectrum, as will be explained below.

[5] Some papers chose to use a fixed optical thickness for the ocean, an often used value is $\tau_{ocean} = 10$ (Chowdhary et al. 2006; Zhai et al. 2010). Indeed, τ_{ocean} varies with wavelength for a fixed geometric ocean depth, but using a fixed geometric ocean depth allows us to easily vary the ocean bottom albedo in future studies. In Appendix B.4 we will show that an almost similar planetary phase curve is obtained if we would use $\tau_{ocean} = 10$ instead of an geometric ocean depth of 100 m.

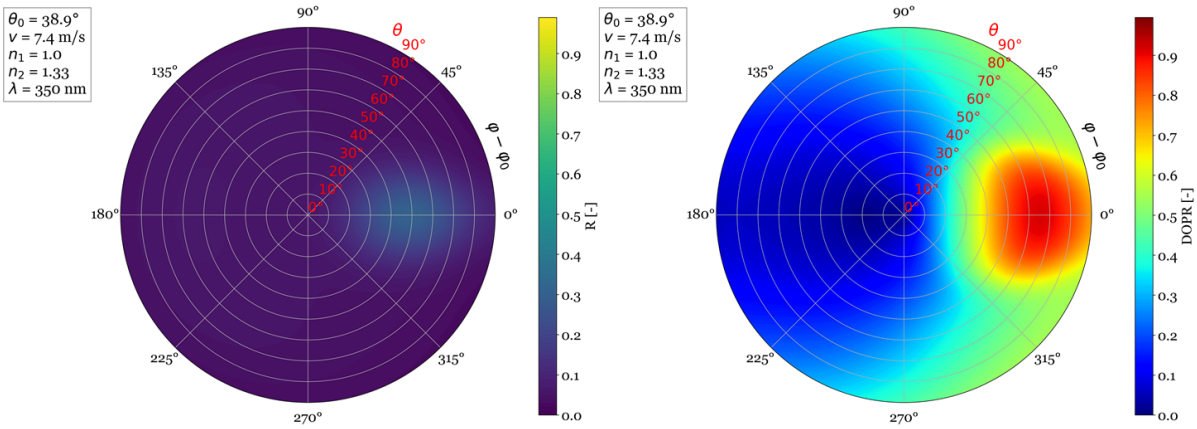

Figure 6.2: Polar plots of the upper left element (left plot) and degree of polarization (right plot) of the ocean reflection matrix, $\boldsymbol{R}_{OCEAN}$, at λ = 350 nm for an incidence angle of 38.9°, an ocean depth of 100 m and a wind speed of 7.4 m/s. The unpolarized light source is located at $\varphi - \varphi_0$ = 180°. The viewing zenith angle is indicated in red.

Figure 6.3 shows the cross-section of the polar plot of the (1,1) element of $\boldsymbol{R}_{OCEAN}$ (Figure 6.2) at $\varphi - \varphi_0 = 0°$. Indeed, outside the glint region, the reflectance does not decrease towards 0, contrary to the reflection by the interface only, but goes to approximately 0.05. Because the degree of polarization is a measure of the polarized flux with respect to the total flux, and because the total flux is increased outside the glint region due to the water-leaving light which is only partly polarized, the degree of polarization is decreased outside the glint region (Figure 5.16). Inside the glint region, where the Fresnel reflection is most significant, the degree of polarization is still relatively large.

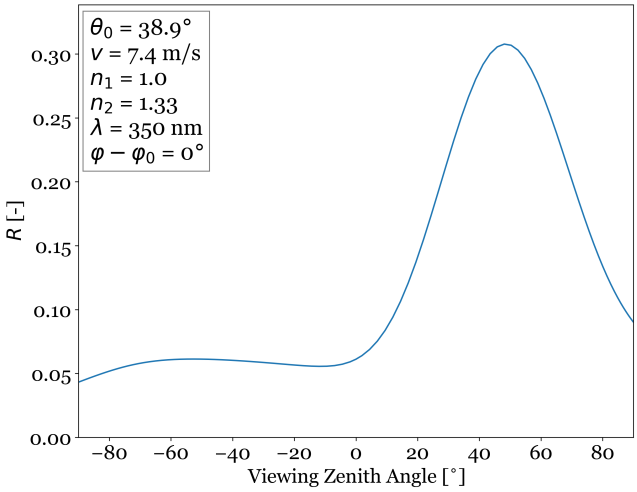

Figure 6.3: Cross-section of the polar plot of the (1,1) element of $\boldsymbol{R}_{OCEAN}$ (Figure 6.2) at $\varphi - \varphi_0 = 0°$, at λ = 350 nm. Outside the glint region the reflectance does not decrease towards 0, contrary to the reflection by the interface only, but goes to approximately 0.05, due to the additional water-leaving light.

III

Flux and Degree of Polarization of Starlight Reflected by Extrasolar Planets

7

Phase Curves of Exoplanet Models Containing Oceans

In the former chapters the theory of transfer of polarized light in the planetary atmosphere and the reflection by the ocean were discussed. We explained how the reflected light at the TOA (top of the atmosphere) can be computed in terms of the Stokes vector with the adding-doubling method, and we presented the extension to this algorithm to implement the reflection by the ocean. Let us now assume that the atmosphere and ocean in the computations are the atmosphere and ocean of a planet outside our solar system orbiting its parent star. In what follows, we will refer to these planets as *exoplanets*. As discussed in the Background and Motivation pages in the beginning of this report, light originating from a solar type star, incident on the exoplanet, may be considered as unpolarized. In this chapter, we will present the modeled flux, degree of polarization and the polarized flux of this starlight that is reflected by oceanic exoplanets in the direction of the observer.

In Section 7.1 it will be explained how the disk-integrated signal can be computed from the local reflection at the top of the atmosphere on the exoplanet, in Section 7.2 the planetary phase curves will be presented of horizontally homogeneous ocean planets and in Section 7.3 the horizontally inhomogeneous ocean planets will be discussed. That is, we introduce clouds that do not cover the complete planet, but only partly, in the form of patchy clouds and a substellar cloud. Finally, we will investigate in Section 7.3.3 whether the planetary phase curves can also be computed with the often used quasi horizontally inhomogeneous approach, which is an additive sum of the planetary phase curves of horizontally homogeneous planets.

7.1. Integration over the Planetary Disk

The geometry of the observation of an exoplanet is sketched in Figures 7.1a and 7.1b. The planetary phase angle α is defined by the angle between the observer and star as measured from the center of the planet ($0^o \leq \alpha \leq 180^o$) and $\alpha = 180^o - \Theta$ where Θ is the scattering angle (Stam 2008). As illustrated in Fig. 6b of Stam (2008), for increasingly face-on orbits ($i \rightarrow 0°$) the flux and polarization signal dependency on phase angle will approach zero. However, Stam (2008) explained that the degree of polarization is smallest when it is most difficult to directly observe the planet (for i close to 90° combined with $\alpha = 0, 180^o$, or 360^o), which is a beneficial coincidence. In all our simulations in this research we assume an orbital inclination of 90^o.

The starlight reflected by an exoplanet measured at a distance d by an instrument nowadays is spatially unresolved, that is, all information of the measured signal is stored in one pixel. Consequently, the computed Stokes vectors of the locally reflected light emerging at the top of the atmosphere of the exoplanet with the adding-doubling method (Chapter 3) should be integrated over the illuminated part of the planetary disk to obtain the total flux (and its polarization) of the reflected light. Stam et al. (2006) provided an integration method that is based on the expansion of the radiation field of a spherical, horizontally homogeneous planet into spherical functions. The computed total and polarized locally reflected fluxes may then be integrated over the illuminated part of the planetary disk to simulate the total received (polarized) flux for arbitrary

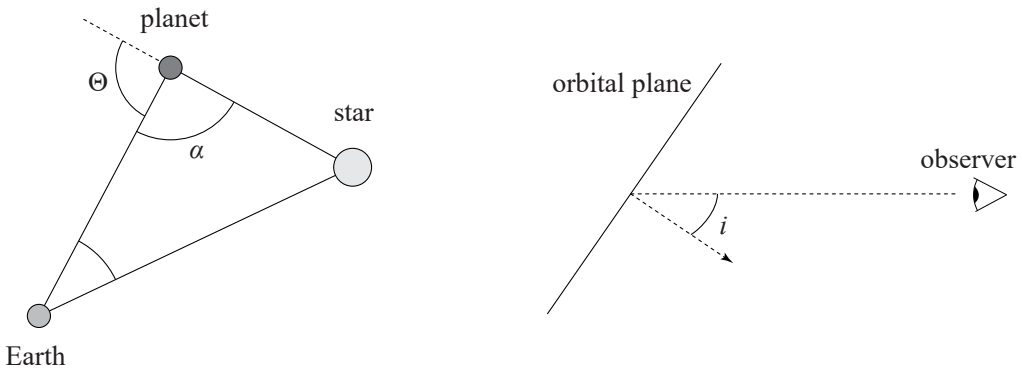

Figure 7.1: Geometry of the observation of an exoplanet. (a) Observation in the scattering plane for an edge-on orbit. Planet and star radii are assumed to be much smaller than distances between the bodies (Stam et al. 2004, Fig. 1). (b) Definition of the orbital inclination. Edge-on orbits correspond to $i = 90^{\mathrm{o}}$ and face-on orbits correspond to $i = 0^{\mathrm{o}}$.

planetary phase angles according to (see Stam et al. 2006, Eq. 16)

$$\begin{aligned} \pi \boldsymbol{F}(\alpha) &= \frac{1}{d^2} \int_{\mathrel{)}} \mu \boldsymbol{I}'(\mu, \mu_0, \varphi - \varphi_0) dO \\ &= \frac{1}{d^2} \int_{\mathrel{)}} \mu \mu_0 \boldsymbol{R}_1'(\mu, \mu_0, \varphi - \varphi_0) F_0 dO \end{aligned} \tag{7.1}$$

where $\mu dO/d^2$ is the solid angle under which a surface element dO of a planet is seen by the observer, $\mathrel{)}$ indicates the illuminated part of the planetary disk, μ_0 is the directional cosine of the local stellar zenith angle positively towards the planet surface, F_0 is the incident stellar flux on the exoplanet divided by π in W m^{-2} sr^{-1} and α is the planetary phase angle. We assume an incident unpolarized stellar beam with a flux of π measured perpendicular to the direction of propagation, such that F_0=1 (as in de Haan et al. (1987)). It should be noted that the resulting Stokes vector from the adding-doubling method was defined with respect to the local meridian plane of the planet. Therefore, $\boldsymbol{I}'$ is defined as the Stokes vector with respect to the planetary scattering plane, obtained by rotating the polarization axes of $\boldsymbol{I}$ by a positive angle β in the anti-clockwise direction when looking in the direction of propagation (cf. Equation 1.13). This rotation may be written as $\boldsymbol{R}_1' = \boldsymbol{L}(\beta)\boldsymbol{R}_1$ where $\boldsymbol{L}$ is the rotation matrix of Equation 1.13 and $\boldsymbol{R}_1$ is the local reflection matrix of the atmosphere-ocean system on the exoplanet (see Part I and Part II). For a detailed discussion of this integration method the reader is referred to Stam et al. (2006).

In case of a horizontally *inhomogeneous* model planet the approach of Stam et al. (2006) mentioned above may be employed by using weighted sums of horizontally homogeneous planets (see Stam 2008). However, these *quasi* horizontally inhomogeneous model planets would not account for the actual spatial distribution of the inhomogeneities. For example, if the surface of the rotating model planet is divided into a specular reflecting ocean surface and a vegetated ground surface, a differentiation of the local reflection properties may be desired. This may be done by replacing the integration of Equation 7.1 by the summation over N visible and illuminated pixels on the planet described by (see Stam et al. 2014, Eq. 13)

$$\pi \boldsymbol{F}(\alpha) = \frac{F_0}{d^2} \sum_{n=1}^{N} \mu_n \mu_{0n} \boldsymbol{L}(\beta_n) \boldsymbol{R}_1(\mu_n, \mu_{0n}, \varphi_n - \varphi_{0n}) dO_n \tag{7.2}$$

where all parameters with the subscript n, including $\boldsymbol{R}_1$, depend on the location on the planet as seen from the observer and are consequently unique for each pixel. Also, μ_0, $\varphi - \varphi_0$ and β are functions of the phase angle. The 2D projection of the planet perpendicular to the line of sight is divided into square pixels. The pixel area as seen by the observer is μdO, as illustrated in Figure 7.2.

We take a minimum of 40x40 pixels at each phase angle, resulting in a decreased number of illuminated pixels N at crescent phase. The phase curves of the horizontally inhomogeneous planets are computed with the Python shell PyMieDAP (Rossi et al. 2018) which assigns the TOA reflection matrices to the pixels of model

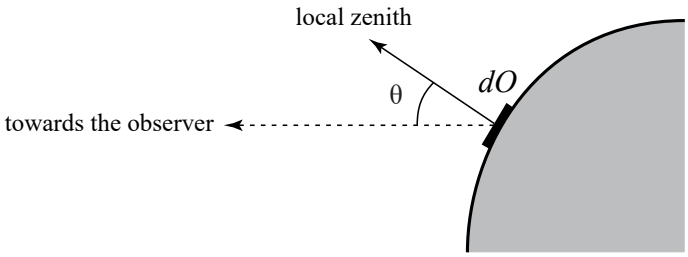

Figure 7.2: Sketch of a surface area dO on the planet (side view) and its projection perpendicular to the observer. The observed pixel area equals $\cos\theta dO$ where θ is the local viewing zenith angle (Rossi et al. 2018, Fig. 3).

planets having varying configurations (e.g. patchy cloud covers instead of a homogeneous cloud deck). In this research we used PyMieDAP only to import the precomputed TOA reflection matrices (Chapter 3) and to combine them in the horizontally inhomogeneous model planet. We refer to Rossi et al. (2018) for a detailed explanation of the PyMieDAP code.

Furthermore, we remark that the flux phase curves presented in the following sections are normalized such that at zero phase angle the reflected flux πF_0 equals the planet's geometric albedo A_G given by

$$A_G = \frac{\pi F(0°)}{\pi F_0}\frac{d^2}{r^2} \tag{7.3}$$

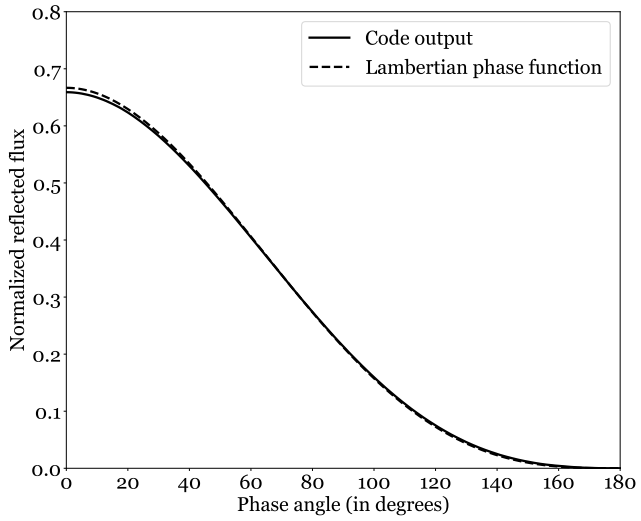

Figure 7.3: Solid curve: disk-integrated flux as a function of planetary phase angle α for a Lambertian sphere (a_s = 1) computed with Equation 7.2 and normalized such that at $\alpha = 0°$ it equals its geometric albedo A_G. Dashed curve: phase function of a Lambertian reflecting, spherical planet (a_s=1) computed with the analytical expression of van de Hulst (1980).

It should be noted that A_G is wavelength dependent. Physically, the geometric albedo describes the reflected flux from the planet at phase angle 0° that could be observed at a distance d with respect to the reflected flux from a Lambertian sphere, which receives the same incoming flux and subtends the same solid angle $\pi r^2/d^2$. The phase curve of the reflected flux of Equation 7.2 normalized by 7.3 can be tested against the analytical expression found by van de Hulst (1980) for the phase function of a Lambertian reflecting, spherical planet

$$\psi(\alpha) = \frac{2}{3\pi}a_s(\sin\alpha + \pi\cos\alpha - \alpha\cos\alpha) \tag{7.4}$$

where a_s is the surface albedo of the Lambertian planet. Figure 7.3 shows the output of the code (i.e. Equation 7.2) when taking $a_s = 1$ compared to the analytical expression 7.4. The output of the code can hardly be distinguished from the analytical expression.

Note in Figure 7.3 that the reflected flux from the Lambertian planet is at its maximum at full phase ($\alpha = 0°$) and decreases with increasing phase angle because the illuminated fraction of the disk decreases (cf. Figure 7.1a). In the following sections we will see that the shape of the phase curve significantly changes when an atmosphere and ocean are introduced in the model.

7.2. Horizontally Homogeneous Planets

In the former section it was explained how the TOA reflection locally on the planet can be integrated over the planetary disk to obtain the modeled signal from the planet as a point light source. Although the spatial resolution is only one pixel, the observations may be observed at various wavelengths if the telescope has enough *spectral resolution* and, additionally, the degree of polarization may be analyzed if a polarimeter is integrated in the optics of the telescope. This section shows the planetary phase curves of the flux, the degree of polarization and the polarized flux of horizontally homogeneous exoplanets, that is, without horizontal variations of the atmosphere or surface type in the model planet.

7.2.1. Lambertian Planet vs. Ocean Planet

Figure 7.4b shows the planetary phase curves of the reflected flux of a planet completely covered by an ocean and a wind speed of 7 m/s. The atmosphere consists of a homogeneous gas layer in hydrostatic equilibrium, where a bottom pressure of 1 bar and top pressure of 0 bar is assumed. The ocean water layer is assumed 100 meter deep.[1] The bottom of the ocean is a black Lambertian surface. The parameters of the atmosphere and ocean are listed in Table 7.1. Note that the air refractive index used for the Fresnel computations is set equal to 1.0, while the air refractive index to compute the scattering cross section of the gas molecules (Equations 2.8) varies with wavelength using the dispersion formula of Peck and Reeder (1972). In Figure 7.4b, also the phase curves of the reflection from the rough air-water interface at 7 m/s are presented (i.e. a black sub-interface ocean and no atmosphere), including whitecaps and without whitecaps. Figure 7.4a shows the planetary phase curves for the reflected flux when the ocean surface is replaced by a Lambertian surface with a surface albedo of 0 (but having the same gaseous atmosphere on top).[2] The planet with a black Lambertian surface is an approximation of for example a very dark rocky planet. The following features may be observed:

- The reflected flux from the Lambertian planet with a gaseous atmosphere (Figure 7.4a) is at its maximum at full phase ($\alpha = 0°$) and decreases with increasing planetary phase angle while the illuminated fraction of the disk decreases, similar to the flux phase curve of the Lambertian planet with nonzero surface reflection and without an atmosphere (Figure 7.3). The reflected flux at shorter wavelengths is higher due to the more effective Rayleigh scattering in the atmosphere at shorter wavelengths proportional to $1/\lambda^4$ (see Equation 2.8).

- The reflected flux from the ocean planet with a gas atmosphere (Figure 7.4b) is higher than the reflected flux from the Lambertian planet with a gas atmosphere at approximately all wavelengths. This increase is more significant for the shorter wavelengths at smaller phase angles (approximately for α between 0° and 90°) and is more significant for the longer wavelengths at higher phase angles (approximately for α between 90° and 180°). The increase at shorter wavelengths when an ocean is included may be caused by (1) the direct contribution of the glint at the TOA, (2) the part of the glint that is multiply scattered in the atmosphere, (3) the repeated reflections between the glint and the atmosphere and (4) contribution of the ocean color. The direct contribution of the glint at the TOA at small phase angles seems to be minor because of the small reflection angles at the wave facets at these phase angles, causing weak Fresnel reflection (Chapter 4). This low and approximately constant glint contribution at small phase angles is

[1] The recomputed albedo of the water layer is approximately equal to this albedo if we would use an optical thickness of 10 for the chosen set of wavelengths, which is shown in Appendix B.4. Using one depth allows us to compare these results with phase curves for oceans having nonzero ocean bottom reflection in future studies.

[2] Comparing the ocean reflection with the reflection by a black Lambertian surface allows us to fully investigate the effect of the ocean only. Also, the black Lambertian surface is immediately a good test case, because we will see that the glint reflection yields an high degree of polarization at red wavelengths but polarized singly scattered light by gaseous molecules above a black Lambertian surface at long wavelengths also results in a high degree of polarization, because it is not depolarized by multiple scattering and, in this case, surface reflection (cf. Fig. 4 of Stam 2008).

Table 7.1: Parameters of our standard atmosphere and ocean. Unless stated otherwise, the values listed in this table are used. For the Lambertian planet, the ocean is replaced by a Lambertian surface with a surface albedo, a_s, equal to 0.

Atmosphere Parameters	Symbol	Value
Surface pressure [bar]	p_s	1.0
Depolarization factor	δ	0.03
Mean molecular mass [g/mol]	m_g	29
Acceleration of gravity [m/s^2]	g	9.81
Ocean Parameters		
Wind speed [m/s]	v	7.0
Foam albedo	a_{foam}	0.22
Depolarization factor	δ_w	0.09
Air refractive index just above air-water interface	n_1	1.0
Water refractive index just below air-water interface	n_2	1.33
Chlorophyll concentration [mg/m^3]	[Chl]	0
Ocean depth [m]	z	100
Ocean bottom surface albedo	a_{bs}	0

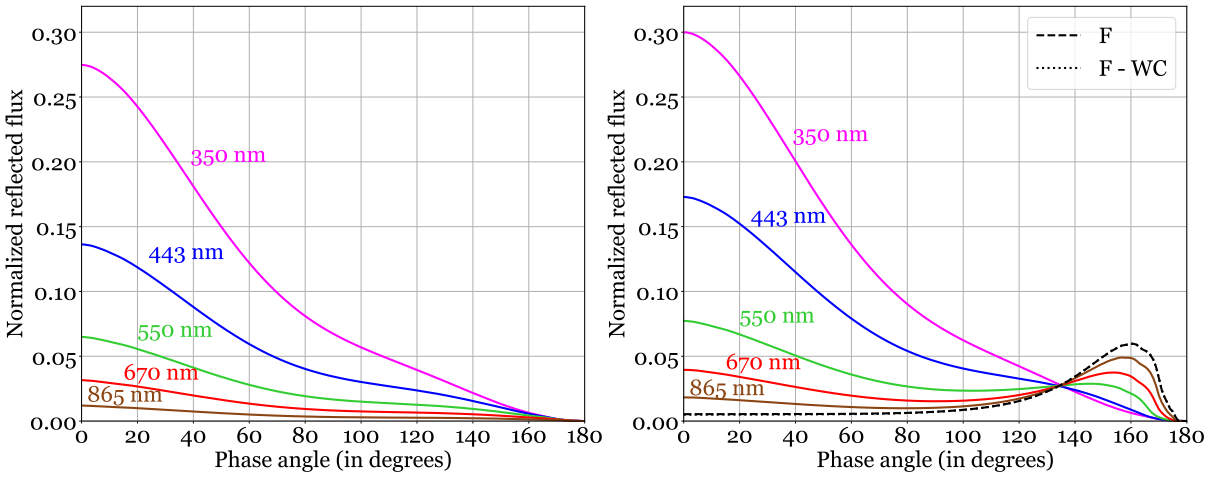

Figure 7.4: Disk-integrated flux as a function of planetary phase angle α for the (a) Lambertian planet with a gas atmosphere, surface albedo = 0 and the (b) ocean planet with a gas atmosphere. Also, the rough Fresnel interface (F) and rough Fresnel interface without whitecaps (F - WC) are drawn, where the surface pressure is set equal to 0 bar and the subinterface ocean scattering is neglected. The wind speed is 7 m/s for all curves. The lines for F and $F - WC$ can hardly be distinguished.

represented by the dashed curve in Figure 7.4b where the scattering in the atmosphere and ocean is ignored. A similar result was found by Williams and Gaidos (2008), who also ignored the scattering of light in the atmosphere and sub-interface ocean. In order to distinguish between the contribution of the ocean color and the part of the glint multiply scattered or repeatedly reflected, we analyze the differences between the phase curves for a black ocean and colored ocean, both with gaseous atmospheres on top, in Section 7.2.2.

- The increase of the reflected flux at big phase angles (approximately for α between 90° and 180°) for long wavelengths is mainly caused by the direct contribution of the glint. This can be concluded from the increased Fresnel reflection (dashed curve and dotted curves in Figure 7.4b) at big phase angles due to big reflection angles on the wave facets and an increased glint fraction of the crescent shaped illuminated disk (Williams and Gaidos 2008). The light beams of longer wavelengths are less effectively scattered by Rayleigh scattering which allows them to have longer path lengths in the atmosphere,

compared to the shorter wavelengths. They are more likely to penetrate through the atmosphere at these big phase angles, to be reflected by the ocean, and to reach the TOA again without being multiply scattered in the atmosphere. These light beams of longer wavelengths travelling upwards to the TOA are strongly reflected by the Fresnel reflection, which we assumed to be wavelength independent. Note that in Section 7.2.6 we will check the validity of the assumption of the wavelength independent refractive index of water when modeling the Fresnel reflection.

- The dotted and dashed lines can hardly be distinguished from each other at all phase angles which means that the phase curve of the reflected flux by the air-water interface alone is not affected by the whitecap contribution in Figure 7.4a. This may be explained by the relatively low whitecap percentage of 0.28% at 7 m/s (cf. Equation 6.2). In Section 7.2.3 we will vary the wind speed and analyze the whitecap contribution.

- Note that the reflected flux for various wavelengths intersect at $\alpha = 135°$. As discussed above, the reflected flux by an oceanic exoplanet with a gas atmosphere is a superposition of two phenomena: (1) the decreasing reflection by the atmosphere with increasing wavelength and (2) the increasing contribution of the air-water interface at the TOA with increasing wavelength. Since the scattering optical thickness of the gaseous atmosphere scales with $1/\lambda^4$ and both the reflection and attenuation by the atmosphere are a function of the scattering optical thickness, the location of the intersection point may be determined by considering the two limits: (1) the phase curve at 350 nm, where at the location of the intersection point (between ≈120° and ≈140° phase angle) the contribution of the air-water interface reflection may be neglected and (2) the phase curve for the Fresnel solution where no atmosphere is present, which represents the phase curve at a wavelength long enough such that atmospheric Rayleigh scattering may be ignored. Note that, also, light originating from the subinterface ocean may be neglected at long wavelengths in the visible domain. At 550 nm and local incidence zenith angle of 30° we compute a subinterface ocean albedo of 0.00581 in the absence of chlorophyll, which further decreases with increasing wavelength, due to the absorption by the water. The location of the intersection point in the normalized reflected flux is then defined by value of α for which

$$\sum_{n=1}^{N} \mu_{0n} R_1'(\mu_n, \mu_{0n}, \varphi_n - \varphi_{0n}, \lambda = 350 \text{ nm}) = \sum_{n=1}^{N} \mu_{0n} R_1''(\mu_n, \mu_{0n}, \varphi_n - \varphi_{0n}, n_1, n_2, \sigma) \tag{7.5}$$

where R_1' is the reflectance of the atmosphere only at 350 nm, R_1'' is the reflectance of the rough air-water interface, n_1 is the refractive index of air, n_2 is the refractive index of the water and σ is the standard deviation of the wave facet inclinations as in Section 5.3. All angles in Equation 7.5 depend on α and the location of the corresponding pixel n on the illuminated part of the disk. Equation 7.5 shows that the location of the intersection point of the disk-integrated reflected flux in terms of α is determined by (1) the directional reflection properties of the atmosphere at a short wavelength ($\lambda = 350$ nm), (2) the directional reflectance of the surface that is encountered by light of long wavelengths, but also by (3) the fraction of the illuminated disk that is dominated by this atmospheric or surface reflection. Thus, if we want to understand the sensitivity of the location of the intersection point on the surface reflection, we need to take into account the spatial coverage of this reflection on the illuminated disk as well.

Figure 7.5a and 7.5b show the degree of polarization of the model planets with a Lambertian surface and ocean respectively. The polarization phase curve for the Lambertian planet with 0 surface albedo is fairly symmetrical around $\alpha = 90°$ which is caused by the symmetrical degree of polarization around $\alpha = 90°$ of the singly scattered light by the gaseous molecules. Stam (2008) explained that there is much less multiple scattering at longer wavelengths, which is the reason for the most apparent symmetric degree of polarization at $\lambda = 865$ nm. Compared to the Lambertian planet, the polarization peak of the ocean planet is shifted towards bigger planetary phase angles with increasing wavelength, which was also found by Zugger et al. (2010). They attributed this shift to the less effective Rayleigh scattering in the atmosphere, which causes the polarization peak to approach two times the Brewster angle. Recall from Section 4.1.3 that the Brewster angle can be computed as $\arctan n_2/n_1 = 53°$, which corresponds to a planetary phase angle of 106° (cf. Figure 7.1a). It can be seen in Figure 7.5b that the peak in the degree of polarization is indeed located at $\alpha = 106°$. Note that we use a wind speed of 7 m/s, but that the degree of polarization is independent of wind speed, as will be explained in Section 7.2.3. Furthermore, note that at $\alpha > 100°$ and with increasing wavelength, the phase curves of the

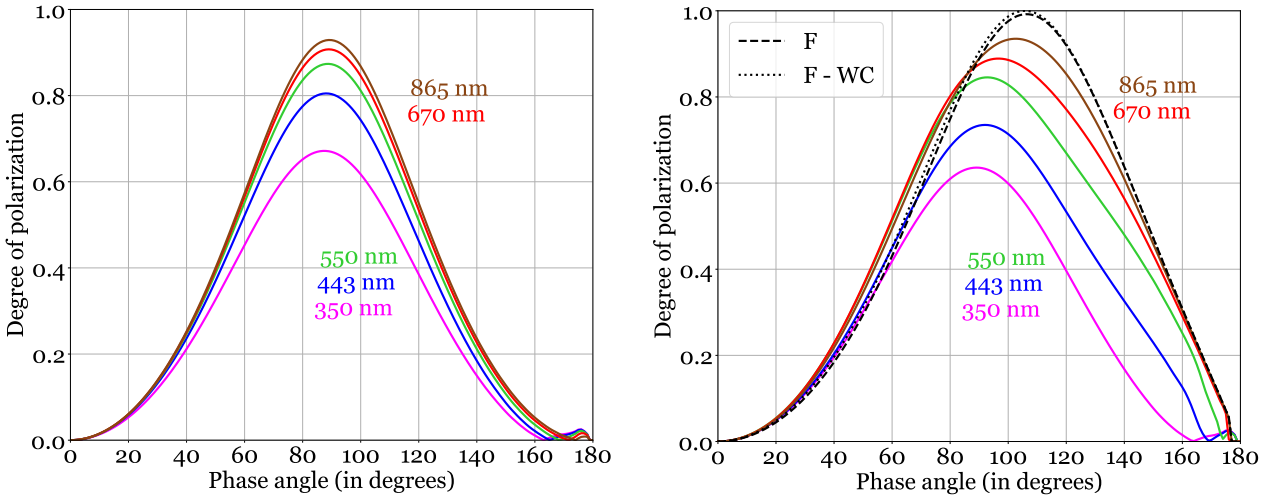

(a) (b)

Figure 7.5: Degree of polarization as a function of planetary phase angle α for (a) the Lambertian planet with a gas atmosphere, surface albedo = 0 and (b) the ocean planet with a gas atmosphere. Also, the reflected flux from the rough Fresnel interface (F) and rough Fresnel interface without whitecaps (F - WC) are drawn, where the surface pressure is set equal to 0 bar and the subinterface ocean scattering is neglected. The wind speed is 7 m/s for all curves.

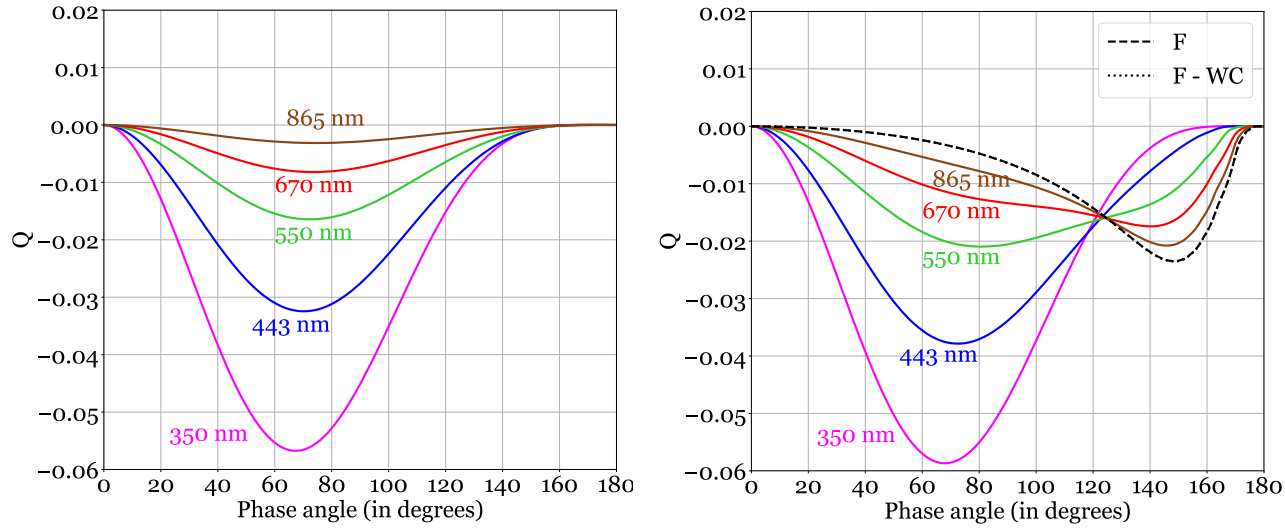

(a) (b)

Figure 7.6: Stokes parameter Q as a function of planetary phase angle α for (a) the Lambertian planet with a gas atmosphere, surface albedo = 0 and (b) the ocean planet with gas atmosphere. Also, the reflected flux from the rough Fresnel interface (F) and rough Fresnel interface without whitecaps (F - WC) are drawn. The wind speed is 7 m/s for all curves. The lines for F and $F-WC$ can hardly be distinguished.

degree of polarization are separated from the symmetrical bell shaped curve of Rayleigh scattering.

Stam (2008) showed that Lambertian surface reflection results in a decrease of the degree of polarization in the phase curve, which is more apparent for higher surface albedos and at long wavelengths where the flux from scattering in the atmosphere is relatively low. In this research, light is also reflected at the bottom of the atmosphere, but because the surface is not a Lambertian surface but a Fresnel reflecting ocean, the light is *not* heavily depolarized in the red part of the visible spectrum. Hence, the order of the degree of polariza-

tion phase curves for the particular wavelengths, with the highest polarization at 865 nm, is similar to this order for the Lambertian planet with 0 surface albedo. The degree of polarization phase curves of the ocean planet (Figure 7.5a) could therefore be confused with the degree of polarization phase curves of the Lambertian planet (Figure 7.5a). However, the degree of polarization is not a measure of the polarized flux. That is, although the degree of polarization phase curves of Figure 7.5a and 7.5b do not seem to differ much except of the shifted peak, the actual polarized flux at long wavelengths differs significantly, as we will explain below.

In Figure 7.6a and Figure 7.6b we plot the polarized flux, in terms of the Stokes parameter Q, for the Lambertian and ocean planet respectively, both again with a gaseous atmosphere in hydrostatic equilibrium.[3] Note the increased polarized flux at long wavelengths at phase angles between 90° and 180°. The order of the phase curves for the particular wavelengths is reversed at approximately $\alpha = 122°$ for the ocean planet, which is not the case in the phase curves of the Lambertian planet. This reversal of 'polarized flux colors' seems to be a better candidate for the characterization of a cloud-free ocean planet than the increased reflected flux at big phase angles because the increased reflected flux at big phase angles may be also caused by the increased domination of reflection from the poles (if present) at crescent phase (Cowan et al. 2012) or by clouds (Section 7.2.5). Also, the intersection of the phase curves for the different wavelengths in Q occurs at $\alpha = 122°$ whose observability may be less limited by the inner working angle of the telescope compared to the intersection in the flux, which occurs around $\alpha = 135°$. The reversal of polarized flux colors seems also to be a better candidate for the characterization of a cloud-free ocean planet than the shift of the polarization peak towards higher phase angles first found by Zugger et al. (2010), because as explained above the high degree of polarization at long wavelengths for the ocean planet may be confused with the high degree of polarization at long wavelengths due to single scattering in the atmosphere above a dark Lambertian surface, while the polarized flux represented by Q differs significantly. That is, in both Figure 7.5a and 7.5b the shift of the peak cannot be detected for 350 nm, 443 nm and 550 nm, but the intersection in Q is clearly visible for these wavelengths in Figure 7.6b while it is absent in Figure 7.6a.

7.2.2. Effect of Ocean Color

In Figure 7.4b it was shown that the planetary phase curve of the reflected flux by the ocean planet was increased at small phase angles compared to the Lambertian planet, in particular at shorter wavelengths. In this section we will compare the results of the former section with a planetary phase curve where a black ocean is assumed in order to investigate the contribution of the ocean color to this increased reflected flux.

The solid lines in Figure 7.7a are the flux phase curves employing the complete atmosphere-ocean model using the Rayleigh scattering approximation within the water layer, while the dotted curves are the results when using a Lambertian surface with zero albedo underneath the air-water interface. The blue color of the ocean indeed is responsible for a substantial part of the increased flux at phase angles between approximately 0° and 90° found in Figure 7.4b at short wavelengths. The effect of the ocean color is largest for 443 nm, as expected from Figure 6.1a. In Figure 7.7b the degree of polarization is lower for the blue ocean, caused by the increased disk-integrated flux at the blue wavelengths which is only partly polarized. Zugger et al. (2010) argued that the degree of polarization peak is limited by 'scattering within the water', however, they modeled their subinterface ocean that accounts for the ocean albedo as a Lambertian surface, which depolarizes the underwater light by definition. In Figure 7.7c it is shown that the polarized flux is actually slightly increased at blue wavelengths for the blue ocean when scattering of polarized underwater light is taken into account.

7.2.3. Effect of Wind Speed

In Figure 7.8a the flux phase curves of the ocean exoplanet are shown for three wind speeds: 1 m/s, 7 m/s and 13 m/s. Recall from Section 5.2 that higher wind speeds cause the glint to be wider. However, the wind speed hardly affects the planetary phase curves between $\alpha = 0°$ and 135°. At short wavelengths, scattering in the atmosphere is too dominant for the glint to be visible, even at big phase angles, which was explained in Section 7.2.1. At long wavelengths, this may be explained by the integration we perform over the planetary disk. That is, although the reflected light from a smooth air-water interface is more intense at certain pixels compared to a rough interface, the amount of glint pixels is smaller because the solid angle of the reflected light is smaller. Approximately the same amount of energy is reflected in the direction of the observer for each of the wind speeds considered.

[3] Because the planets are perfectly symmetrical with respect to the scattering plane, $U = 0$. See also Chapter 1.

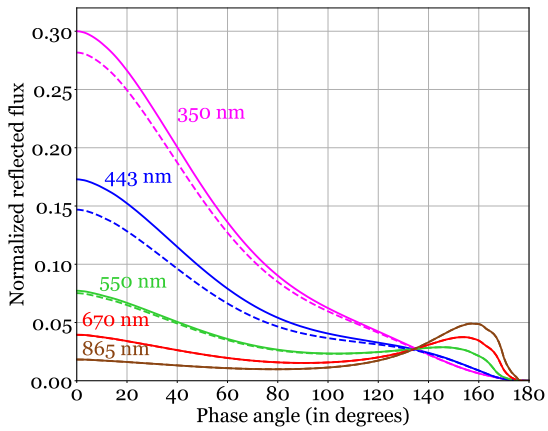

(a)

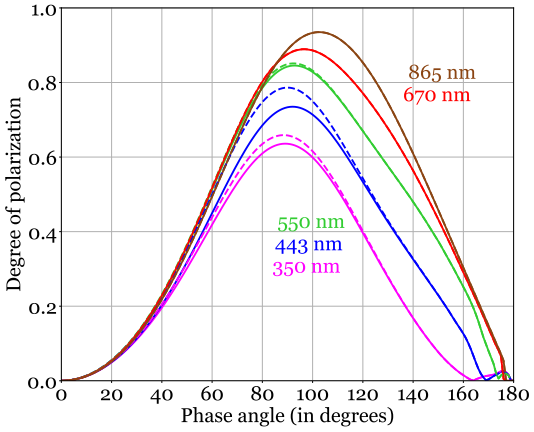

(b)

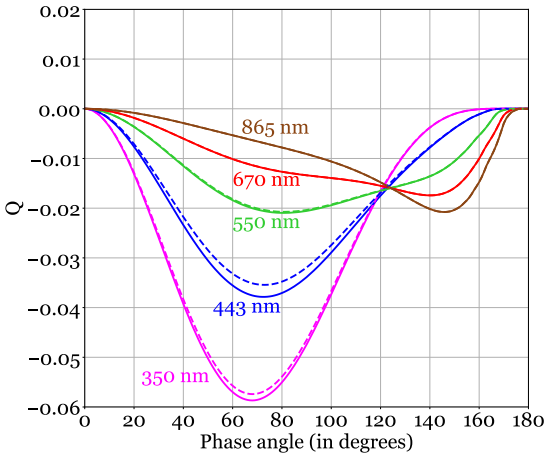

(c)

Figure 7.7: Solid curves: disk-integrated flux (a), degree of polarization (b) and Stokes parameter Q (c) as a function of planetary phase angle α for a homogeneous ocean planet and gas atmosphere. The wind speed is 7 m/s. Dashed curves: similar to the solid curves, but using a black surface underneath the air-water interface instead of a water layer.

The location of the intersection point of the normalized reflected flux in terms of α is independent of the wind speed. At the intersection point the equality of Equation 7.5 holds for all wind speeds considered, while the glint reflectance R_1'' is obviously not invariant with wind speed at the intersection point. However, at low wind speeds the glint is also wider, which results in the same flux when integrated over the illuminated part of the disk.

Between $\alpha \approx 135°$ and 180°, the smaller wind speeds cause the reflection to be more significant. The non-inclined wave facets of an air-water interface at low wind speeds already experience strong Fresnel reflection because of the large phase angle. These optimal reflection geometries are disturbed when the wave facets are randomly inclined in other directions.

Figure 7.8b shows the degree of polarization of the ocean planet at the different wind speeds. At 550 nm, 670 nm and 865 nm the polarization peak is lower for 13 m/s, which may be explained by the increased Lambertian reflection from the whitecaps. The whitecap percentages are $3E^{-4}$%, 0.28% and 2.46% for 1 m/s, 7 m/s and 13 m/s respectively. In order to prove that the depolarization at 865 nm at 13 m/s compared to 7 m/s and 1 m/s indeed is caused by the Lambertian whitecap reflection, we plot the phase curve of the degree of po-

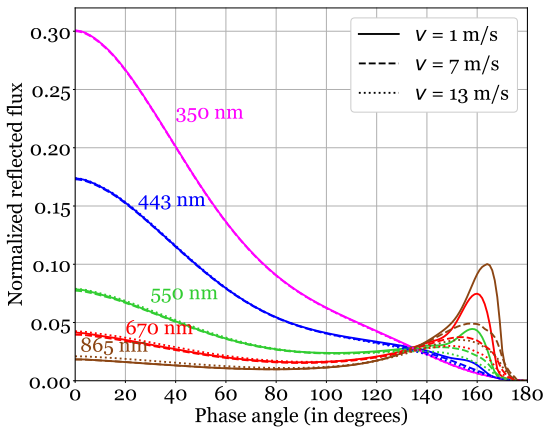

(a)

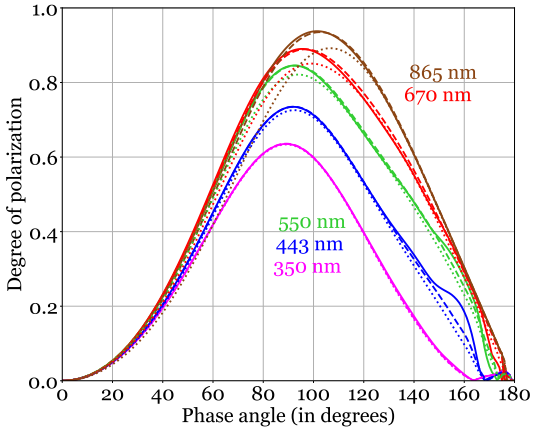

(b)

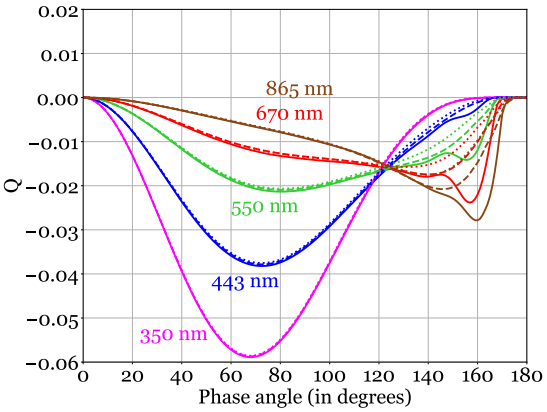

(c)

Figure 7.8: Clear ocean planet: (a), (b), and (c) are the normalized reflected flux, degree of polarization and Stokes parameter Q respectively for the clear ocean planet at the wind speeds 1 m/s (solid curve), 3 m/s (dashed curve) and 7 m/s (dotted curve), presented at 5 wavelengths: 350 nm (purple lines), 443 nm (blue lines), 550 nm (green lines), 670 nm (red lines) and 865 (brown lines).

larization at 13 m/s including (dotted line) and without whitecaps (dashed-dotted line) at 865 nm only, and compare them to 7 m/s including whitecaps (solid line) in Figure 7.9. It can be seen that the disk-integrated normalized reflected flux (Figure 7.9a) is hardly affected by the whitecaps at v = 13 m/s. A small increase for the case including whitecaps may be observed at $\alpha < 100°$ which increases with decreasing α and can be attributed to the additional reflected flux from the Lambertian whitecaps at these small phase angles where the area of the illuminated disk outside the glint region is relatively large. However, this difference is less than 0.01. The decrease of the degree of polarization at 13 m/s with respect to 7 m/s as observed in Figure 7.8b may indeed be explained by the increased whitecap fraction at v =13 m/s, because if there would be no whitecaps (dashed-dotted line) the peak of the degree of polarization phase curve would shift up again towards 0.935 at $\alpha = 103°$. In Figure 7.9c it can be seen that the Stokes parameter Q is hardly affected by the whitecaps when using this scale for the Q-axis in the graph.

In Section 6.1 it was mentioned that the foam albedo of Koepke (1984) has a significant uncertainty of ±0.11. Therefore, we also plot the phase curve using a foam albedo of 0.33 (dashed curve) instead of 0.22, which may be considered as the upper limit of depolarization caused by the whitecaps. In Figure 7.9b it is shown that indeed the peak of the degree of polarization is lower when using a_{foam} = 0.33. We do not consider the lower limit of a_{foam} = 0.11, since it cannot be claimed that this would be actually the lower limit. Recall that we assumed the foam to be a Lambertian reflector and therefore a perfect depolarizer, as suggested in many papers (e.g. Chowdhary et al. 2006; Williams and Gaidos 2008; Zugger et al. 2010). Ideally, the foam reflectance

should be described with a proper scattering matrix for seafoam, which may possibly not result in 100% depolarization. Thus, for the Lambertian approach we can only do an estimate as presented in this section of the *maximum possible* depolarization by the whitecaps if the foam would indeed depolarize perfectly. In what follows, we will again continue with the often used mean value of $a_{foam} = 0.22$, but the uncertainty in the degree of polarization phase curves at long wavelengths should be noted. Another property of Lambertian surface reflection is its equal reflectance in all hemispherical directions. Indeed, in the discussion above it is assumed that the reflectance by the foam is equal in all hemispherical directions.

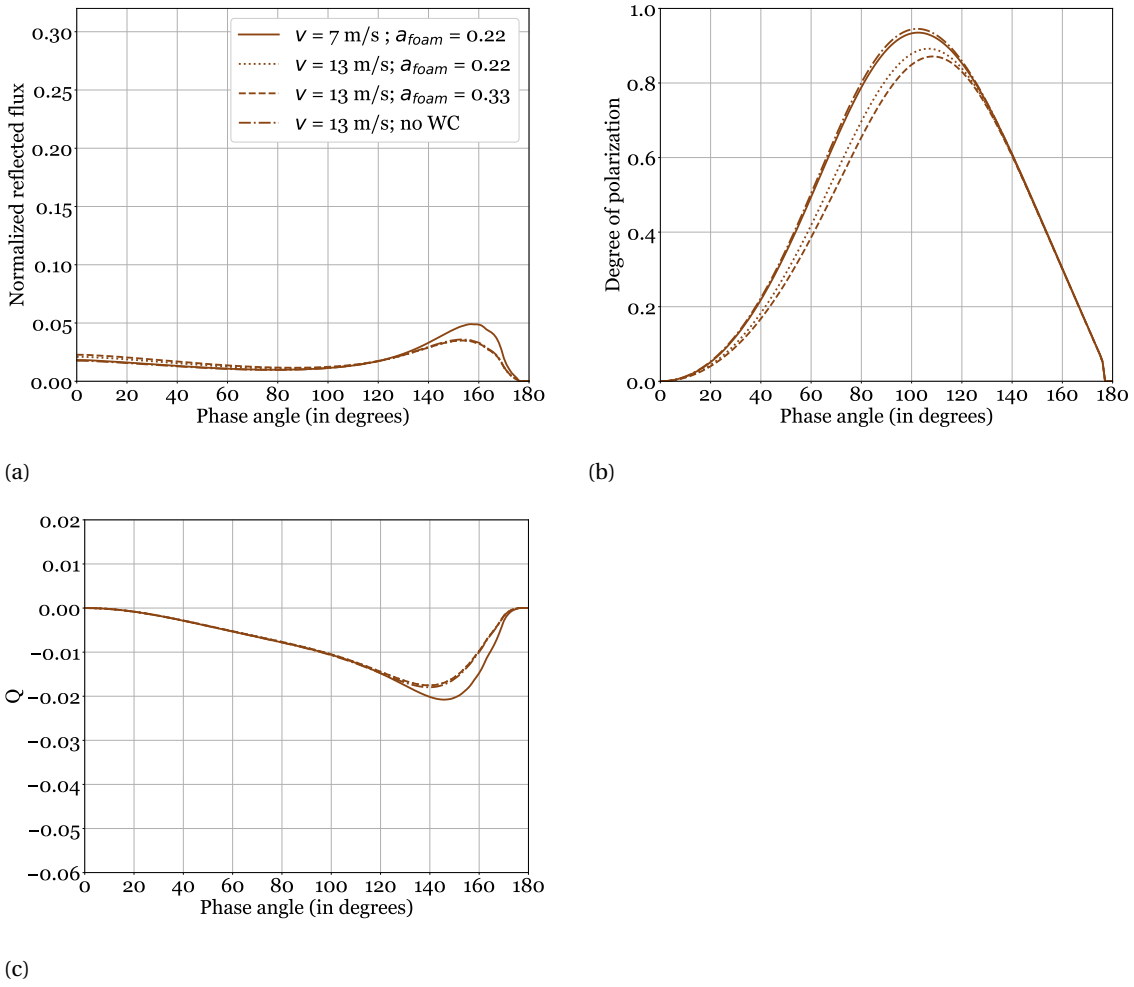

Figure 7.9: Effect of the whitecaps at 865 nm. Solid curves: disk-integrated flux (a), degree of polarization (b) and Stokes parameter Q (c) as a function of planetary phase angle α for a homogeneous ocean planet and gas atmosphere. The solid curves and dotted curves are also found in Figure 7.8b and are for $v = 7$ m/s and 13 m/s respectively. The dashed curves is for $v = 13$ m/s where we change the foam albedo of the whitecaps to 0.33 (for studying the case when the uncertainty of the foam albedo given by Koepke (1984) is added). The dashed-dotted curve is for $v = 13$ m/s where we set the whitecap percentage equal to 0%.

Finally, we note that, in the absence of whitecaps and for a thin atmosphere, the degree of polarization is independent of wind speed, which causes the location of the polarization peak at two times the Brewster angle to be independent of wind speed. This may be explained by the fact that the probability distribution of Cox and Munk (1954, 1956) for the wave slope inclinations, and the corresponding geometry terms, are multiplied with the Fresnel reflection matrix to obtain the reflection matrix for polarized light of the interface. This redistribution of the wave facets thus influences the reflected flux, but not the degree of polarization since all these terms are eliminated by division (cf. Equation 5.33). Physically, this means that the polarized flux from an inclined wave facet may differ compared to a non-inclined facet, but since the total flux is lower in this viewing geometry the degree of polarization is unaffected (see Figure 5.13).

7.2.4. Effect of Surface Pressure

In the former sections, the surface pressure, p_s, was assumed to be 1 bar. However, it is reasonable to consider planets with surface pressures that differ from 1 bar, since there is no evidence that the Earth's atmospheric pressure has always been 1 bar in the history of planet Earth, nor that surface pressures of oceanic exoplanets are constrained to 1 bar. In this section we will present the planetary phase curves of the cloud free ocean planets with a surface pressure of 0.5 bar, 5 bar and 10 bar respectively. The wind speed equals 7 m/s. The corresponding boiling temperature, i.e. the approximate maximum atmospheric surface temperature for an oceanic exoplanet, can be determined from the phase diagram for liquid water. The Clausius-Clapeyron relation may be used to compute the boiling temperature of water, T^*, at a certain pressure p^*, when it is written in the form:

$$T^* = \left[\frac{R}{L_s} \ln \frac{p_0}{p^*} + \frac{1}{T_0} \right]^{-1} \tag{7.6}$$

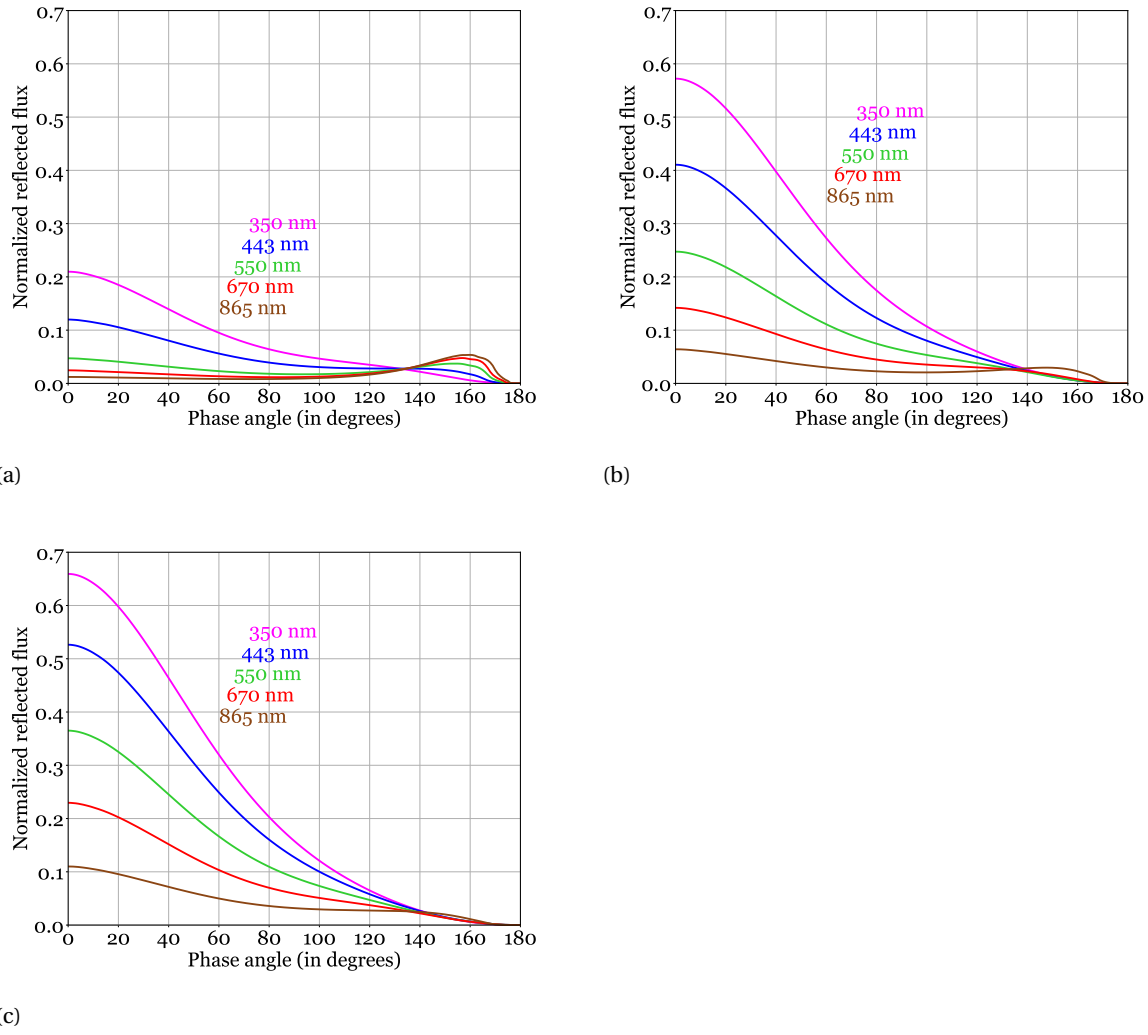

Figure 7.10: Planetary phase curves of the normalized reflected flux by the clear ocean planet for a surface pressure of (a) 0.5 bar, (b) 5 bar and (c) 10 bar at 5 wavelengths.

where $R = 8.3145$ J mol^{-1} K is the gas constant, $L_s = 40700$ J mol^{-1} is the latent heat for water and $T_0 = 373$ K and $p_0 = 1$ bar are the standard surface temperature and pressure. The boiling temperatures at 0.5 bar, 5 bar and 10 bar are then respectively 354 K (81 °C), 425 K (152 °C) and 452 K (179 °C). Consequently, the extension of the habitable zone, i.e. the distance from the star where liquid water can exist, may depend on surface pressure. An attempt to estimate the habitable zone dependency on surface pressure has been made already

by Vladilo et al. (2013), who found an increase of the habitable zone of 0.25 AU with an increasing surface pressure from 1/3 bar to 3 bar, for planets with an Earth-like atmospheric composition.

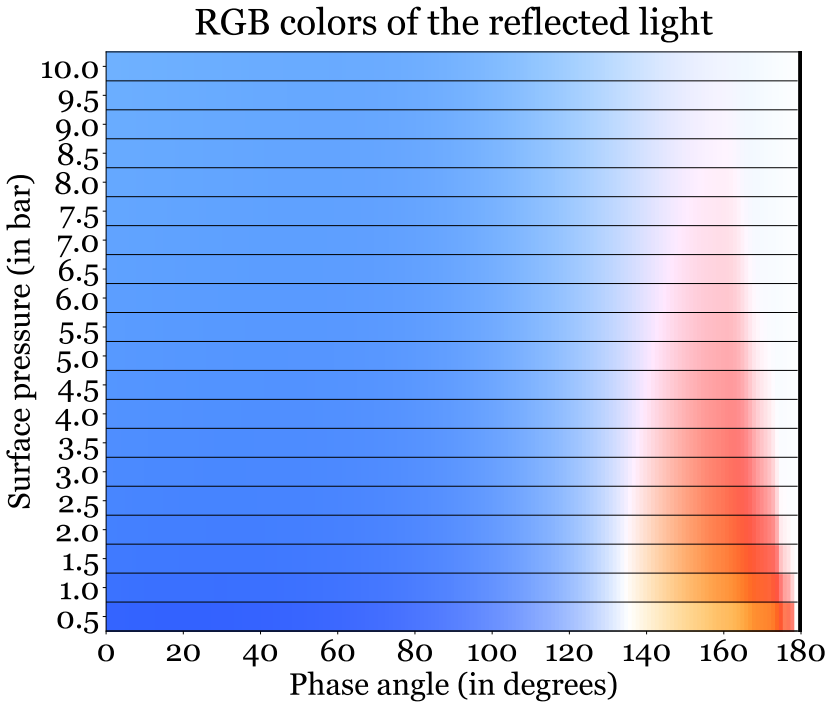

Figure 7.11: RGB colors of the reflected light by the clear ocean planet for surface pressures varying between 0.5 bar and 10 bar in steps of 0.5 bar. The white color at $\alpha \approx 135°$ corresponds to the intersection point of the phase curves for different wavelengths as observed in Figure 7.10. With increasing surface pressure, the planets start to have a white color at the full range of large phase angles.

Figure 7.10a, 7.10b and 7.10c show the planetary phase curves of the normalized reflected flux reflected by the clear ocean planet with a surface pressure of 0.5 bar, 5 bar and 10 bar respectively. As the scattering optical thickness of the gas, b^m_{sca}, in our model scales with the column density of the gas molecules and the vertical pressure difference in the atmospheric layer (see Equation 2.7), the Rayleigh scattering intensity of the gaseous atmosphere decreases with decreasing surface pressure. This explains why the magnitude of the normalized reflected flux at a surface pressure of 0.5 bar (Figure 7.10a) is smaller at all wavelengths compared to the similar graph for a surface pressure of 1 bar (Figure 7.8a), 5 bar and 10 bar at small phase angles where the atmospheric Rayleigh scattering dominates the reflection by the ocean. Recall from Section 7.2.1 that at small phase angles the Fresnel reflection is weak. At large phase angles the reflected flux in Figure 7.10a at all wavelengths intersect again at $\alpha = 135°$. The color reversal becomes weaker with increasing surface pressure (see Figures 7.10b and 7.10c), which may be explained by the fact that for a high surface pressure, the light at long wavelengths is also not able to travel to the air-water interface and subsequently reach the TOA again. Note that the path length of the light at these large phase angles is already relatively long, and the attenuation is increased at higher surface pressures due to the higher scattering optical thickness. Consequently, the planet appears white at these large phase angles and this 'whitening' increases with increasing surface pressure.

The RGB colors of the ocean planet for α between 0° and 180° and surface pressures varying from 0.5 bar to 10 bar are plotted in Figure 7.11.[4] In this figure the increased whitening of the planet with increasing surface pressure is apparent. Note that, in the absence of a color reversal, a *false negative* for the presence of an ocean may be found when the surface pressure is higher than 10 bar if only the reflected flux would be analyzed, because there was also no color reversal found for a Lambertian planet already at a surface pressure of 1 bar.

[4]The RGB colors are computed using weighted additive color mixing of the phase curves at $\lambda = 443$ nm (blue), $\lambda = 550$ nm (green) and $\lambda = 670$ nm (red), such that for an equal measured flux at these wavelengths the mixed signal is perfectly white.

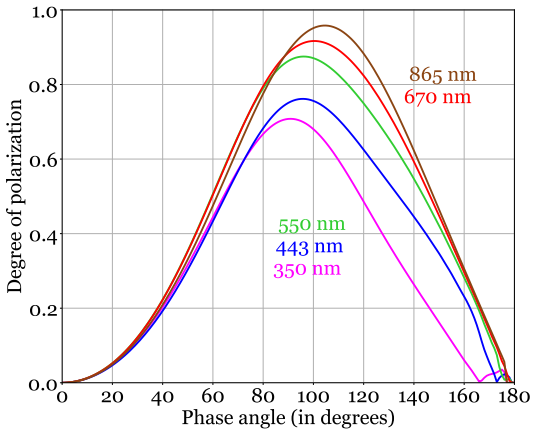

(a)

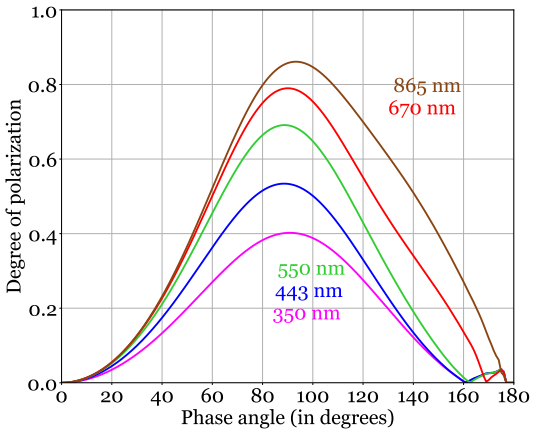

(b)

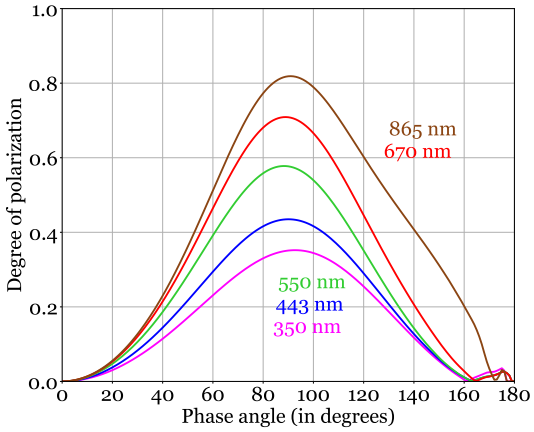

(c)

Figure 7.12: Planetary phase curves of the degree of polarization of light reflected by the clear ocean planet for a surface pressure of (a) 0.5 bar, (b) 5 bar and (c) 10 bar at 5 wavelengths.

Figures 7.12a, 7.12b and 7.12c show the planetary phase curve of the degree of polarization of starlight reflected by the clear ocean planet with a surface pressure of 0.5 bar, 5 bar and 10 bar respectively. Figures 7.13a, 7.13b and 7.13c are the corresponding graphs for the Stokes parameter Q. The following features may be observed:

- The degree of polarization generally decreases with increasing surface pressure, which may be attributed to the increase of multiple scattering by the gas with increasing scattering optical thickness of the gas. Recall that this scattering optical thickness also increases with decreasing wavelength according to $1/\lambda^4$. This explains, for example, why the shape of the phase curve of the degree of polarization at 550 nm at 5 bar surface pressure (Figure 7.12b) is approximately similar to the shape of the curve at 670 nm at 10 bar surface pressure (Figure 7.12c).

- The shift of the peak of the degree of polarization towards two times the Brewster angle ($\alpha = 106°$) with increasing wavelength, which was observed for 1 bar surface pressure, cannot be detected anymore for surface pressures of 5 bar and 10 bar.

- With increasing surface pressure and decreasing wavelength, the phase curves of the degree of polarization start to follow the bell shaped curve of Rayleigh scattering again that is symmetrical about $\alpha \approx 90°$. At 10 bar, only the degree of polarization of the disk-integrated light at 865 nm seems to be significantly

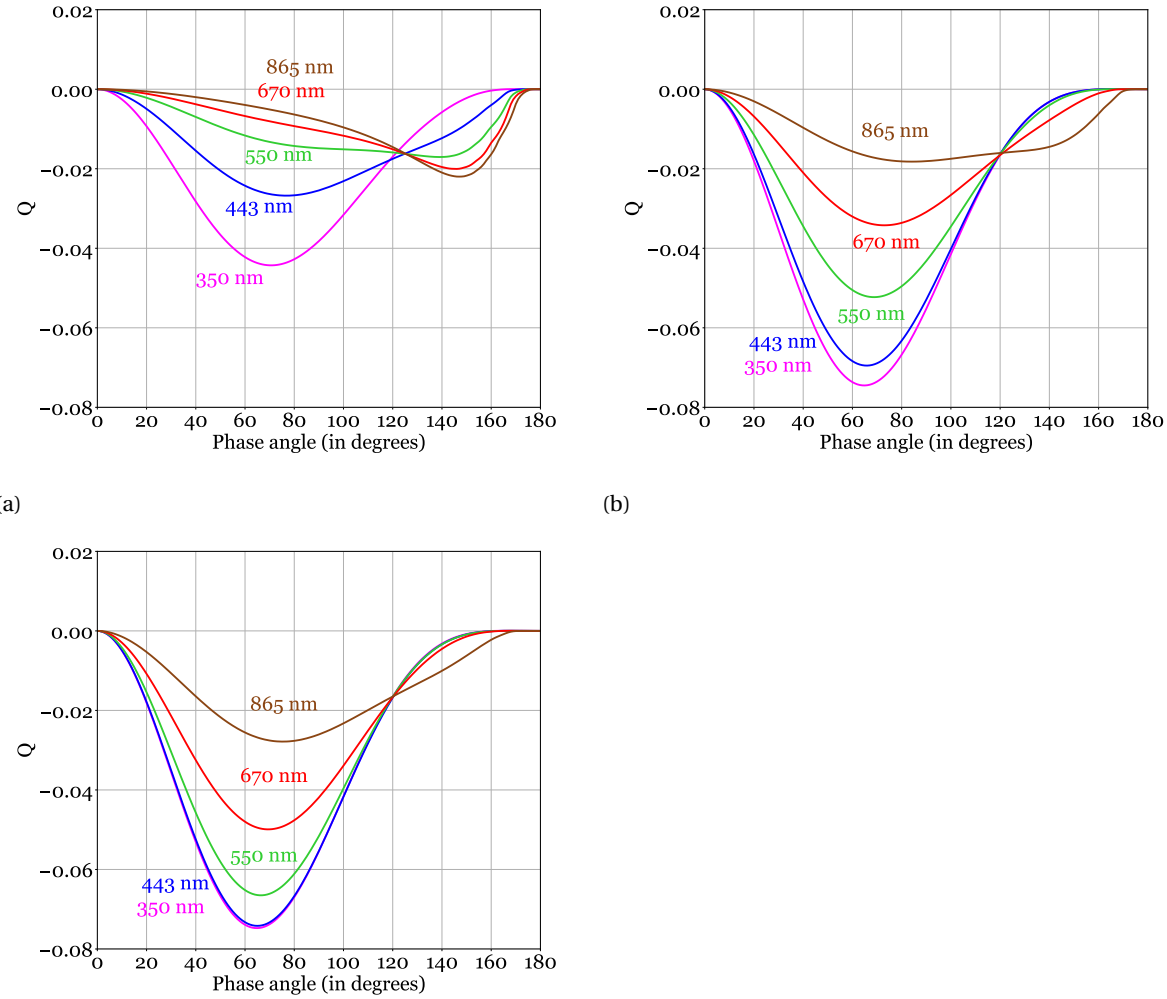

(a)

(b)

(c)

Figure 7.13: Planetary phase curves of the stokes parameter Q of light reflected by the clear ocean planet for a surface pressure of (a) 0.5 bar, (b) 5 bar and (c) 10 bar at 5 wavelengths.

affected by the Fresnel reflection, which is the only curve that is clearly separated from the others at $\alpha > 120°$. The separation of the phase curves at these large phase angles thus remains visible at $p_s = 5$ and 10 bar, while the shift of the polarization peak does not. This separation of phase curves, together with the color analysis of the planet in the reflected flux, could help estimating the surface pressure on the ocean planet. Note that we do not yet introduced clouds and that we only may conclude this for the clear ocean planet. However, in Section 7.3.1 we will show that, in case of patchy clouds, for a surface pressure of 1 bar, the cloudy ocean planet starts to follow the clear ocean phase curves again, where the separation of the phase curves is again visible. We will see that the phase angle at which this separation is visible again depends on the cloud fraction or substellar cloud size.

- The intersection point in the Stokes parameter Q caused by Fresnel reflection remains visible and its location at $\alpha \approx 120 - 122°$ is hardly affected (only a small shift towards $\approx 122°$ may be observed at a surface pressure of 0.5 bar). It should be noted, however, that the intersection at 10 bar is only apparent due to the inclusion of 865 nm in the graph.

From the discussion above, it is reasonable to conclude that the increase of the wavelength range increases the detectability of the intersection point in the Stokes parameter Q and therefore increases the chance of detecting ocean planets, assuming these ocean planets may have a surface pressure that differs from 1 bar. Also, we showed that the intersection in Q remains visible at surface pressures up to 10 bar, contrary to the shift in

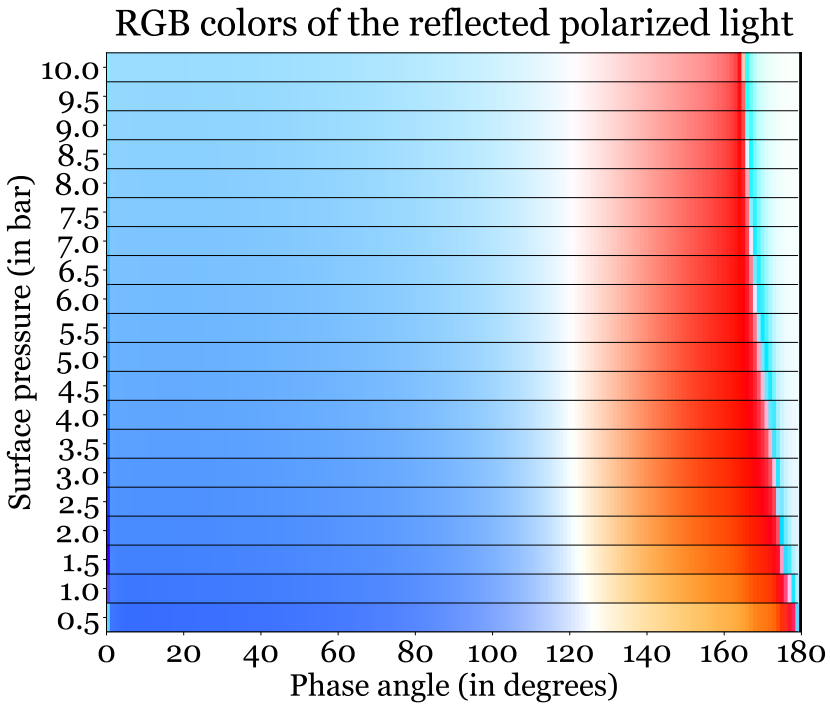

Figure 7.14: RGB colors of the polarized reflected light in terms of $|Q|$ by the clear ocean planet for surface pressures varying between 0.5 bar and 10 bar in steps of 0.5 bar. The white color at $\alpha \approx 120° - 122°$ corresponds to the intersection point of the phase curves for different wavelengths as observed in Figure 7.13. With increasing surface pressure, the location of this intersection point is unaffected.

the degree of polarization suggested by Zugger et al. (2010) which already disappeared at 5 bar, provided that measurements at short or moderate wavelengths in the visible domain are combined with measurements in the near-infrared.

Figure 7.14 shows the RGB colors of the polarized reflected light in terms of the magnitude of the Stokes parameter Q. The white color at $\alpha \approx 120° - 122°$ corresponds to the intersection point of the phase curves for different wavelengths as observed in Figure 7.13. It may be observed that, with increasing surface pressure, the location of this intersection point is unaffected. However, from the analysis of Figure 7.13 we again emphasize that the required measurement accuracy at the different wavelengths would need to increase with increasing surface pressure, or that measurements at a longer wavelength are required.

7.2.5. Cloudy Ocean Planet

In the former section it was shown that the ocean on an exoplanet manifests itself in the planetary phase curves as an increased reflected flux at large phase angles and long wavelengths, a shift of the polarization peak towards two times the Brewster angle with increasing wavelength and as the reversal of the order of the wavelengths in Q with an intersection point at a phase angle around 122°. In this section we will investigate whether these features are still visible when the exoplanet is covered with a homogeneous cloud deck above the ocean. The specification of the clouds are listed in Table 7.2.

Spherical cloud droplets are assumed which allows us to use the Mie algorithm to compute the elements of the aerosol scattering matrix (see Section 2.1.2). We use a two-parameter gamma distribution for the particles (Hansen and Travis (1974)). The real refractive index of the water cloud droplets is assumed 1.33 and we neglect absorption of light by these droplets (i.e. $b^{\mathrm{a}} = b^{\mathrm{a}}_{sca}$ in Section 2.1.3). The cloud optical thickness varies with wavelength because of the wavelength dependence of the droplet's extinction cross-section. In particular, at $\lambda = 350$ nm, $b^{\mathrm{a}} = 4.87016316$ and at $\lambda = 865$ nm, $b^{\mathrm{a}} = 5.00155958$, which we obtained by linearly scaling b^c with the droplet's extinction cross-section assuming a constant column density of the cloud particles. The effect of particle size distribution and optical thickness of the clouds will not be treated in this study because it has already been studied by Karalidi et al. (2011, 2012). Note that these studies did not include an

Table 7.2: Parameters of the clouds. Unless stated otherwise, the values listed in this table are used in the cloudy atmosphere models.

Cloud Parameters	Symbol	Value
Cloud particle effective radius [μm]	r_{eff}	10.0
Cloud particle effective variance	v_{eff}	0.1
Cloud optical thickness (at $\lambda = 858$ nm)	b^{a}	5.0
Cloud-top pressure [bar]	p_{ct}	0.7
Cloud-bottom pressure [bar]	p_{cb}	0.8

ocean underneath the clouds, but knowledge about the expected dependency of the scattered light by clouds on varying size distributions and optical thicknesses can be retrieved from these papers. We will also not vary the influence of varying cloud-top pressure, which was already done by Rossi and Stam (2017), albeit for clouds above a flat air-water interface yielding an infinitely narrow beam of reflected light representing the stellar glint.[5]

In Figure 7.15a the phase curves of the reflected flux are shown for the cloudy ocean planet at three wind speeds. For comparison, the phase curves for a cloudy Lambertian planet with a surface albedo of 0 are also given.

The following features may be observed :

- At all wavelengths the normalized reflected flux of the cloudy ocean planet for α between approximately 0° and 110° is higher than the cloudy Lambertian planet.
- The order of the wavelengths in the phase curves of the reflected flux reverses at $\alpha = 110°$, for both the cloudy ocean and cloudy Lambertian planet, due to Rayleigh scattering above the clouds. Analogous to the discussion in Section 7.2.1, the longer wavelengths are reflected by the clouds and reach the TOA more easily because of the 'thinner' gas layer above the clouds at the longer wavelengths.
- The phase curves for the reflected flux from the cloudy ocean planet are indistinguishable for the three wind speeds considered.

In conclusion, the reflection by the ocean underneath the cloud deck increases the reflected flux at small phase angles, however, the disk-integrated reflected flux is independent of glint size. At long wavelengths, the phase curves of both the cloudy ocean planet and cloudy Lambertian planet are altered at big phase angles and the phase curves of the different wavelengths intersect. We may conclude that (1) it would be difficult to retrieve the glint through the homogeneous cloud deck and (2) the intersection point is not a characteristic that belongs to the presence of an ocean only. The location of the intersection point, however, could be useful in estimating the cloud cover, as we will show in Section 7.3.1.

Figure 7.15b shows the degree of polarization of the cloudy ocean planet and Figure 7.15c shows the corresponding Stokes parameter Q. The following features may be observed:

- At $\alpha \approx 40°$ a strong increase is found in the degree of polarization and the magnitude of Q and is commonly known as the rainbow feature, which can be explained by geometrical scattering where the light ray is internally reflected once inside the liquid spherical cloud droplets (recall Figure 2.2). The increased polarization occurs where the angle of incidence within the droplet is close to the Brewster angle. The rainbow feature is also visible in the flux, but less apparent. At $\alpha \approx 56°$ a small bump may be observed in the degree of polarization and Q which is a hint of the secondary rainbow, caused by twice internal reflection in the droplet. The occurrence of a rainbow is a well-known indicator of spherical particles in the atmosphere (Bailey 2007; Hansen and Travis 1974; Karalidi et al. 2012). Bailey (2007) showed that a slight deviation of the particle from sphericity would result in a rapid fade out of the rainbow feature. According to Bailey (2007): '*Small liquid droplets are naturally spherical, since surface tension is the dominant force controlling their shape. Scattering from solid particles in an atmosphere is*

[5] An infinitely narrow glint may be scattered in the atmosphere adding some multiple scattering to it, however, the glint has no size and can therefore probably not be captured as a specularly reflected beam by the Gauss points.

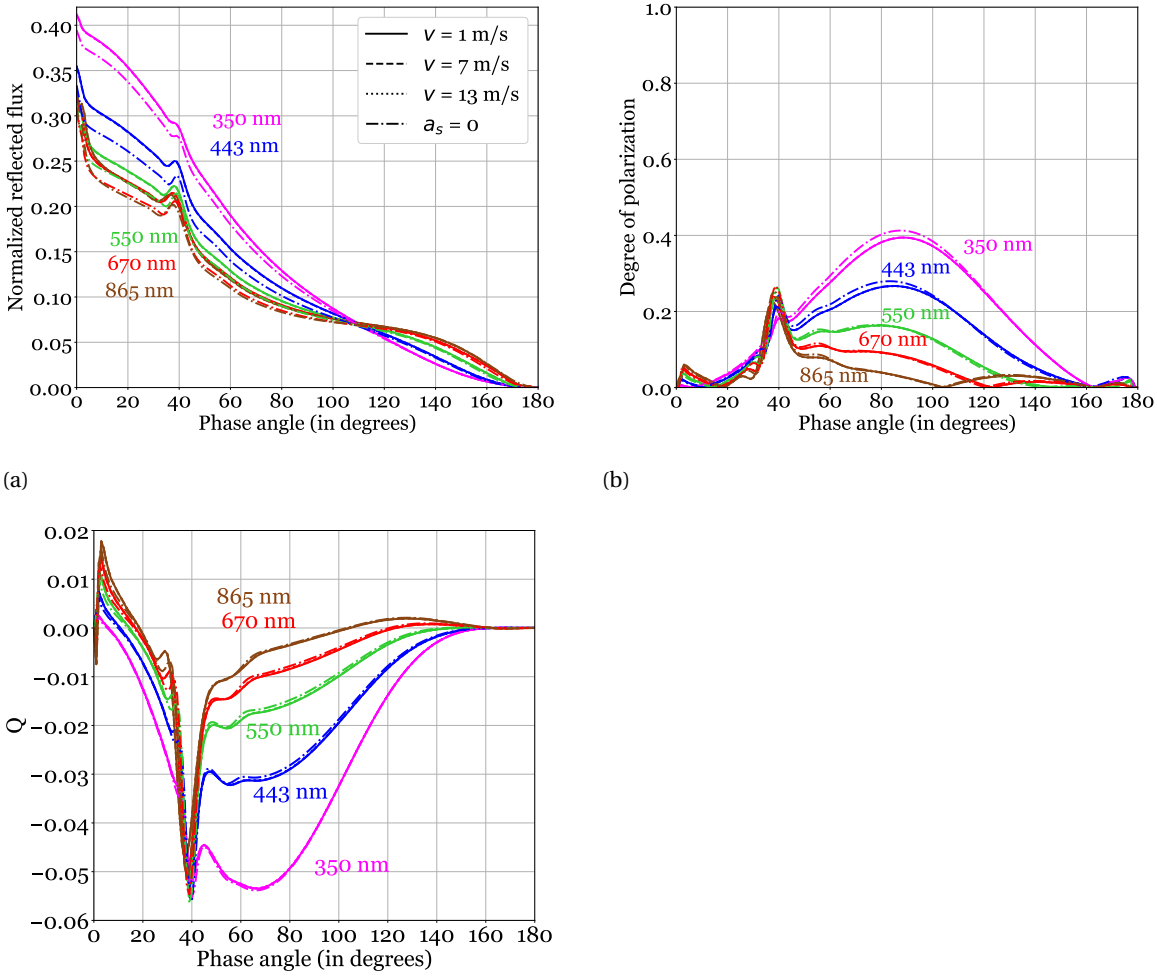

Figure 7.15: Cloudy ocean planet: (a), (b), and (c) are the normalized reflected flux, degree of polarization and Stokes parameter Q respectively where the planet is completely covered with clouds at the wind speeds 1 m/s (solid curve), 3 m/s (dashed curve) and 7 m/s (dotted curve), presented at 5 wavelengths: 350 nm (purple lines), 443 nm (blue lines), 550 nm (green lines), 670 nm (red lines) and 865 (brown lines). Additionally, the phase curves for the Lambertian planet with the same atmosphere are shown (dashed-dotted curve), with a surface albedo of 0.

very unlikely to result in a rainbow, since small size, nonsphericity, absorption, or a combination of these is likely to prevent the occurrence of rainbow scattering.'

- The direction of polarization changes sign with respect to the reference frame at several instances along the phase curves. Since the degree of polarization is a measure between 0 and 1 (i.e. the Stokes parameters were squared in the computation), the sign of the slope of the phase curves changes abruptly at zero degree of polarization.

- The order of the phase curves of the degree of polarization corresponding to a particular wavelength is reversed compared to the degree of polarization of the clear ocean (Figure 7.5b). That is, light in the red part of the visible spectrum is significantly depolarized by the clouds. The low degree of polarization of cloudy planets compared to that of planets with clear atmospheres was explained by Stam (2008) and is caused by (1) the increased multiply scattering of light within the atmosphere due to the cloud particles, which decreases the degree of polarization, (2) the lower degree of polarization of the singly-scattered light by the cloud particles compared to the singly-scattered light by the gaseous molecules and (3) the opposite direction of polarization of light singly-scattered by the cloud particles compared

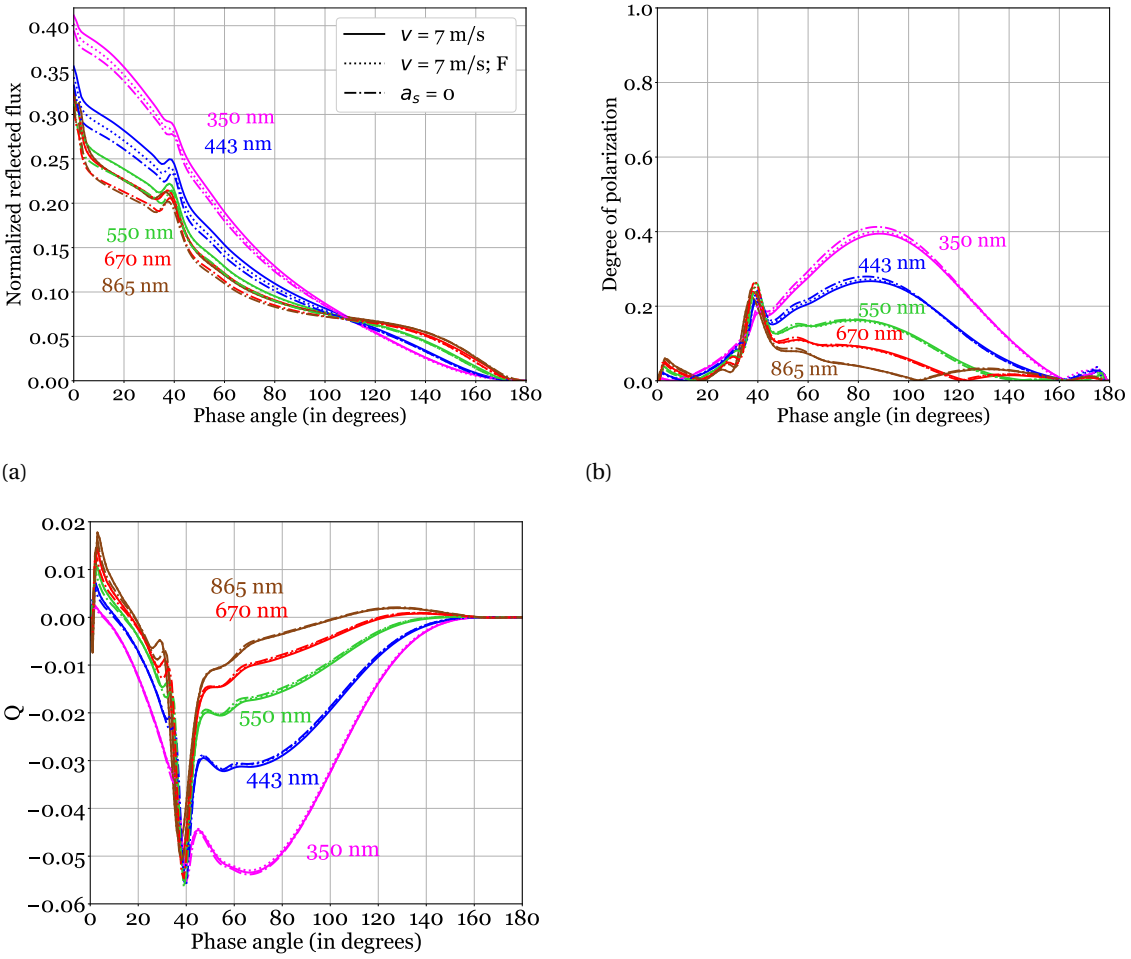

Figure 7.16: Same as Figure 7.15: wind speed 7 m/s (solid line) and when the ocean is replaced by a Lambertian surface (dashed-dotted line). We do not plot the other wind speeds, but instead the phase curve for a wind speed of 7 m/s is plotted again but now without ocean color (dotted line), i.e. the Fresnel interface only, but including whitecaps and the same atmosphere with clouds on top.

to that of the singly-scattered light by the gaseous molecules. Because the molecular scattering optical thickness of the gas is much lower at long wavelengths compared to the cloud optical thickness, almost all the reflected light at 865 nm is reflected by the clouds.

- The degree of polarization at 350 nm, 443 nm and 550 nm of the cloudy ocean planet is less than for the cloudy Lambertian planet, because of the increased diffusely reflected flux at blue wavelengths (cf. Figure 7.7b). However, in Figure 7.15a it can be seen that at 865 nm the reflected flux at small phase angles of the cloudy ocean planet is also higher than the reflected flux at small phase angles of the cloudy Lambertian planet. It is likely that the increased flux and lower degree of polarization at short wavelengths is caused by the extra flux from the color of the ocean, and that the increased flux (but no depolarization) at long wavelengths is caused by glint. We test this hypothesis by a small experiment: we replace the subinterface ocean by a black Lambertian surface in order to distinguish between the glint and ocean color contribution. In Figure 7.16 we plot this phase curve with a dotted line, again next to the curve of the Lambertian planet (dashed-dotted line) and the phase curve of the regular colored ocean (solid line). At λ = 865 nm and 670 nm indeed both the colored and colorless ocean planet models give the same normalized reflected flux, while a flux difference can be observed at the shorter wavelengths. The increased flux at short wavelengths with respect to the Lambertian planet is thus

indeed caused by the glint, as in our hypothesis.[6] The increased flux at short wavelengths is caused by both the ocean color and glint contributions. At short wavelengths, the glint (besides the ocean color) also results in a slightly lower degree of polarization, which may probably be explained by the portion of the glint that is multiply scattered in the gaseous atmosphere and clouds.

- Note that no intersection point in Q is found in Figure 7.15c. Also, there is not shift of the peak of the degree of polarization towards two times the Brewster angle, which was the case for the clear ocean planet in Section 7.2.1.

From this section it may be concluded that all ocean-related planetary phase curve features that were observed for the clear ocean in Section 7.2.1 (i.e. an increased reflected flux at large phase angles compared to small phase angles at long wavelengths[7], a shift of the polarization peak towards two times the Brewster angle with increasing wavelength and the reversal of the order of the wavelengths in Q with an intersection point at around 122°) cannot be detected with a homogeneous cloud deck that is specified by the settings in Table 7.2. Moreover, all phase curves for the cloudy ocean are approximately of a similar shape compared to the cloudy Lambertian planet, meaning that the ocean could not be retrieved.

7.2.6. Effect of Refractive Index

In Section 7.2.1 we saw that the phase curves of the normalized reflected flux reflected by a clear ocean planet intersect for the different wavelengths at a certain phase angle (Figure 7.4b). An intersection of the curves for all wavelengths except 350 nm was also found in the Stokes parameter Q (Figure 7.6b). It was explained that the intersection in a single point could be attributed to the dependency of the atmospheric scattering and attenuation of the stellar light on the scattering optical thickness of the gas that scales with $1/\lambda^4$, while the surface reflection is assumed to be equally intensive at all wavelengths. The latter assumption may, however, affect the intersection point. Recall that we assumed the real refractive index of the ocean water to be constant with wavelength and equal to 1.33, which we found a good approximation since it varies in the visible domain only between 1.328 (at 875 nm) and 1.343 (at 350 nm) (Hale and Querry 1973). The impact of this assumption on the planetary phase curve of the normalized reflected flux, the degree of polarization and Stokes parameter Q, will be discussed in this section.

Figures 7.17a, 7.17b and 7.17c show the phase curves of the normalized reflected flux, degree of polarization and Q respectively for an ocean planet with a black subinterface ocean and a surface pressure of 0 bar. That is, the incident starlight is only reflected by the rough air-water interface. The wind speeds are 1 m/s and 7 m/s. No whitecaps are included. The solutions are shown for the range of the refractive index in the visible domain ($n = 1.33$ and $n = 1.34$), but also for $n = 1.31$, corresponding to a mean value of the real refractive index of water ice in the visible domain (Warren 1984), and for $n = 1.29$, corresponding to a mean value for the real refractive index of liquid methane in the visible domain at a temperature of $\approx 100K$ (Badoz et al. 1992). It may be observed that the phase curves of the flux and degree of polarization are hardly affected when using $n = 1.33$ or $n = 1.34$. The magnitude of the Stokes parameter Q is slightly bigger for 1.34 than for 1.33, which was expected because a larger difference in refractive index of the air and liquid causes a stronger Fresnel reflection, which is mainly visible in the polarized flux. Note the axis of the graph of Q: if we would rescale the axis of the normalized reflected flux graph, a small difference would also be visible for 1.33 and 1.34. We decided not to do so, such that the figures remain consistent throughout the report.

The disturbance of the intersection point in the reflected flux in terms of α, caused by a difference in refractive index of the oceanic water between low and high wavelengths in the visible domain, would be small (<0.5°) and hard to detect in the near future. The degree of polarization peaks at $\alpha = 2\theta_B = 106.1°$ for $n = 1.33$ and at $\alpha = 2\theta_B = 106.5°$ for $n = 1.34$ and is independent of wind speed (see Section 7.2.3). The difference in planetary phase angle near the intersection point of Figure 7.6b, corresponding to a similar value of Stokes parameter Q, would be less than 2°. Thus, only the phase curves for the highest wavelengths in the visible domain may

[6] The alert reader may notice that, if the degree of polarization stays approximately equal at long wavelengths, Q should have increased as well. A small increase of the absolute magnitude of Q indeed occurs compared to the Lambertian planet at long wavelengths (most visible around $\alpha = 30°$), however the values of Q are relatively small and the division by a small number in the computation of the degree of polarization results in a relatively large effect.

[7] Note that there is an increase a long wavelengths in Figure 7.15a, but this would not directly appear as a false positive for the glint since for long wavelengths at small phase angles the phase curves of the clear and cloudy ocean significantly differ, unless only measurements at big phase angles are done. If the cloud cover would strongly vary throughout the orbit of the planet, with e.g. a seasonal dependent cloud cover, a false positive for the glint could possibly occur because of the clouds (not shown in this report).

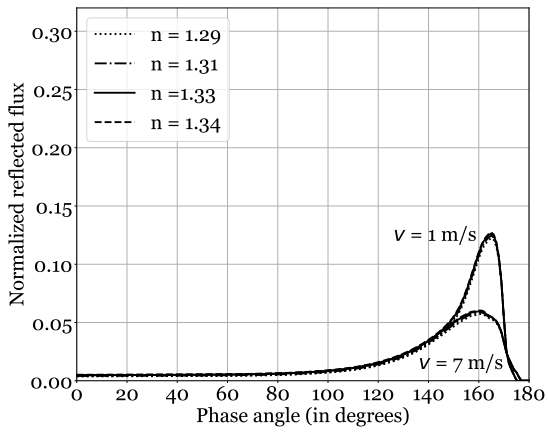

(a)

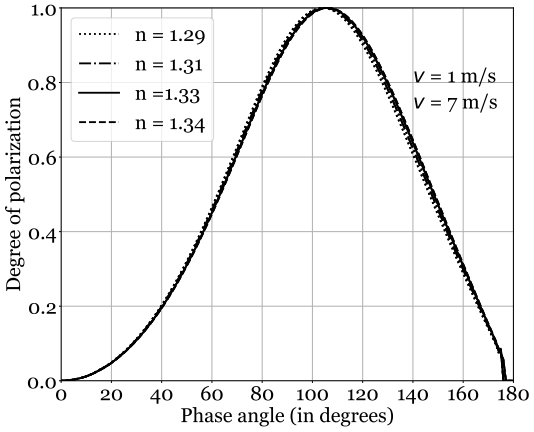

(b)

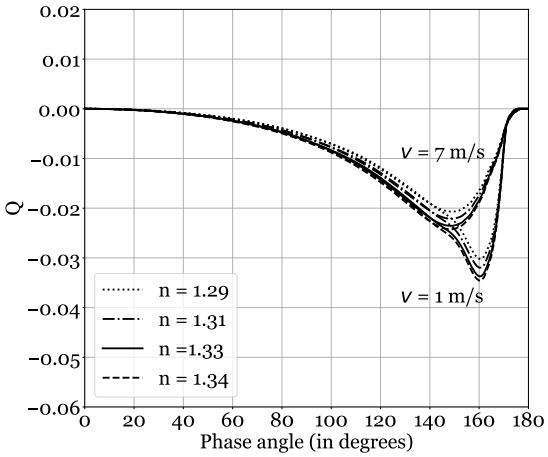

(c)

Figure 7.17: Normalized flux (a), degree of polarization (b) and polarized flux in terms of the Stokes parameter Q (c) for the disk-integrated light reflected by the air-water interface only for a water refractive index of 1.29 (dotted curve), 1.31 (dashed-dotted curve), 1.33 (solid curve), 1.34 (dashed curve) at two wind speeds: 1 m/s and 7 m/s.

show a maximum deviation of about 2°.[8] We may conclude that the assumption of a wavelength independent refractive index of water does not affect our conclusions of the former sections about the approximate location of the intersection point and the order of colors reversal in the phase curves of the normalized reflected flux and Stokes parameter Q.

The medium of the refractive beam may, however, consist of other substances than liquid water. The flux and degree of polarization phase curves corresponding to a refractive index of 1.29 (liquid methane) and 1.31 (water ice) can hardly be distinguished from each other and from the phase curves corresponding to a refractive index of 1.33 and 1.34. The peak polarization of water ice is at $\alpha = 105.3°$ and of liquid methane is at $\alpha = 104.4°$. The changes in Stokes parameter Q seems to be more apparent, however, the smaller scale of the Q-axis of Figure 7.17c compared to the normalized reflected flux axis of Figure 7.17a magnifies these differences. When interpreting the curves for $n = 1.31$ and $n = 1.29$ we should remember the following:

- A surface roughness corresponding to a wind speed of 1 m/s and 7 m/s was assumed. The surface of the water ice planet thus consists of patches having random orientations which are defined by the

[8] Note the air-water interface solution may be considered as the end-member case for an infinitely thin atmosphere and a black ocean (Figure 7.5b), where the Fresnel reflection impact at the TOA is strongest.

Gaussian slope distribution and standard deviation that belongs to water facets ruffled by these wind speeds. The ice planet is thus not a perfect sphere but the surface is roughened.

- It would be challenging to distinguish between Fresnel reflection by water and by water ice only from the inspection of planetary phase curves. However, Fresnel reflection from an icy planet may only occur when this ice is clean and free of dust, snow, rocks or other substances.

- We may conclude that Fresnel reflection from a methane ocean can hardly be distinguished from Fresnel reflection from a water ocean from the inspection of the phase curves of the normalized reflected flux and degree of polarization. Note that we did not model an atmosphere on top of the methane ocean, since our atmosphere is Earth-like which may not be appropriate for the methane planet with a methane-based meteorological cycle. There seems to be some difference in Q, however, these differences are not more apparent than the differences in the reflected flux, but are magnified due to the scale of the Q-axis of the graph.

- We did not take into account the wave slope inclinations dependency on the viscosity of liquid substance (Ghafoor et al. 2000; Lorenz et al. 2010). The phase curves for $n = 1.29$ presented in this section may thus be interpreted as theoretical curves that show the influence of the refractive index only. Recall from Section 7.2.3 that, since the location of the intersection point in the flux and Q is not affected by wind speed, it may be expected that the location of the intersection point will not change with viscosity if the reflected light by a realistic methane planet with an appropriate atmosphere would be modeled. This, however, remains to be shown.

- Zugger et al. (2010) already mentioned that, despite the approximately similar reflection properties of water and liquid methane, the detection of a Fresnel reflecting planet combined with knowledge about the equilibrium temperature derived from the orbital period of the planet and the star's luminosity could help distinguishing between these liquids, since at a surface pressure of 1 bar the boiling point of liquid methane is below 112 K (compared to 373 K for water). If the planet would have a meteorological cycle similar to the water cycle on Earth, knowledge about the nature of the cloud droplets could help characterizing the liquid. That is, the location of the rainbow feature at $\alpha \approx 40°$ for water cloud droplets would shift towards bigger phase angles if the cloud droplets are made of methane and have a similar size distribution (Bailey 2007). The location of the rainbow feature on the planetary phase curve cannot be used for a unique retrieval of the liquid of the spherical droplets, since more liquids may have the same refractive index. However, the observation of a rainbow feature at $\alpha \approx 40°$, together with the detection of the absorption band of water vapor from the analysis of the spectrum, could be a strong indicator of a hydrological cycle rather than a methane cycle. This would increase the likelihood that the ocean, or the clear ice, is made out of water instead of methane.

7.3. Horizontally Inhomogeneous Planets

Each pixel on the planetary disk of a cloud free planet observed at a certain phase angle uniquely contributes to the disk-integrated flux and polarization because it has its own illumination and viewing geometry and consequently, for the ocean planet, the pixel may lie either inside or outside the glint region. If some of these pixels would be overcasted by clouds, while others are not, the shape of the planetary phase curve would depend on the configuration of these clouds. It is expected that the glint appearing and hiding behind these *patchy clouds* induces rapid oscillations in the planetary phase curve when the planet rotates around its rotation axis. Additionally, it should be remembered that the phase function of the cloud droplets and the degree of polarization of scattered light by the gas molecules, both strongly depend on the scattering geometry.

In this section the planetary curves of the horizontally inhomogeneous planets will be presented. First, the patchy clouds will be discussed, and thereafter the results are shown for planet models with a substellar cloud, located and fixed at the substellar point, which may be expected for tidally-locked planets. Finally, we investigate whether the phase curves of the patchy cloudy ocean planets may be reproduced by a weighted sum of horizontally homogeneous model planets.

7.3.1. Patchy Clouds

We model the patchy clouds as clouds of varying horizontal shapes randomly located over the planet, whose configuration is determined by the cloud fraction F_c on the full disk and the asymmetry parameters related

to a zonal-oriented pattern similar to that observed on Earth (Rossi et al. 2018).[9] Instead of using a rotating planet, we use a different and randomly chosen cover of patchy clouds at each interval of the planetary phase curve. The cloud covers are thus independent and possible seasonal autocorrelation is ignored. The value for F_c is kept constant for a certain model planet. We present the mean phase curves of the 300 iterations and its variability in terms of its ±1 standard deviation.[10] Cloud cover examples used in the planetary phase curve computations for $F_c = 0.25, 0.50$ and 0.75 are shown in Figure 7.18.

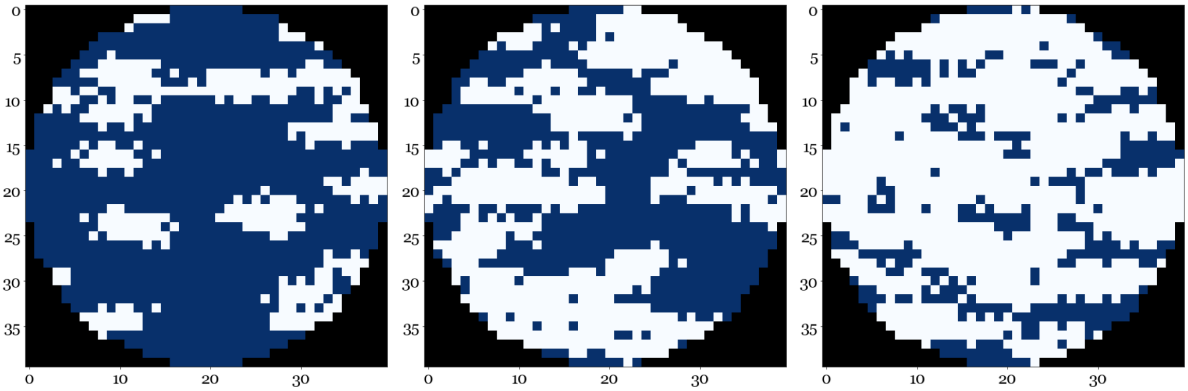

(a) $F_c = 0.25$ (b) $F_c = 0.50$ (c) $F_c = 0.75$

Figure 7.18: Cloud cover examples for three different cloud fractions that are used in the planetary phase curve computations.

The planetary phase curves for the normalized reflected flux by the ocean planets are simulated at three wind speed (v = 1 m/s, 7 m/s and 13 m/s) and three cloud fractions (F_c = 0.25, 0.50 and 0.75). In Figure 7.19 these planetary phase curves are shown for each combination of wind speed and cloud fraction. In the figures in the bottom row of Figure 7.19 the planetary phase curves are shown for the planet with a black Lambertian surface. The following features may be observed:

- With decreasing wind speed the variability in the reflected flux at big phase angles increases because, at low wind speeds, the narrow glint may be either free of clouds or be completely overcasted. Because the air-water interface at these large phase angles is a stronger reflector than the clouds, in particular at long wavelengths (cf. Figure 7.8a and 7.15a), the disk-integrated reflected flux starts alternating between the visible glint and non-visible glint cases. At higher wind speeds, the chance that the wider glint is either completely cloud free or completely overcasted decreases, simply because of its bigger area, and different patchy cloud configurations above the wide glint, with the same local cloud fraction, will less affect the disk-integrated result.

- For a wind speed of 1 m/s and big phase angles, also the *mean* reflected flux for the 300 iterations at long wavelengths is increased compared to the higher wind speed cases, because we already concluded in Section 7.2.3 that a smaller wind speed allows for stronger Fresnel reflection at this beneficial reflection geometry. Also, the chance of a cloud free glint occurring may expected to be higher at low wind speeds.

- At short wavelengths (λ = 350 nm) the variability in reflected flux is unaffected by the wind speed, because (1) at small phase angles both the reflected flux phase curves of the cloudy and cloud free ocean planets are independent of wind speed (Section 7.2.3 and 7.2.5), and (2) at large phase angles, the glint is not visible at in the disk-integrated flux at 350 nm, because the effective Rayleigh scattering in the atmosphere (cf. Figure 7.8a).

- With increasing cloud fraction, the disk-integrated reflected flux at small phase angles increases at all wavelengths. Near the intersection point ($\alpha \approx 110° - 130°$) only the flux at long wavelengths (λ = 550 nm, 670 nm and 865 nm) is still increased due to the increased cloud fraction. This may be explained by the long path lengths at these large phase angles, causing the Rayleigh scattering above the clouds to

[9] We use the default settings of PyMieDAP, which are $x_{scale} = 0.1$ and $y_{scale} = 0.01$.

[10] Its ±2 standard deviation can simply be obtained by multiplying the standard deviation by 2, but is not considered to keep the figures readable.

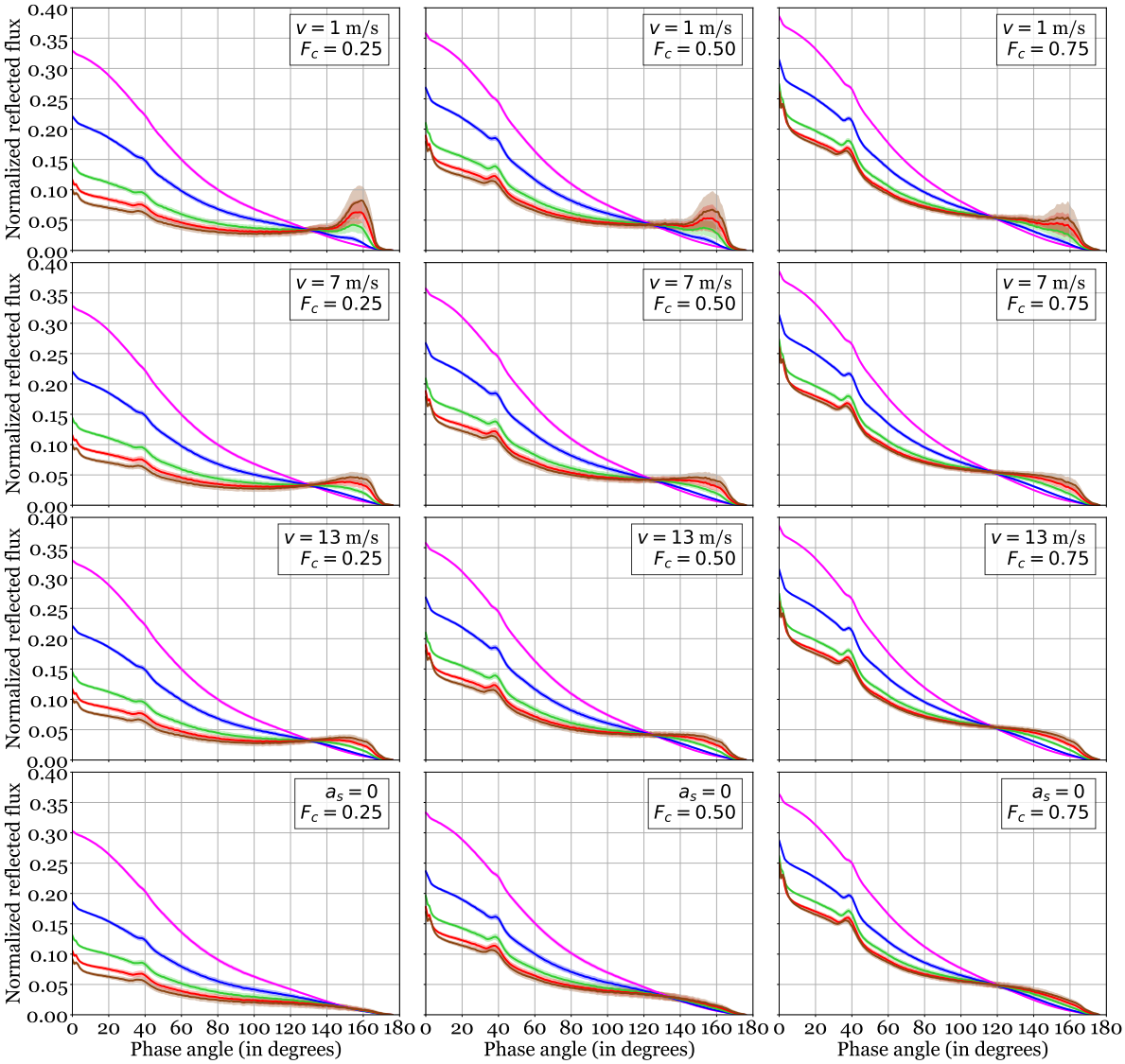

Figure 7.19: Normalized flux of reflected starlight by oceanic exoplanets with patchy clouds for a wind speed of 1 m/s (top row), 7 m/s (second row), 13 m/s (third row) and a Lambertian exoplanet with patchy clouds (bottom row) with zero surface albedo. The cloud fractions are 25% (first column), 50% (second column) and 75% (third column). A surface pressure of 1 bar is assumed. The lines are the mean curves from 300 iterations of cloud configurations randomly chosen at each phase angle and the 1 standard deviation variability is represented by the shaded areas for each of the 5 wavelengths. At full phase ($\alpha = 0^\circ$), the normalized reflected flux is highest for $\lambda = 350$ nm and decreases with increasing λ for all curves.

be dominant at short wavelengths resulting in the cloud-fraction independent disk-integrated flux at these phase angles. Because the light beams of long wavelengths do reach the cloud top or the air-water interface, they are affected by the cloud fraction. This causes the intersection point of the phase curves to shift towards smaller phase angles with increasing cloud fraction. From the end member cases 'clear ocean' and 'cloudy ocean' as discussed in Sections (7.2.3 and 7.2.5) we may expect that the intersection point shifts from $\alpha \approx 135^\circ$ for $F_c = 0.0$ towards $\alpha \approx 110^\circ$ for $F_c = 1.0$.

- The planetary phase curve of the Lambertian planet with a black surface does not show a clear intersection point for $F_c = 0.25$, but instead appears 'white' from $\alpha = 140^\circ$ towards transit ($\alpha = 180^\circ$). With increasing cloud fraction the intersection becomes more visible.

In Figure 7.20 the planetary phase curves of the degree of polarization are shown for each combination of wind speed and cloud fraction. Again, in the figures in the bottom row the planetary phase curves are shown for the planet with a black Lambertian surface. We will simultaneously discuss the planetary phase curves of

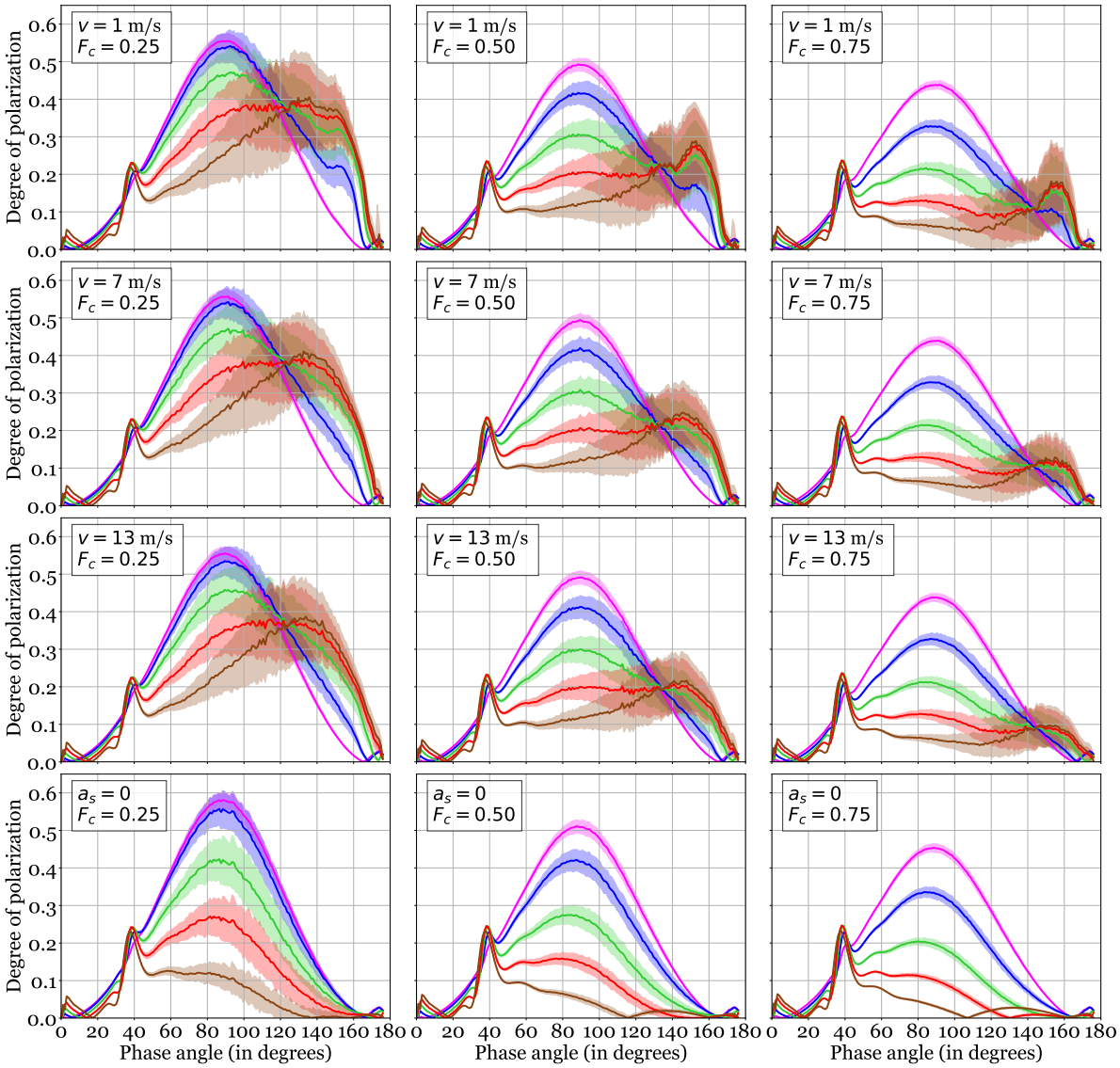

Figure 7.20: Degree of polarization of the reflected starlight by oceanic exoplanets with patchy clouds for a wind speed of 1 m/s (top row), 7 m/s (second row), 13 m/s (third row) and a Lambertian exoplanet with patchy clouds (bottom row) with zero surface albedo. The cloud fractions are 25% (first column), 50% (second column) and 75% (third column). The lines are the mean curves from 300 iterations of cloud configurations randomly chosen at each phase angle and the 1 standard deviation variability is represented by the shaded areas for each of the 5 wavelengths. For $\alpha = 90°$, the mean degree of polarization is highest for $\lambda = 350$ nm and decreases with increasing λ for all curves.

the Stokes parameter Q (Figure 7.20). Let us first analyze the Lambertian planet, where the following features may be observed:

- The degree of polarization generally decreases with increasing cloud fraction, simply because the scattered light from the clouds increases the reflected flux (cf. bottom row of Figure 7.19) but does not necessarily add polarized flux (recall Section 7.2.5), which may be concluded from the plot of the Stokes parameter Q (bottom row of Figure 7.21).

- The variability in degree of polarization decreases with increasing cloud fraction. Rossi and Stam (2017) explained this by the increase of possible locations for the cloudy pixels on the planet. Recall that we define F_c on the full disk, and that the probability that the illuminated part of the disk is completely cloud-free increases with decreasing F_c.

- The order of the wavelengths is preserved for both the degree of polarization and Q at all phase angles,

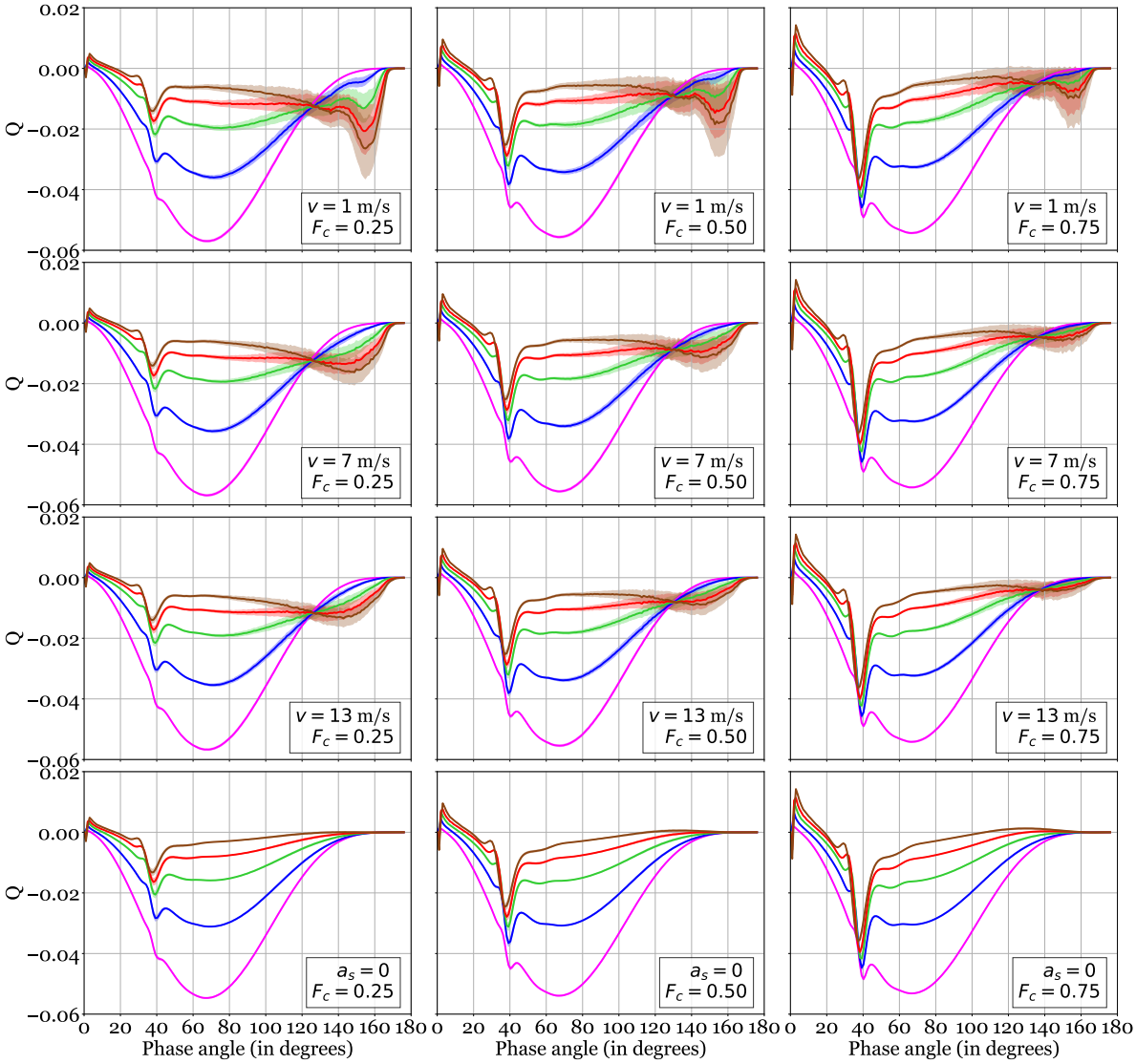

Figure 7.21: Polarized flux in terms of the Stokes parameter Q of the reflected starlight by oceanic exoplanets with patchy clouds for a wind speed of 1 m/s (top row), 7 m/s (second row), 13 m/s (third row) and a Lambertian exoplanet with patchy clouds (bottom row) with zero surface albedo. The cloud fractions are 25% (first column), 50% (second column) and 75% (third column). The lines are the mean curves from 300 iterations of cloud configurations randomly chosen at each phase angle and the 1 standard deviation variability is represented by the shaded areas for each of the 5 wavelengths. For $\alpha = 90^\circ$, the absolute magnitude of Q is biggest for $\lambda = 350$ nm and decreases with increasing λ, for all curves.

except for the points in the degree of polarization where the polarization direction changes sign, as discussed in Section 7.2.5.

- The rainbow feature at $\alpha \approx 40^\circ$ is clearly visible and followed by all wavelengths. It seems approximately independent of cloud fraction, however, by inspection of Q we may conclude that the polarized flux from the rainbow is much more apparent at high cloud fractions. The *wavelength dependent significance of the rainbow feature in Q* may help estimating the cloud fraction.

Let us now analyze the degree of polarization and Q for the case with patchy clouds above the ocean.[11] We may observe the following features:

- At long wavelengths, again the degree of polarization decreases with increasing cloud fraction, because

[11] Note that the polarized flux can only be presented in terms of Q if $U = 0$, which happens in a perfectly symmetrical planet about the scattering plane. This may not be the case for the patchy clouds, however, we find very small values for U whose mean is centered around $U \approx 0$.

of the depolarization by the clouds (recall Section 7.2.5). However, the degree of polarization of the light beams of longer wavelengths which penetrate through the atmosphere, strongly depends on whether these beams reach a cloud top or the air-water interface. This results in a high variability because the disk-integrated polarized signal starts alternating between the visible and non-visible glint cases. This variability increases with increasing phase angle because of the stronger Fresnel reflection at higher phase angles, where the degree of polarization starts to 'follow' the degree of polarization curve of the cloud free ocean planet (cf. Figure 7.8b). This may also be concluded by comparing the plots of Q for the cloudy and cloud-free ocean (Figures 7.6b and 7.15c), where it can be seen that the polarized flux from the glint rapidly increases for $\alpha > 100°$. In the most extreme situation, the curve for 865 nm alternates between the degree of polarization phase curves of the cloud free ocean planet (Figure 7.8b) and the completely cloudy ocean planet (7.15b). Because the difference between these two end member cases is largest at 865 nm, the variability at 865 nm is largest.

- The intersection point in the degree of polarization strongly depends on cloud fraction. Thus, for a low cloud fraction, the degree of polarization phase curve of the cloud free ocean starts to dominate the degree of polarization phase curve of the cloudy ocean already at smaller phase angles, compared to the case of high cloud fraction. The intersection points are located at $\alpha \approx 122°$, $132°$ and $145°$ for $F_c = 0.25$, $F_c = 0.50$ and $F_c = 0.75$ respectively. Note that the phase curve for 350 nm seems not to follow the intersection point precisely, probably because the reflected light at 350 nm has not reached the air-water interface.

- As mentioned earlier in this report, the degree of polarization is independent of wind speed at long wavelengths (except for the whitecap contribution), which causes the location of the polarization peak at two times the Brewster angle to be independent of wind speed. We explained that this independence is caused by the division of the wind speed related terms when computing the degree of polarization, but the the (polarized) flux would not be independent of wind speed. Indeed, we see that Q for the clear ocean in Figure 7.8c does depend on wind speed and, consequently, Q for the patchy cloudy ocean depends on wind speed as well (Figure 7.21). The value for Q at big phase angles increases with decreasing wind speed at all wavelengths except for 350 nm.

- The location of the intersection point in Q is unaffected by wind speed, but shifts from $\alpha \approx 128°$ at $F_c = 0.25$ towards $\alpha \approx 136°$ at $F_c = 0.75$. Together with the wavelength dependence of the significance of the rainbow feature the location of this intersection point (and also the intersection point in the degree of polarization) may help estimating the cloud fraction.

We may conclude that the most apparent features that are found in the phase curves of the cloudy ocean planet, which are not found in the phase curves of the cloudy Lambertian planet, are the (1) intersection point in the degree of polarization, (2) the much stronger variability at the (near-infra)red wavelengths compared to the short wavelengths and (3) the intersection point in Q.

7.3.2. Substellar Cloud

The cloud cover of an exoplanet is not necessarily randomly distributed in its latitudinal and longitudinal directions. For example, the cloud cover on tidally-locked planets may be concentrated at and approximately symmetrical about its substellar point. Yang et al. (2013) argued that the substellar cloud would increase the planetary albedo and would lower the surface temperature. They explained that, contrary to non-tidally locked planets, the albedo is expected to increase with increasing stellar flux, due to the increased convection at the substellar point, which would expand the inner edge of the habitable zone. They mentioned that, since the clouds block the outgoing *longwave radiation*, this contrast between the day and nightside of the planet could be detected with the James Webb Telescope. In this section we will model the planetary phase curves of the flux and degree of polarization, again at various wavelengths in the visible domain, of ocean planets with a substellar cloud.

In our model, the cloud is concentrated at and symmetrical about its substellar point. The angular size of the cloud, σ_C, is defined as the local zenith angle at the substellar point that is subtended by the cloud. Because the planet is tidally-locked it does not rotate around its rotation axis and the phase curve may be presented as a single line without variability. We model the tidally-locked planets again at $v = 1$ m/s, $v = 7$ m/s and $v = 13$ m/s. The substellar clouds are modeled at $\sigma_c = 15°$, $\sigma_c = 30°$ and $\sigma_c = 45°$.

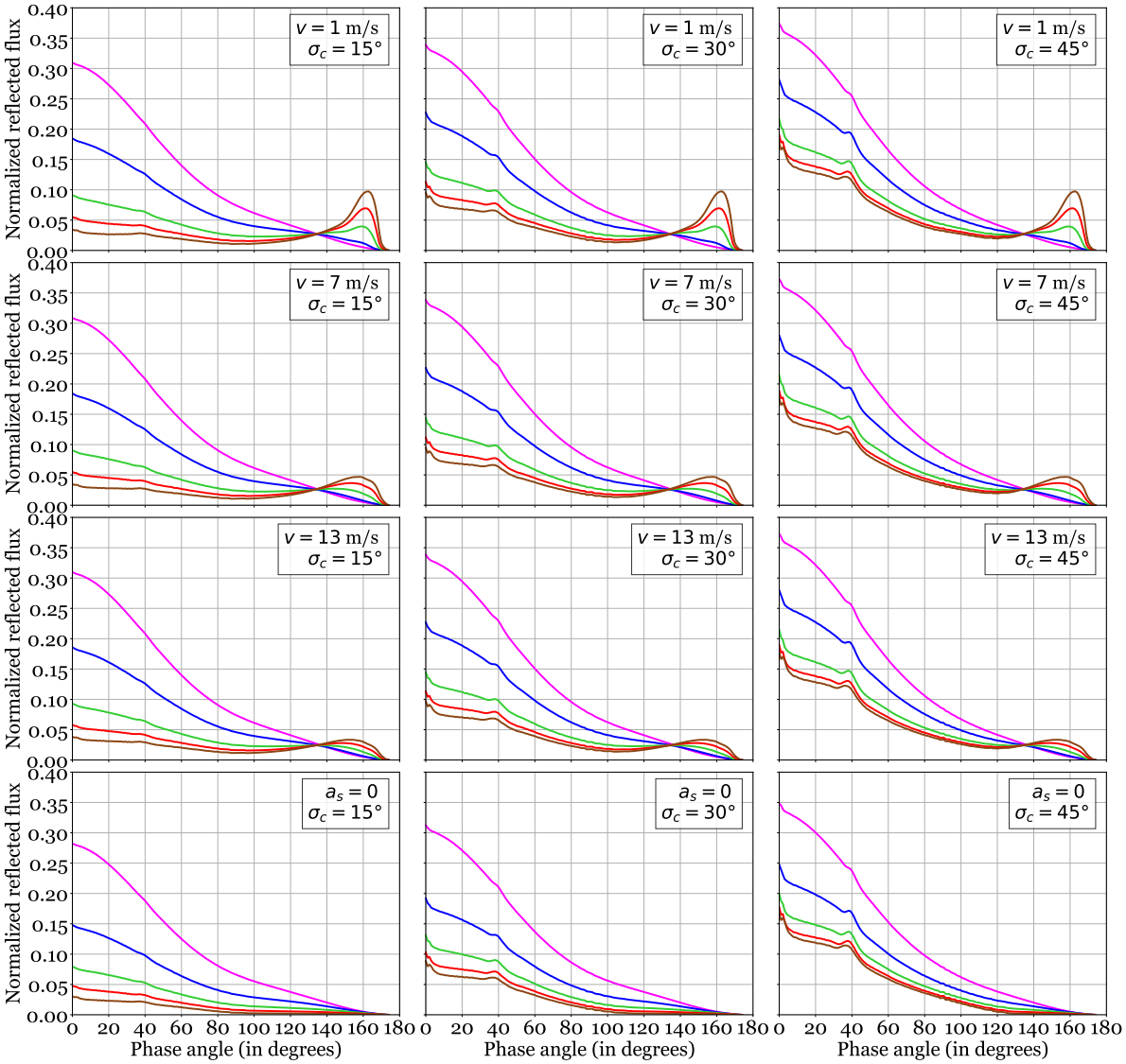

Figure 7.22: Normalized flux of the reflected starlight by oceanic exoplanets with a substellar cloud for a wind speed of 1 m/s (top row), 7 m/s (second row), 13 m/s (third row) and a Lambertian exoplanet with a substellar cloud (bottom row) with zero surface albedo. The cloud sizes σ_c are 15° (first column), 30° (second column) and 45° (third column). The curves are again drawn for λ = 350 nm, 443 nm, 550 nm, 670 nm and 865 nm. At full phase ($\alpha = 0°$), the normalized reflected flux is highest for λ = 350 nm and decreases with increasing λ for all curves.

Figure 7.22 shows the normalized reflected flux at each combination of v and σ_c. In the bottom row of Figure 7.22 the ocean is replaced by a black Lambertian surface again. The main differences in the planetary phase curves of the normalized reflected flux with respect to these phase curves for the model planets with patchy clouds (Figure 7.19) are the following:

- As mentioned above, it is expected that the planetary phase curve of the tidally-locked planet is approximately free of variations about its mean.
- The intersection point of the phase curves for various wavelengths is located at $\alpha = 135°$ for all ocean planets in Figure 7.22. Note that the intersection point for the clear ocean planet (Section 7.2.1) is also located at $\alpha = 135°$. At these large phase angles, the substellar cloud does not cover the glint anymore since it is rotated away from the observer.

Figure 7.23 shows the planetary phase curves of the degree of polarization of the substellar cloud. Figure 7.24 shows the corresponding planetary phase curves of the Stokes parameter Q. The following features may be observed:

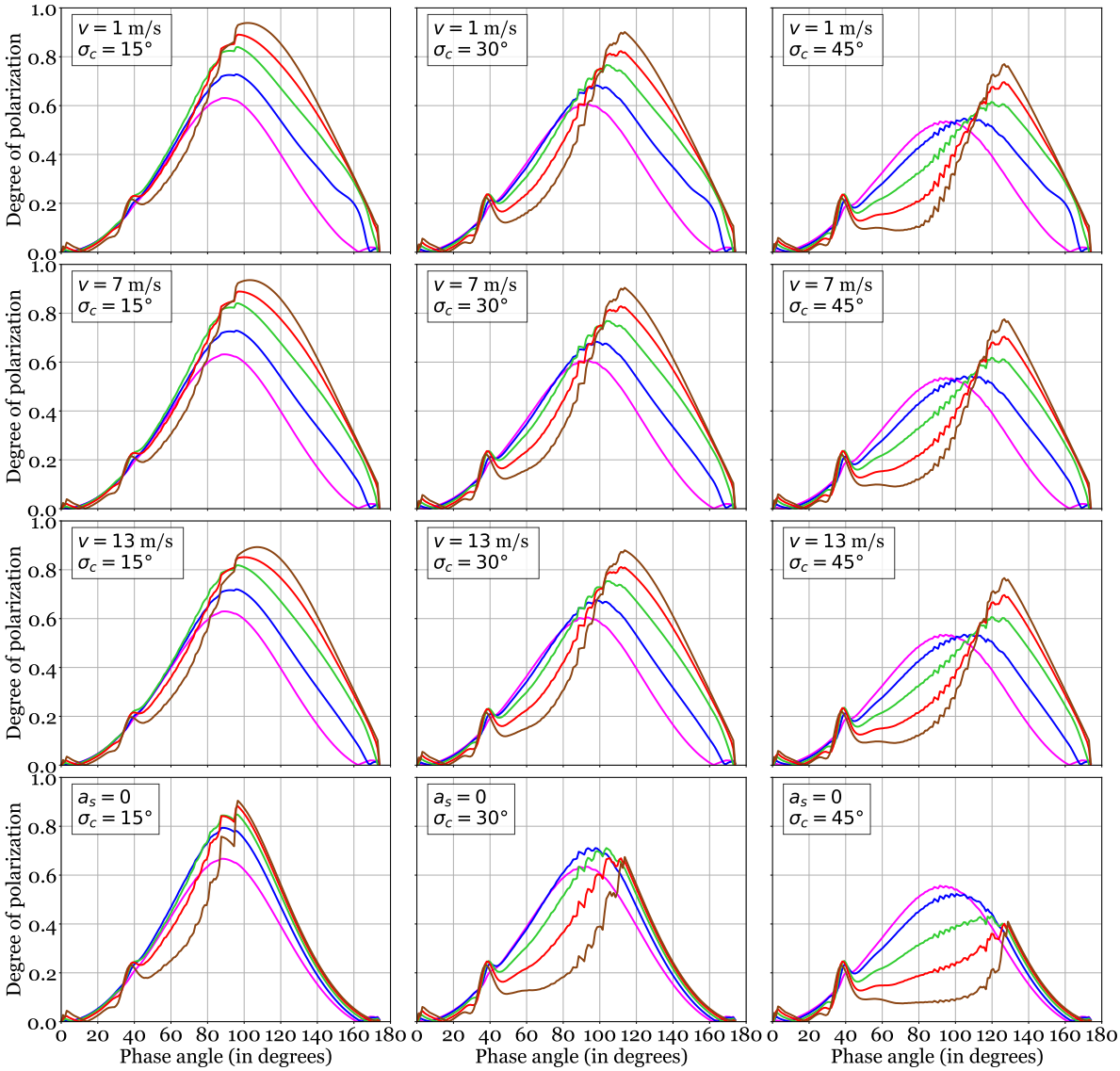

Figure 7.23: Degree of polarization of the reflected starlight by oceanic exoplanets with a substellar cloud for a wind speed of 1 m/s (top row), 7 m/s (second row), 13 m/s (third row) and a Lambertian exoplanet with a substellar cloud (bottom row) with zero surface albedo. The cloud sizes σ_c are 15° (first column), 30° (second column) and 45° (third column). The curves are again drawn for λ = 350 nm, 443 nm, 550 nm, 670 nm and 865 nm. For α = 140°, the degree of polarization is highest for λ = 865 nm and decreases with decreasing λ for all curves.

- The phase curves of the degree of polarization oscillate at certain ranges. These oscillations and the range at which they occur mainly depend on the size of the substellar cloud. These oscillations occur because of the pixellation of the cloud and have no physical meaning. However, these oscillations indicate where the pixels of the substellar cloud disappear from the visible and illuminated part of the planetary disk. They are caused by the discretized removal of cloudy pixels when the substellar cloud rotates away from the observer with increasing planetary phase angle. These oscillations would decrease if the number of pixels would increase (see also Rossi and Stam 2017). We used 60x60 pixels for these computations, which turned out to be a good compromise between sufficient phase curve smoothness and reasonable computation times.

- For phase angles bigger than the phase angle at which the substellar cloud has been rotated away from the disk, no oscillations in the degree of polarization due to the pixellated cloud are visible anymore and the phase curves completely follow the phase curves of the cloud free planets (Figure 7.5b and 7.5a). The phase angles at which the substellar cloud is out of view are 93°, 111° and 126° for σ_c = 15°,

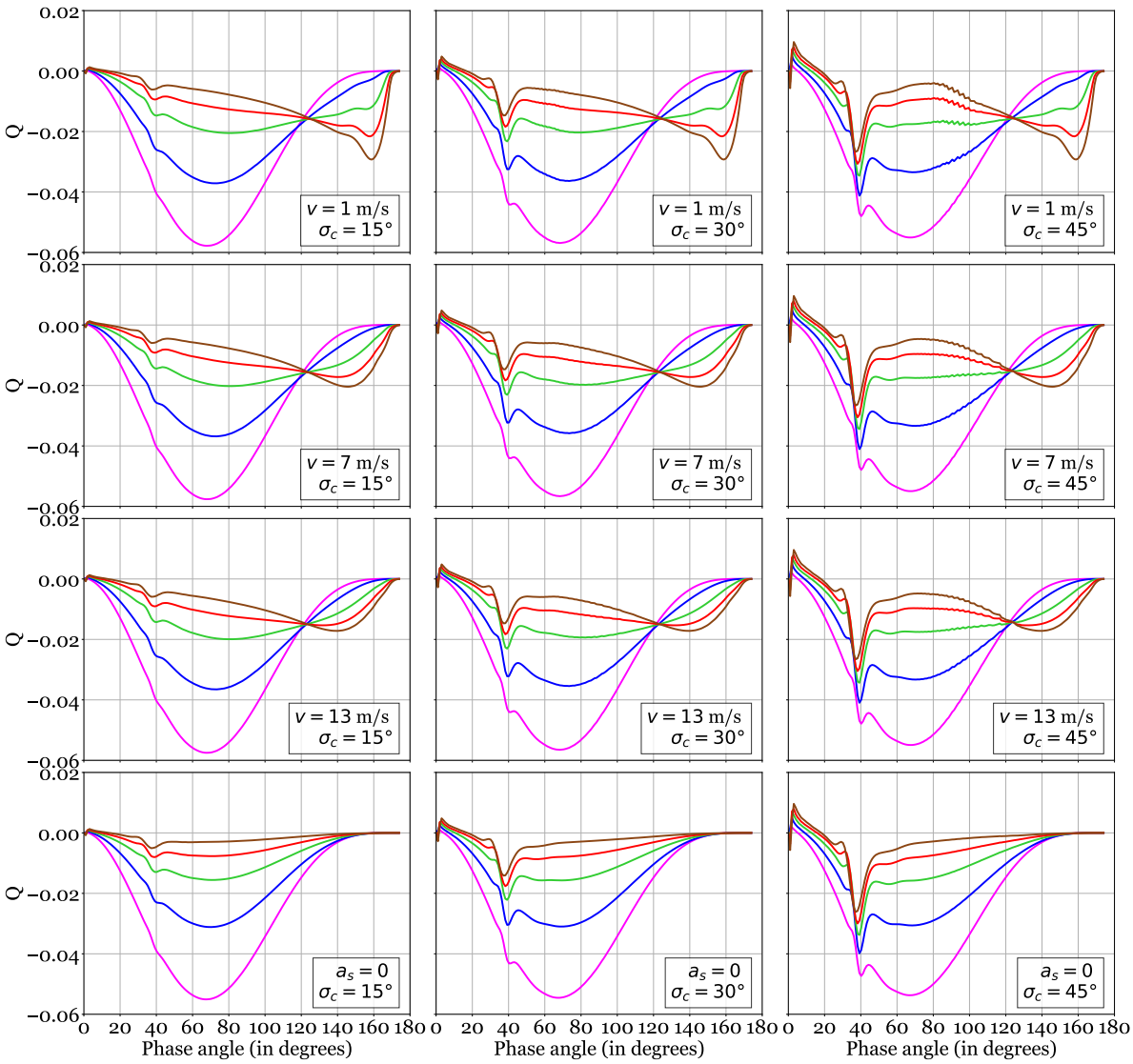

Figure 7.24: Polarized flux in terms of the Stokes parameter Q of the reflected starlight by oceanic exoplanets with a substellar cloud for a wind speed of 1 m/s (top row), 7 m/s (second row), 13 m/s (third row) and a Lambertian exoplanet with a substellar cloud (bottom row) with zero surface albedo. The cloud sizes σ_c are 15° (first column), 30° (second column) and 45° (third column). The curves are again drawn for λ = 350 nm, 443 nm, 550 nm, 670 nm and 865 nm. For $\alpha = 90°$, the absolute magnitude of Q is highest for λ = 350 nm and decreases with increasing λ for all curves.

$\sigma_c = 30°$ and $\sigma_c = 45°$ respectively. It should be noted that these phase angles are all smaller than 135°, which explains why the intersection point in the flux at $\alpha = 135°$ (Figure 7.22) is independent of σ_c.

- At small phase angles ($\alpha < 50°$), the phase curves are approximately invariant with wind speed and approximately equal the phase curves if the ocean would be replaced by a black Lambertian surface.
- For planets with a substellar cloud of significant size ($\sigma_c = 30°$ and $\sigma_c = 45°$), the reversal of colors in the degree of polarization becomes clear. As the substellar cloud rotates away from the planetary disk, the phase curves begin to 'follow' the planetary phase curves of the clear ocean (Figure 7.5b), which has a strong degree of polarization in the red wavelengths. If the surface would be replaced by the black Lambertian planet, the colors of the degree of polarization are also reversed due to less multiple scattering at long wavelengths, but the color difference after the reversal is less significant. That is, the separation of the phase curves for the particular wavelengths at these phase angles is much larger for the ocean planets.
- The latter bullet point implicates that the intersection of the colors in the degree of polarization found

for a patchy cloudy ocean planet (Figure 7.20), may also appear when a substellar cloud is present above an extremely dark surface. However, recall from Section 7.2.1 that the actual scattered polarized light in the atmosphere has a negligible flux at these long wavelengths compared to the polarized flux caused by the glint for the ocean planet. The latter becomes evident when analyzing the stokes parameter Q which is illustrated Figure 7.24. In this figure it may be observed that the polarized flux at these big phase angles is near 0 for the Lambertian planet, while the polarized flux of the ocean planet increases significantly at large phase angles. Hence, we would like to emphasize that if the surface albedo of the Lambertian planet would be nonzero, the high degree of polarization in the red of the Lambertian planet would rapidly vanish (see Fig 4.b of Stam 2008).

- The intersection point in the phase curves of the Stokes parameter Q is only visible for the ocean planets. The location of the intersection point ($\alpha = 122°$) is independent of wind speed (which was also observed for the patchy clouds), but is also independent of cloud size. Note that at $\alpha = 122°$ the substellar cloud has been rotated away from the visible and illuminated part of the planetary disk for $\sigma_c = 15°$ and $\sigma = 30°$, but not for $\sigma = 45°$ where the cloud is only completely out of view at $\alpha = 126°$. However, in the latter case, the glint is not overcasted by the substellar cloud anymore. For this cloud, the glint appears at $\alpha > 80°$, which may be concluded from the oscillations due to the pixellation of the cloud at this phase angle.
- The rainbow feature at $\alpha \approx 40°$ is visible again in the degree of polarization and becomes slightly more apparent with increasing cloud size. The rainbow feature in Q, however, is much more evident and becomes more significant with increasing cloud size, which was also observed for an increasing cloud fraction for the patchy cloudy planets.

We may conclude that the intersection point in the degree of polarization, that was an apparent ocean feature in the patchy cloudy case, is not a unique characteristic of an ocean, since it is also observed for the Lambertian planet with a substellar cloud. However, (1) the color reversal is much less significant for the Lambertian planet and may be expected to rapidly disappear for nonzero surface albedos, (2) after the intersection, the separation between the lines could serve as an ocean indicator and/or help estimating the surface pressure (recall Section 7.2.4) and (3) the intersection point in Q is still only observed for the ocean planet and not for the Lambertian planet.

7.3.3. Quasi Horizontally Inhomogeneous Planets

In the former sections the exoplanets were modeled taking into account the horizontal inhomogeneities of the planet by assigning either a cloudy or clear local atmosphere-surface model to each pixel. This was done for patchy clouds having a random configuration on the disk and for a substellar cloud that was fixed at the substellar point. This approach allowed us to analyze the variability of the planetary phase curves caused by the glint appearing and hiding behind the patchy clouds and to analyze the transition of the phase curves from cloudy-like to ocean-like when the substellar cloud rotates away from the observer. In previous studies to cloudy exoplanets, however, the planets often have been modeled in a quasi horizontally homogeneous way (e.g. Stam 2008). This means that the phase curves of the clear planet and the cloudy planet are added using a weighted sum:

$$\boldsymbol{F}(\lambda,\alpha) = \sum_{m=1}^{M} f_m \boldsymbol{F}_m(\lambda,\alpha) \quad \text{with} \quad \sum_{m=1}^{M} f_m = 1 \tag{7.7}$$

where f_m are weighing factors and $\boldsymbol{F}_m$ are the planetary phase curves of M homogeneous end-member model planets. In this section, we set f_m equal to the cloud fraction and use the end member model planets of this chapter for $\boldsymbol{F}_m$: the clear ocean planet and the cloudy ocean planet (M=2). Figures 7.25, 7.26 and 7.27 show that this quasi horizontally inhomogeneous approach is a good approximation of the mean phase curves for the patchy clouds (Figures 7.19, 7.20 and 7.21). However, (1) information is lost about the variability of the signal (e.g. we cannot see the glint hiding and appearing behind patchy clouds) and (2) the quasi horizontally inhomogeneous approach only approximates the patchy cloudy case. It could certainly not be used to model the signal of a tidally-locked planet with a substellar cloud, and it may be expected that the performance of the quasi horizontally inhomogeneous approach deteriorates when other horizontal inhomogeneities would be introduced, such as continents below the clouds. The latter argument remains to be proven and we leave this for future studies.

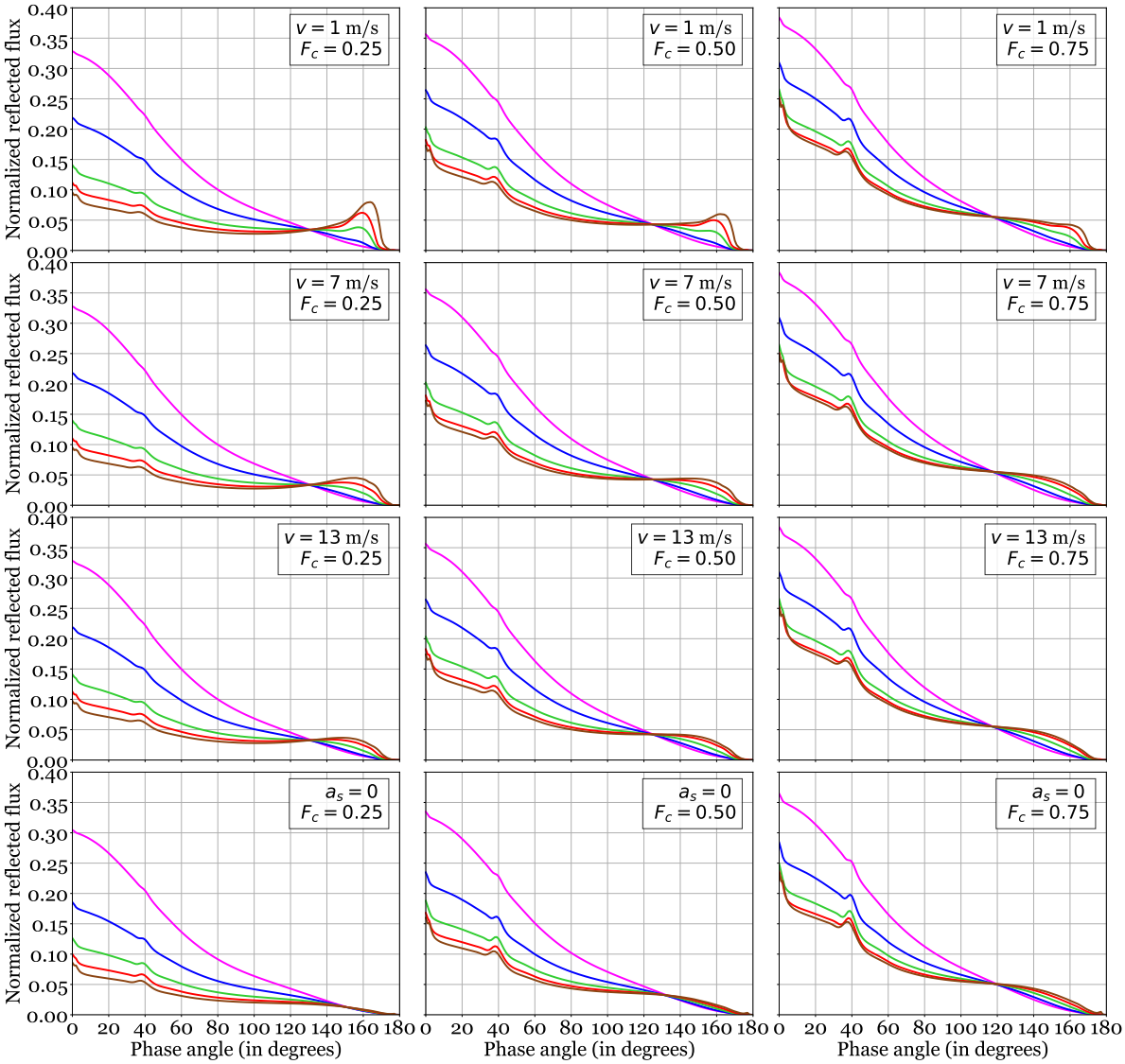

Figure 7.25: Normalized flux reflected by the quasi horizontally homogeneous cloudy ocean planet. The cloud fraction is the weighing factor for the cloudy ocean planet. The curves are again drawn for λ = 350 nm, 443 nm, 550 nm, 670 nm and 865 nm. At full phase ($\alpha = 0°$), the normalized reflected flux is highest for λ = 350 nm and decreases with increasing λ, for all curves.

An advantage of the quasi horizontally inhomogeneous approach is that, once phase curves of the the end member bases are computed, the results for various cloud fractions are easily computed with a computation time of only a few seconds. Figures 7.28 show the RGB colors of the reflected flux for both the cloudy ocean planet (Figure (a)) and the cloudy Lambertian planet (Figure (b)). The Lambertian planet does not show a major intersection point in the absence of clouds, contrary to the ocean planet, which was already shown earlier. The Lambertian planet thus appears white at large phase angles, while with increasing cloud fraction the whiteness occurs already at smaller phase angles and the planets starts to look red. It should be remembered that the clear ocean planet at high surface pressures (p_s > 10 bar) may also look white only at large phase angles without a major color reversal (Figure 7.11). Note that (1) these RGB results show the reflection by the planet assuming a *wavelength independent* incoming flux and (2) the intensity of the reflected light decreases with increasing phase angle. The actual color may depend on the stellar spectrum of the incident light on the planet. However, our results can be used for any stellar spectrum after a correction for this stellar spectrum, which directly can be measured, is applied.

Figure 7.29a and 7.29b show the RGB colors of the polarized flux, in terms of Stokes parameter Q, respectively, for both the cloudy ocean planet (Figure (a)) and the cloudy Lambertian planet (Figure (b)). The intersection

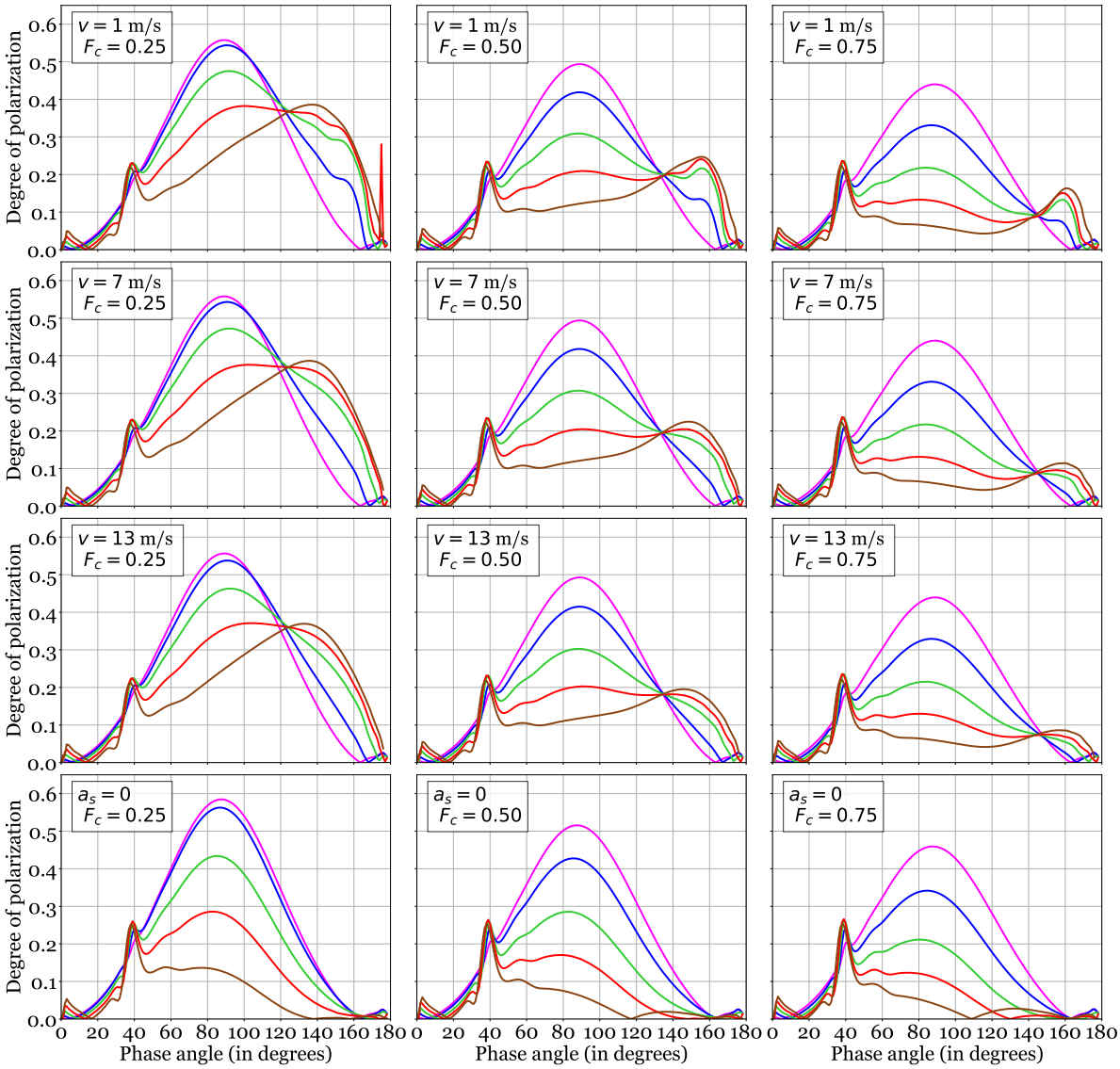

Figure 7.26: Degree of polarization of the reflected light by the quasi horizontally homogeneous cloudy ocean planet. The cloud fraction is the weighing factor for the cloudy ocean planet. The curves are again drawn for λ = 350 nm, 443 nm, 550 nm, 670 nm and 865 nm. For $\alpha = 90^\circ$, the degree of polarization is highest for λ = 350 nm and decreases with increasing λ for all curves.

point in Q remains visible for the cloudy ocean planet up to a cloud fraction of 95%. No major intersection (i.e. color reversal) is found for the Lambertian planet. The bright yellow and purple colors at large phase angles are caused by the sign change of Q.

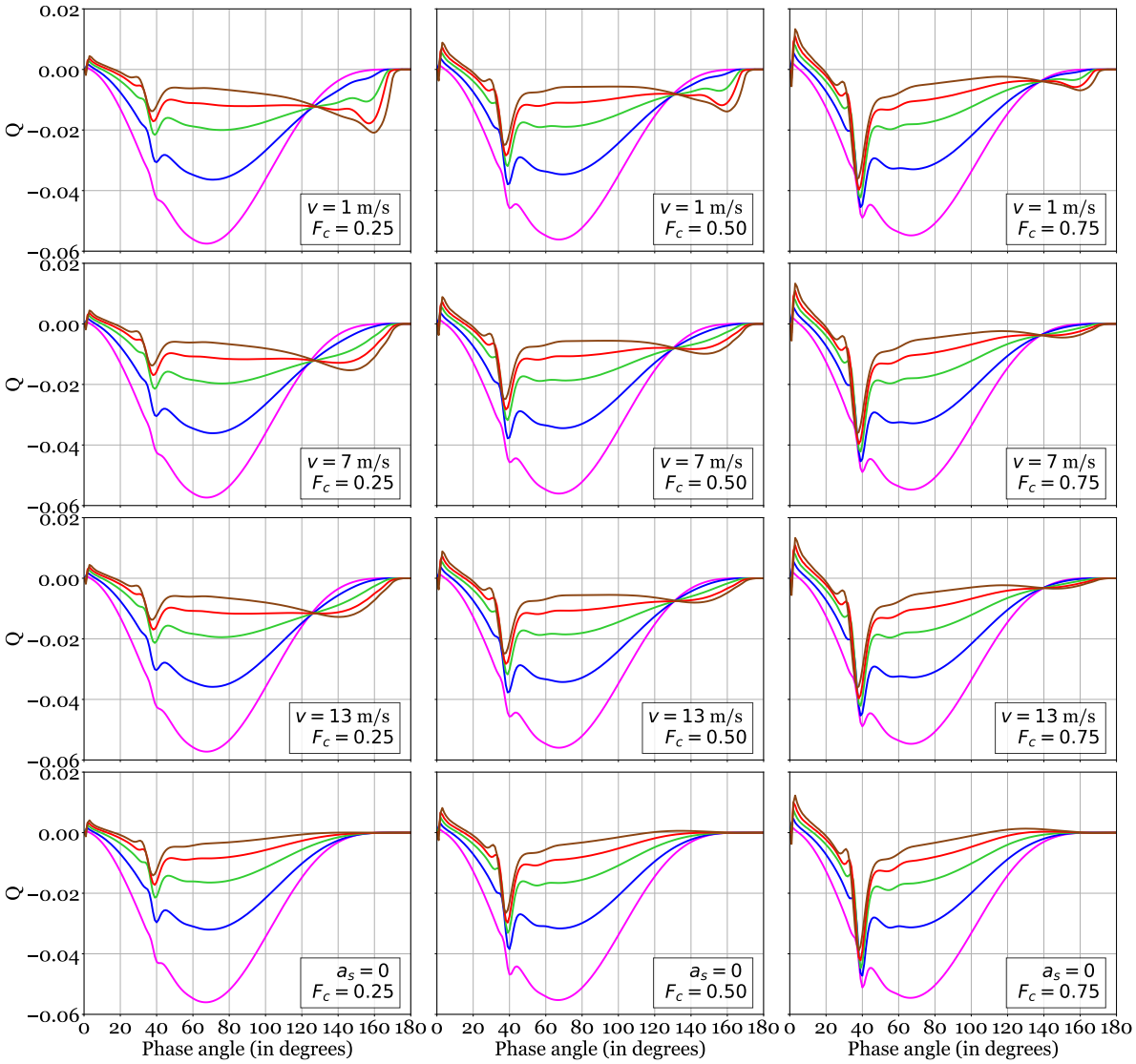

Figure 7.27: Polarized flux reflected by the quasi horizontally homogeneous cloudy ocean planet in terms of Stokes parameter Q. The cloud fraction is the weighing factor for the cloudy ocean planet. The curves are again drawn for λ = 350 nm, 443 nm, 550 nm, 670 nm and 865 nm. For $\alpha = 90°$, the absolute magnitude of Q is biggest for λ = 350 nm and decreases with increasing λ for all curves.

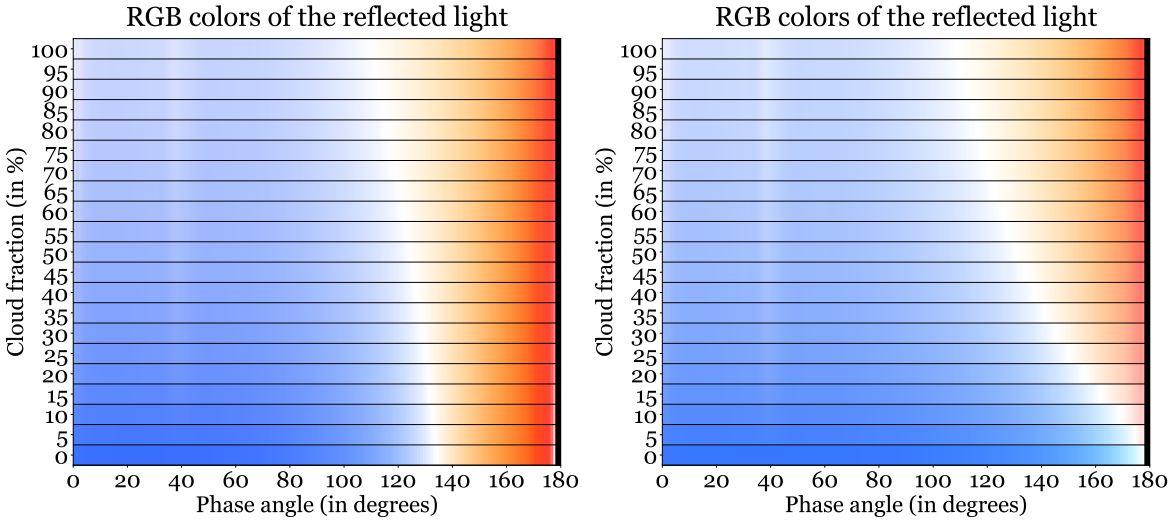

(a) (b)

Figure 7.28: RGB colors of the reflected light by (a) the cloudy ocean planet and (b) the cloudy Lambertian planet for cloud fractions varying between 0% and 100% in steps of 5%, using the quasi horizontally inhomogeneous approach. The white color at corresponds to the intersection point of the phase curves for different wavelengths as observed in Figure 7.25.

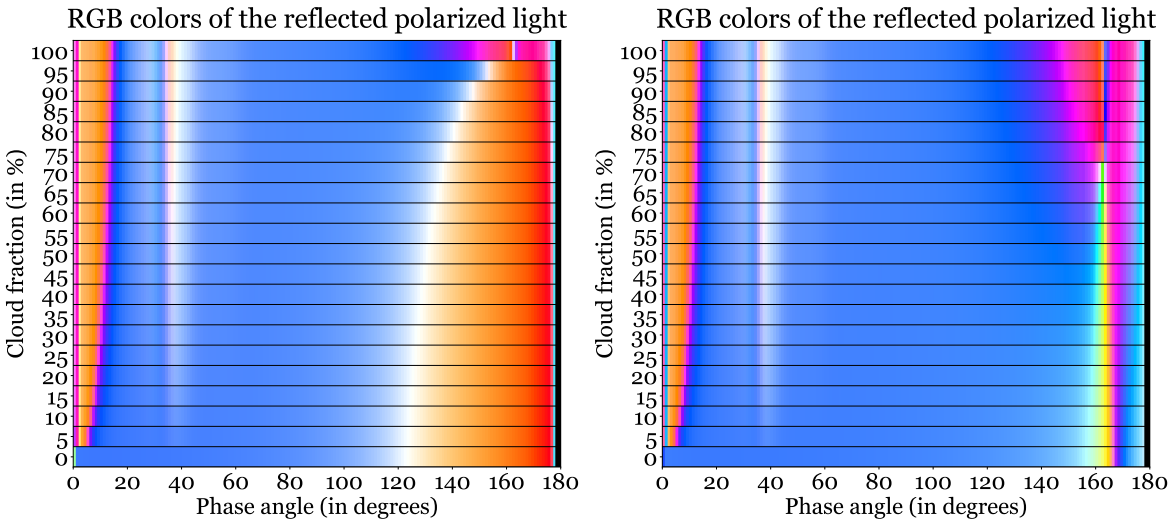

(a) (b)

Figure 7.29: RGB colors of the polarized reflected light, in terms of Stokes parameter Q, by (a) the cloudy ocean planet and (b) the cloudy Lambertian planet for cloud fractions varying between 0% and 100% in steps of 5%, using the quasi horizontally inhomogeneous approach. The white color at corresponds to the intersection point of the phase curves for different wavelengths as observed in Figure 7.27. Note that no major intersection point is found in the colors of Q for the Lambertian planet. The bright yellow and purple colors at large phase angles are caused by the sign change of Q.

IV

Discussion, Concluding Remarks and Recommendations

8

Discussion and Concluding Remarks

In this research we presented the modeled planetary phase curves of the normalized flux, polarized flux and degree of polarization of light reflected by various oceanic exoplanets, whose air-water interface roughness depends on wind speed. We included whitecaps, the contribution of the ocean color and the polarization effects of scattering within the ocean. We studied the effect of two horizontal inhomogeneous cloud covers: patchy clouds and a substellar cloud. We varied the wind speed, surface pressure, refractive index of the liquid, cloud fraction and substellar cloud size at the wavelengths 350 nm, 443 nm, 550 nm, 670 nm and 865 nm. We included a gaseous Rayleigh scattering layer above the clouds, similar to a realistic Earth-like atmosphere. The results were compared to the planetary phase curves if the ocean would be replaced by a black Lambertian surface. Finally we compared the patchy cloud results with the quasi horizontally inhomogeneous approach. Recall that the research objective was to investigate the signatures of an ocean in the planetary phase curves. The main conclusions of this research are presented below.

Normalized reflected flux
The planetary phase curves of the normalized reflected flux by a clear ocean planet at the considered wavelengths intersect at a phase angle of 135°, which we explained by the wavelength dependence of the reflection and attenuation by the atmospheric gas layer versus the wavelength independent Fresnel reflection. We semi-analytically showed that the location of the intersection point is independent of wind speed which can be explained by the integration over the planetary disk. We showed that when a set of wavelengths is used the intersection in the flux is not a unique characteristic of reflection by an ocean, since it also appears when clouds are modeled with a Rayleigh scattering gas layer on top. The location of the intersection point, however, could help estimating the cloud fraction, since it shifts towards smaller planetary phase angles with increasing clouds fraction, for both the patchy cloudy planet and a quasi horizontally inhomogeneous mix of a clear and cloudy ocean planet. We showed that in that case we should not forget that (1) the intersection point may *not* move away from $\alpha = 135°$ in the presence of a substellar cloud, which may have been rotated away from the observer at big phase angles, and that (2) the intersection point also moves towards bigger phase angles with increasing surface pressure.

Furthermore, we showed that the *absence* of an apparent intersection may be a *false negative* of an ocean, when the surface pressure is higher than about 10 bar. Finally, the variability in the phase curves of the patchy clouds at big phase angles increases with decreasing wind speed, which can be explained by the glint appearing and hiding behind the patchy clouds. This variability is strongest at long wavelengths but should be interpreted with care because we did not consider possible other types of surface reflection below the clouds.

Degree of polarization and polarized flux
In the presence of an ocean, the peak of the degree of polarization shifts, from the symmetrical bell-shape around $\alpha \approx 90°$, in the direction of $\alpha = 106°$ which corresponds to the local Brewster angle. With increasing wavelength, i.e. decreasing scattering optical thickness of the atmosphere, the reflection by the ocean becomes more dominant and the shift is more apparent. This shift was suggested by Zugger et al. (2010, 2011*a*) as a potential indicator of an exoplanetary ocean. We showed that the shift of the peak degree of polarization

of light reflected by a clear ocean planet is sensitive to surface pressure: the peak shift can hardly be detected for a surface pressure of 5 bar and is absent for a surface pressure of 10 bar.

The degree of polarization of both the clear ocean planet and the clear Lambertian planet with a black surface increases with wavelength. The high degree of polarization for the ocean planets is caused by the Fresnel reflection and decreased attenuation in the atmosphere, while the high degree of polarization in the red for the Lambertian planet is caused by singly scattered (and limited multiply scattered) light from the gas. The degree of polarization only does, however, not provide information about how much *polarized flux* actually can be measured. An intersection point in the polarized flux, in terms of Stokes parameter Q, is found for the phase curves of the considered wavelengths in case of a clear ocean planet, which is absent for the clear Lambertian planet because of the low polarized flux from molecular single scattering. The intersection in the polarized flux may be more useful than the degree of polarization peak shift for the detection of an ocean because (1) at short wavelengths (350 nm, 443 nm, and 550 nm) no shift of the peak degree of polarization can be detected for both the clear ocean planet and the clear Lambertian planet, while the intersection in Q is already apparent at these wavelengths only for the ocean planet, (2) the shift of the peak degree of polarization is increasingly diminished with increasing surface pressure, while the intersection in Q is hardly affected (provided that a near-infrared wavelength is combined with a short wavelength), (3) a substellar cloud on a black Lambertian planet may also result in an intersection in the degree of polarization. The substellar cloud causes a small color reversal for the Lambertian planet when the cloud has been rotated away from the observer, due to polarization of single scattering at long wavelengths in the absence of a cloud, while Q shows an intersection in the presence of an ocean underneath the cloud only.

We concluded that for a homogeneous cloud deck with a gas layer on top the ocean could not be retrieved. The clouds were also one of the limiting factors for the peak polarization shift due to Fresnel reflection in the work of Zugger et al. (2010, 2011*a*). We showed that, when modeling the phase curves for planets of random patchy cloud cover configurations, the degree of polarization approximately alternates between the cloudy and clear ocean planet phase curves, since the degree of polarization, in particular in the red, is mostly determined by the glint appearing and hiding behind patchy clouds. Because the difference in the degree of polarization between the end-member cases (i.e. cloudy and clear ocean planets) is largest at 865 nm, the variability in the phase curves is largest.

The location of the intersection point in the mean phase curves for the patchy clouds strongly depends on cloud fraction. Together with the wavelength dependence of the magnitude of the rainbow feature in Q, the location of the intersection point could therefore help estimating the cloud fraction. Note that, because we modeled the planetary phase curves at a set of wavelengths, and because our model includes a gas layer above the clouds, the clouds are *not* necessarily a limiting factor in the detection of an ocean. Actually, their presence is the reason that an intersection is observed in the degree of polarization, which is absent for the Lambertian cloudy planet. This is a direct result of the opposite order of wavelengths in the degree of polarization for the clear ocean planet compared to the cloudy planets, while the ocean reflection increasingly dominates with increasing phase angle.

Final remarks

The most apparent ocean feature in the degree of polarization, for cloud fractions smaller than 100%, is the intersection of the phase curves of the degree of polarization at the considered wavelengths, which is visible for either the patchy clouds, substellar cloud and the quasi horizontally inhomogeneous model. At low cloud fractions, this intersection occurs at beneficial planetary phase angles ($\alpha \approx 122^\circ - 132^\circ$ for cloud fractions of 25%-50%) which does not require unrealistically small inner working angles of the telescope. However, a color reversal could, although no very apparent, also be found in case of a substellar cloud above an extremely dark surface (e.g. a dark rocky planet).

The most robust feature related to the presence of an ocean is the intersection in the Stokes parameter Q at approximately 120° (and shifts towards bigger phase angles with increasing cloud fraction). This color reversal in the polarized flux was observed in the presence of an ocean for surface pressures up to 10 bar and cloud fractions up to 95% and was *never* found when the ocean was absent. We concluded that, if the aim is to increase the ocean detectability (i.e. at a larger range of surface pressures), it is recommended to increase the wavelength range. For example, if at least two wavelengths are combined, where one wavelengths is in

the near-infrared and the other in the short or mid-visible range, the intersection point in Q is more apparent for 10 bar. Note, however, that we showed in Section 7.2.6 that it would be hard to distinguish between water, water ice and liquid methane in the near future by inspection of the phase curves only. The following two hypotheses should not be confused:

1. If the exoplanet is completely covered by a (frozen) ocean, then an intersection point in Stokes parameter Q may be found.

2. If an intersection point in Stokes parameter Q is measured, then a (frozen) ocean is present on the planet.

Hypothesis 1 can already be rejected from this research, since, although the intersection point in Q appears to be very robust compared to the shift of the peak in the degree of polarization towards the Brewster angle, it is vanished for 100% cloud fraction. Also, it is reasonable to expect, by inspection of Figure 7.13c, that for very high surface pressures (e.g. more than 20 bar) the intersection in Q would vanish. Of course, if we would add to the hypothesis idealized circumstances for the planet, Hypothesis 1 could be modified such that it can be accepted. However, in that case these circumstances for the planet should first be proven. If we would assume, for some reason, that the atmospheres on oceanic exoplanets are Earth-like, from the results of this research the modified Hypothesis 1 could temporarily be accepted, provided that any other attempt in the future to model an Earth-like atmosphere on top of an ocean planet also yields an intersection point in Q.

Hypothesis 2 can be rejected if there are *no planets without an ocean* that cause an intersection point in the planetary phase curves of the Stokes parameter Q. We showed that a cloud deck (with a gas layer on top) on a Lambertian planet may increase the normalized reflected flux at long wavelengths, but an intersection point in Q was absent. Highly reflecting poles may possibly increase the flux in the crescent phase as well (Cowan et al. 2012). However, unless the surface reflection by the poles is strongly polarizing, it may be expected that the *polarized flux* does *not* significantly increase at red and near-infrared wavelengths, compared to the polarized flux from Fresnel reflection. In fact, *it remains to be shown that the intersection in Stokes parameter Q may also occur when an ocean on the planet is absent.*

Finally, it should be mentioned that one of the limiting factors in the work of Zugger et al. (2010, 2011*a*) were the maritime aerosols in the atmosphere, such as a mixture of water droplets and crystals of sea salt above the sea surface. We did not take these maritime aerosols into account in our clear (i.e. cloud free) models. Since atmospheric aerosols generally decrease the polarization signal, the polarization results in this research thus may be interpreted as the maximum polarization signals that could be detected in the absence of atmospheric aerosols. This is useful because (1) it is unknown what the potential characteristics are of the aerosol profiles of oceanic exoplanets and (2) neglecting the atmospheric aerosols limited the parameter space which allowed us to describe the sensitivity of the signal on the ocean parameters and the horizontally inhomogeneous cloud covers only. For the purpose of realistically modeling an Earth-like atmosphere the implementation of these aerosols is desired, and will be done in a future study.

9

Recommendations

Below the recommendations for future studies are listed.

- In this research the direction of wind speed was assumed to be isotropic. Zugger et al. (2010) mentioned that for the application to horizontal homogeneous oceanic exoplanets, where no continents are present to break the winds, the winds may be very strong and unidirectional. This could result in a highly asymmetric shape of the planetary phase curves. In that case, a wind-anisotropic probability distribution of the wave facet may be more appropriate, which can be modeled with the Gram-Charlier series expansion (Equation 5.20).

- The features of an ocean that were found at wavelengths where the atmosphere is thin enough to approach the Fresnel solution (i.e. the increased reflected flux at large phase angles, the shift of the polarization peak towards two times the Brewster angle and the increase in magnitude of Q at big phase angles) may also be detected when the ocean consists of another substance than liquid water but with a real refractive index in the same range (1.29-1.34), or even when it would be frozen, clear and uncovered by other materials. Nevertheless, the estimation of the temperature of the planet, the location of the rainbow in the planetary phase curve and the detection of the gaseous absorption bands together may potentially constrain the chemical cycle present on the planet. If, additionally, the oceanic features mentioned above are detected in the planetary phase curves, these constraints would most likely also constrain the material of the (frozen) ocean, provided that this ocean is a main contributor to the chemical cycle similar to the oceans on planet Earth. For an Earth-like atmospheric composition (and for various pressures and cloud covers), the phase curves presented in this research can be used. If the chemical cycle will be, for example, based on methane, the phase curves need to be modeled for planets with Titan-like atmospheres on top of the oceans. In that case, also the dependency of the relation between wind speed and interface roughness on the viscosity of the liquid should preferably be corrected for, as explained in Section 7.2.6.

- Although we decided not to include hydrosols in the water layer, the code is ready for implementation of these hydrosols if their scattering matrix elements are properly determined. Thus, Equation 6.3 can be used to compute the single scattering matrix of the water where hydrosols are included, where the single scattering matrix elements of the hydrosols are implemented through $\boldsymbol{F}_b$ and the absorption and scattering coefficient can be computed with the bio-optical model for Case 1 Waters of Morel and Maritorena (2001), following the equations stated in Chowdhary et al. (2006). It should, however, be remembered that the retrieval of hydrosols from space in Earth-observation is already a challenging task and the top of the atmosphere total and polarized reflectance sensitivities to chlorophyll concentration are small (see Fig. 5 en 6 of Chowdhary et al. 2012). Nevertheless, in a hypothetical exoplanetary ocean (1) the chlorophyll concentration may possibly be extremely high or (2) the oceans may possibly be shallow (note that the depth of the ocean can be varied in the code and that the albedo of the bottom of the ocean can be set). In the latter case it should be checked whether the assumption of Case 1 Waters is still valid, since the category *Case 2 Waters* is usually employed in oceanography for shallow waters (Gitelson et al. 2009).

- In a second version of the code, the water layer is replaced by a *subinterface* Lambertian surface with an ocean albedo that (1) is computed with the bio-optical model of Morel and Maritorena (2001) (including chlorophyll concentration) or (2) is defined by the user. Option (2) was used in this study to model the black ocean by setting the albedo equal to zero. Note that in Figure 6.1a we saw that the recomputed ocean albedo from the adding-doubling method was slightly different than the output of the bio-optical model when using option (1). Nevertheless, this second version of the code may be useful if one wants to neglect the color of the ocean as a first order approximation, for example if the code will be used for modeling Fresnel reflection by a methane ocean on a Titan-like planet. Note that, contrary to the equations for the air-water interface presented in most Earth-observation papers (e.g. Mishchenko and Travis 1997; Zhai et al. 2010), we analytically re-derived all reflection and transmission solutions through the interface keeping the refractive index of air, n_1, in the equations (i.e. instead of eliminating this parameter since $n_1 \approx 1$ for an Earth-like atmosphere). Hence, in future studies, *both* the refractive index of the atmosphere and liquid can be varied in the interface computations of the code.

- Zugger et al. (2010, 2011*a*,*b*) used Lorenz-Mie theory to show that atmospheric maritime aerosols just above the ocean surface decrease the degree of polarization signal. It is desired to investigate the sensitivity of the signal on maritime aerosols, such as a mix of salt crystals and water droplets, when horizontally inhomogeneous model planets are used. On the other hand, only analyzing the end member case of a clear (i.e. non-cloudy) ocean with maritime aerosols could already answer the question whether an intersection point can be expected in Q. A deliberate study to the effect of Earth-like aerosols and aerosol profiles, but also to the effect of hypothetical aerosols and aerosol profiles to explore the parameter space for exoplanets, is strongly recommended to increase the knowledge about the limitations of the research presented in this thesis.

- Hypothesis 2 of the former section implies that it remains to be shown that the intersection in the Stokes parameter Q may also occur when an ocean on the planet is *absent*. In other words, there is a need to model the phase curves of potential model planets that cause a high reflected polarized flux at red and near-infrared wavelengths at big phase angles. If all these model planets do not show an intersection point in Q, Hypothesis 2 could temporarily be accepted. As a first step, one can assume that the atmospheric composition (from transit spectroscopy) and surface temperature (from stellar luminosity and orbital period) are approximately determined. In order to look for false positives for the presence of an ocean, the phase curves can be modeled for planets with all kind of hypothetical surface reflections that could occur underneath Earth-like atmospheres (e.g. desert planets, realistic rocky planets, planets covered by snow or dirty ice and vegetated planets, either cloudy, partly cloudy and clear, and possibly in the form of continents or poles).

- Note that in this research we did not investigate the effect of continents. While the planets rotates around its axis, a longitudinal inhomogeneous land cover would probably induce oscillations in the flux, degree of polarization and polarized flux because the glint appears and disappears. These oscillations would differ from the oscillations caused by patchy clouds, because the patchy clouds are modeled randomly while the continents would induce a periodic signal. It could be studied (1) what the effect is on the ocean related features in the (polarized) flux and degree of polarization, (2) what knowledge could be retrieved about the land cover and (3) what knowledge could be retrieved about the rotation rate of the planet. Possibly, an autocorrelation study could be performed, however, it should be kept in mind that near future telescopes require a certain integration time for their measurements. This potential future research would benefit from a literature study to realistic integration times of near future and far future telescopes and expected ranges of planetary rotation rates. Also, we showed that the quasi horizontally inhomogeneous approach is a good approximation for the mean phase curves in case of patchy clouds above an ocean planet. However, when other horizontal inhomogeneities would be introduced, it may be expected that the quasi horizontally inhomogeneous approach loses performance compared to the horizontally inhomogeneous approach. It remains to be shown what the differences are in the results of both methods when continents are introduced.

A

Appendix

A.1. Relation between the Amplitude and Scattering Matrix

This appendix shows the computation of the scattering matrix elements from the amplitude matrix elements as was presented by van de Hulst (1957). First, reconsider the amplitude matrix as in Equation 2.1:

$$\begin{pmatrix} S_2 & S_3 \\ S_4 & S_1 \end{pmatrix} \tag{A.1}$$

Then, compute the real numbers M_k, S_{kj}, S_{jk}, D_{kj} and D_{jk} from the relations:

$$M_k = S_k S_k^* = |S_k|^2 \tag{A.2}$$

$$B_{kj} = B_{jk} = \frac{1}{2}(S_j S_k^* + S_k S_j^*) \tag{A.3}$$

$$-D_{kj} = D_{jk} = \frac{i}{2}(S_j S_k^* - S_k S_j^*) \tag{A.4}$$

where j,k = 1, 2, 3, 4 and the asterisk denotes the complex conjugate. Then, by substitution of these real numbers the scattering matrix yields (see van de Hulst 1957, Sec 5.14)

$$\boldsymbol{F} = \begin{pmatrix} \frac{1}{2}(M_2 + M_3 + M_4 + M_1) & \frac{1}{2}(M_2 - M_3 + M_4 - M_1) & B_{23} + B_{41} & -D_{23} - D_{41} \\ \frac{1}{2}(M_2 + M_3 - M_4 - M_1) & \frac{1}{2}(M_2 - M_3 - M_4 + M_1) & B_{23} - B_{41} & -D_{23} + D_{41} \\ B_{24} + B_{31} & B_{24} - B_{31} & B_{21} + B_{34} & -D_{21} + D_{34} \\ D_{24} + D_{31} & D_{24} - D_{31} & D_{21} + D_{34} & B_{21} - B_{34} \end{pmatrix} \tag{A.5}$$

A.2. Second Order of Scattering

Following the iterative scheme presented in 2.2.1 the expression for the scattered intensity of the second order (see Hovenier 1971, Eq. A-25) is derived in this Appendix.

1. **Compute intensity of the downward beam not scattered at all at the top of the medium for $n = 0$.**
   Assuming the incident to be in the downward direction ($u > 0$), from Equation 2.49 we have

$$\boldsymbol{I}_0(\tau, u, \mu_0, \varphi - \varphi_0) = e^{-\tau/u}\delta(u - \mu_0)\delta(\varphi - \varphi_0)\pi\boldsymbol{F}_0 \tag{A.6}$$

2. **Compute source vector of the beam scattered once in the medium, so $n = 1$.**

$$\boldsymbol{I}_{n-1} = \boldsymbol{I}_0 = \boldsymbol{I}_0(\tau, u, \mu_0, \varphi' - \varphi_0) \tag{A.7}$$

$$\boldsymbol{J}_1(\tau, u, \mu_0, \varphi - \varphi_0) = \frac{a}{4\pi}\int_{-1}^{1} du' \int_0^{2\pi} d\varphi' \boldsymbol{Z}(u, u', \varphi - \varphi')\boldsymbol{I}_0(\tau, u', \mu_0, \varphi' - \varphi_0) \tag{A.8}$$

$$= \frac{a}{4\pi}\int_{-1}^{1} du' \int_0^{2\pi} d\varphi' \boldsymbol{Z}(u, u', \varphi - \varphi')\left[e^{-\tau/u'}\delta(u' - \mu_0)\delta(\varphi' - \varphi_0)\pi\boldsymbol{F}_0\right] \tag{A.9}$$

$$= \frac{a}{4}\boldsymbol{Z}(u, \mu_0, \varphi - \varphi_0)e^{-\tau/\mu_0}\boldsymbol{F}_0 \tag{A.10}$$

3. **Compute intensities of the beam scattered once in the medium.**
   Hovenier (1971) defined the functions

$$c(\tau, u, \mu_0) = \int_0^{\tau} \frac{d\tau'}{u} e^{-\tau'/\mu_0} e^{-(\tau - \tau')/u} = \begin{cases} \frac{\mu_0}{\mu_0 - u}\left(e^{-\tau/\mu_0} - e^{-\tau/u}\right) & (u \neq \mu_0) \\ \frac{\tau}{\mu_0} e^{-\tau/\mu_0} & (u = \mu_0) \end{cases} \tag{A.11}$$

   and

$$d(\tau, u, \mu_0) = \int_{\tau}^{b} \frac{d\tau'}{(-u)} e^{-\tau'/\mu_0} e^{-(\tau' - \tau)/(-u)} = \frac{\mu_0}{\mu_0 - u}\left(e^{-\tau/\mu_0} - e^{(b-\tau)/u} e^{-b/\mu_0}\right) \tag{A.12}$$

   Using these functions, for the downward direction ($u > 0$) we find

$$\begin{aligned} \boldsymbol{I}_1(\tau, u, \mu_0, \varphi - \varphi_0) &= \int_0^{\tau} \frac{d\tau'}{u} \boldsymbol{J}_1(\tau', u, \mu_0, \varphi - \varphi_0) e^{-(\tau - \tau')/u} \\ &= \int_0^{\tau} \frac{d\tau'}{u} \frac{a}{4} \boldsymbol{Z}(u, \mu_0, \varphi - \varphi_0) e^{-\tau'/\mu_0} e^{-(\tau - \tau')/u} \boldsymbol{F}_0 \\ &= \frac{a}{4} \boldsymbol{Z}(u, \mu_0, \varphi - \varphi_0) c(\tau, u, \mu_0) \boldsymbol{F}_0 \end{aligned} \tag{A.13}$$

   By analogy, for the upward direction ($u < 0$) we find

$$\boldsymbol{I}_1(\tau, u, \mu_0, \varphi - \varphi_0) = \frac{a}{4} \boldsymbol{Z}(u, \mu_0, \varphi - \varphi_0) d(\tau, u, \mu_0) \boldsymbol{F}_0 \tag{A.14}$$

   and for $u = 0$

$$\boldsymbol{I}_1(\tau, 0, \mu_0, \varphi - \varphi_0) = \frac{a}{4} \boldsymbol{Z}(0, \mu_0, \varphi - \varphi_0) e^{-\tau/\mu_0} \boldsymbol{F}_0 \tag{A.15}$$

4. **Set $n = 2$ and go back to step 2**

5. **Calculate source vector of the beam scattered twice in the medium, so $n = 2$.**

$$\boldsymbol{I}_{n-1} = \boldsymbol{I}_1 = \boldsymbol{I}_1(\tau, u, \mu_0, \varphi' - \varphi_0) \tag{A.16}$$

   The 2nd order source vector may be written as

$$\begin{aligned} \boldsymbol{J}_2(\tau, u, \mu, \varphi - \varphi') &= \frac{a}{4\pi}\int_{-1}^{1} du' \int_0^{2\pi} d\varphi' \boldsymbol{Z}(u, u', \varphi - \varphi')\boldsymbol{I}_1(\tau, u', \mu_0, \varphi' - \varphi_0) \\ &= \frac{a^2}{16\pi}\int_0^{1} du' \int_0^{2\pi} d\varphi' \left[\boldsymbol{Z}(u, u', \varphi - \varphi')\boldsymbol{Z}(u', \mu_0, \varphi' - \varphi)c(\tau, u', \mu_0)\boldsymbol{F}_0\right. \\ &\quad \left. + \boldsymbol{Z}(u, -u', \varphi - \varphi')\boldsymbol{Z}(-u', \mu_0, \varphi' - \varphi_0)d(\tau', -u', \mu_0)\boldsymbol{F}_0\right] \end{aligned} \tag{A.17}$$

   It may be noted that in the expression above the incident directional cosines are replaced by their negative counterparts ($u' = -u'$) for the upward direction such that the integral is evaluated from 0 to 1.

6. **Compute intensities of the beam scattered twice in the medium.**

$$\begin{aligned}\boldsymbol{I}_2(\tau,u,\mu_0,\varphi-\varphi_0) &= \int_0^\tau \frac{d\tau'}{u}\boldsymbol{J}_2(\tau',u,\mu_0,\varphi-\varphi_0)e^{-(\tau-\tau')/u} \\ &= \int_0^\tau \frac{d\tau'}{u}\frac{a^2}{16\pi}\int_0^1 du'\int_0^{2\pi} d\varphi'\left[\boldsymbol{Z}(u,u',\varphi-\varphi')\boldsymbol{Z}(u',\mu_0,\varphi'-\varphi)c(\tau',u',\mu_0)\boldsymbol{F}_0\right. \\ &\quad \left.+\boldsymbol{Z}(u,-u',\varphi-\varphi')\boldsymbol{Z}(-u',\mu_0,\varphi'-\varphi_0)d(\tau',-u',\mu_0)\boldsymbol{F}_0\right]e^{-(\tau-\tau')/u}\end{aligned} \tag{A.18}$$

Write out c and d again for $u \neq \mu_0$ in the expression above.

$$\begin{aligned}\boldsymbol{I}_2(\tau,u,\mu_0,\varphi-\varphi_0) = \int_0^\tau \frac{d\tau'}{u}\frac{a^2}{16\pi}\int_0^1 du'\int_0^{2\pi} d\varphi'\Big[&\boldsymbol{Z}(u,u',\varphi-\varphi')\boldsymbol{Z}(u',\mu_0,\varphi'-\varphi) \\ &\cdot\int_0^\tau \frac{d\tau'}{u}e^{-\tau'/\mu_0}e^{-(\tau-\tau')/u}\frac{\mu_0}{\mu_0-u'}\left(e^{-\tau'/\mu_0}-e^{-\tau'/u'}\right)\boldsymbol{F}_0 \\ &+\boldsymbol{Z}(u,-u',\varphi-\varphi')\boldsymbol{Z}(-u',\mu_0,\varphi'-\varphi_0) \\ &\cdot\int_\tau^b \frac{d\tau'}{(-u)}e^{-\tau'/\mu_0}e^{-(\tau'-\tau)/(-u)}\frac{\mu_0}{\mu_0+u'}\left(e^{-\tau'/\mu_0}-e^{(b-\tau')/(-u')}e^{-b/\mu_0}\right)\boldsymbol{F}_0\Big]e^{-(\tau-\tau')/u}\end{aligned} \tag{A.19}$$

Evaluate the integrals.

$$\frac{\mu_0}{\mu_0-u'}\int_0^\tau \frac{d\tau'}{u}\left(e^{-\tau'/\mu_0}-e^{-\tau'/-u'}e^{-(\tau-\tau')/u}\right) = \frac{\mu_0}{\mu_0-u'}\left[c(\tau,u,\mu_0)-c(\tau,u,u')\right] \tag{A.20}$$

$$\begin{aligned}&\frac{\mu_0}{\mu_0+u'}\int_0^\tau \frac{d\tau'}{u}\left(e^{-\tau'/\mu_0}-e^{(b-\tau')/(-u')}e^{-b/\mu_0}\right)e^{-(\tau-\tau')/u} \\ &= \frac{\mu_0}{\mu_0+u'}\left[c(\tau,u,\mu_0)-\int_0^\tau \frac{d\tau'}{u}e^{(b-\tau')/u'}e^{-b/\mu_0}e^{-(\tau-\tau')/u}\right] \\ &= \frac{\mu_0}{\mu_0+u'}\left[c(\tau,u,\mu_0)-\int_0^\tau \frac{d\tau'}{u}e^{-\tau'/u'}e^{-b\left(\frac{1}{\mu_0}+\frac{1}{u'}\right)}e^{-(\tau-\tau')/u}\right] \\ &= \frac{\mu_0}{\mu_0+u'}\left[c(\tau,u,\mu_0)-e^{-b\left(\frac{1}{\mu_0}+\frac{1}{u'}\right)}c(\tau,u,-u')\right]\end{aligned} \tag{A.21}$$

Substituting the evaluated integrals into Equation A.19 yields the intensity vector for the second order of scattering for $u > 0$ (Equation A.22). The expression for $u < 0$ may be obtained by replacing functions c by functions d (Hovenier et al. 2004).

$$\begin{aligned}\boldsymbol{I}_2(\tau,u,\mu_0,\varphi-\varphi_0) = \frac{a^2\mu_0}{16\pi}\int_0^1 du'\int_0^{2\pi} d\varphi' \\ \cdot\left[\frac{c(\tau,u,\mu_0)-e^{-b\left(\frac{1}{\mu_0}+\frac{1}{u'}\right)}c(\tau,u,-u')}{\mu_0+u'}\boldsymbol{Z}(u,-u',\varphi-\varphi')\boldsymbol{Z}(-u',\mu_0,\varphi'-\varphi_0)\boldsymbol{F}_0\right. \\ \left.+\frac{c(\tau,u,\mu_0)-c(\tau,u,u')}{\mu_0-u'}\boldsymbol{Z}(u,u',\varphi-\varphi')\boldsymbol{Z}(u',\mu_0,\varphi'-\varphi_0)\boldsymbol{F}_0\right] \qquad (u>0)\end{aligned} \tag{A.22}$$

This latter expression is equivalent to Equation 4.27 in Hovenier et al. (2004) and was first derived in Hovenier (1971).

A.3. Derivation of the Adding Equations

This appendix shows the derivation of the adding equations of Hovenier (1971) including all intermediate steps, which is particularly useful if one wants to understand how these adding equations originate from the description of light reflected and transmitted by an interface separating two plane-parallel layers.

In Section 3.1 the descriptions of the intensity vector of the first three crossings of the interface illustrated in Figure 3.1 were presented as

$$\boldsymbol{I}^{(1)}(b',\mu,\varphi) = e^{-b'/\mu}\boldsymbol{I}_0(0,\mu,\varphi) + \frac{1}{\pi}\int_0^{+1}\mu' d\mu' \int_0^{2\pi} d\varphi' \boldsymbol{T}'(\mu,\mu',\varphi-\varphi')\boldsymbol{I}_0(0,\mu',\varphi') \tag{A.23}$$

$$\boldsymbol{I}^{(2)}(b',-\mu,\varphi) = \frac{1}{\pi}\int_0^{+1}\mu' d\mu' \int_0^{2\pi} d\varphi' \boldsymbol{R}''(\mu,\mu',\varphi-\varphi')\boldsymbol{I}^{(1)}(b',\mu',\varphi') \tag{A.24}$$

$$\boldsymbol{I}^{(3)}(b',\mu,\varphi) = \frac{1}{\pi}\int_0^{+1}\mu' d\mu' \int_0^{2\pi} d\varphi' \boldsymbol{R}'^{*}(\mu,\mu',\varphi-\varphi')\boldsymbol{I}^{(2)}(b',-\mu',\varphi') \tag{A.25}$$

where $\boldsymbol{I}^{(1)}$ and $\boldsymbol{I}^{(3)}$ are traveling downward and $\boldsymbol{I}^{(2)}$ is in the upward direction. Thus, following Hovenier et al. (2004), Equation A.25 may also be written as (Hovenier et al. 2004, Eq. 5.4 and 5.5)

$$\boldsymbol{I}^{(3)}(b',\mu,\varphi) = \frac{1}{\pi}\int_0^{+1}\mu' d\mu' \int_0^{2\pi} d\varphi' \boldsymbol{Q}_1(\mu,\mu',\varphi-\varphi')\boldsymbol{I}^{(1)}(b',\mu',\varphi') \tag{A.26}$$

where

$$\boldsymbol{Q}_1(\mu,\mu_0,\varphi-\varphi_0) = \frac{1}{\pi}\int_0^{+1}\mu' d\mu' \int_0^{2\pi} d\varphi' \boldsymbol{R}'^{*}(\mu,\mu',\varphi-\varphi')\boldsymbol{R}'^{*}(\mu',\mu_0,\varphi'-\varphi_0) \tag{A.27}$$

By the continuation of this approach, the fifth crossing of the interface may indeed be written as (Hovenier et al. 2004, Eq. 5.6)

$$\boldsymbol{I}^{(5)}(b',\mu,\varphi) = \frac{1}{\pi}\int_0^{+1}\mu' d\mu' \int_0^{2\pi} d\varphi' \boldsymbol{Q}_1(\mu,\mu',\varphi-\varphi')\boldsymbol{I}^{(3)}(b',\mu',\varphi') \tag{A.28}$$

As mentioned in Section 3.1 this may be recognized as the start of an infinite series (Hovenier et al. 2004, cf. Eq. 5.8 and 5.9). Hence, the total radiance traveling downward at the interface may be given by

$$I^{(tot,down)}(b',\mu,\varphi) = \boldsymbol{I}^{(1)}(b',\mu,\varphi) + \boldsymbol{I}^{(3)}(b',\mu,\varphi) + \sum_{p=1}^{\infty}\boldsymbol{I}^{(2p+3)}(b',\mu,\varphi) \tag{A.29}$$

with

$$I^{(2p+3)}(b',\mu,\varphi) = \frac{1}{\pi}\int_0^{+1}\mu' d\mu' \int_0^{2\pi} d\varphi' \boldsymbol{Q}_{p+1}(\mu,\mu',\varphi-\varphi')\boldsymbol{I}^{(1)}(b',\mu',\varphi') \tag{A.30}$$

and where

$$\boldsymbol{Q}_{p+1}(\mu,\mu_0,\varphi-\varphi_0) = \frac{1}{\pi}\int_0^{+1}\mu' d\mu' \int_0^{2\pi} d\varphi' \boldsymbol{Q}_1(\mu,\mu',\varphi-\varphi')\boldsymbol{Q}_p(\mu',\mu_0,\varphi'-\varphi_0) \tag{A.31}$$

for $p = 1,2,3,\ldots$ (see Hovenier et al. 2004, Section 5.2). Recall, however, that the total downward traveling radiance for a multiple scattering event at $\tau = b'$ may be presented by Equation 2.54

$$I(b',\mu,\varphi) = \frac{1}{\pi}\int_0^{1}\mu' d\mu' \int_0^{2\pi} d\varphi' \boldsymbol{D}(b',\mu,\mu',\varphi-\varphi')\boldsymbol{I}_0(0,\mu',\varphi') + e^{-b'/\mu}\boldsymbol{I}_0(0,\mu,\varphi) \tag{A.32}$$

Equating Equations A.29 and A.32 yields the expression

$$\frac{1}{\pi}\int_0^{1}\mu' d\mu' \int_0^{2\pi} d\varphi' \boldsymbol{D}(b',\mu,\mu',\varphi-\varphi')\boldsymbol{I}_0(0,\mu',\varphi') + e^{-b'/\mu}\boldsymbol{I}_0(0,\mu,\varphi) = \boldsymbol{I}^{(1)}(b',\mu,\varphi) + \boldsymbol{I}^{(3)}(b',\mu,\varphi) + \sum_{p=1}^{\infty}\boldsymbol{I}^{(2p+3)}(b',\mu,\varphi) \tag{A.33}$$

Substitute for $\boldsymbol{I}^{(1)}(b',\mu,\varphi)$ (Equation A.23)

$$\begin{aligned}&\frac{1}{\pi}\int_0^1 \mu' d\mu' \int_0^{2\pi} d\varphi' \boldsymbol{D}(b',\mu,\mu',\varphi-\varphi')\boldsymbol{I}_0(0,\mu',\varphi') + e^{-b'/\mu}\boldsymbol{I}_0(0,\mu,\varphi) = \\ &e^{-b'/\mu}\boldsymbol{I}_0(0,\mu,\varphi) + \frac{1}{\pi}\int_0^{+1} \mu' d\mu' \int_0^{2\pi} d\varphi' \boldsymbol{T}'(\mu,\mu',\varphi-\varphi')\boldsymbol{I}_0(0,\mu',\varphi') + \boldsymbol{I}^{(3)}(b',\mu,\varphi) \\ &+ \sum_{p=1}^{\infty} \boldsymbol{I}^{(2p+3)}(b',\mu,\varphi)\end{aligned} \tag{A.34}$$

Note that the primes for the symbols b and $\boldsymbol{T}$ do *not* indicate integrand variables, as for μ and φ, but rather denote the upper layer here. Consider the incident light beam to be monodirectional such that $\boldsymbol{I}_0(0,\mu,\varphi) = \delta(\mu-\mu_0)\delta(\varphi-\varphi_0)\pi\boldsymbol{F}_0$ where δ is the Dirac delta function (see Section 2.2.1)

$$\mu_0\boldsymbol{D}(b',\mu,\mu_0,\varphi-\varphi_0)\boldsymbol{F}_0 + e^{-b'/\mu_0}\pi\boldsymbol{F}_0 = e^{-b'/\mu_0}\pi\boldsymbol{F}_0 + \mu_0\boldsymbol{T}'(\mu,\mu_0,\varphi-\varphi_0)\boldsymbol{F}_0 + \boldsymbol{I}^{(3)}(b',\mu,\varphi) + \sum_{p=1}^{\infty}\boldsymbol{I}^{(2p+3)}(b',\mu,\varphi) \tag{A.35}$$

Eliminate $e^{-b'/\mu_0}\pi\boldsymbol{F}_0$ on both sides.

$$\mu_0\boldsymbol{D}(b,\mu,\mu_0,\varphi-\varphi_0)\boldsymbol{F}_0 = \mu_0\boldsymbol{T}'(\mu,\mu_0,\varphi-\varphi_0)\boldsymbol{F}_0 + \boldsymbol{I}^{(3)}(b',\mu,\varphi) + \sum_{p=1}^{\infty}\boldsymbol{I}^{(2p+3)}(b',\mu,\varphi) \tag{A.36}$$

As an intermezzo, evaluate the last two terms of Equation A.36 by substituting $\boldsymbol{I}^{(3)}$ (Equation A.26) and $\boldsymbol{I}^{(2p+3)}$ (Equation A.30).

$$\begin{aligned}\boldsymbol{I}^{(3)}(b',\mu,\varphi) + \sum_{p=1}^{\infty}\boldsymbol{I}^{(2p+3)}(b',\mu,\varphi) = &\frac{1}{\pi}\int_0^{+1}\mu' d\mu'\int_0^{2\pi} d\varphi' \boldsymbol{Q}_1(\mu,\mu',\varphi-\varphi')\boldsymbol{I}^{(1)}(b',\mu',\varphi') \\ &+ \sum_{p=1}^{\infty}\frac{1}{\pi}\int_0^{+1}\mu' d\mu'\int_0^{2\pi} d\varphi' \boldsymbol{Q}_{p+1}(\mu,\mu',\varphi-\varphi')\boldsymbol{I}^{(1)}(b',\mu',\varphi')\end{aligned} \tag{A.37}$$

Substitute for $\boldsymbol{I}^{(1)}(b',\mu,\varphi)$ (Equation A.23) such that

$$\begin{aligned}\boldsymbol{I}^{(3)}(b',\mu,\varphi) + \sum_{p=1}^{\infty}\boldsymbol{I}^{(2p+3)}(b',\mu,\varphi) = &\frac{1}{\pi}\int_0^{+1}\mu' d\mu'\int_0^{2\pi} d\varphi' \boldsymbol{Q}_1(\mu,\mu',\varphi-\varphi')\Big[e^{-b'/\mu'}\boldsymbol{I}_0(0,\mu',\varphi') \\ &+\frac{1}{\pi}\int_0^{+1}\mu'' d\mu''\int_0^{2\pi} d\varphi'' \boldsymbol{T}'(\mu',\mu'',\varphi'-\varphi'')\boldsymbol{I}_0(0,\mu'',\varphi'')\Big] \\ &+ \sum_{p=1}^{\infty}\frac{1}{\pi}\int_0^{+1}\mu' d\mu'\int_0^{2\pi} d\varphi' \boldsymbol{Q}_{p+1}(\mu,\mu',\varphi-\varphi')\Big[e^{-b'/\mu'}\boldsymbol{I}_0(0,\mu',\varphi') \\ &+\frac{1}{\pi}\int_0^{+1}\mu'' d\mu''\int_0^{2\pi} d\varphi'' \boldsymbol{T}'(\mu',\mu'',\varphi'-\varphi'')\boldsymbol{I}_0(0,\mu'',\varphi'')\Big]\end{aligned} \tag{A.38}$$

where an extra prime is added for μ and φ when a second integration over solid angle (in between the square brackets) is performed. Note that $\boldsymbol{Q}_1 + \sum_{p=1}^{\infty}\boldsymbol{Q}_{p+1} = \sum_{p=1}^{\infty}\boldsymbol{Q}_p$, therefore

$$\begin{aligned}\boldsymbol{I}^{(3)}(b',\mu,\varphi) + \sum_{p=1}^{\infty}\boldsymbol{I}^{(2p+3)}(b',\mu,\varphi) = &\sum_{p=1}^{\infty}\frac{1}{\pi}\int_0^{+1}\mu' d\mu'\int_0^{2\pi} d\varphi' \boldsymbol{Q}_p(\mu,\mu',\varphi-\varphi')\Big[e^{-b'/\mu'}\boldsymbol{I}_0(0,\mu',\varphi') \\ &+\frac{1}{\pi}\int_0^{+1}\mu'' d\mu''\int_0^{2\pi} d\varphi'' \boldsymbol{T}'(\mu',\mu'',\varphi'-\varphi'')\boldsymbol{I}_0(0,\mu'',\varphi'')\Big]\end{aligned} \tag{A.39}$$

Consider again the incident light beam to be monodirectional writing it as $\boldsymbol{I}_0(0,\mu,\varphi) = \delta(\mu-\mu_0)\delta(\varphi-\varphi_0)\pi\boldsymbol{F}_0$

where δ is the Dirac delta function (see Section 2.2.1) and substitute this into Equation A.39.

$$
\begin{aligned}
&\boldsymbol{I}^{(3)}(b',\mu,\varphi)+\sum_{p=1}^{\infty}\boldsymbol{I}^{(2p+3)}(b',\mu,\varphi)\\
&=\sum_{p=1}^{\infty}\frac{1}{\pi}\int_0^{+1}\mu' d\mu'\int_0^{2\pi}d\varphi'\boldsymbol{Q}_p(\mu,\mu',\varphi-\varphi')\Big[e^{-b'/\mu'}\delta(\mu'-\mu_0)\delta(\varphi'-\varphi_0)\pi\boldsymbol{F}_0\\
&+\frac{1}{\pi}\int_0^{+1}\mu'' d\mu''\int_0^{2\pi}d\varphi''\boldsymbol{T}'(\mu',\mu'',\varphi'-\varphi'')\delta(\mu''-\mu_0)\delta(\varphi''-\varphi_0)\pi\boldsymbol{F}_0\Big]\\
&=\sum_{p=1}^{\infty}\frac{1}{\pi}\int_0^{+1}\mu' d\mu'\int_0^{2\pi}d\varphi'\boldsymbol{Q}_p(\mu,\mu',\varphi-\varphi')\Big[e^{-b'/\mu'}\delta(\mu'-\mu_0)\delta(\varphi'-\varphi_0)\pi\boldsymbol{F}_0\Big]\\
&+\sum_{p=1}^{\infty}\frac{1}{\pi}\int_0^{+1}\mu' d\mu'\int_0^{2\pi}d\varphi'\boldsymbol{Q}_p(\mu,\mu',\varphi-\varphi')\Big[\frac{1}{\pi}\int_0^{+1}\mu'' d\mu''\int_0^{2\pi}d\varphi''\boldsymbol{T}'(\mu',\mu'',\varphi'-\varphi'')\delta(\mu''-\mu_0)\delta(\varphi''-\varphi_0)\pi\boldsymbol{F}_0\Big]\\
&=\sum_{p=1}^{\infty}\boldsymbol{Q}_p(\mu,\mu_0,\varphi-\varphi_0)e^{-b'/\mu_0}\mu_0\boldsymbol{F}_0+\sum_{p=1}^{\infty}\frac{1}{\pi}\int_0^{+1}\mu' d\mu'\int_0^{2\pi}d\varphi'\boldsymbol{Q}_p(\mu,\mu',\varphi-\varphi')\boldsymbol{T}'(\mu',\mu_0,\varphi'-\varphi_0)\mu_0\boldsymbol{F}_0
\end{aligned}
\tag{A.40}
$$

Introduce the notation $\boldsymbol{Q}(\mu,\mu_0,\varphi-\varphi_0)=\sum_{p=1}^{\infty}\boldsymbol{Q}_p$ of Hovenier et al. (2004) (Eq. 5.13), and substitute the latter result into Equation A.36, yielding the expression

$$
\begin{aligned}
\mu_0\boldsymbol{D}(b',\mu,\mu_0,\varphi-\varphi_0)\boldsymbol{F}_0&=\mu_0\boldsymbol{T}'(\mu,\mu_0,\varphi-\varphi_0)\boldsymbol{F}_0+\boldsymbol{Q}(\mu,\mu_0,\varphi-\varphi_0)e^{-b'/\mu_0}\mu_0\boldsymbol{F}_0\\
&+\frac{1}{\pi}\int_0^{+1}\mu' d\mu'\int_0^{2\pi}d\varphi'\boldsymbol{Q}(\mu,\mu',\varphi-\varphi')\boldsymbol{T}'(\mu',\mu_0,\varphi'-\varphi_0)\mu_0\boldsymbol{F}_0
\end{aligned}
\tag{A.41}
$$

Dividing both sides of Equation A.41 by $\mu_0\boldsymbol{F}_0$ gives the desired adding equation for the downward traveling light at the interface (cf. Equation 3.7):

$$
\boxed{
\begin{aligned}
\boldsymbol{D}(b',\mu,\mu_0,\varphi-\varphi_0)&=\boldsymbol{T}'(\mu,\mu_0,\varphi-\varphi_0)+e^{-b'/\mu_0}\boldsymbol{Q}(\mu,\mu_0,\varphi-\varphi_0)\\
&+\frac{1}{\pi}\int_0^{+1}\mu' d\mu'\int_0^{2\pi}d\varphi'\boldsymbol{Q}(\mu,\mu',\varphi-\varphi')\boldsymbol{T}'(\mu',\mu_0,\varphi'-\varphi_0)
\end{aligned}
}
\tag{A.42}
$$

The next step is to derive the adding equation for the upward traveling light at the interface in Figure 3.1 which is relatively straightforward since the adding equation for the downward traveling light at the interface was obtained above. That is, the upward traveling light crossing the interface is the reflected light from the bottom layer, emerging at the top of the bottom layer (at $\tau=b'$), presented by (cf. Equation 2.55 and 2.56)

$$
\boldsymbol{I}(b',-\mu,\varphi)=\frac{1}{\pi}\int_0^{1}\mu' d\mu\int_0^{2\pi}d\varphi'\boldsymbol{R}''(\mu,\mu',\varphi-\varphi')\boldsymbol{I}_{inc}(b',\mu',\varphi')
\tag{A.43}
$$

where $\boldsymbol{R}''$ is again the reflection matrix of the bottom layer and $\boldsymbol{I}_{inc}$ is the downweling incident beam at the top of the bottom layer originating from the top layer given by (cf. Equation 2.54)

$$
\boldsymbol{I}_{inc}(b',\mu',\varphi')=e^{-b'/\mu}\boldsymbol{I}_0(0,\mu,\varphi)+\frac{1}{\pi}\int_0^{1}\mu' d\mu'\int_0^{2\pi}d\varphi'\boldsymbol{D}(b',\mu,\mu',\varphi-\varphi')\boldsymbol{I}(0,\mu',\varphi')
\tag{A.44}
$$

Substituting Equation A.44 into A.43 gives

$$
\begin{aligned}
\boldsymbol{I}(b',-\mu,\varphi)=&\frac{1}{\pi}\int_0^{1}\mu' d\mu\int_0^{2\pi}d\varphi'\boldsymbol{R}''(\mu,\mu',\varphi-\varphi')\Big[e^{-b'/\mu'}\boldsymbol{I}_0(0,\mu',\varphi')\\
&+\frac{1}{\pi}\int_0^{1}\mu'' d\mu''\int_0^{2\pi}d\varphi''\boldsymbol{D}(b',\mu',\mu'',\varphi'-\varphi'')\boldsymbol{I}(0,\mu'',\varphi'')\Big]
\end{aligned}
\tag{A.45}
$$

where again an extra prime is added when a second integration is performed over the solid angle (in between the square brackets) to distinguish the integrand variables. Substituting again for $\boldsymbol{I}_0(0,\mu,\varphi)=\delta(\mu-\mu_0)\delta(\varphi-$

$\varphi_0)\pi\boldsymbol{F}_0$ gives

$$\begin{aligned}\boldsymbol{I}(b',-\mu,\varphi) =& \frac{1}{\pi}\int_0^1 \mu' d\mu \int_0^{2\pi} d\varphi' \boldsymbol{R}''(\mu,\mu',\varphi-\varphi')\left[e^{-b'/\mu'}\delta(\mu'-\mu_0)\delta(\varphi'-\varphi_0)\pi\boldsymbol{F}_0\right.\\ &\left.+\frac{1}{\pi}\int_0^1 \mu'' d\mu'' \int_0^{2\pi} d\varphi'' \boldsymbol{D}(b',\mu',\mu'',\varphi'-\varphi'')\delta(\mu''-\mu_0)\delta(\varphi''-\varphi_0)\pi\boldsymbol{F}_0\right]\\ =& \frac{1}{\pi}\int_0^1 \mu' d\mu \int_0^{2\pi} d\varphi' \boldsymbol{R}''(\mu,\mu',\varphi-\varphi')\left[e^{-b'/\mu'}\delta(\mu'-\mu_0)\delta(\varphi'-\varphi_0)\pi\boldsymbol{F}_0\right]\\ &+\frac{1}{\pi}\int_0^1 \mu' d\mu \int_0^{2\pi} d\varphi' \boldsymbol{R}''(\mu,\mu',\varphi-\varphi')\\ &\left[\frac{1}{\pi}\int_0^1 \mu'' d\mu'' \int_0^{2\pi} d\varphi'' \boldsymbol{D}(b',\mu',\mu'',\varphi'-\varphi'')\delta(\mu''-\mu_0)\delta(\varphi''-\varphi_0)\pi\boldsymbol{F}_0\right]\\ =& \mu_0\boldsymbol{R}''(\mu,\mu_0,\varphi-\varphi_0)\left[e^{-b'/\mu_0}\boldsymbol{F}_0\right]\\ &+\frac{1}{\pi}\int_0^1 \mu' d\mu \int_0^{2\pi} d\varphi' \boldsymbol{R}''(\mu,\mu',\varphi-\varphi')\boldsymbol{D}(b',\mu',\mu_0,\varphi'-\varphi_0)\mu_0\boldsymbol{F}_0 \end{aligned} \tag{A.46}$$

Recall from Equations 2.58 and 2.56 that the light traveling upward at the interface for a monodirectional incident beam may be presented by

$$\boldsymbol{I}(b',-\mu,\varphi) = \mu_0\boldsymbol{U}(b',\mu,\mu',\varphi-\varphi')\boldsymbol{F}_0 \tag{A.47}$$

Equation Equations A.46 and A.47 gives

$$\begin{aligned}&\mu_0\boldsymbol{U}(b',\mu,\mu',\varphi-\varphi')\boldsymbol{F}_0 =\\ &\mu_0\boldsymbol{R}''(\mu,\mu_0,\varphi-\varphi_0)e^{-b'/\mu_0}\boldsymbol{F}_0 + \frac{1}{\pi}\int_0^1 \mu' d\mu \int_0^{2\pi} d\varphi' \boldsymbol{R}''(\mu,\mu',\varphi-\varphi')\boldsymbol{D}(b',\mu',\mu_0,\varphi'-\varphi_0)\mu_0\boldsymbol{F}_0 \end{aligned} \tag{A.48}$$

Dividing both sides of Equation A.48 by $\mu\boldsymbol{F}_0$ gives the desired adding equation for the upward traveling light at the interface (cf. Equation 3.8):

$$\boxed{\begin{aligned}\boldsymbol{U}(b',\mu,\mu_0,\varphi-\varphi_0) =& e^{-b'/\mu_0}\boldsymbol{R}''(\mu,\mu_0,\varphi-\varphi_0)\\ &+\frac{1}{\pi}\mu' d\mu' \int_0^{2\pi} d\varphi' \boldsymbol{R}''(\mu,\mu',\varphi-\varphi')\boldsymbol{D}(b',\mu',\mu_0,\varphi'-\varphi_0)\end{aligned}} \tag{A.49}$$

The light traveling upward at the interface is also the incident light at the bottom of the top layer, hence, at the top of the top layer $\tau = 0$ the upward traveling radiance is (cf. Equation 2.63)

$$\begin{aligned}\boldsymbol{I}(0,-\mu,\varphi) =& e^{-b'/\mu}\boldsymbol{I}_{inc}(b',-\mu,\varphi) + \frac{1}{\pi}\int_0^1 \mu' d\mu' \int_0^{2\pi} d\varphi \boldsymbol{T}'^*(\mu,\mu',\varphi-\varphi')\boldsymbol{I}_{inc}(b',-\mu,\varphi)\\ =& e^{-b'/\mu}\left[\mu_0\boldsymbol{U}(b',\mu,\mu_0,\varphi-\varphi_0)\boldsymbol{F}_0\right] + \frac{1}{\pi}\int_0^1 \mu' d\mu' \int_0^{2\pi} d\varphi \boldsymbol{T}'^*(\mu,\mu',\varphi-\varphi')\left[\mu_0\boldsymbol{U}(b',\mu',\mu_0,\varphi'-\varphi_0)\boldsymbol{F}_0\right]\end{aligned} \tag{A.50}$$

Note that the light described by Equation A.50 emerging at the top of the top layer represents *only* the contribution of the bottom layer to the reflected light by the combined layer. Therefore, we can write

$$\begin{aligned}&\mu_0\left[\boldsymbol{R}(\mu,\mu_0,\varphi-\varphi_0) - \boldsymbol{R}'(\mu,\mu_0,\varphi-\varphi_0)\right]\boldsymbol{F}_0 =\\ &e^{-b'/\mu}\left[\mu_0\boldsymbol{U}(b',\mu,\mu_0,\varphi-\varphi_0)\boldsymbol{F}_0\right] + \frac{1}{\pi}\int_0^1 \mu' d\mu' \int_0^{2\pi} d\varphi \boldsymbol{T}'^*(\mu,\mu',\varphi-\varphi')\left[\mu_0\boldsymbol{U}(b',\mu',\mu_0,\varphi'-\varphi_0)\boldsymbol{F}_0\right]\end{aligned} \tag{A.51}$$

By dividing both sides of Equation A.51 by $\mu_0\boldsymbol{F}_0$ the desired adding equation for the reflected light at the top of the combined layer may be given by (cf. Equation 3.9)

$$\boxed{\begin{aligned}\boldsymbol{R}(\mu,\mu_0,\varphi-\varphi_0) =& \boldsymbol{R}'(\mu,\mu_0,\varphi-\varphi_0) + e^{-b'/\mu}\boldsymbol{U}(b',\mu,\mu_0,\varphi-\varphi_0)\\ &+\frac{1}{\pi}\int_0^1 \mu' d\mu' \int_0^{2\pi} d\varphi \boldsymbol{T}'^*(\mu,\mu',\varphi-\varphi')\boldsymbol{U}(b',\mu',\mu_0,\varphi'-\varphi_0)\end{aligned}} \tag{A.52}$$

The light traveling downward at the interface is also the incident light at the top of the bottom layer, hence, at the bottom of the bottom layer ($\tau = b''$) the transmitted radiance is (cf. Equation 2.54)

$$\begin{aligned}\boldsymbol{I}(b'',\mu,\varphi) &= \frac{1}{\pi}\int_0^1 \mu' d\mu' \int_0^{2\pi} d\varphi' \boldsymbol{T}''(\mu,\mu',\varphi-\varphi')\boldsymbol{I}_{inc}(b',\mu',\varphi') + e^{-b''/\mu}\boldsymbol{I}_{inc}(b',\mu',\varphi') \\ &= \frac{1}{\pi}\int_0^1 \mu' d\mu' \int_0^{2\pi} d\varphi' \boldsymbol{T}''(\mu,\mu',\varphi-\varphi')\left[\mu_0\boldsymbol{D}(b',\mu,\mu_0,\varphi-\varphi_0)\boldsymbol{F}_0\right] + e^{-b''/\mu}\left[\mu_0\boldsymbol{D}(b',\mu,\mu_0,\varphi-\varphi_0)\boldsymbol{F}_0\right]\end{aligned} \tag{A.53}$$

Note that the light described by Equation A.53 emerging at the bottom of the bottom layer represents *only* the transmittance of the incident light at the interface that was scattered at least once in the upper layer (see Section 2.2.2 for the definition of the multiple scattering matrices). Therefore, we can write for the combined layer

$$\begin{aligned}&\mu_0\boldsymbol{T}(\mu,\mu_0,\varphi-\varphi_0)\boldsymbol{F}_0 = \boldsymbol{I}_{inc,unscattered}(b',\mu,\mu_0,\varphi-\varphi_0)\boldsymbol{T}''(\mu,\mu_0,\varphi-\varphi_0) \\ &+\frac{1}{\pi}\int_0^1 \mu' d\mu' \int_0^{2\pi} d\varphi' \boldsymbol{T}''(\mu,\mu',\varphi-\varphi')\left[\mu_0\boldsymbol{D}(b',\mu,\mu_0,\varphi-\varphi_0)\boldsymbol{F}_0\right] + e^{-b''/\mu}\left[\mu_0\boldsymbol{D}(b',\mu,\mu_0,\varphi-\varphi_0)\boldsymbol{F}_0\right] \\ &= \mu_0 e^{-b'/\mu_0}\boldsymbol{T}''(\mu,\mu_0,\varphi-\varphi_0)\boldsymbol{F}_0 + \frac{1}{\pi}\int_0^1 \mu' d\mu' \int_0^{2\pi} d\varphi' \boldsymbol{T}''(\mu,\mu',\varphi-\varphi')\left[\mu_0\boldsymbol{D}(b',\mu,\mu_0,\varphi-\varphi_0)\boldsymbol{F}_0\right] \\ &+ e^{-b''/\mu}\left[\mu_0\boldsymbol{D}(b',\mu,\mu_0,\varphi-\varphi_0)\boldsymbol{F}_0\right]\end{aligned} \tag{A.54}$$

By dividing both sides of Equation A.54 by $\mu_0\boldsymbol{F}_0$ the desired adding equation for the transmitted light at the bottom of the combined layer may be given by (cf. Equation 3.10)

$$\boxed{\begin{aligned}\boldsymbol{T}(\mu,\mu_0,\varphi-\varphi_0) = e^{-b''/\mu}\boldsymbol{D}(b',\mu,\mu_0,\varphi-\varphi_0) + e^{-b'/\mu_0}\boldsymbol{T}''(\mu,\mu_0,\varphi-\varphi_0) \\ +\frac{1}{\pi}\int_0^1 \mu' d\mu' \int_0^{2\pi} d\varphi' \boldsymbol{T}''(\mu,\mu',\varphi-\varphi')\boldsymbol{D}(b',\mu',\mu_0,\varphi'-\varphi_0)\end{aligned}} \tag{A.55}$$

A.4. Supermatrix Multiplications

In the following the supermatrix multiplications are explained with examples using hypothetical small Gauss sets. First, for the 'normal' situation which may be used in one medium, either air or water, such that the supermatrices are square as in the paper of de Haan et al. (1987). Then, we show the supermatrix multiplications that occur when the light beam travels from one medium to the other, where different Gauss sets are used for the two media such that rectangular supermatrices need to be employed.

A.4.1. Square Supermatrices

This appendix provides an elaborated example of the multiplication of two multiple scattering matrices $\boldsymbol{L}$ and $\boldsymbol{M}$ which is used in the doubling-adding routine of de Haan et al. (1987). Recall from Equation 3.21 that this multiplication could be written as

$$\boldsymbol{K}^j(\mu,\mu_0) = 2\int_0^1 \mu' d\mu' \boldsymbol{L}^j(\mu,\mu')\boldsymbol{M}^j(\mu,\mu_0) \tag{A.56}$$

where j is the Fourier index that will be omitted in what follows, μ is the directional cosine of the zenith angle of the scattered beam by $\boldsymbol{L}$, μ_0 is the directional cosine of the zenith angle of the incident beam in $\boldsymbol{M}$ and μ' is the directional cosine of the zenith angle of the beam transferred from the scattering event described by $\boldsymbol{M}$ towards the scattering event described by $\boldsymbol{L}$. Note that the integration needs to be performed over μ' for which we can use numerical Gauss integration. Let us take a hypothetical Gauss set: $\{\mu_i\}_{i=1}^2=[\mu_1,\mu_2]$, which is both used for the incident, transferred and scattered light, i.e.: $\{\mu'\}=\{\mu_0\}=\{\mu\}$. This means that, for the incident and scattered directions of the resulting matrix $\boldsymbol{K}$, we have 4 combinations: $\mu_1\mu_1$, $\mu_1\mu_2$, $\mu_2\mu_1$ and $\mu_2\mu_2$. Writing the right hand side of Equation A.56, for the first combination, as the integrand function $f(\mu')$ of the numerical Gaussian quadrature formula (Equation 3.20), Equation A.56 becomes

$$\boldsymbol{K}(\mu_1,\mu_1) = \sum_{i=1}^{2} 2\omega_i\mu_i\boldsymbol{L}(\mu_1,\mu_i)\boldsymbol{M}(\mu_i,\mu_1) \tag{A.57}$$

$$= 2\omega_1\mu_1\boldsymbol{L}(\mu_1,\mu_1)\boldsymbol{M}(\mu_1,\mu_1) + 2\omega_2\mu_2\boldsymbol{L}(\mu_1,\mu_2)\boldsymbol{M}(\mu_2,\mu_1) \tag{A.58}$$

Similar expressions can be found for the other three combinations in our example: $\mu_1\mu_2$, $\mu_2\mu_1$ and $\mu_2\mu_2$, which can also be written as a matrix multiplication:

$$\begin{pmatrix} \boldsymbol{K}(\mu_1,\mu_1) & \boldsymbol{K}(\mu_1,\mu_2) \\ \boldsymbol{K}(\mu_2,\mu_1) & \boldsymbol{K}(\mu_2,\mu_2) \end{pmatrix} = \begin{pmatrix} 2\omega_1\mu_1\boldsymbol{L}(\mu_1,\mu_1) & 2\omega_2\mu_2\boldsymbol{L}(\mu_1,\mu_2) \\ 2\omega_1\mu_1\boldsymbol{L}(\mu_2,\mu_1) & 2\omega_2\mu_2\boldsymbol{L}(\mu_2,\mu_2) \end{pmatrix} \begin{pmatrix} \boldsymbol{M}(\mu_1,\mu_1) & \boldsymbol{M}(\mu_1,\mu_2) \\ \boldsymbol{M}(\mu_2,\mu_1) & \boldsymbol{M}(\mu_2,\mu_2) \end{pmatrix} \tag{A.59}$$

which is called a multiplication of *supermatrices*. In order to obtain maximum symmetry de Haan et al. (1987) wrote the supermatrices (Equation 3.22) as

$$\begin{pmatrix} s_1\boldsymbol{K}(\mu_1,\mu_1)s_1 & s_1\boldsymbol{K}(\mu_1,\mu_2)s_2 \\ s_2\boldsymbol{K}(\mu_2,\mu_1)s_1 & s_2\boldsymbol{K}(\mu_2,\mu_2)s_2 \end{pmatrix} = \begin{pmatrix} s_1\boldsymbol{L}(\mu_1,\mu_1)s_1 & s_1\boldsymbol{L}(\mu_1,\mu_2)s_2 \\ s_2\boldsymbol{L}(\mu_2,\mu_1)s_1 & s_2\boldsymbol{L}(\mu_2,\mu_2)s_2 \end{pmatrix} \begin{pmatrix} s_1\boldsymbol{M}(\mu_1,\mu_1)s_1 & s_1\boldsymbol{M}(\mu_1,\mu_2)s_2 \\ s_2\boldsymbol{M}(\mu_2,\mu_1)s_1 & s_2\boldsymbol{M}(\mu_2,\mu_2)s_2 \end{pmatrix} \tag{A.60}$$

where s_1 and s_2 are the supermatrix factors $\sqrt{2\omega_1\mu_1}$ and $\sqrt{2\omega_1\mu_1}$ respectively. It can readily be shown that Equation A.60 is equivalent to the multiplication of Equation A.59 when the supermatrix factors are taken care of properly:

$$\begin{pmatrix} s_1\boldsymbol{L}(\mu_1,\mu_1)s_1 & s_1\boldsymbol{L}(\mu_1,\mu_2)s_2 \\ s_2\boldsymbol{L}(\mu_2,\mu_1)s_1 & s_2\boldsymbol{L}(\mu_2,\mu_2)s_2 \end{pmatrix} \begin{pmatrix} s_1\boldsymbol{M}(\mu_1,\mu_1)s_1 & s_1\boldsymbol{M}(\mu_1,\mu_2)s_2 \\ s_2\boldsymbol{M}(\mu_2,\mu_1)s_1 & s_2\boldsymbol{M}(\mu_2,\mu_2)s_2 \end{pmatrix} = \tag{A.61}$$

$$\begin{pmatrix} s_1^4\boldsymbol{L}(\mu_1,\mu_1)\boldsymbol{M}(\mu_1,\mu_1) + s_1^2s_2^2\boldsymbol{L}(\mu_1,\mu_2)\boldsymbol{M}(\mu_2,\mu_1) & s_1^3s_2\boldsymbol{L}(\mu_1,\mu_1)\boldsymbol{M}(\mu_1,\mu_2) + s_1s_2^3\boldsymbol{L}(\mu_1,\mu_2)\boldsymbol{M}(\mu_2,\mu_2) \\ s_1^3s_2\boldsymbol{L}(\mu_2,\mu_1)\boldsymbol{M}(\mu_1,\mu_1) + s_2^3s_1\boldsymbol{L}(\mu_2,\mu_2)\boldsymbol{M}(\mu_2,\mu_1) & s_1^2s_2^2\boldsymbol{L}(\mu_2,\mu_1)\boldsymbol{M}(\mu_1,\mu_2) + s_2^4\boldsymbol{L}(\mu_2,\mu_2)\boldsymbol{M}(\mu_1,\mu_2) \end{pmatrix} =$$

$$\begin{pmatrix} s_1^2(s_1^2\boldsymbol{L}(\mu_1,\mu_1)\boldsymbol{M}(\mu_1,\mu_1) + s_2^2\boldsymbol{L}(\mu_1,\mu_2)\boldsymbol{M}(\mu_1,\mu_2)) & s_2s_1(s_1^2\boldsymbol{L}(\mu_1,\mu_1)\boldsymbol{M}(\mu_1,\mu_2) + s_2^2\boldsymbol{L}(\mu_1,\mu_2)\boldsymbol{M}(\mu_2,\mu_2)) \\ s_2s_1(s_1^2\boldsymbol{L}(\mu_2,\mu_1)\boldsymbol{M}(\mu_1,\mu_1) + s_2^2\boldsymbol{L}(\mu_2,\mu_2)\boldsymbol{M}(\mu_2,\mu_1)) & s_2^2(s_1^2\boldsymbol{L}(\mu_2,\mu_1)\boldsymbol{M}(\mu_1,\mu_2) + s_2^2\boldsymbol{L}(\mu_2,\mu_2)\boldsymbol{M}(\mu_1,\mu_2)) \end{pmatrix} =$$

$$\begin{pmatrix} s_1\boldsymbol{K}(\mu_1,\mu_1)s_1 & s_1\boldsymbol{K}(\mu_1,\mu_2)s_2 \\ s_2\boldsymbol{K}(\mu_2,\mu_1)s_1 & s_2\boldsymbol{K}(\mu_2,\mu_2)s_2 \end{pmatrix} \tag{A.62}$$

Removing the supermatrix factors s_1 and s_2 results in the left-hand side of Equation A.59.

A.4.2. Rectangular Supermatrices

In Section 6.3 it was explained that, when using a different set of Gauss points for the atmosphere and ocean, the transmission matrix of the interface for illumination from above, $\boldsymbol{T}_i$, and below, $\boldsymbol{T}_i^*$, become rectangular. Here we will show that using rectangular transmission matrices we indeed still can use the adding equations in supermatrix form of de Haan et al. (1987). We show two examples, one for Equation 6.10 and one for Equation 6.12, since in only these equations the rectangular transmission matrices appear. The supermatrix $\boldsymbol{D}$ is also rectangular, but the dimensions in its multiplication by $\boldsymbol{R}_W$ in Equation 6.11 are equivalent to the supermatrix dimensions in Equation 6.12.

Let us first analyze Equation 6.10: $\boldsymbol{D} = \boldsymbol{T}_i + \boldsymbol{Q}\boldsymbol{T}_i$. In this appendix we focus only on the supermatrix multiplication $\boldsymbol{Q}\boldsymbol{T}_i$, because the addition of two supermatrices of equal dimensions is a straightforward element-wise matrix addition. Recall from Equation 3.21 that the multiplication of the two multiple scattering matrices, before writing them in supermatrix form, can be written as

$$\boldsymbol{K}^j(\mu,\mu_0) = 2\int_0^1 \mu' d\mu' \boldsymbol{Q}^j(\mu,\mu')\boldsymbol{T}_i^j(\mu,\mu_0) \tag{A.63}$$

where j is the Fourier index that will be omitted in what follows, μ is the directional cosine of the zenith angle of the scattered beam by $\boldsymbol{Q}$, μ_0 is the directional cosine of the zenith angle of the incident beam in $\boldsymbol{T}_i$ and μ' is the directional cosine of the zenith angle of the beam transferred from the scattering event described by $\boldsymbol{T}_i$ towards the scattering event described by $\boldsymbol{Q}$. Note again that the integration needs to be performed over μ' for which we can use numerical Gauss integration. Let us take a hypothetical Gauss set for the atmosphere: $\{\mu_i\}_{i=8}^{9}$=[μ_8,μ_9] and a hypothetical Gauss set for the ocean: $\{\mu_i\}_{i=1}^{3}$=[μ_1,μ_2,μ_3]. It should be emphasized that these sets have a different number of Gauss points, but that the Gauss points among the sets also differ from each other, which is illustrated by the different subscript used for each Gauss point. So, in this case, we have $\{\mu\} = \{\mu'\} = [\mu_1,\mu_2,\mu_3]$ and $\{\mu_0\} = [\mu_8,\mu_9]$. This means that, for the incident and scattered directions of the resulting matrix $\boldsymbol{K}$, we have 6 combinations: $\mu_1\mu_8$, $\mu_2\mu_8$, $\mu_3\mu_8$, $\mu_1\mu_9$, $\mu_2\mu_9$, $\mu_3\mu_9$. Writing the right hand side of Equation A.63, for the first combination, as the integrand function $f(\mu')$ of the numerical Gaussian quadrature formula (Equation 3.20), Equation A.63 becomes

$$\boldsymbol{K}(\mu_1,\mu_1) = \sum_{i=1}^{3} 2\omega_i\mu_i\boldsymbol{Q}(\mu_1,\mu_i)\boldsymbol{T}_i(\mu_i,\mu_8) \tag{A.64}$$

$$= 2\omega_1\mu_1\boldsymbol{Q}(\mu_1,\mu_1)\boldsymbol{T}_i(\mu_1,\mu_8) + 2\omega_2\mu_2\boldsymbol{Q}(\mu_1,\mu_2)\boldsymbol{T}_i(\mu_2,\mu_8) + 2\omega_3\mu_3\boldsymbol{Q}(\mu_1,\mu_3)\boldsymbol{T}_i(\mu_3,\mu_8) \tag{A.65}$$

Similar expressions can be found for the other five combinations in our example: $\mu_2\mu_8$, $\mu_3\mu_8$, $\mu_1\mu_9$, $\mu_2\mu_9$, $\mu_3\mu_9$, which can also be written as a matrix multiplication:

$$\begin{pmatrix} \boldsymbol{K}(\mu_1,\mu_8) & \boldsymbol{K}(\mu_1,\mu_9) \\ \boldsymbol{K}(\mu_2,\mu_8) & \boldsymbol{K}(\mu_2,\mu_9) \\ \boldsymbol{K}(\mu_3,\mu_8) & \boldsymbol{K}(\mu_3,\mu_9) \end{pmatrix} = \begin{pmatrix} 2\omega_1\mu_1\boldsymbol{Q}(\mu_1,\mu_1) & 2\omega_2\mu_2\boldsymbol{Q}(\mu_1,\mu_2) & 2\omega_3\mu_3\boldsymbol{Q}(\mu_1,\mu_3) \\ 2\omega_1\mu_1\boldsymbol{Q}(\mu_2,\mu_1) & 2\omega_2\mu_2\boldsymbol{Q}(\mu_2,\mu_2) & 2\omega_3\mu_3\boldsymbol{Q}(\mu_2,\mu_3) \\ 2\omega_1\mu_1\boldsymbol{Q}(\mu_3,\mu_1) & 2\omega_2\mu_2\boldsymbol{Q}(\mu_3,\mu_2) & 2\omega_3\mu_3\boldsymbol{Q}(\mu_3,\mu_3) \end{pmatrix} \begin{pmatrix} \boldsymbol{T}_i(\mu_1,\mu_8) & \boldsymbol{T}_i(\mu_1,\mu_9) \\ \boldsymbol{T}_i(\mu_2,\mu_8) & \boldsymbol{T}_i(\mu_2,\mu_9) \\ \boldsymbol{T}_i(\mu_3,\mu_8) & \boldsymbol{T}_i(\mu_3,\mu_9) \end{pmatrix} \tag{A.66}$$

which is again a multiplication of supermatrices. In order to obtain maximum symmetry we may write

$$\begin{pmatrix} s_1\boldsymbol{R}_{WL}(\mu_1,\mu_8)s_1 & s_1\boldsymbol{R}_{WL}(\mu_1,\mu_9)s_2 \\ s_2\boldsymbol{R}_{WL}(\mu_2,\mu_8)s_1 & s_2\boldsymbol{R}_{WL}(\mu_2,\mu_9)s_2 \\ s_3\boldsymbol{R}_{WL}(\mu_3,\mu_8)s_1 & s_3\boldsymbol{R}_{WL}(\mu_3,\mu_9)s_2 \end{pmatrix} = \begin{pmatrix} s_1\boldsymbol{U}(\mu_1,\mu_1)s_1 & s_1\boldsymbol{U}(\mu_1,\mu_2)s_2 & s_1\boldsymbol{U}(\mu_1,\mu_3)s_3 \\ s_2\boldsymbol{U}(\mu_2,\mu_1)s_1 & s_2\boldsymbol{U}(\mu_2,\mu_2)s_2 & s_2\boldsymbol{U}(\mu_2,\mu_3)s_3 \\ s_3\boldsymbol{U}(\mu_3,\mu_1)s_1 & s_3\boldsymbol{U}(\mu_3,\mu_2)s_2 & s_3\boldsymbol{U}(\mu_3,\mu_3)s_3 \end{pmatrix} \begin{pmatrix} s_1\boldsymbol{T}_i(\mu_1,\mu_8)s_1 & s_1\boldsymbol{T}_i(\mu_1,\mu_9)s_2 \\ s_2\boldsymbol{T}_i(\mu_2,\mu_8)s_1 & s_2\boldsymbol{T}_i(\mu_2,\mu_9)s_2 \\ s_3\boldsymbol{T}_i(\mu_3,\mu_8)s_1 & s_3\boldsymbol{T}_i(\mu_3,\mu_9)s_2 \end{pmatrix} \tag{A.67}$$

where s_1, s_2 and s_3 are the supermatrix factors $\sqrt{2\omega_1\mu_1}$, $\sqrt{2\omega_2\mu_2}$ and $\sqrt{2\omega_3\mu_3}$ respectively. Note that the supermatrix factors originate from the matrix $\boldsymbol{Q}$ only, which means that *only the Gauss set of the ocean* is used for the supermatrix factors. It can readily be shown that Equation A.67 is equivalent to the multiplication of Equation A.66 when the supermatrix factors are taken care of properly, analogous to the multiplication of Equation A.62 of the former chapter.

Let us now analyze Equation 6.12: $\boldsymbol{R}_{WL} = \boldsymbol{T}_i^*\boldsymbol{U}$. Again, before writing the matrices in supermatrix form, we can write as a multiplication of multiple scattering matrices as

$$\boldsymbol{R}_{WL}^{j}(\mu,\mu_0) = 2\int_0^1 \mu' d\mu' \boldsymbol{T}_i^{*j}(\mu,\mu')\boldsymbol{U}^{j}(\mu,\mu_0) \tag{A.68}$$

where j is the Fourier index that will be omitted in what follows, μ is the directional cosine of the zenith angle of the scattered beam by $\boldsymbol{T}_i^*$, μ_0 is the directional cosine of the zenith angle of the incident beam in $\boldsymbol{U}$ and μ' is the directional cosine of the zenith angle of the beam transferred from the scattering event described by $\boldsymbol{U}$ towards the scattering event described by $\boldsymbol{T}_i^*$. For this equation, we may use $\{\mu'\} = [\mu_1,\mu_2,\mu_3]$ and $\{\mu_0\} = \{\mu\} = [\mu_8,\mu_9]$. This means that, for the incident and scattered directions of the resulting matrix $\boldsymbol{R}_{WL}(\mu,\mu_0)$, we have only 4 combinations: $\mu_8\mu_8$, $\mu_8\mu_9$, $\mu_9\mu_8$, $\mu_9\mu_9$. Following similar steps as in the former paragraphs of this appendix, it may readily be shown that

$$\begin{pmatrix} s_1\boldsymbol{T}_i^*(\mu_8,\mu_1)s_1 & s_1\boldsymbol{T}_i^*(\mu_8,\mu_2)s_2 & s_1\boldsymbol{T}_i^*(\mu_8,\mu_3)s_3 \\ s_2\boldsymbol{T}_i^*(\mu_9,\mu_1)s_1 & s_2\boldsymbol{T}_i^*(\mu_9,\mu_2)s_2 & s_2\boldsymbol{T}_i^*(\mu_9,\mu_3)s_3 \end{pmatrix} \begin{pmatrix} s_1\boldsymbol{U}(\mu_1,\mu_8)s_1 & s_1\boldsymbol{U}(\mu_1,\mu_9)s_2 \\ s_2\boldsymbol{U}(\mu_2,\mu_8)s_1 & s_2\boldsymbol{U}(\mu_2,\mu_9)s_2 \\ s_3\boldsymbol{U}(\mu_3,\mu_8)s_1 & s_3\boldsymbol{U}(\mu_3,\mu_9)s_2 \end{pmatrix} = \begin{pmatrix} s_1\boldsymbol{R}_{WL}(\mu_8,\mu_8)s_1 & s_1\boldsymbol{R}_{WL}(\mu_8,\mu_9)s_2 \\ s_2\boldsymbol{R}_{WL}(\mu_9,\mu_8)s_1 & s_2\boldsymbol{R}_{WL}(\mu_9,\mu_9)s_2 \end{pmatrix} \tag{A.69}$$

Removing the supermatrix factors s_1, s_2 and s_3 yields the multiple scattering matrix $\boldsymbol{R}_{WL}$ at all geometry combinations of the Gauss set *for the atmosphere*.

B

Appendix

B.1. Brewster Angle

This appendix shows the derivation of the Brewster angle for air-to-water reflection. The Fresnel reflection coefficient for the perpendicular component of the electric field vector can be evaluated as (Equation 4.43)

$$\begin{aligned} R_{\parallel} &= \frac{n_2 \cos\theta_i - n_1 \cos\theta_t}{n_2 \cos\theta_i + n_1 \cos\theta_t} \\ &= \frac{\cos\theta_i - n_1/n_2 \cos\theta_t}{\cos\theta_i + n_1/n_2 \cos\theta_t} \end{aligned} \tag{B.1}$$

Substituting Snell's law $n_1/n_1 = \sin\theta_t/\sin\theta_i$ gives

$$\begin{aligned} R_{\parallel} &= \frac{\cos\theta_i \sin\theta_i - \cos\theta_t \sin\theta_t}{\sin\theta_i \cos\theta_i + \cos\theta_t \sin\theta_t} \\ &= \frac{\cos\theta_i \sin\theta_i (\cos^2\theta_t + \sin^2\theta_t) - \cos\theta_t \sin\theta_t (\cos^2\theta_i + \sin^2\theta_i)}{\sin\theta_i \cos\theta_i (\cos^2\theta_t + \sin^2\theta_t) + \cos\theta_t \sin\theta_t (\cos^2\theta_i + \sin^2\theta_i)} \\ &= \frac{\cos\theta_i \sin\theta_i \cos^2\theta_t + \cos\theta_i \sin\theta_i \sin^2\theta_t - \cos\theta_t \sin\theta_t \cos^2\theta_i - \cos\theta_t \sin\theta_t \sin^2\theta_i}{\cos\theta_i \sin\theta_i \cos^2\theta_t + \cos\theta_i \sin\theta_i \sin^2\theta_t + \cos\theta_t \sin\theta_t \cos^2\theta_i + \cos\theta_t \sin\theta_t \sin^2\theta_i} \\ &= \frac{(\cos\theta_i \cos\theta_t - \sin\theta_i \sin\theta_t)(\sin\theta_i \cos\theta_t - \cos\theta_i \sin\theta_t)}{(\cos\theta_i \cos\theta_t + \sin\theta_i \sin\theta_t)(\sin\theta_t \cos\theta_t + \cos\theta_i \sin\theta_t)} \end{aligned} \tag{B.2}$$

Using the trigonometric identities $\sin(\alpha \pm \beta) = \sin\alpha\cos\beta \pm \cos\alpha\sin\beta$ and $\cos(\alpha \pm \beta) = \cos\alpha\cos\beta \mp \sin\alpha\sin\beta$ gives

$$R_{\parallel} = \frac{\cos(\theta_i + \theta_b)\sin(\theta_i - \theta_t)}{\cos(\theta_i - \theta_t)\sin(\theta_i + \theta_t)} \tag{B.3}$$

or (Goldstein 2003, Eq. 8-24b)

$$R_{\parallel} = \frac{\tan(\theta_i - \theta_t)}{\tan(\theta_i + \theta_t)} \tag{B.4}$$

We aim to find the combination of θ_i and θ_t where $R_{\parallel} = 0$. Note that $\tan\gamma \to \infty$ for $\gamma \to 90^{\circ}$. Therefore, $R_{\parallel} = 0$ for $\theta_i + \theta_t = 90^{\circ}$. In other words, the combination of the incidence and transmission angles at which $R_{\parallel} = 0$ are the incidence and transmission Brewster angles related by $\theta_{i,B} = 90^{\circ} - \theta_{B,t}$ or $\theta_{B,t} = 90^{\circ} - \theta_{i,B}$. This result can be substituted in Snell's law as

$$\begin{aligned} n_1 \sin\theta_{i,B} &= n_2 \sin\theta_{B,t} \\ &= n_2 \sin(90^{\circ} - \theta_{i,B}) \\ &= n_2 \cos(\theta_{i,B}) \end{aligned} \tag{B.5}$$

or

$$\tan\theta_{i,B} = \frac{n_2}{n_1} \tag{B.6}$$

Therefore, the Brewster incidence angle at which $R_\parallel$ vanishes is

$$\boxed{\theta_{i,B} = \tan^{-1}\left(\frac{n_2}{n_1}\right)} \quad \checkmark\text{Goldstein (2003)} \tag{B.7}$$

B.2. Total Internal Reflection

In this appendix the mathematical description of the reflection matrix for total internal reflection is shown. In Section 4.5 it was explained that at incidence angles bigger than the critical incidence angle zero transmission and total reflection occurs, called total internal reflection, and $\theta_t = 90^o$. The critical incidence angle was given by

$$\theta_{c,i} = \sin^{-1}\left(\frac{n_2}{n_1}\right) \tag{B.8}$$

It should be noted that at incidence angles $> \theta_{i,c}$ the polarization upon reflection and transmission versus incidence angle is not constant, as illustrated by the elements (3,3), (3,4), (4,3) and (4,4) in Figures 4.12 and 4.13. The question to be answered is: how can total internal reflection mathematically be expressed?

At total internal reflection the following holds:

$$\theta_i > \theta_{i,c} \tag{B.9a}$$

$$\sin\theta_i > \sin\theta_{i,c} \equiv \frac{n_2}{n_1} \tag{B.9b}$$

Multiply both sides by n_1/n_2

$$\frac{n_1}{n_2}\sin\theta_i > \frac{n_2}{n_1}\frac{n_1}{n_2} \tag{B.10a}$$

$$\frac{n_1}{n_2}\sin\theta_i > 1 \tag{B.10b}$$

Now, as an intermediate step we rewrite Snell's law as

$$n_1\sin\theta_i = n_2\sin\theta_t \tag{B.11a}$$

$$\sin\theta_t = \frac{n_1}{n_2}\sin\theta_i \tag{B.11b}$$

$$\sqrt{1-\cos^2\theta_t} = \frac{n_1}{n_2}\sin\theta_i \tag{B.11c}$$

$$1-\cos^2\theta_t = \frac{n_1^2}{n_2^2}\sin^2\theta_i \tag{B.11d}$$

$$\cos^2\theta_t = -\left(\frac{n_1^2}{n_2^2}\sin^2\theta_i - 1\right) \tag{B.11e}$$

$$\cos\theta_t = \sqrt{-\left(\frac{n_1^2}{n_2^2}\sin^2\theta_i - 1\right)} \tag{B.11f}$$

We know that for total internal reflection $\frac{n_1^2}{n_2^2}\sin^2\theta_i > 1$ from squaring both sides Equation B.10b. Therefore, we introduce the imaginary number $i = \sqrt{-1}$ and write Equation B.11f as

$$\cos\theta_t = i\sqrt{\frac{n_1^2}{n_2^2}\sin^2\theta_i - 1} \tag{B.12}$$

Substituting this result for $\cos\theta_t$ in the Fresnel reflection coefficient for the perpendicular component of the electric field vector yields the complex expression (Equation 4.21)

$$R_\perp = \frac{n_1\cos\theta_i - i n_2\sqrt{\frac{n_1^2}{n_2^2}\sin^2\theta_i - 1}}{n_1\cos\theta_i + i n_2\sqrt{\frac{n_1^2}{n_2^2}\sin^2\theta_i - 1}} \tag{B.13}$$

Equation B.13 may be recognized as a complex number of the form (see also Sec. 8.4.4 of Goldstein 2003)

$$y = \frac{a - ib}{a + ib} \tag{B.14}$$

where $a = n_1 \cos\theta_i$ and $b = n_2\sqrt{n_1^2/n_2^2 \sin^2\theta_i - 1}$. Now we may note the following:

$$y = \frac{a-ib}{a+ib}\frac{a-ib}{a-ib} = \frac{a^2 + 2aib - b^2}{a^2+b^2} = \frac{a^2-b^2}{a^2+b^2} + i\frac{2ab}{a^2+b^2} \tag{B.15a}$$

It can readily be shown that $y \cdot y^* = 1$:

$$y \cdot y^* = \left(\frac{a^2-b^2}{a^2+b^2} + i\frac{2ab}{a^2+b^2}\right)\left(\frac{a^2-b^2}{a^2+b^2} - i\frac{2ab}{a^2+b^2}\right) \tag{B.16a}$$

$$= \frac{a^4 - 2a^2b^2 + b^4}{a^4 + 2a^2b^2 + b^4} + \frac{4a^2b^2}{a^4+2a^2b^2+b^4} \tag{B.16b}$$

$$= \frac{a^4 + 2a^2b^2 + b^4}{a^4 + 2a^2b^2 + b^4} \tag{B.16c}$$

$$= 1 \tag{B.16d}$$

Consequently, we can write

$$y = \frac{a-ib}{a+ib} = \cos\delta_2 - i\sin\delta_2 \tag{B.17}$$

where δ_2 is the phase shift of the reflected perpendicular wave component with respect to the incident perpendicular wave component (see Section 4.2). Hence, we can distinguish between $R_\perp$ and its complex conjugate $R_\perp^*$

$$R_\perp = \frac{a^2-b^2}{a^2+b^2} - i\frac{2ab}{a^2+b^2} \tag{B.18a}$$

$$R_\perp^* = \frac{a^2-b^2}{a^2+b^2} + i\frac{2ab}{a^2+b^2} \tag{B.18b}$$

Similarly, the Fresnel reflection coefficient for the parallel component becomes

$$R_\parallel = \frac{n_2^2\cos\theta_i - in_1\sqrt{\frac{n_1^2}{n_2^2}\sin^2\theta_i - 1}}{n_2^2\cos\theta_i + in_1\sqrt{\frac{n_1^2}{n_2^2}\sin^2\theta_i - 1}} \tag{B.19}$$

and we may distinguish

$$R_\parallel = \frac{c^2-d^2}{c^2+d^2} - i\frac{2cd}{c^2+d^2} \tag{B.20a}$$

$$R_\parallel^* = \frac{c^2-d^2}{c^2+d^2} + i\frac{2cd}{c^2+d^2} \tag{B.20b}$$

where $c = n_2^2\cos\theta_i$ and $d = n_1\sqrt{n_1^2/n_2^2\sin^2\theta_i - 1}$.

Now let us analyze the reflection matrix elements. We already proved above that $y \cdot y^* = R_\perp \cdot R_\perp^* = |R_\perp|^2 = 1$. Similarly, $|R_\perp|^2 = 1$ and the first four upper left elements of the reflection matrix for $\theta_i > \theta_{i,c}$ are (cf. Equation 4.66)

$$R_{f1,1} = \frac{1}{2}(|R_\parallel|^2 + |R_\perp|)^2 = 1 \tag{B.21}$$

$$R_{f1,2} = \frac{1}{2}(|R_\parallel|^2 + |R_\perp|)^2 = 0 \tag{B.22}$$

$$R_{f2,1} = \frac{1}{2}(|R_\parallel|^2 + |R_\perp|)^2 = 0 \tag{B.23}$$

$$R_{f2,2} = \frac{1}{2}(|R_\parallel|^2 + |R_\perp|)^2 = 1 \tag{B.24}$$

✓Garcia (2012*a*)

The remaining matrix elements are:

$$\boxed{\begin{aligned} R_{f3,3} &= \mathrm{Re}(R_{\parallel} R_{\perp}^{*}) \\ R_{f3,4} &= \mathrm{Im}(R_{\parallel} R_{\perp}^{*}) \\ R_{f4,3} &= \mathrm{Im}(R_{\perp} R_{\parallel}^{*}) \\ R_{f4,4} &= \mathrm{Re}(R_{\parallel} R_{\perp}^{*}) \end{aligned}} \quad \checkmark \text{Garcia (2012}a\text{)} \tag{B.25–B.28}$$

where the complex numbers $R\parallel$, $R_{\parallel}^{*}$, $R_{\perp}$ and $R_{\perp}^{*}$ were defined by Equations B.20a, B.20b, B.18a and B.18b.

B.3. Computing the Bulk Ocean Reflection with a Bio-optical Model for Case 1 Waters

This appendix explains the approach of Morel (1988) and Morel and Maritorena (2001) of semi-analytically modelling the reflectance of oceanic Case 1 Waters as functions of chlorophyll concentration. Case 1 Waters were defined by Morel and Prieur (1977) as waters whose optical properties are dominated by phytoplankton and their derivatives rather than by yellow substance.[1] Note that we only apply this model for the comparison with our results from the adding-doubling method in the water.

The bulk ocean reflection has a very strong dependence on wavelength and pigment concentration but a weak dependence on geometry (Sayer et al. 2010). Accordingly, Sun and Lukashin (2013) assumed the subsurface oceanic layer reflection to be Lambertian, similar to the whitecap reflection, meaning that only the scalar case for unpolarized reflected light may be considered. The model of Morel (1988) was used, who parameterized the reflectance of the underwater volume as (Morel 1988, Eq. 15)

$$R_W = f \cdot b_b(\lambda)/a(\lambda) \tag{B.29}$$

which is valid for $b_b \ll a$ and where R_W is the wavelength dependent ratio of the upwelling and downwelling unpolarized flux and $b_b(\lambda)$ and $a(\lambda)$ are the wavelengths dependent backscattering and absorption coefficients respectively for the oceanic water volume. The scalar f was set at 0.33 by Morel (1988); later Morel and Gentili (1991) expanded the expression for f as functions of solar zenith angle and the proportion of backscattering due to water molecules ($\eta_b = b_{bw}/b_b$). According to Morel and Gentili (1991) their expression for f is accurate within 1.5 % for $\vartheta_0 < 70^o$ and 4% for $70^o < \vartheta_0 < 80^o$. In our computations, we set f equal to 0.33. In the next paragraphs it will be explained how b_b and a may be determined.

An apparent optical property that is relatively insensitive to environmental factors and is strongly correlated with chlorophyll concentration is the *diffuse attenuation coefficient for downward irradiance* K_d in m^{-1} defined through (Mobley 1994, Eq. 3.21)

$$E_d(z,\lambda) = E_d(0,\lambda)\exp\left[-\int_0^z K_d(z',\lambda)dz'\right] \approx E_d(0,\lambda)\exp\left[-\overline{K}_d(z,\lambda)z\right] \tag{B.30}$$

where $E_d(z,\lambda)$ is the downwelling irradiance at depth z and $\overline{K}_d$ is the mean diffusive attenuation coefficient for downward irradiance over the depth 0 to z. The mean quantity $\overline{K}_d$ is generally employed (see e.g. Chowdhary et al. 2006; Morel 1988; Morel and Maritorena 2001) and therefore the overbar is omitted in what follows. Also, for convenience, the subscript d is omitted. Since K depends weakly on depth for vertically well mixed water (Mobley 1994, p. 71) it may be written in that case as (Morel and Maritorena 2001, Eq. 3)

$$K(\lambda) = K_w(\lambda) + K_{bio}(\lambda) \tag{B.31}$$

with

$$K_w(\lambda) = a_w(\lambda) + 0.5 b_w(\lambda) \tag{B.32}$$

and

$$K_{bio}(\lambda) = \chi(\lambda)[\mathrm{Chl}]^{e(\lambda)} \tag{B.33}$$

where the absorption coefficient of the seawater a_w and the scattering coefficient of the seawater b_w may be obtained from Smith and Baker (1981) and Pope and Fry (1997) respectively. K_{bio} represents the diffuse attenuation coefficient of all biogenic matter (particulate and dissolved) and possibly bubbles (see Morel and Maritorena 2001, Sec. 3.1). Morel and Maritorena (2001) used measurements of the JGOFS[2] (Joint Global Ocean Flux Study) cruises to study the relation between $[K(\lambda) - K_w(\lambda)]$ and [Chl] on a logarithmic scale and retrieved the coefficients $\chi(\lambda)$ and $e(\lambda)$ from linear regression analyses of the log-transformed data. These coefficients were tabulated and may be found in Table 2 of Morel and Maritorena (2001) for λ ranging from 350 to 525 nm.[3]

[1] More than 98% of the world ocean waters is presumably in this category (Morel 1988).
[2] See `http://usjgofs.whoi.edu/`.
[3] The remaining values for λ up to 700 nm were not updated by Morel and Maritorena (2001) and may be found in the 'old data set' in Table 2 of Morel (1988).

The backscattering coefficient $b_b(\lambda)$ appearing in Equation B.29 may be computed according to (Morel and Prieur 1977)

$$b_b(\lambda) = \frac{1}{2} b_w(\lambda) + b_{bp}(\lambda) \tag{B.34}$$

where b_{bp} is the backscattering coefficient for the particles and the backscattering coefficient for the water equals $b_{bw} = \frac{1}{2} b_w$ due to the symmetry of the molecular volume scattering function (Morel 1980). The values for b_w for pure water were tabulated by Morel and Prieur (1977) (380 nm - 700 nm) and by Smith and Baker (1981) (200 nm - 800 nm).

Morel and Gentili (1991) pointed out that for most open oceans [Chl] is smaller than 1 mg m^{-3}.[4] Following Morel and Maritorena (2001), the scattering coefficient for the oceanic particles in case 1 waters may then be modeled by

$$b_p(\lambda) = b_p^0 [\text{Chl}]^{0.766} (550/\lambda), \qquad b_p^0 = 0.416 \tag{B.35}$$

where b_p is again the scattering coefficient of the particles as in Equation B.34. The backscattering coefficient of the particles b_{bp} may be written in terms of the backscattering efficiency of the particle scattering q_p as (see Chowdhary et al. 2006)

$$b_{bp}(\lambda) = b_p(\lambda) q_p(\lambda) = b_p(\lambda) \left[2\pi \int_{\pi/2}^{\pi} \frac{F_p(\theta, \lambda)}{4\pi} \sin(\theta) d\theta \right] \tag{B.36}$$

where θ is the scattering angle and F_p is the particulate scattering function (or the upper left entry of the particle scattering matrix as will be discussed in the next subsection). Morel (1988) parameterized the expression for q_p based on theoretical considerations for case 1 waters described in Morel (1988) and in situ measurements. The updated version by Morel and Maritorena (2001) reads

$$q_p(\lambda) = 0.002 + 0.01\{0.50 - 0.25 \log_{10}[\text{Chl}] (\lambda/550)^k\} \tag{B.37}$$

where

$$k = \begin{cases} 0.5(\log_{10}[\text{Chl}] - 0.3) & 0.02 \leq [\text{Chl}] \leq 2 \text{ mg m}^{-3} \\ 0 & \text{otherwise} \end{cases} \tag{B.38}$$

Neglecting the change of the albedo of the bulk ocean R_W with depth and using the Gershun's divergence law for irriadiance (see Prieur and Sathyendranath 1981), Morel and Maritorena (2001) used for the absorption coefficient a the following analytical relation

$$a(\lambda) = K(\lambda)[1 - R_W(\lambda)] \frac{\mu_d \mu_u}{\mu_d R_W(\lambda) + \mu_u} \tag{B.39}$$

where μ_d and μ_u are the average directional cosines for upward and downward underwater radiative transfer respectively which were tabulated by Morel and Maritorena (2001). Consequently, from Equations B.38, B.37 and B.35 the value for b_{bp} may be computed with Equation B.36. Substituting b_{bp} into Equation B.34 will give the backscattering coefficient b_b. Then, by substituting Equation B.29 into B.39 the absorption coefficient a and albedo of the bulk ocean R_W may solved for simultaneously (Chowdhary et al. 2006).

[4] Morel and Maritorena (2001) argued that in this case b_w at $\lambda = 550$ nm may be neglected which results in the relation of Equation B.35. The complete argumentation may be found in Section 3.4 of Morel and Maritorena (2001).

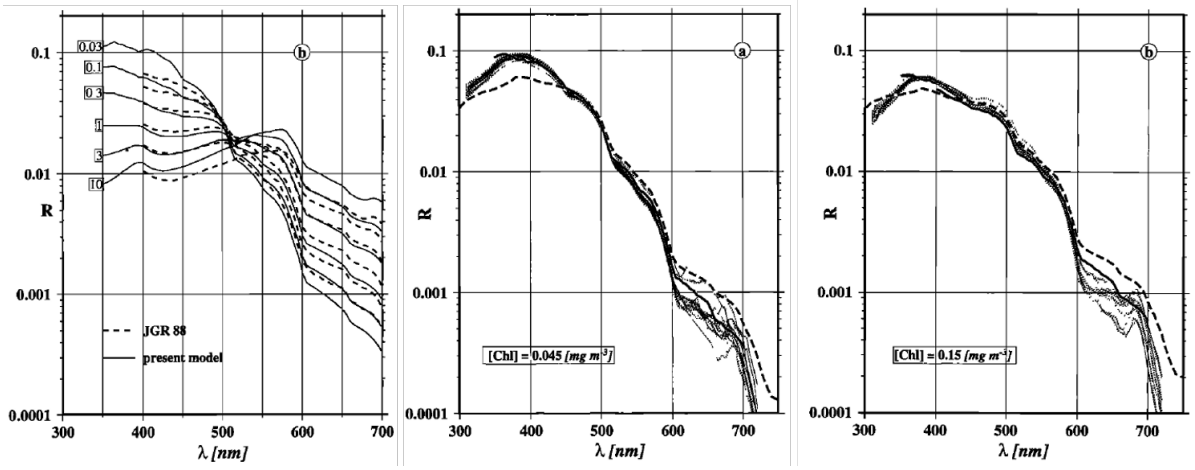

Figure B.1: Left figure: modeled underwater reflectance with bio-optical model of Morel (1988) (dashed line) and Morel and Maritorena (2001) (solid line) as functions of wavelength for distinct chlorophyll concentrations. Middle and right figure: comparison between modeled and measured underwater reflectance data during five days at two locations in the tropical Pacific. Solid line = model of Morel and Maritorena (2001); dashed line = model of Morel (1988); dotted line = measured data. The average chlorophyll concentrations at 0-15 m for both locations are presented in the legends. (Morel and Maritorena 2001, Fig. 8 and 10)

Figure B.1 shows the results of the bio-optical model of Morel (1988) and Morel and Maritorena (2001) and compares them with the measured underwater reflectance. It should be noted that the models do not take into account inelastic scattering. According to Morel and Maritorena (2001), the negligence of Raman scattering might be the explanation of the 8-15% underestimation, though barely visible in Figure B.1, of the Morel and Maritorena (2001) model w.r.t the measurements. The second peak in the data for [Chl] = 0.15 mg m^{-3} (right figure) around 683 nm is the fluorescence contribution which was also neglected in the models. For excellent reported applications of the bio-optical model of Morel and Maritorena (2001) the reader is referred to Chowdhary et al. (2006) (Sec. 2B) and Chowdhary et al. (2012) (Sec. 3.2).

B.4. Effect of Assumption of Geometric Water Layer Thickness

In many papers (Chowdhary et al. 2006; Xu et al. 2016; Zhai et al. 2010), often an optical thickness of 10 is taken for the water layer. Using one optical thickness for all wavelengths is a good assumption when the water layer represents an ocean that is infinitely deep. That is, all the light beams are allowed to travel into the deep sea until they are attenuated until a similar limit, allowing the geometric path lengths to be longer for the blue wavelengths (where there is little absorption) than the red wavelengths.

In this research, however, we defined the water layer thickness by its geometric ocean depth (see Chapter 6) which we set equal to 100 m (Chapter 6). By multiplying with the beam attenuation coefficient, the optical thickness was computed. This may seem less realistic than the approach mentioned in the former paragraph, but (1) it is uncertain how deep the oceans are on exoplanets (i.e. there is no evidence that the ocean on exoplanets do not have a finite geometric depth) and (2) using a finite depth allows us to use a nonzero ocean bottom in future studies. Most importantly, however, it can be shown that the two approaches do not yield significant different results.

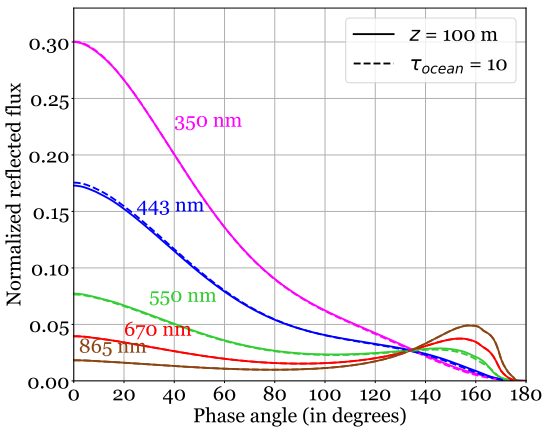

(a)

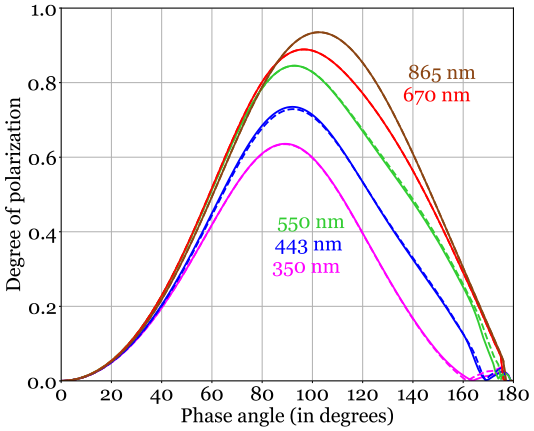

(b)

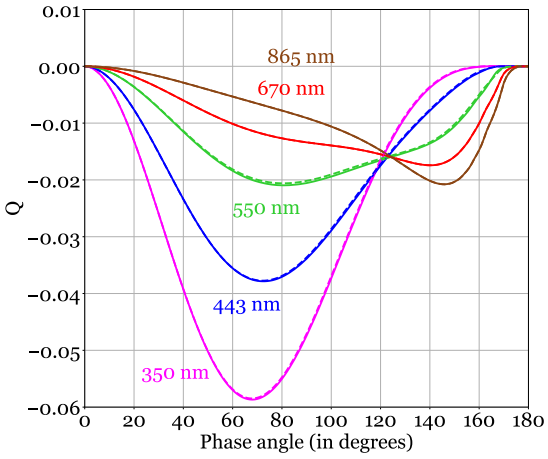

(c)

Figure B.2: Normalized reflected flux (a), degree of polarization (b) and Stokes parameter Q (c) of light reflected by a clear ocean planet. Solid line: ocean depth is defined by its geometric ocean depth, $z = 100$ m. Dashed line: ocean depth is defined by its optical thickness, $\tau_{ocean} = 10$. The wind speed equals 7 m/s in all curves.

Figure B.2 shows the planetary phase curve of the normalized reflected flux, degree of polarization and Stokes parameter Q of light reflected by a clear ocean planet. Only 443 nm seems to be slightly affected, the changes at the other wavelengths can hardly be detected. This may be explained by the fact that in both cases the

ocean is thick enough such that the scattering increase with layer thickness is converged at short wavelengths, and that at long wavelengths absorption is dominant. Because of the uncertainties of the absorption coefficient at 443 nm (which were mentioned in Chapter 6), we conclude that the geometric depth of 100 m is a valid assumption for this application.

Bibliography

Badoz, J., Liboux, M. L., Nahoum, R., Israel, G., Raulin, F. and Torre, J. P. (1992), 'A sensitive cryogenic refractometer. Application to the refractive index determination of pure or mixed liquid methane, ethane, and nitrogen', *Review of Scientific Instruments* **63**, 2967–2973.

Bailey, J. (2007), 'Rainbows, Polarization, and the Search for Habitable Planets', *Astrobiology* **7**, 320–332.

Beichman, C., Doyon, R., Greene, T., Hodapp, K., Horner, S., Krist, J., McCarthy, D., Meyer, M., Rieke, M., Stansberry, J., Stauffer, J., Trauger, J. and NIRCam Team (2014), The Near-Infrared Camera on the James Webb Space Telescope: The Next Great Step in Exoplanet Research, *in* D. Apai and P. Gabor, eds, 'Search for Life Beyond the Solar System. Exoplanets, Biosignatures & Instruments', p. 4.12.

Boccaletti, A., Lagage, P.-O., Baudoz, P., Beichman, C., Bouchet, P., Cavarroc, C., Dubreuil, D., Glasse, A., Glauser, A. M., Hines, D. C., Lajoie, C.-P., Lebreton, J., Perrin, M. D., Pueyo, L., Reess, J. M., Rieke, G. H., Ronayette, S., Rouan, D., Soummer, R. and Wright, G. S. (2015), 'The Mid-Infrared Instrument for the James Webb Space Telescope, V: Predicted Performance of the MIRI Coronagraphs', *Publications of the Astronomical Society of the Pacific* **127**, 633.

Boesche, E., Stammes, P. and Bennartz, R. (2009), 'Aerosol influence on polarization and intensity in near-infrared O_2 and CO_2 absorption bands observed from space', *Journal of Quantitative Spectroscopy and Radiative Transfer* **110**, 223–239.

Born, M. and Wolf, E. (1959), *Principles of Optics*, Pergamon Press, London.

Breon, F. M. (1993), 'An analytical model for the cloud-free atmosphere/ocean system reflectance', *Remote Sensing of Environment* **43**, 179–192.

Bréon, F. M. and Henriot, N. (2006), 'Spaceborne observations of ocean glint reflectance and modeling of wave slope distributions', *Journal of Geophysical Research (Oceans)* **111**, C06005.

Chandrasekhar, S. (1950), *Radiative transfer.*, Clarendon Press, Oxford.

Chowdhary, J. (1999), Multiple scattering of polarized light in atmosphere- ocean systems: Application to sensitivity analyses of aerosol polarimetry, PhD thesis, COLUMBIA UNIVERSITY.

Chowdhary, J., Cairns, B. and Travis, L. D. (2006), 'Contribution of water-leaving radiances to multiangle, multispectral polarimetric observations over the open ocean: bio-optical model results for case 1 waters', *Applied Optics* **45**, 5542–5567.

Chowdhary, J., Cairns, B., Waquet, F., Knobelspiesse, K., Ottaviani, M., Redemann, J., Travis, L. and Mishchenko, M. (2012), 'Sensitivity of multiangle, multispectral polarimetric remote sensing over open oceans to water-leaving radiance: Analyses of RSP data acquired during the MILAGRO campaign', *Remote Sensing of Environment* **118**, 284–308.

Cowan, N. B., Abbot, D. S. and Voigt, A. (2012), 'A False Positive for Ocean Glint on Exoplanets: The Latitude-Albedo Effect', *The Astrophysical Journal* **752**, L3.

Cox, C. and Munk, W. (1954), 'Measurement of the roughness of the sea surface from photographs of the sun's glitter', *Journal of the Optical Society of America (1917-1983)* **44**, 838–850.

Cox, C. and Munk, W. (1956), 'Slopes of the sea surface deduced from photographs of sun glitter', *Scripps Institution of Oceanography* **44**, 401–488.

de Haan, J. F., Bosma, P. B. and Hovenier, J. W. (1987), 'The adding method for multiple scattering calculations of polarized light', *Astronomy & Astrophysics* **183**, 371–391.

de Rooij, W. A. and van der Stap, C. C. A. H. (1984), 'Expansion of Mie scattering matrices in generalized spherical functions', *Astronomy & Astrophysics* **131**, 237–248.

Deirmendjian, D. (1969), *Electromagnetic scattering on spherical polydispersions.*, Elsevier Scientific Publishing, New York.

Deschamps, P.-Y., Breon, F.-M., Leroy, M., Podaire, A., Bricaud, A., Buriez, J.-C. and Seze, G. (1994), 'The POLDER mission: instrument characteristics and scientific objectives', *IEEE Transactions on Geoscience and Remote Sensing* **32**, 598–615.

Deuzé, J. L., Herman, M. and Santer, R. (1989), 'Fourier series expansion of the transfer equation in the atmosphere-ocean system', *Journal of Quantitative Spectroscopy & Radiative Transfer* **41**, 483–494.

Donelan, M. A. and Pierson, W. J. (1987), 'Radar scattering and equilibrium ranges in wind-generated waves with application to scatterometry', *Journal of Geophysics Research* **92**, 4971–5029.

Ebuchi, N. and Kizu, S. (2001), 'Probability Distribution of Surface Wave Slope Derived Using Sun Glitter Images From Geostationary Meteorological Satellite and Surface Vector Winds From Scatterometers', *Journal of Oceanography* **58**, 477–486.

Garcia, R. D. M. (2012*a*), 'Fresnel boundary and interface conditions for polarized radiative transfer in a multilayer medium', *Journal of Quantitative Spectroscopy and Radiative Transfer* **113**, 306–317.

Garcia, R. D. M. (2012*b*), 'Response to "Comment on the transmission matrix for a dielectric interface"', *Journal of Quantitative Spectroscopy and Radiative Transfer* **113**, 2251–2254.

Ghafoor, N. A. L., Zarnecki, J. C., Challenor, P. and Srokosz, M. A. (2000), 'Wind-driven surface waves on Titan', *Journal of Geophysical Research* **105**, 12077–12092.

Giancoli, D. C. (2008), *Physics for Scientists and Engineers with Modern Physics*, Pearson Education, Inc, London.

Gitelson, A. A., Gurlin, D., Moses, W. J. and Barrow, T. (2009), 'A bio-optical algorithm for the remote estimation of the chlorophyll-a concentration in case 2 waters', *Environmental Research Letters* **4**, 045003.

Goldstein, D. (2003), *Polarized light*, Marcel Dekker Inc., New York.

Hale, G. M. and Querry, M. R. (1973), 'Optical constants of water in the 200-nm to 200-micrometer wavelength region', *Applied Optics* **12**, 555–563.

Hansen, J. E. and Hovenier, J. W. (1974*a*), 'Interpretation of the polarization of Venus.', *Journal of Atmospheric Sciences* **31**, 1137–1160.

Hansen, J. E. and Hovenier, J. W. (1974*b*), Nature of the Venus clouds as derived from their polarization., *in* 'Exploration of the Planetary System', Vol. 65, pp. 197–200.

Hansen, J. E. and Travis, L. D. (1974), 'Light scattering in planetary atmospheres', *Space Science Reviews* **16**, 527–610.

Hovenier, J. W. (1969), 'Symmetry Relationships for Scattering of Polarized Light in a Slab of Randomly Oriented Particles.', *Journal of Atmospheric Sciences* **26**, 488–499.

Hovenier, J. W. (1971), 'Multiple Scattering of Polarized Light in Planetary Atmospheres', *Astronomy & Astrophysics* **13**, 7–29.

Hovenier, J. W., Van Der Mee, C. and Domke, H., eds (2004), *Transfer of polarized light in planetary atmospheres : basic concepts and practical methods*, Vol. 318 of *Astrophysics and Space Science Library*.

Hovenier, J. W. and van der Mee, C. V. M. (1983), 'Fundamental relationships relevant to the transfer of polarized light in a scattering atmosphere', *Astronomy & Astrophysics* **128**, 1–16.

Jonasz, M. and Fournier, G. (2011), *Light scattering by particles in water: theoretical and experimental foundations*, Elsevier.

Joos, F., Schmid, H. M., Gisler, D., Feldt, M., Brandner, W., Stam, D. M., Quirrenbach, A. and Stuik, R. (2005), Spectropolarimetry of CH4 bands of solar system planets, *in* 'Astronomical Polarimetry: Current Status and Future Directions', Vol. 343, p. 189.

Kamp, A. (2007), *Space Instrumentation Engineering, Lecture Notes*, Delft University of Technology, Faculty of Aerospace Engineering, Astrodynamics and Satellite Systems, Delft.

Karalidi, T., Stam, D. M. and Hovenier, J. W. (2011), 'Flux and polarisation spectra of water clouds on exoplanets', *Astronomy and Astrophysics* **530**, A69.

Karalidi, T., Stam, D. M. and Hovenier, J. W. (2012), 'Looking for the rainbow on exoplanets covered by liquid and icy water clouds', *Astronomy and Astrophysics* **548**, A90.

Kasper, M., Beuzit, J.-L., Verinaud, C., Gratton, R. G., Kerber, F., Yaitskova, N., Boccaletti, A., Thatte, N., Schmid, H. M., Keller, C., Baudoz, P., Abe, L., Aller-Carpentier, E., Antichi, J., Bonavita, M., Dohlen, K., Fedrigo, E., Hanenburg, H., Hubin, N., Jager, R., Korkiakoski, V., Martinez, P., Mesa, D., Preis, O., Rabou, P., Roelfsema, R., Salter, G., Tecza, M. and Venema, L. (2010), EPICS: direct imaging of exoplanets with the E-ELT, *in* 'Ground-based and Airborne Instrumentation for Astronomy III', Vol. 7735 of *Proceedings of the International Society for Optical Engineering*, pp. 77352E–77352E–9.

Keller, C. U. (2006), Design of a polarimeter for extrasolar planetary systems characterization, *in* 'Society of Photo-Optical Instrumentation Engineers (SPIE) Conference Series', Vol. 6269 of *Proceedings of the SPIE*, p. 62690T.

Kemp, J. C., Henson, G. D., Steiner, C. T., Beardsley, I. S. and Powell, E. R. (1987), 'The optical polarization of the Sun, measured at a sensitivity of parts in ten million', *Nature* **328**, 92.

Koepke, P. (1984), 'Effective reflectance of oceanic whitecaps', *Applied Optics* **23**, 1816–1824.

Lacis, A. A. and Hansen, J. (1974), 'A Parameterization for the Absorption of Solar Radiation in the Earth's Atmosphere.', *Journal of Atmospheric Sciences* **31**, 118–133.

Lenoble, J., Herman, M., Deuzé, J. L., Lafrance, B., Santer, R. and Tanré, D. (2007), 'A successive order of scattering code for solving the vector equation of transfer in the earth's atmosphere with aerosols', *Journal of Quantitative Spectroscopy and Radiative Transfer* **107**, 479–507.

Levy, R. C., Remer, L. A. and Kaufman, Y. J. (2004), 'Effects of Neglecting Polarization on the MODIS Aerosol Retrieval Over Land', *IEEE Transactions on Geoscience and Remote Sensing* **42**, 2576–2583.

Lorenz, R. D., Newman, C. and Lunine, J. I. (2010), 'Threshold of wave generation on Titan's lakes and seas: Effect of viscosity and implications for Cassini observations', *Icarus* **207**, 932–937.

Mason, J. D., Cone, M. T. and Fry, E. S. (2016), 'Ultraviolet (250-550 nm) absorption spectrum of pure water', *Applied Optices* **55**, 7163.

Mermelstein, M. D., Shettle, E. P., Takken, E. H. and Priest, R. G. (1994), 'Infrared radiance and solar glint at the ocean-sky horizon', *Applied Optics* **33**, 6022–6034.

Mie, G. (1908), 'Beiträge zur Optik trüber Medien, speziell kolloidaler Metallösungen', *Annalen der Physik* **330**, 377–445.

Mishchenko, M. I. and Travis, L. D. (1997), 'Satellite retrieval of aerosol properties over the ocean using polarization as well as intensity of reflected sunlight', *Journal of Geophysical Research* **102**, No.D14:16989–17013.

Mishchenko, M. I., Travis, L. D. and Lacis, A. A. (2002), *Scattering, absorption, and emission of light by small particles*, Cambridge University Press.

Mobley, C. D. (1994), *Light and water: radiative transfer in natural waters*, Academic press, University of Michigan.

Mobley, C. D., Werdell, J., Franz, B., Ahmad, Z. and Bailey, S. (2016), Atmospheric correction for satellite ocean color radiometry, Technical report, NASA Goddard Space Flight Center.
URL: *https://oceancolor.gsfc.nasa.gov/docs/technical/NASA-TM-2016-217551.pdf*

Monahan, E. C. and Ó Muircheartaigh, I. (1980), 'Optimal Power-Law Description of Oceanic Whitecap Coverage Dependence on Wind Speed', *Journal of Physical Oceanography* **10**, 2094–2099.

Morel, A. (1974), 'Optical properties of pure water and pure sea water', *Optical Aspects of Oceanography* **1**, 1–24.

Morel, A. (1980), 'In-water and remote measurements of ocean color', *Boundary-Layer Meteorology* **18**, 177–201.

Morel, A. (1988), 'Optical modeling of the upper ocean in relation to its biogenous matter content (case I waters)', *Journal of Geophysics Research* **93**, C9: 10749–10768.

Morel, A. and Gentili, B. (1991), 'Diffuse reflectance of oceanic waters: its dependence on sun angle as influenced by the molecular scattering contribution', *Applied Optics* **30**, 4427–4438.

Morel, A. and Maritorena, S. (2001), 'Bio-optical properties of oceanic waters: A reappraisal', *Journal of Geophysics Research* **106**, 7163–7180.

Morel, A. and Prieur, L. (1977), 'Analysis of variations in ocean color', *Limnology and oceanography* **22**(4), 709–722.

Naderi, F. M., Freilich, M. H. and Long, D. G. (1991), 'Spaceborne radar measurement of wind velocity over the ocean - An overview of the NSCAT scatterometer system', *IEEE Proceedings* **79**, 850–866.

Nakajima, T. (1983), 'Effect of wind-generated waves on the transfer of solar radiation in the atmosphere-ocean system', *Journal of Quantitative Spectroscopy and Radiative Transfer* **29**, 521–537.

NOAA (2016), 'National Oceanic and Atmospheric Administration', *National Ocean Serive, US Deparment of Commerce* .
URL: *https://oceanservice.noaa.gov/*

Peck, E. R. and Reeder, K. (1972), 'Dispersion of Air', *Journal of the Optical Society of America (1917-1983)* **62**, 958.

Pope, R. M. and Fry, E. S. (1997), 'Absorption spectrum (380 -700 nm) of pure water. II. Integrating cavity measurements', *Applied Optics* **36**, 8710–8723.

Prieur, L. and Sathyendranath, S. (1981), 'An optical classification of coastal and oceanic waters based on the specific spectral absorption curves of phytoplankton pigments, dissolved organic matter, and other particulate materials', *Limnology and Oceanography* **26**(4), 671–689.

Ricker, G. R., Winn, J. N., Vanderspek, R., Latham, D. W., Bakos, G. A., Bean, J. L., Berta-Thompson, Z. K., Brown, T. M., Buchhave, L., Butler, N. R., Butler, R. P., Chaplin, W. J., Charbonneau, D., Christensen-Dalsgaard, J., Clampin, M., Deming, D., Doty, J., De Lee, N., Dressing, C., Dunham, E. W., Endl, M., Fressin, F., Ge, J., Henning, T., Holman, M. J., Howard, A. W., Ida, S., Jenkins, J. M., Jernigan, G., Johnson, J. A., Kaltenegger, L., Kawai, N., Kjeldsen, H., Laughlin, G., Levine, A. M., Lin, D., Lissauer, J. J., MacQueen, P., Marcy, G., McCullough, P. R., Morton, T. D., Narita, N., Paegert, M., Palle, E., Pepe, F., Pepper, J., Quirrenbach, A., Rinehart, S. A., Sasselov, D., Sato, B., Seager, S., Sozzetti, A., Stassun, K. G., Sullivan, P., Szentgyorgyi, A., Torres, G., Udry, S. and Villasenor, J. (2014), 'Transiting exoplanet survey satellite', *Journal of Astronomical Telescopes, Instruments, and Systems* **1**(1), 014003.
URL: *http://dx.doi.org/10.1117/1.JATIS.1.1.014003*

Rossi, L., Berzosa-Molina, J. and Stam, D. M. (2018), 'PyMieDAP: a Python–Fortran tool to compute fluxes and polarization signals of (exo)planets', *ArXiv e-prints* p. arXiv:1804.08357.

Rossi, L. and Stam, D. M. (2017), 'Using polarimetry to retrieve the cloud coverage of Earth-like exoplanets', *Astronomy & Astrophysics* **607**, A57.

Rozanov, V. V., Rozanov, A. V., Kokhanovsky, A. A. and Burrows, J. P. (2014), 'Radiative transfer through terrestrial atmosphere and ocean: Software package SCIATRAN', *Journal of Quantitative Spectroscopy and Radiative Transfer* **133**, 13–71.

Sancer, M. (1969), 'Shadow-corrected electromagnetic scattering from a randomly rough surface', *IEEE Transactions on Antennas and Propagation* **17**, 577–585.

Sayer, A. M., Thomas, G. E. and Grainger, R. G. (2010), 'A sea surface reflectance model for (A)ATSR, and application to aerosol retrievals', *Atmospheric Measurement Techniques* **3**, 813–838.

Schmid, H. M., Beuzit, J.-L., Feldt, M., Gisler, D., Gratton, R., Henning, T., Joos, F., Kasper, M., Lenzen, R., Mouillet, D., Moutou, C., Quirrenbach, A., Stam, D. M., Thalmann, C., Tinbergen, J., Verinaud, C., Waters, R. and Wolstencroft, R. (2006), Search and investigation of extra-solar planets with polarimetry, *in* C. Aime and F. Vakili, eds, 'IAU Colloq. 200: Direct Imaging of Exoplanets: Science & Techniques', pp. 165–170.

Shaw, J. A. and Churnside, J. H. (1997), 'Scanning-laser glint measurements of sea-surface slope statistics', *Applied Optics* **36**, 4202–4213.

Shkuratov, Y., Kreslavsky, M., Kaydash, V., Videen, G., Bell, J., Wolff, M., Hubbard, M., Noll, K. and Lubenow, A. (2005), 'Hubble Space Telescope imaging polarimetry of Mars during the 2003 opposition', *Icarus* **176**, 1–11.

Smith, B. (1967), 'Geometrical shadowing of a random rough surface', *IEEE Transactions on Antennas and Propagation* **15**, 668–671.

Smith, R. C. and Baker, K. S. (1981), 'Optical properties of the clearest natural waters (200-800 nm)', *Applied Optics* **20**, 177–184.

Sogandares, F. M. and Fry, E. S. (1997), 'Absorption spectrum (340 -640 nm) of pure water. I. Photothermal measurements', *Applied Optics* **36**, 8699–8709.

Stam, D. M. (2008), 'Spectropolarimetric signatures of Earth-like extrasolar planets', *Astronomy & Astrophysics* **482**, 989–1007.

Stam, D. M., Aben, I. and Helderman, F. (2002), 'Skylight polarization spectra: Numerical simulation of the Ring effect', *Journal of Geophysical Research (Atmospheres)* **107**, 4419.

Stam, D. M., de Rooij, W. A., Cornet, G. and Hovenier, J. W. (2006), 'Integrating polarized light over a planetary disk applied to starlight reflected by extrasolar planets', *Astronomy & Astrophysics* **452**, 669–683.

Stam, D. M., Hovenier, J. W. and Waters, L. B. F. M. (2004), 'Using polarimetry to detect and characterize Jupiter-like extrasolar planets', *Astronomy & Astrophysics* **428**, 663–672.

Stam, D. M., Karalidi, T., Batista, S. and de Haan, J. (2014), PRM: A database with (exo)Planetary Reflection Matrices. Manuscript.
URL: *ftp://deos.tudelft.nl/pub/daphne/PRM_DATABASE/DMStam_PRM_database_draft_paper.pdf*

Sun, W. and Lukashin, C. (2013), 'Modeling polarized solar radiation from the ocean-atmosphere system for CLARREO inter-calibration applications', *Atmospheric Chemistry & Physics* **13**, 10303–10324.

Takashima, T. (1975), 'A new approach of the adding method for the computations of emergent radiation of an inhomogeneous plane-parallel planetary atmosphere', *Astrophysics and Space Science* **36**, 319–328.

Thomas, G. E. and Stamnes, K. (2002), *Radiative Transfer in the Atmosphere and Ocean*.

Tsang, L., Kong, J. A. and Shin, R. T. (1985), *Theory of microwave remote sensing*, Wiley Interscience, New York.

van de Hulst, H. C. (1957), *Light scattering by small particles*, Dover Publications Inc., New York.

van de Hulst, H. C. (1980), *Multiple light scattering. Vols. 1 and 2*, Academic Press, New York.

Vladilo, G., Murante, G., Silva, L., Provenzale, A., Ferri, G. and Ragazzini, G. (2013), 'The Habitable Zone of Earth-like Planets with Different Levels of Atmospheric Pressure', *The Astrophysical Journal* **767**, 65.

Voss, K. J. and Fry, E. S. (1984), 'Measurement of the Mueller matrix for ocean water', *Applied Optics* **23**, 4427–4439.

Wallace, J. M. and Hobbs, P. V. (2006), *Atmospheric science: an introductory survey*, Elsevier Academic Press, Amsterdam, Boston.

Warren, S. G. (1984), 'Optical constants of ice from the ultraviolet to the microwave', *Applied Optic* **23**, 1206–1225.

Whitlock, C. H., Bartlett, D. S. and Gurganus, E. A. (1982), 'Sea foam reflectance and influence on optimum wavelength for remote sensing of ocean aerosols', *Geophysics Research Letters* **9**, 719–722.

Williams, D. M. and Gaidos, E. (2008), 'Detecting the glint of starlight on the oceans of distant planets', *Icarus* **195**, 927–937.

Wolszczan, A. and Frail, D. A. (1992), 'A planetary system around the millisecond pulsar PSR1257 + 12', *Nature* **355**, 145–147.

Wu, J. (1972), 'Sea-Surface Slope and Equilibrium Wind-Wave Spectra', *Physics of Fluids* **15**, 741–747.

Xu, F., Dubovik, O., Zhai, P.-W., Diner, D. J., Kalashnikova, O. V., Seidel, F. C., Litvinov, P., Bovchaliuk, A., Garay, M. J., van Harten, G. and Davis, A. B. (2016), 'Joint retrieval of aerosol and water-leaving radiance from multispectral, multiangular and polarimetric measurements over ocean', *Atmospheric Measurement Techniques* **9**, 2877–2907.

Yang, J., Cowan, N. B. and Abbot, D. S. (2013), 'Stabilizing Cloud Feedback Dramatically Expands the Habitable Zone of Tidally Locked Planets', *The Astrophysical Journal* **771**, L45.

Young, A. T. (1982), 'Rayleigh scattering', *Physics Today* **35**, 42–48.

Zhai, P.-W., Hu, Y., Chowdhary, J., Trepte, C. R., Lucker, P. L. and Josset, D. B. (2010), 'A vector radiative transfer model for coupled atmosphere and ocean systems with a rough interface', *Journal of Quantitative Spectroscopy and Radiative Transfer* **111**, 1025–1040.

Zhai, P.-W., Kattawar, G. W. and Hu, Y. (2012), 'Comment on the transmission matrix for a dielectric interface', *Journal of Quantitative Spectroscopy and Radiative Transfer* **113**, 1981–1984.

Zhang, H. and Wang, M. (2010), 'Evaluation of sun glint models using MODIS measurements', *Journal of Quantitative Spectroscopy and Radiative Transfer* **111**, 492–506.

Ziemer, R. E., Tranter, W. H. and Fanin, D. R. (1993), *Signals and systems: Continuous and discrete*, Macmillan Publishing Company, New York, Toronto.

Zugger, M. E., Kasting, J. F., Williams, D. M., Kane, T. J. and Philbrick, C. R. (2010), 'Light Scattering from Exoplanet Oceans and Atmospheres', *The Astrophysical Journal* **723**, 1168–1179.

Zugger, M. E., Kasting, J. F., Williams, D. M., Kane, T. J. and Philbrick, C. R. (2011*a*), 'Erratum: 'Light Scattering from Exoplanet Oceans and Atmospheres'', *The Astrophysical Journal* **739**, 55(5pp).

Zugger, M. E., Kasting, J. F., Williams, D. M., Kane, T. J. and Philbrick, C. R. (2011*b*), 'Searching for Water Earths in the Near-infrared', *The Astrophysical Journal* **739**, 12.